Measurement of protein synthesis rate and synaptic density by using [^{11}C]leucine and [^{18}F]UCB-H PET tracers respectively in a model for Alzheimer's disease, rat TgF344-AD

A thesis submitted to the University of Manchester for the degree of Doctor of Philosophy in the Faculty of Biology, Medicine and Health

2020

Daniela Bochicchio
School of Health Sciences

Table of Contents

List of figures 5
List of tables 12
List of abbreviations 13
Abstract 19
Declaration 21
Copyright Statement 22
Dedication 23
Acknowledgements 24
1 Introduction 25
1.1 Genetics causes and risk factors for Alzheimer's disease 25
1.2 Symptoms and biomarkers for Alzheimer's disease 28
1.3 Alzheimer's disease theories and mechanisms 30
1.3.1 The APP protein 32
1.3.2 Tau 37
1.3.3 Alterations in neurotransmission system 40
1.3.4 Neuroinflammation 46
1.3.5 The Blood Brain Barrier 50
1.4 Memory deficits in AD 52
1.5 Protein synthesis 54
1.5.1 eIF2 and the UPR pathway 55
1.5.2 mTORC 59
1.6 Apoptosis and organelles involvement 61
1.7 PSR and Alzheimer's disease 64
1.8 The synaptic vesicles SV2A 65
1.9 Animal model of Alzheimer's disease 67
1.9.1 Mice 67
1.9.2 Rats 69
1.9.3 TgF344-AD rat model used in this work 70
1.10 PET imaging 73
1.10.1 PET imaging physics 73
1.10.2 Data correction Inveon PET/CT 73

1.10.3 Use of PET in Alzheimer's disease 76
1.11 [^{11}C]Leucine and [^{18}F]UCBH: new tracers for Alzheimer's disease? 79
1.11.1 Amino acids PET tracer : [^{11}C]leucine 80
1.11.2 PET tracer for synaptic vesicles 87
2 Aims of project 89
3 Materials and methods 91
3.1 Animals 91
3.2 Scanning protocol 92
3.3 [^{11}C]Leucine study and measurement of the Arterial Input Function (AIF) 93
3.4 [^{18}F]UCB-H Study 95
3.5 Image analysis 96
3.6 Modelling of [^{11}C]leucine uptake to determine PSR using MICK software 96
3.7 Behaviour tests 98
3.7.1 Morris water maze and reversal Morris water Maze 98
3.7.2 Open Field 100
3.7.3 Smell tests 101
3.8 Immunohistochemistry (IHC) 102
3.8.1 DAB staining protocol 102
3.8.2 Western blot analysis 103
3.9 Statistical analysis of PET data 105
4 Results of the PET studies 106
4.1 [^{11}C]leucine 106
4.1.1 [^{11}C]leucine as a tool to measure the protein synthesis rate in brain 109
4.1.2 Measurement of unlabelled leucine in plasma 110
4.1.3 [^{11}C]leucine free fraction in plasma 113
4.1.4 PSR analysis by using individual IF and individual unlabelled leucine concentration in arterial plasma 116
4.1.5 Validation of [^{11}C]leucine as a tracer to measure PSR 117
4.1.6 Input Function measurement for longitudinal study 119
4.1.7 K_{cplx} and PSR in longitudinal study 121
4.2 [^{18}F]UCB-H study 126
5 Behaviour 133

5.1 Morris water maze and reversal MWM 133
5.2 Open Field 146
5.3 Smell tests 148
6 Ex-vivo analysis 151
6.1 Immunohistochemistry (IHC) 151
6.2 Western Blot 152
7 Discussion 153
7.1 [^{11}C]leucine PET 153
7.2 [^{18}F]UCB-H 164
7.3 Behavioural and *ex-vivo* studies 168
8 Conclusions and future perspectives 176
9 References 178
10 Appendix 195
10.1 Appendix: future publications planned 195
10.2 Appendix: previous published work 195
10.3 Appendix: poster and oral presentation 195
10.4 Ex-vivo protocols 196
10.4.1 Immunohistochemistry (IHC)/Immunofluorescence 196
10.4.2 DAB staining protocol 197
10.4.3 Homogenisation samples 199
10.4.4 Bradford protein assay 200
10.4.5 Western Blot 201

Word Count: 45,216

List of figures

FIGURE 1: AGE OF ALZHEIMER'S DISEASE ONSET AS A FUNCTION OF THE GENES INVOLVED. PEOPLE AFFECTED BY DOWN'S SYNDROME HAVE A HIGH RISK TO DEVELOP AD AT AN EARLIER AGE. EARLY ONSET AD STARTS BEFORE 65 YEARS OF AGE AND THE LATE ONSET AFTER 65 YEARS. DIFFERENT GENE MUTATIONS ARE INVOLVED IN THE DEVELOPING OF AD. APOE, APOLIPOPROTEIN E GENE; APP, AMYLOID PRECURSOR PROTEIN GENE; EOAD, EARLY ONSET ALZHEIMER'S DISEASE; LOAD, LATE-ONSET ALZHEIMER'S DISEASE; PSEN1/2, PRESENILIN 1/2 GENE [10]. 26

FIGURE 2: DIAGRAM SHOWING DIFFERENT BRAIN ALTERATIONS DURING THE PROGRESSION OF AD. HALLMARKS, AMYLOID AND TAU, ARE PRESENT BEFORE THE START OF THE MEMORY IMPAIRMENTS SO THAT THE COGNITIVE SYMPTOMS (GREEN CURVE) APPEAR ONLY LATER ON WHEN THE BRAIN HAS BEEN ALREADY COMPROMISED [29]. 30

FIGURE 3: AMYLOID HYPOTHESIS. THE AMYLOID HYPOTHESIS IS BASED ON THE ASSUMPTION THAT THE AB AGGREGATION PROMOTES A CASCADES OF EVENTS STARTING WITH SYNAPTIC DYSFUNCTION AND NEUROINFLAMMATION, THEN NFT THAT LEADS AT NEURONAL DEATH [36]. 31

FIGURE 4: THE AMYLOIDOGENIC AND NON-AMYLOIDOGENIC PATHWAYS OF APP. THE NON-AMYLOIDOGENIC PATHWAY IS CHARACTERISED BY THE A-SECRETASE CUT THAT GENERATES THE SAPP-A AND C83 FRAGMENT. B-SECRETASE CLEAVAGE PROMOTES THE AMYLOIDOGENIC PATHWAY AND THE PRODUCTION OF SAPP-B AND THE FRAGMENT C99. C99 AND C83 ARE THEN CLEAVED BY Γ-SECRETASE PRODUCING ACID AND P3 FRAGMENTS (NON-AMYLOIDOGENIC PATHWAY) (NOT SHOWN IN FIGURE) AND ACID AND AB PEPTIDE (AMYLOIDOGENIC PATHWAY). THE AMYLOID PEPTIDE CAN AGGREGATE AND FORMS OLIGOMERS AND SENILE PLAQUES [64]. 35

FIGURE 5: TAU ISOFORMS IN HUMAN BRAIN. DIFFERENT SPLICING OF EXONS 2, 3 AND 10 INDUCE THE PRODUCTION OF SIX ISOFORMS THAT DIFFER FOR THE C-TERMINAL REGIONS AND THE N-TERMINAL REGION AND THEREFORE CHANGING OF MICROTUBLES R DOMAIN AT C-TERMINAL AND THE BINDING AT NEURAL PLASMA N DOMAIN AT THE N-TERMINAL. EXONS 4A, 6 NAD 8 ARE NOT TRANSCRIBED IN BRAIN [78]. 38

FIGURE 6: REPRESENTATION OF THE MAIN CENTRAL CHOLINERGIC PATHWAYS IN HEALTHY BRAIN (A) AND AD BRAIN (B). BLUE ARROWS ARE THE NORMAL PATHWAY AND RED ARROWS THE DEGENERATED PATHWAYS IN ALZHEIMER'S DISEASE. BRAIN REGIONS CC: CORPUS CALLOSUM; CB: CEREBELLUM; C: CORTEX; H: HIPPOCAMPUS; TH: *THALAMUS*; OB: OLFACTORY BULB; OT: OLFACTORY TRACT; A: AMYGDALA. CH1: MEDIAL SEPTUM; CH2: ASCENDING DIAGONAL BAND OF BROCA; CH3: HORIZONTAL LIMB DIAGONAL BAND OF BROCA, CH4: *NUCLEUS BASALIS* OF MEYNERT; CH5: *PEDUNCOLO-PONTINE NUCLEUS* ; CH6: DORSOLATERAL TEGMENTAL *NUCLEUS*. IV: 4TH VENTRICLE. THE CHOLINERGIC SYSTEM NOT INVOLVED IN NEURODEGENERATION IS NOT SHOWN IN THIS PICTURE [90]. 40

FIGURE 7: ACETYLCHOLINE SYNTHESIS AND DEGRADATION. ACETYLCHOLINE (ACH) IS SYNTHESIZED IN NEURONS FROM CHOLINE AND ACETYL-COENZYME A BY THE ENZYME ACETYLTRANSFERASE. ACH IS THEN PACKED IN SYNAPTIC VESICLES AND RELEASED INTO THE SYNAPTIC CLEFT WHERE IT BINDS MUSCARINIC AND NICOTINIC RECEPTORS. RELEASED ACH IS DEGRADED INTO CHOLINE AND ACETATE BY THE ENZYME ACETYLCHOLINESTERASE (ACHE) AND CHOLINE IS RECYCLED BACK INTO NEURONS [91]. 42

FIGURE 8: LTP AND LTD EFFECT ON POST-SYNAPTIC NEURONS. A WEAK ACTIVATION IN PRESYNAPTIC NEURONS INDUCES A MODERATE CALCIUM INFLUX THROUGH NMDA RECEPTORS. THIS EVENT LEADS THE ACTIVATION OF PHOSPHATASES THAT DEPHOSPHORYLATE AMPA RECEPTORS AND INDUCE THE RECEPTOR ENDOCYTOSIS. A STRONG ACTIVATION CAUSES A STRONG DEPOLARIZATION THAT IS ABLE TO TRIG LTP AND ACTIVATE THE CAMKII, RECEPTOR PHOSPHORYLATION, AND EXOCYTOSIS [105]. 43

FIGURE 9: BRAIN REGIONS INVOLVED IN THE FORMATION AND STORAGE OF MEMORY. MEMORY CAN BE DEVIDED IN TWO TYPES DECLARATIVE AND NON DELARATIVE. DECLARATIVE MEMORY IS THE EXPLICIT LONG TERM MEMORY ACQUIRED BY EXPIRIENCES. THE IMPLICIT LONG TERM MEMORY, ALSO CALLED PROCEDURAL IS ACQUIRED BY UNCONSCIUS MEMORIES SUCH AS SKILLS [173]. 53

FIGURE 10: HIPPOCAMPAL CIRCUITS. INFORMATION COMING FROM THE ENTORHINAL CORTEX REACH THE HIPPOCAMPUS THROUGH THE PERFORANT PATHWAYS. THE PERFORANT PATHWAY CAN PROJECT DIRECTLY TO THE CA1 REGIONS OR STARTS THE TRI-SYNAPTIC EXCITATORY PATHWAY. IN THE TRI-SYNAPTIC EXCITATORY PATHWAY, THE *GYRUS DENTATUS* IS EXCITED BY THE PERFORANT PATHWAY, THEN THE *GYRUS DENTATUS* PROJECTS EXCITATORY SYNAPSES TO THE PYRAMIDAL CELLS IN THE CA3 REGION THROUGH THE MOSSY FIBRE PATHWAY. CA3 PROJECT TO CA1 THROUGH THE SCHAFFER COLLATERAL PATHWAY AND FROM THERE THE PROJECTIONS GO BACK TO THE CORTICAL SENSORY AREA FROM WHICH THE INPUT HAS STARTED [177]. 54

FIGURE 11: ATTENUATION OF PROTEIN SYNTHESIS DUE TO THE PHOSPHORYLATION OF A-SUBUNIT BY DIFFERENT KINASES. THE EUKARYOTIC INITIATION FACTOR 2 (EIF2) IS A TERNARY COMPLEX CONSISTING OF A, B, AND Γ SUBUNITS. EIF2 CAN BIND THE GDP (INACTIVE) AND GTP (ACTIVE), BUT ONLY THE ACTIVE FORM CAN BIND MET-TRNA$_i$. THE ACTIVE FORM PROMOTES THE DELIVERY OF THE INITIATOR MET-TRNA$_i$ TO THE 40S RIBOSOMAL SUBUNIT AND INDUCE THE INITIATION OF TRANSLATION. STRESS CONDITION CAN INDUCE THE ACTIVATION OF KINASES THAT PHOSPHORYLATE THE A SUBUNIT OF EIF2 LOCKING EIF2 IN AN INACTIVE EIF2 COMPLEX WITH EIF2B [186]. 57

FIGURE 12: ACTIVATION OF UPR PATHWAY DURING STRESS CONDITION. ALTERATION IN CELLULAR HOMEOSTASIS PROMOTE THE ACTIVATION OF THREE STRESS ER SENSORS, PERK, IRE-1 AND ATF6. DIFFERENT RESPONSE CAN BE INDUCED: ATTENUATION OF PROTEIN SYNTHESIS, PRO-SURVIVAL MECHANISMS SUCH AS ERAD BUT THE PROLONGED ACTIVITY CAN ALSO PROMOTES THE CELLULAR DEATH, THEREFORE THE APOPTOTIC PROCESSES [190]. 58

FIGURE 13: MTORC SIGNALLING IN NEURONS. DIFFERENT STIMULI CAN PROMOTE THE ACTIVATION OF MTORC1 AND MTORC2 SUCH AS NUTRIENTS, CYTOKINES AND HORMONES. THE ACTIVATION OF THESE FACTORS INDUCES DIFFERENT CELLULAR RESPONSES. MTORC1 IS MAINLY INVOLVED IN THE REGULATION OF PROTEIN SYNTHESIS, AUTOPHAGY, LIPID METABOLISM AND CONTROL OF MITOCHONDRIA; MTORC2 HAS THE ROLE TO CONTROL CYTOSKELETAL FUNCTIONS AND CELLULAR PROLIFERATION [207]. 61

FIGURE 14: REGULATION OF APOPTOSIS DURING ER STRESS CONDITION. ER ALTERATION CAN INDUCE THE ACTIVATION OF PERK AND IRE1A. UPON ACTIVATION PERK PROTEINS CAN INDUCES THE TRANSCRIPTION OF GENES INVOLVED IN APOPTOSIS. ON THE OTHER HAND IRE1A SERVES AS A SCAFFOLD PROTEIN TO FORM A COMPLEX WITH TRAF2 THAT PROMOTES ALSO THE EXTRINSIC APOPTOTIC PATHWAY. EXCESSIVE TRANSFER OF CA^{2+} FROM ER CAUSES THE OPENING OF THE PERMEABILITY TRANSITION PORE (PTP), WHICH LEADS TO MITOCHONDRIAL DYSFUNCTION AND THE ACTIVATION OF INTRINSIC APOPTOSIS PATHWAY [206]. ... 63

FIGURE 15: REPRESENTATION OF COMMUNICATION BETWEEN TWO NEURONS. WHEN AN ACTION POTENTIAL REACHES THE PRESYNAPTIC NEURON TERMINAL, IT INDUCES THE FUSION OF SYNAPTIC VESICLES WITH THE MEMBRANE, STIMULATING THE RELEASE OF NEUROTRANSMITTERS. THE NEUROTRANSMITTERS IN THE SYNAPTIC CLEFT IS ABLE TO BIND RECEPTORS EXPRESSED ON THE POST-SYNAPTIC NEURONS, PROMOTING THEIR ACTION. LGIC = LIGAND-GATED ION CHANNELS AND GPCR = G-PROTEIN–COUPLED RECEPTORS [227]. 65

FIGURE 16: REPRESENTATION OF ANNIHILATION PROCESS OF A POSITRON AND AN ELECTRON. WHEN THE ANNIHILATION HAPPENS 2 PHOTONS 511KEV, ARE EMITTED IN OPPOSITE DIRECTION (180˚). 73

FIGURE 17: DIFFERENT TYPES OF COINCIDENCES DETECTED BY PET SCAN [258]. SCATTERED COINCIDENCE ARE CAUSED WHEN TWO PHOTONS ARE DIRECTED TO FALSE LOCATIONS ON THE DETECTOR AND RANDOM COINCIDENCE CAN ALSO BE DETECTED FROM TWO SEPARATE ANNIHILATIONS THAT HIT DETECTORS WITHIN THE COINCIDENCE TIMING WINDOW OF THE DETECTOR. 75

FIGURE 18: BRAIN UPTAKE OF [^{18}F]FDG AND PIB. EVALUATION OF [^{18}F]FDG AND PIB. IN CONTROL, NON-AMNESTIC MCI, AMNESTIC MCI AND PATIENTS AFFECTED BY AD. REGIONS WITH GREATER UPTAKE ARE SHOWN IN YELLOW AND RED [267]. . 77

FIGURE 19: AD PATIENTS AND HEALTHY CONTROLS (HC) PET SCAN BY USING [^{18}F]FLORTAUCIPIR ALSO KNOWN AS [^{18}F]T807. THE RADIOTRACER [^{18}F]T807 SHOWS A HIGH SPECIFICITY FOR PAIRED HELICAL FILAMENTS OF TAU. PATIENTS AFFECTED BY AD HAVE A HIGH UPTAKE MAINLY IN NEOCORTEX REGIONS [270]. 78

FIGURE 20: AMINO ACID STRUCTURE. COOH IS THE CARBOXYLIC ACID GROUP (1-C, GREEN), -NH2 THE AMINO GROUP (RED), AN ALPHA-CARBON ATOM -C- AND A BRANCHED-CHAIN GROUP (R, BLUE). 82

FIGURE 21: FULL MODEL OF LEUCINE IN BRAIN. CP IS THE CONCENTRATION OF LEUCINE FROM PLASMA TO TISSUE; CE THE CONCENTRATION IN THE EXTRACELLULAR SPACE, AND CM INTRACELLULAR. CP, CE, AND CM * ARE THE CONCENTRATION OF LABELLED LEUCINE. THE CONTRIBUTION OF LEUCINE RNAT ARE SHOWN AS CPP AND CPP* RESPECTIVELY WHEN IS LEUCINE UNLABELLED AND LABELLED BY ^{14}C. K ARE THE RATE CONSTANTS: K_1 FROM PLASMA TO TISSUE; K_2 FROM TISSUE TO PLASMA; K_3 FOR LEUCINE CATABOLISM; K_4 FOR LEUCINE INCORPORATED INTO PROTEINS; K_5 FREE LEUCINE COMING FROM THE DEGRADATION OF PROTEINS; K_6 AND K_7 FOR THE PRODUCTION OF RNA_T AND VICE VERSA; K_8 AND K_9 ARE RESPECTIVELY FOR THE TRANSPORT OF LEUCINE FROM THE EXTRACELLULAR SPACE TO THE INTRACELLULAR SPACE AND VICE VERSA [293]. 84

FIGURE 22: SIMPLIFIED COMPARTMENTAL MODEL TO MEASURE THE PSR BY USING [^{11}C]LEUCINE. K_1 IS THE RATE CONSTANT FOR LEUCINE UPTAKE IN BRAIN, K_2 THE LOSS OF THE LEUCINE FROM THE BRAIN AND K_3 IS THE RATE CONSTANT REPRESENTING THE EFFECTIVE LEUCINE INCORPORATION IN PROTEINS. CP IS THE CONCENTRATION OF LEUCINE IN BLOOD, CF+M IS THE CONCENTRATION OF FREE AND METABOLISED LEUCINE IN BRAIN AND CB THE CONCENTRATION OF LEUCINE IN PROTEINS [297]. 85

FIGURE 23: TRACERS DEVELOPED TO STUDY THE SYNAPTIC DENSITY [299]. 87

FIGURE 24: [^{11}C]LEUCINE STUDY PLAN. THE STUDY WAS PERFORMED WITH THE AIM TO DEVELOP A METHODOLOGY FOR PET QUANTIFICATION AND IMPLEMENT THE DATA ACQUIRED FOR THE LONGITUDINAL STUDY. TO DETERMINE THE FIRST STEP, WISTAR RATS AND SOME WT AND TG AT 12 AND 18 MONTHS OF AGE HAD A PET/CT SCAN BUT ALSO A TERMINAL PROCEDURE TO DETERMINE THE ARTERIAL INPUT FUNCTION (TOP). FOR THE LONGITUDINAL STUDY, THE SAME RATS WERE USED AT 6, 12 AND 18 MONTHS OF AGE AND HAD A PET/CT SCAN AND THE DETERMINATION OF THE IMAGE DERIVED INPUT FUNCTION (IDIF) WITHOUT BLOOD SAMPLING. THE SAME RATS USED FOR PET, WERE TESTED BEHAVIOURALLY AT 12 AND 18 MONTHS OF AGE. A SECOND GROUP OF RATS WAS ADDED FOR BEHAVIOURAL TESTS AT 6 MONTHS AND ALSO AT 12 MONTHS. *EX-VIVO* ANALYSIS ON OTHER WT AND TG WERE PERFORMED AT EACH TIME POINT. 91
FIGURE 25: [^{18}F]UCB-H STUDY PLAN. TO QUANTIFY PET IMAGES FOR [^{18}F]UCB-H SOME WT AND TG RATS AT 7 AND 15 MONTHS OF AGE WERE INJECTED WITH COLD UCB-J (BLOCKING SCANS) TO DETERMINE THE NON-SPECIFIC BINDING (TOP). THE BLOCKING SCANS (ONE PER GROUP) WERE USED TO QUANTIFY PET IMAGES IN WT AND TG RATS AT 7 AND 15 MONTHS THROUGH THE CALCULATION OF THE NORMALISED UPTAKE VALUE (NUV)..... 92
FIGURE 26: EXPERIMENTAL SETUP TO DETERMINE THE INPUT FUNCTION (IF). DURING THE PET/CT SCAN THE TWILITE DETECTOR WAS USED TO DETERMINE THE RADIOACTIVITY IN WHOLE BLOOD. TWO PUMPS FOR THE INJECTION OF RADIOTRACER AND SALINE FLUSH; A PERISTALTIC PUMP TO MOVE THE BLOOD FROM THE ARTERY TO THE VEIN AND A SYRINGE FOR THE DISCRETE BLOOD SAMPLING. IN THE BACKGROUND IS THE SIEMENS INVEON PET/CT SCANNER. 95
FIGURE 27: MR TEMPLATE WITH EXAMPLE OF ROIS USED FOR QUANTIFICATION..... 96
FIGURE 28: SCREENSHOT OF THE MICK SOFTWARE, USED TO DETERMINE THE RATE CONSTANTS. 97
FIGURE 29: SIMPLIFIED COMPARTMENTAL MODEL OF LEUCINE METABOLISM IN BRAIN [297]. IT IS A TWO-TISSUE COMPARTMENTAL MODEL. THE RATE CONSTANTS K_1 AND K_2 REPRESENT THE TRANSFER OF LEUCINE ACROSS THE BLOOD-BRAIN BARRIER FROM BLOOD TO THE BRAIN AND VICE VERSA. K_3 IS DEFINED FOR THE INCORPORATION OF LEUCINE IN PROTEINS. THE MATHEMATICAL FORMULA FOR THE ESTIMATION OF PSR = PROTEIN SYNTHESIS RATE IS CALCULATED FROM: K_{CPLX} IS THE NET UPTAKE RATE CONSTANT; C IS THE CONCENTRATION OF UNLABELLED LEUCINE IN PLASMA AND Λ IS THE FRACTION OF [^{11}C]LEUCINE IN THE PRECURSOR POOL DERIVED FROM PLASMA. 98
FIGURE 30: (A) EXPERIMENTAL SETUP OF MORRIS WATER MAZE (MWM) AND (B) REVERSAL MWM. STARS INDICATE THE STARTING POINT FROM WHICH THE RAT WAS RELEASED INTO THE POOL. THE BLUE CIRCLE IS THE PLATFORM POSITION DURING THE TEST.99
FIGURE 31: IMAGES OF THE ARENA USED TO PERFORM OPEN FIELD AND SMELL TESTS. THE BOX WAS BLACK 52×52 CM. 101
FIGURE 32: PLATE USED FOR WES ANALYSIS AND µL OF EACH REAGENT. 104
FIGURE 33: REPRESENTATIVE SUM 20-60MIN PET IMAGES OF [^{11}C]LEUCINE UPTAKE (SHOWN AS SUV) IN THE BRAIN OF A WT (TOP) AND TG (BOTTOM) RATS AT 6, 12 AND 18 MONTHS OF AGE. 107
FIGURE 34: SUV GRAPHS OF [^{11}C]LEUCINE BRAIN UPTAKE IN HIPPOCAMPUS (TOP) AND TEMPORAL CORTEX (BOTTOM) AT 6, 12 AND 18 MONTHS OF AGE. THE STATISTICAL ANALYSIS SHOWED AN AGE EFFECT AND GENOTYPE × AGE INTERACTION IN BOTH BRAIN REGIONS; HIPPOCAMPUS: P=0.0013 AND P=0.0321 AND IN TEMPORAL CORTEX: P=0.0014 AND P=0.0169. AN AGE INCREASE OF SUV VALUES WAS EVALUATED IN BOTH GENOTYPES, WITH P VALUES IN WT HIPPOCAMPUS OF 0.0123 BETWEEN 6 AND 18 MONTHS. THE TG RATS WERE STATISTICALLY DIFFERENT BETWEEN 6 AND 18 MONTHS OF AGE (P=0.0060) IN HIPPOCAMPUS. IN TEMPORAL CORTEX WT RATS SHOWED NO STATISTICAL DIFFERENCE WHEREAS TG WERE EVALUATED STATISTICALLY DIFFERENT BETWEEN 6 MONTHS AND 12 MONTHS (P=0.0391) AND 6 MONTHS AND 18 MONTHS (P=0.0031). A GENOTYPE DIFFERENCE WAS REVEALED AT 12 MONTHS OF AGE IN HIPPOCAMPUS (P=0.0239). ALL DATA WERE ANALYSED BY USING MIXED MODEL EFFECT AND SIDAK POST-HOC TEST. DATA WERE EXPRESSED AS MEAN±SD. *P≤0.05; **P≤0.01..... 108
FIGURE 35: ANALYSIS OF UNLABELLED LEUCINE AND A RANGE OF 8 LARGE AMINO ACIDS (LNAA) IN PLASMA. (A) THE EVALUATION OF COLD LEUCINE IN ARTERIAL AND VENOUS PLASMA SAMPLES FROM WT AND TG RATS AT 12 AND 18 MONTHS OF AGE. DATA ANALYSED BY USING TWO-WAY ANOVA AND SIDAK POST HOC TEST SHOW A STATISTICAL DIFFERENCE BETWEEN THE 2 TYPES OF PLASMA SAMPLES (P=0.0001 AT 12 MONTHS AND P=0.0010 AT 18 MONTHS OF AGE). (B) UNLABELLED LEUCINE CONCENTRATION BETWEEN WISTAR, WT AND TG RATS AT 12 AND 18 MONTHS OF AGE USING ONE-WAY ANOVA. (C) THE CONCENTRATION OF UNLABELLED LEUCINE REMAINED UNCHANGED BETWEEN THE WT AND TG RAT GENOTYPES, DATA ANALYSED BY USING UNPAIRED T-TEST. (D) SHOWS THE CONCENTRATION OF THE 8 LNAA IN ARTERIAL PLASMA SAMPLES IN WISTAR AND FISCHER-344 STRAIN (WT AND TG POLLED TOGETHER) AT 12 AND 18 MONTHS OF AGE. THE 8 LNAA ARE: HISTIDINE, METHIONINE, LEUCINE, ISOLEUCINE, VALINE, PHENYLALANINE, TYROSINE AND TRYPTOPHAN. DATA ANALYSED BY ONE-WAY ANOVA SHOWED A STATISTICAL DIFFERENCE IN 8 LNAA CONCENTRATION, WITH A P VALUES OF P=0.0054

between Wistar and Fischer-344 (WT and TG) 12 months and p<0.0013 between Wistar and Fischer-344 (WT and TG) 18 months. **p≤0.01; ***p≤0.001. Data were expressed as mean±SD. 112
Figure 36: Evaluation of free [^{11}C]leucine in plasma in 7 Wistar rats using 5% and 70% PCA. Data show that from 2 to 20 minutes the values of free [^{11}C]leucine were similar and increased at 30 minutes onwards. Two-way ANOVA and Sidak post-hoc test showed a statistical difference at 30 minutes (p=0.0001) and at 40 and 60 minutes (p<0.0001). *** p≤0.001 and **** p<0.0001. Data were expressed as mean±SD. 114
Figure 37: Values of free [^{11}C]leucine in plasma in Wistar rats acquired by using 5% (Y axis) and 70% (X axis) PCA and plotted on an XY graph to determine a calibration curve. The curve-fit indicates the mathematical function describing this calibration. 115
Figure 38: Evaluation of two parameters K_{CPLX} and PSR in hippocampus and temporal cortex in two Wistar rats by using two different AIF. One AIF was measured by using 5% PCA for the evaluation of free [^{11}C]leucine (red dot) and the other AIF was measured by using 70% PCA and corrected by using the conversion formula (green dot). To determine the PSR, averaged values of unlabelled leucine in arterial plasma of Wistar rats were used. 116
Figure 39: PSR study in WT and TG rats at 12 and 18 months by using individual AIF and individual values of unlabelled leucine in arterial plasma. Data showed that at 18 months, WT had higher values of [^{11}C]leucine PSR in the 4 brain regions analysed compared to TG at the same age; the effect size at 18 months of age was >0.80 by using the Choen's d test. Data were expressed as mean±SD. 117
Figure 40: Comparison of K_{CPLX} and PSR of Wistar rats with (n=3) and without (baseline, n=6) anisomycin injection, 60 mg/Kg, 10 minutes before the [^{11}C]leucine PET acquisition. Unpaired *t*-test showed a big difference between baseline and protein synthesis inhibitor. p=0.0024 and p=0.0059 in temporal cortex K_{CPLX} and PSR respectively and p=0.0014 and p=0.0030 in hippocampus K_{CPLX} and PSR. **p≤0.01. Data were expressed as mean±SD..... 118
Figure 41: Representative sum 20-60min PET images of [^{11}C]Leucine uptake (shown as SUV) in the brain (A) without and (B) with injection of anisomycin (PSR inhibitor) @ 60mg/kg i.v. 119
Figure 42: Heart TAC (orange) from one rat and the averaged AIF obtained by the average of blood measurements from 4 WT and 5 TG rats, before applying the ratio to generate a scaled IDIF. 120
Figure 43: Heart TAC of an individual rat (orange curve) and the scaled AIF (IDIF; Purple curve) obtained after the calculation of the ratio between frames 180sec and 240 sec, of TAC and average AIF. The applied ratio calculated by dividing the Individual Heart TAC (frame 180-240 seconds) and the Averaged AIF (frame 180-240 seconds) obtained from the 4 WT and 5 TG rats with blood measurements scaled up the Averaged AIF to the individual heart TAC. 121
Figure 44: K_{CPLX} analysis in WT and TG rats at 6, 12 and 18 months by using averaged and scaled IF (IDIF) and averaged values of unlabelled leucine measured from arterial plasma samples of WT and TG at 12 and 18 months of age. Mixed model analysis shows a significant genotype effect in K_{CPLX} in hippocampus (p=0.0442), whole brain (p=0.0448), *globus pallidus* (p=0.0325) and the *caudate putamen* (p=0.0423). Sidak post-hoc test showed any statistically relevant differences between genotypes or age. Data expressed as mean±SD. 122
Figure 45: PSR evaluation at 6, 12 and 18 months of age, in different brain regions: temporal cortex, hippocampus, cerebellum, cortex somatosensory, frontal cortex, thalamus, cortex cingulate whole brain and caudate putamen by using averaged and scaled IF (IDIF) and averaged values of unlabelled leucine obtained from arterial plasma samples at 12 and 18 months of age in WT and TG. Mixed model effect and Sidak post-hoc test did not show any statistically relevant differences between genotypes and age. Data were expressed as mean±SD. 123
Figure 46: PSR and K_{CPLX} analysis by using averaged and scaled IF (IDIF) and averaged values of unlabelled leucine coming from arterial plasma samples at 12 and 18 months of age in WT and TG. Mixed model effect and Sidak post-hoc analysis in WT and Tg rats at 6, 12 and 18 months of age, shows a significant genotype effect in PSR (top graph, A) in *globus pallidus* (p=0.0295). Unpaired t-test performed at 18 months (graph B and C) show a decrease (-14% for K_{CPLX} and -15% for PSR) in K_{CPLX} and PSR in TG rats statistically relevant (p=0.0427 and p=0.0488, respectively). *p≤0.05. Data expressed as mean±SD. 124
Figure 47: Representative summed PET image (20-60min) of [^{11}C]Leucine uptake (shown as SUV) in the brain of a WT (left) and TG (right) rats at 18 months of age..... 125

FIGURE 48: REPRESENTATIVE CORONAL SECTION SUM 9-20MIN PET IMAGES OF [^{18}F]UCB-H UPTAKE (SHOWN AS SUV) IN THE BRAIN OF A WT 7 MONTHS WITHOUT (LEFT, BASELINE) AND WITH (RIGHT, BLOCK SCAN) INJECTION OF 1MG/KG OF UCB-J BEFORE STARTING THE [^{18}F]UCB-H. 126
FIGURE 49: BASELINE BRAIN SUV TIME ACTIVITY CURVES (TAC) OF [^{18}F]UCB-H (BLUE) AND TAC BLOCKING SCAN AFTER INJECTION OF UCB-J (RED) IN FRONTAL CORTEX. CURVES SHOW A PEAK DURING THE FIRST SECOND THEN FOLLOWED BY A RAPID WASH-OUT. BIG DIFFERENCE BETWEEN BLOCKING (RED) AND NON-BLOCKING (BLUE) SCAN WAS SHOWN BETWEEN 9 AND 20 MINUTES IN ALL GROUPS (SHADOW). THE PRE-SATURATION STUDY (RED CURVES) WAS DEVELOPED BY USING 4 RATS PER GROUP INJECTED WITH 1MG/KG OF UCB-J. THE BLUE CURVES REPRESENTED THE VALUES OF AVERAGED TAC OF [^{18}F]UCB-H IN RATS WITHOUT PRE-SATURATION: 8 WT AT 7 MONTHS WT (A); 7 TG AT 7 MONTHS TG (B); 10 WT AT 15 MONTHS (C) WT AND 10 TG AT 15 MONTHS (D). 127
FIGURE 50: AVERAGED VALUES OF [^{18}F]UCB-H BRAIN UPTAKE IN WT AND TG RATS AT 7 AND 15 MONTHS OF AGE WITHOUT AND WITH A PRIOR INJECTION WITH COLD UCB-J (1MG/KG). THE [^{18}F]UCB-H UPTAKE AFTER BLOCKING STUDY INCREASE WITH AGE IN BOTH GENOTYPES AND IS HIGHER IN TG IN ALL BRAIN REGIONS ANALYSED. DATA WERE EXPRESSED AS MEAN±SD..... 128
FIGURE 51: SUV STUDY IN SOME BRAIN REGIONS: FRONTAL CORTEX, MOTOR CORTEX, HIPPOCAMPUS AND THALAMUS, IN WT AND TG RATS AT 7 AND 15 MONTHS OF AGE WITH (BLOCKED SCAN, UCB-J) AND WITHOUT (BASELINE) PRE-INJECTION WITH UCB-J (1MG/KG) 10 MINUTES BEFORE STARTING THE [^{18}F]UCB-H ACQUISITION. THE ANALYSIS BY USING TWO-WAY ANOVA SHOWED NO STATISTICAL DIFFERENCES BETWEEN GENOTYPE AND AGE IN BASELINE SCANS. ONLY IN FRONTAL CORTEX TG RATS, SHOWED A SIGNIFICANT INCREASE DUE TO THE AGE BETWEEN 7 AND 15 MONTHS OF AGE ($p=0.0264$). THE BLOCKING SCANS SHOWED STATISTICALLY DIFFERENCES IN TG RATS AT 7 AND 15 MONTHS; SPECIFICALLY, IN FRONTAL CORTEX $p=0.0353$; MOTOR CORTEX $p=0.0369$; HIPPOCAMPUS $p=0.0349$ AND THALAMUS $p=0.0241$. IN FRONTAL CORTEX (BLOCKING SCANS) WT AT 7 MONTHS WERE STATISTICALLY LOWER THAN WT AT 15 MONTHS OF AGE $p=0.0382$. # MEANS STATISTICAL DIFFERENCES BETWEEN RATS SAME GENOTYPE BUT DIFFERENT AGE. * AND # $p\leq0.05$. DATA WERE TESTED BETWEEN 9 AND 20 MINUTES AFTER INJECTION AND EXPRESSED AS MEAN±SD. 129
FIGURE 52: REPRESENTATIVE SUM 9-20MIN PET IMAGES OF [^{18}F]UCB-H UPTAKE (SHOWN AS NUV) IN THE BRAIN OF A WT (LEFT) AND TG (RIGHT) RATS AT 7 MONTHS (TOP) AND 15 MONTHS OF AGE (BOTTOM). 131
FIGURE 53: [^{18}F]UCB-H NORMALISED UPTAKE VALUES (NUV_{ND}) ANALYSIS IN DIFFERENT BRAIN REGIONS AT 7 AND 15 MONTHS OF AGE. DATA WERE ANALYSED WITH TWO-WAY ANOVA AND SIDAK POST-HOC TEST. *, ** AND **** INDICATE SIGNIFICANT DIFFERENCE BETWEEN WT AND TG AND BETWEEN AGE AS $p\leq0.05$, $p\leq0.01$ AND $p\leq0.0001$ RESPECTIVELY. DATA WERE EXPRESSED AS MEAN±SD. 132
FIGURE 54: EXPERIMENTAL SETUP OF MWM (A) AND REVERSAL MWM (B). DURING THE TRAINING DAYS OF MWM PLATFORM WAS PLACED IN SOUTH EAST (SE) QUADRANT AND RATS WERE RELEASED IN THE POOL FROM 4 DIFFERENT STARTING POINT. DURING THE PROBE TEST THE PLATFORM WAS REMOVED FROM THE TANK AND RATS WERE RELEASED IN THE POOL FROM THE NORTH. DURING THE REVERSAL MWM THE PLATFORM WAS MOVED AND THE PLATFORM WAS PLACED TO THE OPPOSITE QUADRANT, NORTH WEST (NW). DURING THE PROBE TEST AFTER REMOVING THE PLATFORM, THE RAT WAS RELEASED FROM THE SOUTH. CLUES AND PLATFORM POSITION WERE ALWAYS THE SAME DURING MWM AND REVERSAL MWM AT EACH AGE TESTED.... 133
FIGURE 55: TIME SPENT TO FIND THE PLATFORM DURING THE TRAINING PERIOD OF MWM AT 6 (A), 12 (B) AND 18(C) MONTHS. DATA WERE ANALYSED BY USING TWO-WAY ANOVA AND SIDAK POST-HOC TEST AND SHOWED A STATISTICAL DIFFERENCE BETWEEN DAYS 1 AND 2 ($p=0.0355$) IN WT 6 MONTHS AND BETWEEN 6 AND 18 MONTHS WT ($p=0.0034$) DAY 1. IN TG RATS A STATISTICAL DIFFERENCE WAS EVALUATED AT 6 MONTHS OF AGE, DAYS 1 AND 4 ($p=0.0368$) AND BETWEEN 6 AND 18 MONTHS OF AGE DAY 1 ($p=0.0273$). THE BOTTOM RIGHT PANEL (D) SHOWS ALL DATA ON THE SAME GRAPH. FOR THE MWM WERE USED 11 WT AND 12 TG AT 6 MONTHS OF AGE, 17 WT AND 18 TG AT 12 MONTHS OF AGE AND 10 WT AND 10 TG AT 18 MONTHS OF AGE. DATA WERE EXPRESSED AS MEAN±SD. 135
FIGURE 56: EVALUATION OF THE TIME SPENT IN EACH QUADRANT DURING THE PROBE TEST OF MWM (A). GRAPHS B AND C SHOW THE EVALUATION OF THE TIME SPENT IN EACH QUADRANT IN WT AND TG RATS RESPECTIVELY. DATA WERE ANALYSED BY USING MIXED MODEL AND TWO-WAY ANOVA WITH SIDAK POST-HOC TEST. CIRCLES IN GRAPH A SHOW THE PREFERENCE OF SOUTH QUADRANTS IN WT AND TG RATS AT EACH AGE. *$p\leq0.05$; **$p\leq0.01$; ***$p\leq0.001$ AND ****$p\leq0.0001$. THE NUMBER OF RATS TESTED WAS: $n=11$ WT, $n=12$ TG RATS AT 6 MONTHS OF AGE, $n=17$ WT AND $n=18$ TG AT 12 MONTHS OF AGE, $n=10$ WT AND $n=10$ TG AT 18 MONTHS OF AGE. DATA WERE EXPRESSED AS MEAN±SD. 136
FIGURE 57: TIME SPENT TO FIND THE PLATFORM DURING THE TRAINING PERIOD OF REVERSAL MWM. GRAPHS SHOWED DATA AT 6 (A), 12 (B) AND 18 (C) MONTHS AND $n=11$ WT, $n=12$ TG RATS AT 6 MONTHS OF AGE, $n=17$ WT AND $n=18$ TG AT 12

months of age, n= 10 WT and n=10 TG at 18 months of age were tested. Data were analysed by using Two-way ANOVA and Sidak post-hoc test showed any statistical difference between groups. Data were expressed as mean±SD. 137
Figure 58: Evaluation of the time spent in each quadrant during the reversal MWM graph A shows all rats together, while B and C showed WT and TG respectively. The analysis showed the inability of rats to remember the new platform position and mainly TG rats tended to spent more time in South quadrant (SW) but no in the old platform position (SE). Data were analysed by using Mixed model, Two-way ANOVA and Sidak post-hoc test. The number of rats tested was: n=11 WT, n=12 TG rats at 6 months of age, n=17 WT and n=18 TG at 12 months of age, n= 10 WT and n=10 TG at 18 months of age. Data were expressed as mean±SD. *p≤0.05; **p≤0.01; ***p≤0.001 and ****p≤0.0001. 138
Figure 59: Analysis of the time spent by rats to approach to the platform area during the probe test of MWM (A) and reversal MWM (B). Data tested by Mixed model and Sidak post-hoc test show no difference in both probe tests between age and genotype. N=11 WT and n=12 TG at 6 months of age, n=17 WT and n=18 TG at 12 months of age, n=10 WT and n=10 TG at 18 months of age were used for both tests. Data were expressed as mean±SD. 139
Figure 60: Path efficiency analysed during the MWM at 6 (A), 12 (B) and 18 (C) months of age. The graph D show all age and genotype together. The values of path efficiency were very low highlighting the inability of rats to follow a trajectory as a straight line. Data were analysed by using Two-way ANOVA and Sidak post-hoc test, determining a training effect p=0.0092 in TG rats and a statistically significant increase of values between days 2 and 4 in TG rats (p=0.0307). A genotype effect was found at 6 months day 4 (p=0.0241), with TG performing better than WT. N=11 WT and n=12 TG at 6 months of age, n=17 WT and n=18 TG at 12 months of age, n=10 WT and n=10 TG at 18 months of age were used for the test. Data were expressed as mean±SD. 140
Figure 61: Path efficiency in reversal MWM at 6 (A), 12 (B) and 18 (C) months of age. The graph D show all age and genotype together. Also in reversal MWM rats showed very low values for path efficiency. No statistical differences were found between age or genotype. Data were analysed by using Two-way ANOVA and Sidak post-hoc test. N=11 WT and n=12 TG at 6 months of age, n=17 WT and n=18 TG at 12 months of age, n=10 WT and n=10 TG at 18 months of age were used for the test. Data were expressed as mean±SD. 141
Figure 62: speed analysis during the MWM acquisition (A,B) and probe test (C) and reversal MWM acquisition (D, E) and probe test (F). Data were analysed by using Two-way ANOVA and Mixed model with Sidak post-hoc test. In WT rats the analysis of speed showed an age effect (p≤0.0001) and by using post-hoc test a statistical difference was evaluated on day 1 between 6 and 18 months of age, in which 18 months had lower values (p=0.0033). in TG rats was also determined an age effect (p=0.0122) and a statistical decrease was determined on day 1 between 6 and 18 months of age (p=0.0056). At 12 months of age TG rats had a statistical decrease of speed between day 2 and day 4 (p=0.0077); while the probe test showed similar values between genotypes and age. In reversal MWM an age effect was determined in WT rats (p=0.0062) and on day 2 and 3, 6 months had statistically significant higher values when compared to 12 months (day 2; p=0.0253) and 18 months (day 3; p=0.0149). 6 months WT had a statistically significant difference between days 1 and 2 (p=0.0317) and between days 1 and 3 (p=0.0145) and at 6 months a training effect was determined between both genotypes (p=0.0052). In probe test of RMWM no statistically differences were determined between age or genotype. N=11 WT and n=12 TG at 6 months of age, n=17 WT and n=18 TG at 12 months of age, n=10 WT and n=10 TG at 18 months of age were used for tests. Data were expressed as mean±SD. 143
Figure 63: Analysis of distance travelled during MWM acquisition (A, B) and probe test (C) and during the RMWM acquisition (D,E) and probe test (F) in WT and TG rats. Data were analysed by using Two-way ANOVA and the Mixed model, both with Sidak post-hoc test showing a training (p=0.0357) and age (p=0.0059) effects in WT rats. Statistical difference in WT rats was found on day 1, between 6 and 18 months of age (p=0.0034) and at 6 months between days 1 and 2 (p=0.0487) (Figure 63,A). TG rats showed leaning x age (p=0.0183), training (p=0.0013) and age (p= 0.0058) effects. A statistical difference in TG was evaluated during the day 1 between 6 and 18 months of age (p=0.0028) and at 6 months between days 1 and 4 (p=0.0093). In RMWM and in both probe tests the analysis of duration showed no statistically significant differences between age or genotype.

The number of rats implemented for all tests was: n=11 WT and n=12 TG at 6 months of age, n=17 WT and n=18 TG at 12 months of age, n=10 WT and n=10 TG at 18 months of age. Data were expressed as mean±SD. 145
Figure 64: Open field arena. The arena was divided for the analysis in 3 specific parts: corners (black), centre (grey) borders (white). For the analysis corners and borders were took together. 146
Figure 65: Evaluation of the time spent in exploring a new environment (A), immobile (B) or close to the wall (C) in n=11 WT and n=12 TG at 6 months of age, n=17 WT and n=18 TG at 12 months of age, n=10 WT and n=10 TG at 18 months of age. Data were analysed by using Mixed model effect revealing no statistical differences between groups. Data were expressed as mean±SD. 147
Figure 66: Time spent in smelling during the first and second presentation of an odour at different delay time: 30 minutes (A), 1 hour (B) and 4 hours (C). N=7 WT and n=7 TG at 12 months and n=10 WT and n=10 TG at 18 months were tested and analysed. Data analysed by using Two-way ANOVA and Sidak post-hoc test showed a statistical difference at 12 months between the first and second presentation. During the first presentation at 12 months WT rats showed statistically significant higher values of sniffing when compared to TG. *p≤0.05; **p≤0.01 and ***p≤0.001. Paired t-test at 18 months WT showed a statistically significant differences between the first and second presentation when the two fragrances were presented after an interval of 30 minutes (p=0.0265). Data were expressed as mean±SD. 149
Figure 67: Time spending in smelling two different odour simultaneously, fox and rabbit urine. Data analysed by using Two-way ANOVA and Sidak post-hoc test showed a statistical difference at 18 months TG (p=0.0210) between fox and rabbit urine. The time smelling the fox urine between 12 and 18 months was statistically different (p=0.0287). N=7 WT and n=9 TG at 12 months; n=10 WT and n=10 TG at 18 months were used for the test. Data were expressed as mean±SD. 150
Figure 68: IHC fluorescent staining of amyloid deposition (red) and neuroinflammation (green) detected by the antibodies 6E10 and GFAP respectively in transgenic rat at 6, 12, and 18 months of age. All images have been taken by using a magnification 10X and 20X. 151
Figure 69: Summary of the blood data decision tree. Analysis of unlabelled leucine and LNAA in plasma showed significantly different values between venous and arterial blood samples in WT and TG rats. Therefore, it was established that venous blood was not a reliable proxy of arterial plasma values for the calculation of PSR. The arterial blood values were also different between Wistar and Fischer-344 but not between WT and TG. Therefore, it was decided to pool together the values of WT and TG for the estimation of PSR. 157
Figure 70: Scheme describing the blood circulation in mammals. The Input Function (IF) describes the quantity of radioactivity in arterial plasma during the time. For the AIF blood samples are taken from an artery and in rat the femoral artery was used. The Image derived Input function (IDIF) do not require blood samples to be taken but the estimation of radioactivity can be reached by drawing a ROI over the left ventricle of the heart. 160
Figure 71: PET images at 6, 12 and 18 months of age of WT and TG rats (sum 49-61 min of [^{18}F]ASEM a7 nicotinic receptor) (A). Yellow stars indicate the striatum and white stars the *globus pallidus*. (B) Quantification [^{18}F]ASEM uptake in *globus pallidus*. Chaney *et al.* unpublished data. 162

List of tables

TABLE 1: TRANSGENIC MOUSE MODEL OF AD. TABLE ADAPTED FROM [240]. 68
TABLE 2: TRANSGENIC RAT MODELS OF ALZHEIMER'S DISEASE AND THE PATHOLOGY THAT EACH MUTATION INDUCES IN THE RATS. TABLE ADAPTED FROM [241]..... 69
TABLE 3: AD-LIKE PATHOLOGY IN TGF344-AD. 72
TABLE 4: SUMMARY OF RATS USED FOR THE [^{11}C]LEUCINE. MOST OF WISTAR RATS WERE USED TO DETERMINE THE AIF, 5 OF 19 WISTAR RATS HAD ONLY BLOOD EVALUATION WITHOUT PET/CT SCAN, TO BETTER CHARACTERISE THE CONCENTRATION OF FREE LEUCINE IN PLASMA. 4 WISTAR RATS WERE USED WITHOUT BLOOD SAMPLING AND THEREFORE THEY HAD ONLY PET/CT SCAN. 3 WISTAR RATS WITH FULL ANALYSIS WERE USED TO STUDY THE PROTEIN SYNTHESIS AFTER INJECTION OF AN INHIBITOR. THE OTHER WISTAR RATS (N=7) HAD A COMPLETE ANALYSIS WITH PET/CT AND BLOOD MEASUREMENTS. TWO WT AND 1 TG AT 12 MONTHS OF AGE AND 2 WT AND 4 TG AT 18 MONTHS OF AGE WERE USED FOR THE AIF. THE OTHER FISCHER-344 RATS, 10 WT AND 10 TG AT 6 MONTHS AND 12 MONTHS AND 6 WT AND 9 TG AT 18 MONTHS WERE USED FOR THE LONGITUDINAL STUDY WITH ONLY A PET/CT ACQUISITION AND WITHOUT BLOOD MEASUREMENTS. 110
TABLE 5: SUMMARY OF BLOOD SAMPLES ANALYSED. BLOOD WAS TAKEN FROM THE FEMORAL ARTERY (RED) AND/OR TAIL VEIN (BLUE). N IS THE NUMBER OF SAMPLES ANALYSED. BLOOD SAMPLES FROM WISTAR RATS WERE ALL ARTERIAL. CONCENTRATION: N.MOLE/ML..... 110
TABLE 6: WISTAR AND FISCHER-344 RATS WERE BOTH USED FOR BLOOD MEASUREMENTS. FIFTEEN WISTAR RATS WERE USED FOR BLOOD MEASUREMENTS, OF WHICH 7 HAD THEIR BLOOD TESTED WITH 5% AND 70% PCA SIMULTANEOUSLY. BLOOD OF WT AND TG RATS WERE ALWAYS TESTED BY USING 70% PCA..... 113
TABLE 7: TABLE SUMMARISING THE BEHAVIOURAL TESTS USED TO ASSESS THE SPATIAL MEMORY IMPAIRMENT IN TGF344-AD. NUMBERS ARE THE RAT'S AGE TESTED. VALUES IN GREEN MEANS THAT NO STATISTICALLY SIGNIFICANT DIFFERENCES WERE OBSERVED BETWEEN GENOTYPES, WHILST RED TEXT MEANS SIGNIFICANT DIFFERENCES BETWEEN WT AND TG HAVE BEEN SHOWN. 170
TABLE 8: PREPARATION OF STANDARD BSA..... 200

List of abbreviations

[^{11}C]PiB
Pittsburgh compound B; 25
^{18}F-FDG
[^{18}F] fluoro-2-deoxy-d-glucose; 29
4E-BPs
eIF4E–binding proteins; 60
5-HT
5-hydroxytryptamine; 45
A
amygdala; 40
A1
scavenger receptor; 48
A673V
alanine 673 valine; 26
AA
amino acids; 82
AA-PET
amino acid PET; 80
ABC
ATP-binding cassette transporters; 50
ABCA7
ATP-binding cassette, sub-family A, member 7; 28
ACh
acetylcholine; 40
AChE
acetylcholinesterase; 41
ADAM9, ADAM10 and ADAM17
A disintegrin and metalloproteinase 9, 10 and 17; 34
AGPS
dihydroxyacetonephosphate-synthase; 36
AICD
APP intracellular domain; 34
AIF
Arterial Input Function; 109
AJs
adherens junctions; 50
AMPA
α-amino-3-hydroxyl-5-methyl-4-isoxazole-propionate; 42
AP-1
activating protein 1; 55
APAF-1
activating factor 1; 62
APLP1 and APLP2
amyloid-beta A-beta precursor-like protein; 33
ApoE
ApolipoproteinE; 27
APP
amyloid precursor protein; 25
AQP4
aquaporin 4; 51
Asp678Asn
aspartic acid 678 asparagine; 26
ATF4
activating transcription factor 4; 56
ATF6
activating transcription factor 6; 57
ATP
adenosine triphosphate; 50
BACE 2
beta secretase 2; 35
BACE1
beta secretase 1; 35
Bad
BCL2 associated agonist of cell death protein; 62
Bak
BCL2-antagonist/killer 1; 62
Bax
Bcl-2-associated X protein; 62
BAX
Bcl-2-associated X protein; 62
BBB
blood brain barrier; 27
Bid
BH3 -interacting -domain death agonist; 61
BH3 interacting-domain death agonist; 62
Bik
BCL2 Interacting Killer; 62
Bim
Bcl-2-like protein 11; 62
BIN1
bridging integrator 1; 28
Bmf
Bcl-2-modifying factor; 62
Bok

Bcl-2 related ovarian killer; 62
C
cortex; 40
C/EBP
CCAAT enhancer binding protein; 55
C99
membrane C-terminus domain; 35
CA1
cornu ammonis 1; 39
Ca^{2+}
Calcium 2+; 41
cAMP
Cyclic adenosine monophosphate; 38
CB
cerebellum; 40
CD11b
cluster of differentiation molecule 11B; 48
CD14
cluster of differentiation 14; 48
CD200/R
molecule and receptor for the activation of microglia; 47
CD33
Siglec-3 sialic acid binding Ig-like lectin 3; 28
CD36
cluster of differentiation 36; 48
CD47
Cluster of Differentiation 47; 47
CDK5
cyclin-dependent protein kinase 5; 38
Ch1
medial septum; 40
CH1
gh-affinity sodium-dependent HC-3-sensitive choline transporter; 41
Ch2
ascending diagonal band of Broca; 40
Ch3
horizontal limb diagonal band of Broca; 40
Ch4
Nucleus Basalis of Meynert; 40
Ch5
peduncolo-pontine nucleus; 40
Ch6
dorsolateral tegmental nucleus; 40
ChAT
enzyme choline acetyltransferase; 40
CHOP
CCAAT-enhancer-binding protein homologous protein; 59
Cl
chloride; 50
CLU
clusterin; 28
CN2
control non-derepressible 2; 56
CNS
central nervous system; 42
CR1
complement receptor 1; 28
CR3
phagocytic receptor; 48
CREB
cyclic-AMP response element binding protein; 43
CSF
cerebrospinal fluid; 27
CTFα
C-terminal membrane bound fragment alpha; 34
CX_3CL1
fractalkine; 47
CX_3CR1
fractalkine receptor or G-protein coupled receptor 13 (GPR13); 47
CXC, CC, CX3,C
chemokines families
C is a Cysteine and X is any residue other than cysteine; 49
D1-like and D2-like
dopamine receptors; 45
DA
dopamine; 45
DAP10
adaptor proteins DNAX-activation protein 10; 47
DAP12
adaptor proteins DNAX-activation protein 12; 47
DCC
Netrin receptor; 37

dE9
exon 9 deletion; 67
DISC
death-inducing signalling complex; 61
DNA
deoxyribonucleic acid; 54
DYRK1A
tyrosine-phosphorylation-regulated kinase 1A; 38
E1, E2 and E3
enzymes 1,2 and 3; 59
E693Δ
deletion 693 glutamic acid; 26
EDEMs
degradation-enhancing α-mannosidase-like lectins; 59
Egc
early growth response factor; 55
eIF
eukaryotic initiation factors; 55
EOAD
early onset Alzheimer's disease; 25
ER
endoplasmic reticulum; 27
ERAD
ER-associated degradation; 58
F
phenylalanina; 67
FADD
associated death domain; 61
Flo
Florida; 67
fyn
tyrosine kinase; 54
GABA
neurotransmitter γ-aminobutyric acid; 44
γ-aminobutyric acid; 42
GABA-T
GABA transaminase; 44
GAD
enzyme glutamic acid decarboxylase; 44
glutamic acid decarboxylase; 44
GADD34
growth arrest and DNA damage-inducible protein; 59
GAP
GTPase accelerating protein; 55
GDP
Guanosine-diphosphate; 55
GEF
guanine nucleotide exchange factor; 55
GFAP
glial fibrillary acidic protein; 49
GGA
Golgi-localized γ-ear-containing ARF-binding; 36
Glu682Lys
glutamic acid 682 lysine; 26
GLUT-1
Glucose transporter 1; 50
GPCR
G-protein–coupled receptors; 65
GRP78/BiP
binding immunoglobulin protein; 57
GRP94
heat shock protein 90kDa beta member; 57
GTM
geometric transfer matrix; 76
GTP
guanosine-triphosphate; 55
GWAS
genome-wide association studies; 28
H
hippocampus; 40
HDL
high density lipoprotein; 27
HRI
heme-regulated eIF2α kinase inhibitor; 56
Hrk
Activator of apoptosis harakiri; 62
I
isoleucine; 67
Ibe
Iberian Peninsula; 67
IFN-γ
interferon gamma; 47
IL
interleukin; 47
IL-1R
interleukin 1 receptor; 47
Ind

indiana; 67
IRE1
inositol-requiring enzyme-1; 58
ISF
interstitial fluid; 27
IV
4th ventricle; 40
JAM
junctional adhesion molecule; 50
JIK
c-Jun-N-terminal inhibitory kinase; 62
K
lysine; 67
K^+
potassium; 41
potassium ion; 51
KPI
Kunitz serine protease inhibitor; 33
L
leucine; 67
LAT
large amino acid trasporter; 82
LAT1
L-Type Amino Acid Transporter 1; 50
LDL
low density lipoprotein; 27
LDLR
low density lipoprotein receptor; 27
LMA
Local Means Analysis; 76
LOAD
late onset Alzheimer's disease; 25
Lon
London; 67
LOR
Line of response; 74
LPS
lipopolysaccharide; 47
LRP
low-density lipoprotein receptor-related protein; 36
LRP1
LDLR related protein 1; 27
LRP1b
low-density lipoprotein receptor-related protein 1b; 27
LRP4
low-density lipoprotein receptor-related protein 4; 27
LRP8
low-density lipoprotein receptor-related protein 8; 27
LTM
long term memory; 52
M
methionine; 67
microglia phenotype; 47
MAM
mitochondria-associated membranes; 63
MCI
mild cognitive impairment; 29
MCP-1
monocyte chemoattractant protein 1; 50
mGluR
metabotropic glutamate receptors; 42
MHC
major histocompatibility complex; 51
mLSTR8
mammalian lethal with sec-18 protein 8; 60
the mammalian lethal with sec-18 protein 8; 60
MMP
metalloproteases; 51
MRI
magnetic resonance imaging; 29
mRNA
messenger RNA; 56
mTOR
mechanistic target of rapamycin; 48
mTORC
target of rapamycin complex; 55
N
asparagine; 67
Na^+
sodium; 41
Navβ2
the voltage-gated sodium channel β2 subunit; 36
NBM
nucleus basalis of Meynert; 161
NFT

neurofibrillary tangles; 25
NMDA
N-methyl-d-aspartate; 42
NO
nitric oxide; 46
Noxa
Phorbol-12-myristate-13-acetate-induced protein 1; 62
NRG1
neuregulin-1; 36
NRG3
neuregulin-3; 36
OAPs
orthogonal arrays of particles; 51
OB
olfactory bulb; 40
OF
Open field; 20
Ot
olfactory tract; 40
P3
extracellular peptide; 34
PCA
perchloric acid; 176
PD
Parkinson disease; 64
PDGF-β
platelet-derived growth factor-β; 67
PDI
protein disulfide isomerase; 57
PDPKs
proline directed protein kinases; 38
PERK
PKR-like ER kinase; 57
PET
positron emission tomography; 25
Pi
phosphate; 55
PICALM
phosphatidylinositol binding clathrin assembly protein; 28
PIKK
phosphatidylinositol 3-kinase-related kinase; 60
phosphatidylinositol 3-kinase-related kinase protein; 60
PKA
cAMP dependent protein kinase; 38
PKC
protein kinase C; 34
PKR
protein kinase R; 56; 57
PM
plasma membrane; 27
PP2A and PP5
protein phosphatase 2A and 5; 39
PRAS40
proline-rich Akt substrate 40 kDa; 60
PrP
prion protein; 67
PSEN1
presenilin 1; 25
PSLG-1
P-selectin glycoprotein ligand-1; 36
PSR
protein synthesis rate; 84
Puma
p53 upregulated modulator of apoptosis; 62
RAGE
receptors advanced glycation end products; 49
Rel/NF-kB
Rel/Nuclear factor kB; 55
RMWM
reversal Morris water maze; 19
RNA
ribonucleic acid; 54
ROS
reactive oxygen species; 46
S6K1/2
p70 S6 kinases; 60
sAPPα
APP fragment alpha; 34
SORL1
sortilin related receptor 1; 28
SPT
lipids in brain and serine-palmitoyl transferase; 36
ST
smell tests; 20
STM
short term memory; 52
SV

synaptic vesicles; 65
TCA; 158
TG
transgenic; 19
TGN
trans-Golgi-network; 33
Th
thalamus; 40
Thy1
thymocite differentiation antigen-1; 67
TJs
tight junctions; 50
TLR
toll like receptors; 48
TNF
tumor necrosis factor; 49
TRAF2
TNF receptor-associated factor 2; 62
TREM2
triggering receptor expressed on myeloid cells 2; 28
TSPO
translocator protein; 78
UPR
unfolded protein response; 57
V
valine; 67
V717I
valine 717 isoleucine; 26
VAChT
vesicular acetylcholine transporter; 40
VE
vascular endothelial; 50
vGAT
vesicular GABA transporter; 44
VGluT
vesicular glutamate transporter; 44
VLDL
very low density lipoprotein; 27
VLDLR
very low density lipoprotein receptor; 27
Vt
volume distribution; 167
VTA
Ventral Tegmental Area; 45
WB
western blot; 64
Western Blot; 64
WT
wild type; 19
XBP1
Xbox binding protein-1; 58
ZO-1
zonula occludens; 52
α4β2
The alpha-4 beta-2 nicotinic receptor; 41
α6β1
integrin; 48
α7nAchR
α7 nicotinic receptor; 41
α-KIC
α-ketoglutarate; 83

Abstract

Introduction: Memory alterations are one of the main hallmarks of Alzheimer's disease (AD). Long-term memory storage requires the synthesis of new proteins and synaptic modifications. The aims of this PhD study were hence to (i) investigate the best approach to use [^{11}C]leucine to measure the cerebral protein synthesis rate (PSR) *in-vivo*, (ii) evaluate the PSR in an animal model for AD, the TgF344-AD rats, and (iii) investigate synaptic density with [^{18}F]UCB-H in the same model compared to wild type (WT). In parallel behavioural tests were performed in TG and WT.

Methods: Wistar and 6, 12 and 18 months old TG and WT rats were scanned for 60 min with [^{11}C]leucine with a Siemens Inveon PET-CT. Arterial blood activity was monitored online (Twilite®) and in discrete blood samples (Wistar rats, n=11; WT, n=4; TG, n=5) by γ-counting of whole blood and plasma and cold AA quantification in plasma. The sensitivity of [^{11}C]leucine PET was assessed in Wistar rats by injection of PSR inhibitor anisomycin (60mg/kg) 10min prior to PET acquisition. A different cohort of 7 and 15 months old of age WT and TG rats were scanned with [^{18}F]UCB-H (baseline scans). Non-specific binding was measured in additional rats by injecting cold UCB-J (1mg/kg) 10min prior to [^{18}F]UCB-H injection (block scans). Data were expressed as normalised uptake values (NUV_{ND}) of the ratio between the 9-20 minutes SUV of the baseline over the blocked (non-displaceable SUV_{UCB-J}) SUV for each ROI. For both [^{11}C]leucine and [^{18}F]UCB-H studies, PET images were quantified in BrainVisa and Anatomist software using 28 brain ROIs based on a MRI rat brain atlas. Open field (OF), Morris water maze (MWM) and reversal Morris water maze (RMWM) were all performed at 6, 12 and 18 months of age. Smell tests (ST) were performed only at 12 and 18 months of age. All behavioural tests were analysed using the ANYMAZE software. All data were analysed by using GraphPad Prism 8.4.1.

Results:

[^{11}C]leucine study: the concentration of unlabelled leucine in plasma was statistically different between arterial and venous samples and between strains (Wistar vs. Fischer-344), with no significant difference found between WT and TG. Anisomycin administration significantly reduced the net uptake rate constant (K_{cplx}) of [^{11}C]leucine and PSR (from -77% to -89%) proving the sensitivity of the method to this acute pharmacological inhibition of PSR. For the longitudinal study, averaged population-based whole-blood and plasma input function (IF) and cold leucine concentration were used to calculate K_{cplx} and PSR respectively.

K_{cplx}, but not PSR, was significantly decreased in TG (genotype effect in a mixed-analysis model) in the hippocampus (p=0.0442), whole brain (p=0.0448), *globus pallidus* (p=0.0325) and the caudate putamen (p=0.0423). In the *globus pallidus* K_{cplx} and PSR were significantly reduced (-15%, p=0.0427 and p=0.0488 respectively, unpaired t-test) in TG vs. WT at 18 months of age.

[^{18}F]UCB-H study: pre-saturation with UCB-J blocked up to 70% of the specific binding signal and removed regional differences. Due to the significant variation of non-specific binding with age and genotype, a population-based SUV_{UCB-J} was used to calculate the NUV_{ND} for each group. TG rats had a significantly lower NUV_{ND} than WT at 7m of age in the frontal (-17%, p=0.0028) and motor cortex (-16%, p=0.0066), hippocampus (-12%, p=0.0256), thalamus (-13%, p=0.0202), cerebellum (-17%, p=0.0012), caudate putamen (-15%, p=0.0096) and *globus pallidus* (-13%, p=0.0177) but not in temporal cortex (p=0.0699). There was an age effect of in both WT and TG so that the 15m WT rats were significantly lower than at 7m and TG were no longer significantly different from WT at 15m. Behaviour: In the MWM, WT and TG were able to learn the platform position at all age. In the RMWM, all rats showed an inability to reverse their spatial memory (no statistical differences were found between age or genotype). In the ST, rats memorise an odour when presented twice after an interval time of 30 minutes in WT rats at 12 ($p \leq 0.001$) and 18 months of age (p=0.0265) but were unable to recognise predator urine at 12 and 18 months. in the OF, rats showed elevated levels of anxiety, confirmed by the total inability to explore a new environment.

Conclusion: [^{11}C]Leucine PET is sensitive to measuring brain PSR in rat CNS. However, modelling the data is challenging. Population-based IF returned modest changes in K_{cplx} and PSR in the TG vs. WT. [^{18}F]UCB-H study showed a decreased uptake in TG rats vs. WT at 7m, while normal ageing affected [^{18}F]UCB-H uptake in both genotypes. Despite this, the TG model displaying brain alterations characteristic of AD pathology and these methods provide a good platform for investigating the role of the PSR and alterations in synaptic density for clinical application.

Declaration

No portion of the work referred to in the thesis has been submitted in support of an application for another degree or qualification of this or any other university or other institute of learning.

Copyright Statement

i. The author of this thesis (including any appendices and/or schedules to this thesis) owns certain copyright or related rights in it (the “Copyright”) and s/he has given The University of Manchester certain rights to use such Copyright, including for administrative purposes.

ii. Copies of this thesis, either in full or in extracts and whether in hard or electronic copy, may be made only in accordance with the Copyright, Designs and Patents Act 1988 (as amended) and regulations issued under it or, where appropriate, in accordance with licensing agreements which the University has from time to time. This page must form part of any such copies made.

iii. The ownership of certain Copyright, patents, designs, trademarks and other intellectual property (the “Intellectual Property”) and any reproductions of copyright works in the thesis, for example graphs and tables (“Reproductions”), which may be described in this thesis, may not be owned by the author and may be owned by third parties. Such Intellectual Property and Reproductions cannot and must not be made available for use without the prior written permission of the owner(s) of the relevant Intellectual Property and/or Reproductions.

iv. Further information on the conditions under which disclosure, publication and commercialisation of this thesis, the Copyright and any Intellectual Property and/or Reproductions described in it may take place is available in the University IP Policy (see http://documents.manchester.ac.uk/DocuInfo.aspx?DocID=2442 0), in any relevant Thesis restriction declarations deposited in the University Library, The University Library’s regulations (see http://www.library.manchester.ac.uk/about/regulations/) and in The University’s policy on Presentation of Theses.

Dedication

A te, Papà.

Acknowledgements

Thank you first to my supervisor Herve Boutin, who made this PhD possible. I have really appreciated his help, his patience and his constant availability in solve all my problems. Herve was more than supervisor, he took care of me since the beginning when I was completely lost and alone in a new city, in a foreign country with people speaking a different language. I would also like to thank my co-supervisors Rainer Hinz and Christine Parker for supervising this thesis and supporting me. A special thanks to Lidan Christie, she really helped me in performing PET and in all experiments. I really liked to spend my time in lab with her. Thanks to all guys working at the WMIC in particular Leonie Diffley, Duncan Forster and the all the radiochemistry guys especially Carol Brough, Michael Green and Hamza Al-qasmi.

I would also thank my family especially my lovely nephews that make me always smile and all my friends all over the world especially Yasmin and Irma that made this last year the funniest, my Italian family in Manchester and my old friends always present in my life.

THANK YOU!

1 Introduction

Alzheimer's disease (AD) is a neurodegenerative pathology affecting mainly elderly people one in eight people over the age of 65 and half of those over 85 have AD [1]. It is estimated that approximately 46.8 million people worldwide had dementia in 2015 [2]. The main symptoms of Alzheimer's are memory loss, confusion and brain pathology like neuronal and synaptic connections loss, presence of neurofibrillary tangles (NFT) and β-amyloid plaques [1]. Alzheimer's disease was first described by the German physician Dr Alois Alzheimer in 1906. His first patient was a 51-year-old woman Auguste Deter, who showed strange behaviours and cognitive symptoms, depression and hallucinations. Post-mortem analysis of her brain showed the presence of senile plaques, neurofibrillary tangles (NFT), ventricular enlargement and shrinkage of grey matter [3]. Since the discovery of AD, different studies have been done trying to understand better this condition. In 1984 the cerebrovascular amyloid protein was purified by Glenner and Wong [4]. In 1986, Tau protein was identified as a key component of NFTs, the second pathological feature in AD [5]. In 1991, the first APP transgenic mouse model was created [6] and in 1997 Tacrine, a reversible inhibitor of acetylcholinesterase, was used as first drug trial to improve the symptoms of AD. The first transgenic rat model was developed in 2004 and in the same year the first report describing the use of the radiolabelled PET tracer, Pittsburgh compound B ([^{11}C]PiB) to study amyloid load by PET was published [7].

1.1 Genetics causes and risk factors for Alzheimer's disease

Patients affected by AD are usually classified as either late-onset AD (LOAD) or early-onset AD (EOAD) (Figure 1) according to the age at which symptoms start. The majority of patients develop the symptoms after the age of 65 (LOAD) and only 2-10% have an early onset (EOAD) [8], presenting the first symptoms between 30 and 65 years of age [9]. Dominant mutations in genes such as amyloid precursor protein (APP), presenilin1 (PSEN1) and presenilin2 (PSEN2) are the main cause of familial EOAD (Figure 1) although some sporadic forms without any dominant mutations in these genes have been reported (sporadic EOAD) [10]; conversely other genetic and environmental risk factors are associated with LOAD [11].

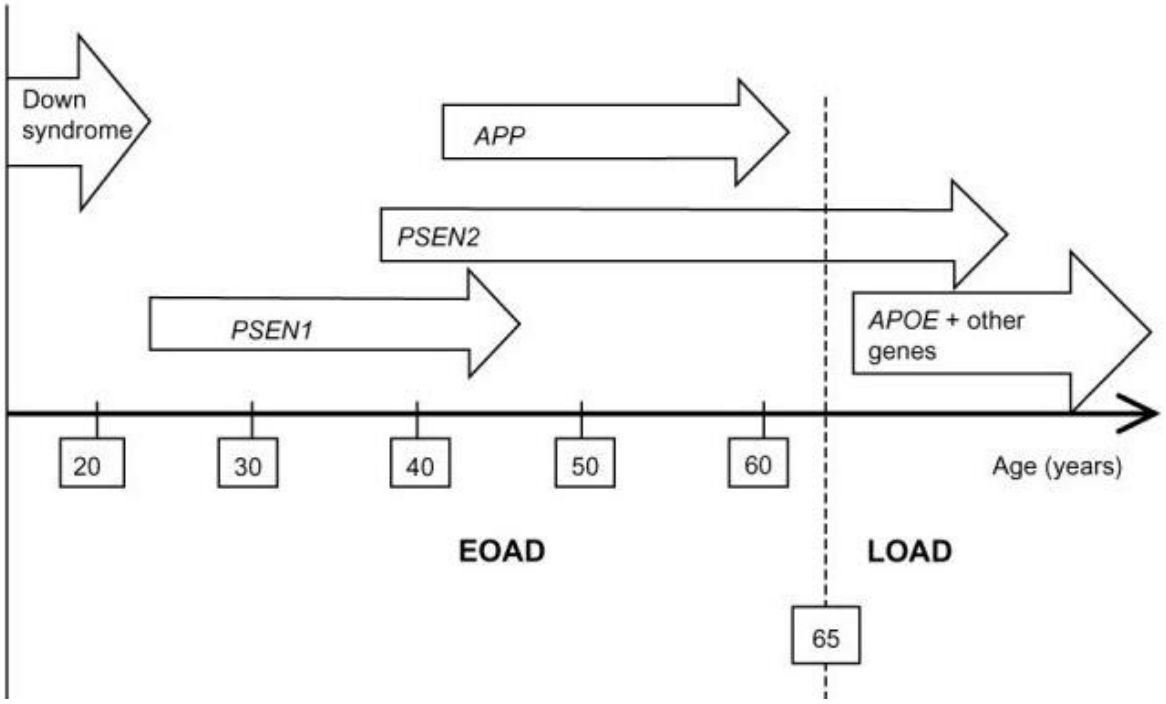

Figure 1: Age of Alzheimer's disease onset as a function of the genes involved. People affected by Down's syndrome have a high risk to develop AD at an earlier age. Early onset AD starts before 65 years of age and the late onset after 65 years. Different gene mutations are involved in the developing of AD. APOE, apolipoprotein E gene; APP, amyloid precursor protein gene; EOAD, early onset Alzheimer's disease; LOAD, late-onset Alzheimer's disease; PSEN1/2, presenilin 1/2 gene [10].

APP genes are located on chromosome 21 and 49 multiples mutations have been discovered thus far. The most well-known APP mutations are dominant and present in the sites of the APP protein cut by β and γ-secretase. For example, the Swedish APP mutation, in which lysine–methionine is replaced by asparagine–leucine, the Tottori mutation (Asp678Asn) and the Leuven mutations (Glu682Lys) are the most common mutation affecting the N-terminus of the Aβ domain adjacent to the β-secretase site. The London mutation (V717I) is the most common affecting the γ-site. There are also two recessive mutations (A673V and E693Δ) which can cause EOAD [12]. Different studies have evaluated that individuals with Down syndrome (trisomy 21) develop the AD pathology faster than normal individuals, due to an over-expression of APP [10]. Mutations can also affect PSEN1 and PSEN2 genes which are both encoding proteins of the γ-secretase complex which cut membrane proteins such as APP. These two genes have a high homology (60%) [13] and mutations in PSEN1 are more common in AD than PSEN2 mutations [8]. The genes PSEN1 and PSEN2 are located on chromosome 14 and chromosome 1 respectively. PSEN1 is present

principally in the plasma membrane (PM) but also in other compartments such as the endoplasmic reticulum (ER), Golgi and mitochondria and is responsible for protein cleavage of many type-I transmembrane proteins such as APP and Notch [14]. Most of the mutations are missense characterised by amino acids substitution that lead to an increase in the Aβ42/Aβ40 ratio [14]. Missense mutations on PSEN2 are rare and cause familial AD but show an incomplete penetrance [8] and AD subjects with PSEN2 mutations have generally a later onset (45-80 years) than patients with APP (45-65 years) or PSEN1 (35-55 years) mutations (EOAD) [13].

As mentioned above, the large majority of cases of AD are LOAD sporadic forms in which different genetic but also environmental factors contribute to the development of AD. Such risk factors include obesity, diabetes, cardiovascular disease as well as cerebral and systemic inflammation [13]. The ApolipoproteinE (ApoE) gene has been linked with an increase in AD risk in LOAD and EOAD [13]; for example, the ε_4 allele increases the risk of AD by 12-fold in patients with two ApoEε4 alleles [12]. The ApoE gene is located on chromosome 19 and has different alleles ε_2, ε_3 and ε_4 encoding for different isoforms that are different in both structures and biological functions [15] through difference in lipid binding affinity [16]. ApoE is a glycoprotein with a N-terminal domain able to bind to the low-density lipoprotein receptor family ((LDLR), LDLR-related protein 1 (LRP1), the very-low-density lipoprotein receptor (VLDLR), megalin, Apoer2 (LRP8), LRP4 and LRP1b) [17], while the C-terminal domain binds lipids [15]. ApoE are produced in the liver and by astrocyte in the brain but also by neurons under stress conditions [16]. Their main role in the brain is to transport phospholipids and cholesterol, essential for synapses, between glia and neurons [18]. ApoE3 and ApoE2 have a preference for high-density lipoproteins (HDL), whereas ApoE4 for very low-density lipoproteins (VLDL) and low-density lipoproteins (LDL) [15].

ApoE4 has been defined as a risk factor because it can interfere with Aβ clearance [17]. Aβ can be degraded by different pathways: via drainage of interstitial fluid (ISF) into the cerebrospinal fluid (CSF), endocytosis by microglia and astrocyte, transport across the blood brain barrier (BBB) and enzymatic degradation by several proteases [19]. The efflux is mediated mainly by the receptor LRP1 and VLDLR through different ligands, ApoE4 unlike ApoE2 and ApoE3, binds the receptor VLDLR which has been shown to have a slower clearance rate of Aβ through the BBB than LRP1 [18], hence increasing Aβ accumulation and fibrillogenesis [16]. ApoE4 also binds Aβ with lower affinity which also contribute to a slower

clearance of amyloid from the brain [20]. ApoE isoforms differentially regulate cholesterol levels and cholesterol is a component for axonal growth, synaptic formation and remodelling; level of lipids and in particular cholesterol have been shown to modulate γ-secretase activity and therefore Aβ production [21]. ApoE can also modulate the activation state of microglia from pro-inflammatory to anti-inflammatory state and the polymorphism ε4 seems to enhance the pro-inflammatory status of microglia cells, increasing the neuronal stress condition [22].

Other genetic factors that contribute to the development of LOAD have been identified by genome-wide association studies (GWAS). These genes can be divided into those related to cholesterol, inflammation or membrane trafficking processes [8]. Regarding the cholesterol pathways, some of the genes involved code for Clusterin (CLU, an apolipoprotein) and ABCA7 (involved in the transport of high-density lipoprotein cholesterol). The genes involved in the immune response are CR1 (also known as C3b/C4b receptor or CD35, and involved in immune regulation), CD33 (which is important for cell-cell contact and endocytosis) and TREM2 (which is expressed by microglia cells and macrophages and involved in down-regulation of inflammatory process). Some of the genes important in trafficking are: BIN1 (implicated in synaptic vesicles), PICALM (involved in clathrin-mediated endocytosis) and SORL1 (important for the trafficking of APP in the intracellular space) [12]. From this, we can see that AD is a multifactorial and complex neurodegenerative disease with strong genetic components or risk factors but regardless of this, both EOAD and LOAD share common symptoms and pathological features that are used to characterise and diagnose AD.

1.2 Symptoms and biomarkers for Alzheimer's disease

In AD, the most prominent cognitive symptom is the episodic memory impairment but semantic and working memory are also affected in the disease [23]. Visuospatial, language alterations and inability to make executive functions ultimately lead to the incapacity of carrying an independent life. It has however been noted that memory alterations are slightly different between EOAD and LOAD. Studies have showed that LOAD patients have mainly a prominent alteration in semantic memory while in EOAD working memory and visuo-constructional skills are the most affected [23]. Brain atrophy is also differently affected in LOAD and EOAD. EOAD is characterised by a prominent atrophy in the

posterior cingulate cortex, inferior parietal lobule, and ventrocaudal and lateral temporal cortex, with a small degree of dorsolateral prefrontal cortical involvement while the hippocampus and the temporal lobe seem quite spared. On the other hand, LOAD patients have prominent atrophy of the hippocampus and anterior temporal cortex and additional atrophy in ventrocaudal and lateral temporal cortex, posterior cingulate cortex, inferior parietal and dorsolateral prefrontal cortices [24]. Patients with AD also develop behavioural alterations such as hallucinations, delusion, depression, euphoria, agitation, aggression, abnormal vocalization, wandering, over-activity, sexual disinhibition, sleep disturbances and apathy [25]. The pathogenic process of AD are thought to start decades before the onset of the disease; the preclinical stage and the Mild Cognitive Impairment (MCI) are characterised by the development of symptoms but in which patients do not yet fulfil the criteria for dementia [26] (Figure 2).

Different biomarkers can be used to diagnose AD; increased level of tau and phosphorylated tau and lower concentration of amyloid beta 1-42 (Aβ42) in CSF are considered relevant biomarkers to diagnose the pathology and changes of these biomarkers are used to evaluate the conversion of MCI to AD [27]. In addition to the analysis of CSF, neuroimaging studies can be used to detect brain changes and disease progression. The main neuroimaging markers are brain atrophy as measured by magnetic resonance imaging (MRI), reduction in 2-[^{18}F]-fluoro-2-deoxy-d-glucose ([^{18}F]FDG) uptake and increase in Aβ load with tracers such as [^{11}C]-labelled Pittsburgh Compound B (PiB) measured by positron emission tomography (PET) [28].

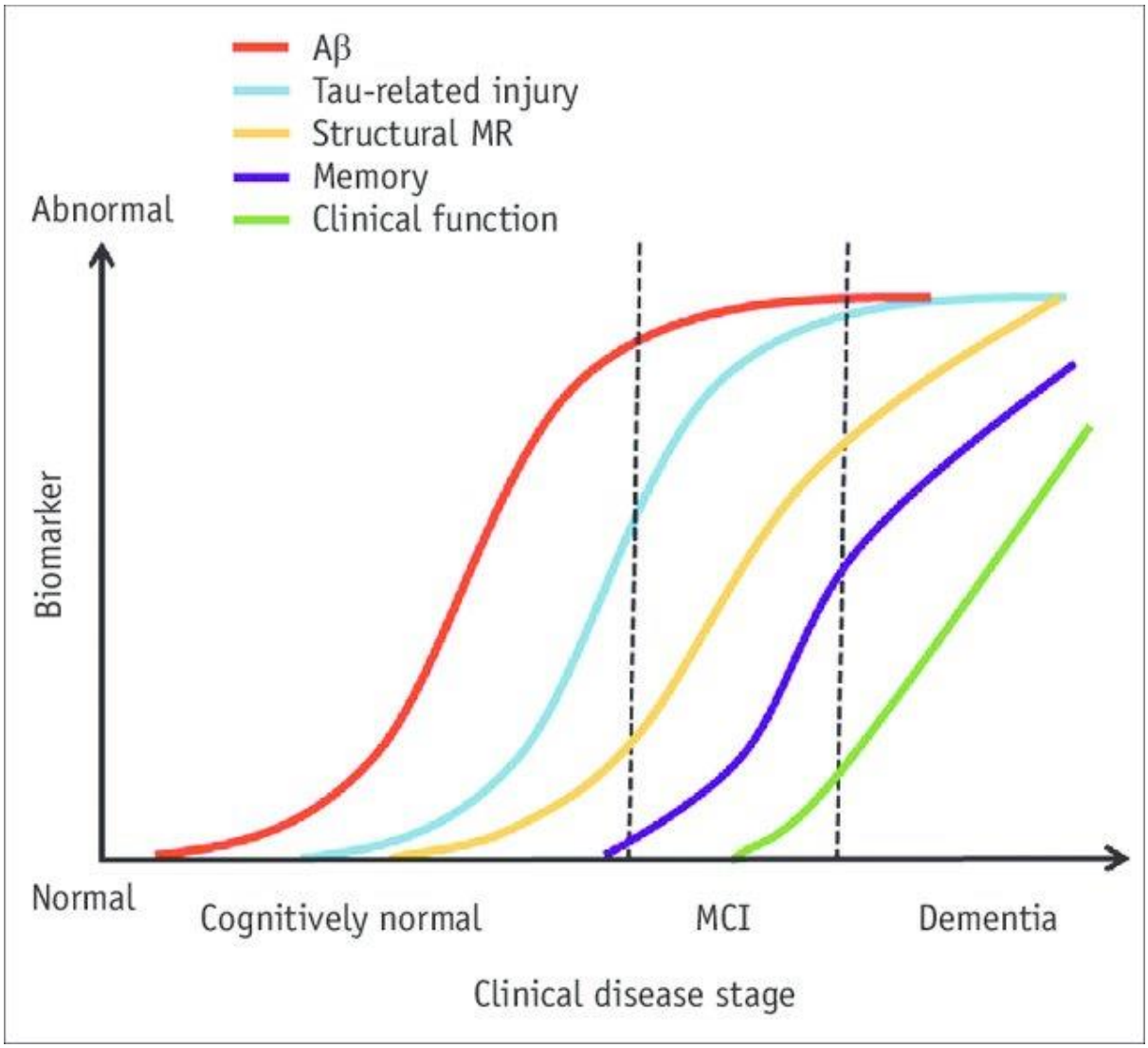

Figure 2: Diagram showing different brain alterations during the progression of AD. Hallmarks, amyloid and Tau, are present before the start of the memory impairments so that the cognitive symptoms (green curve) appear only later on when the brain has been already compromised [29].

1.3 Alzheimer's disease theories and mechanisms

The β-amyloid peptide has been considered the main molecule that leads AD physiopathology since its discovery in 1984. In 1992, Hardy and Higgins described for the first time the amyloid hypothesis, called the βaptist doctrine, in which the accumulation of Aβ peptide is the central event of Alzheimer's [30]. This theory is based on the fact that Aβ can trigger different neurotoxic events such as mitochondria dysfunction, increased oxidative stress, neuroinflammation and these alteration can lead to decrease in neuroplasticity and neurogenesis, hyperphosphorylation of Tau protein and neuronal death [31]. The evidence supporting the βaptist doctrine are based on *in-vivo* and *in-vitro* studies such as the discovery of APP and presenilin mutations that lead to EOAD, the predisposition

of subjects with Down syndrome to develop of AD (Figure 3) and also the generation of a variety animal models that have mutation in APP and/or γ-secretase complex and these animals are characterised by substantial deposits of amyloid in their brains and show modest cognitive symptoms [30]. Much evidences have demonstrated the flaws of this theory; indeed studies in human based on the removal of amyloid plaques by using anti-amyloid antibodies have shown only a reduction in plaque burdens but the cognitive decline was still present and continued to worsen [32]. Aβ plaques have been found also in normal aging without developing AD in life [33]. Another piece of evidence against this doctrine is that the memory impairment may correlate more with NFT than Aβ deposition [34]. Taken together these data have assumed that Aβ remains a central part of pathophysiology of AD but may not be the central factor causing AD [35].

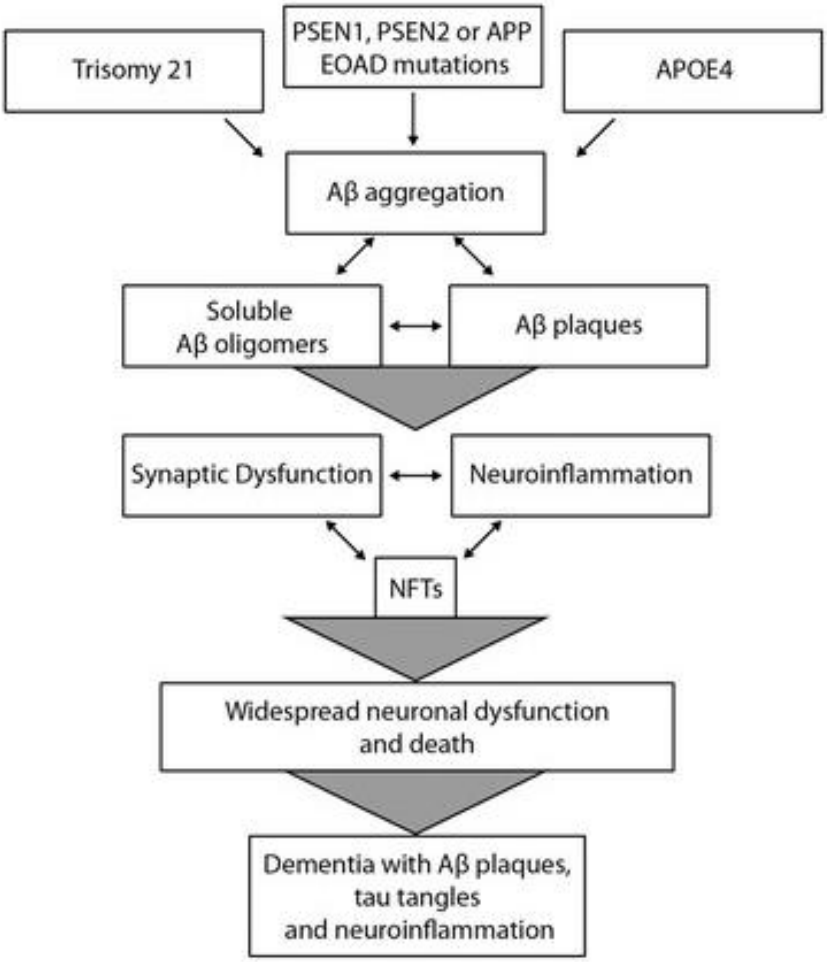

Figure 3: Amyloid hypothesis. The amyloid hypothesis is based on the assumption that the Aβ aggregation promotes a cascades of events starting with synaptic dysfunction and neuroinflammation, then NFT that leads at neuronal death [36].

The other hypothesis trying to explain the molecular pathogenesis of AD is the Tau and tangle hypothesis, called the Tauist doctrine, that gives at the formation of NFT the primary as cause pathogenesis of AD due to hyper phosphorylation of Tau protein. The Tau and tangles hypothesis is quite recent compared to the amyloid doctrine. It had received more attention following the failure of treatment against amyloid deposition. The Tauist doctrine has been supported by the fact that tangle formation happens with increased phosphorylation and aggregation of Tau protein in brain areas that are crucial for memory processes, and the formation of NFT causes neuronal death [37]. The distribution of NFT in brain correlates better with cognitive impairment than amyloid deposition [38] and hyperphosphorylated Tau can be found in brain of demented patients at the early stage without Aβ deposition [31]. Tau has gained much more attention in these years and new clinical trials are focusing on preventing or reverting Tau aggregation.

Amyloid and tangles appear to be related, with the amyloid pathology appearing able to exacerbate Tau effects in memory impairment [37]. Development of new biomarkers are needed to better understand how AD pathology is initiated and potentially find a common factor able to resolve the gaps present in both theories. New theories are being raised with the aim to include and expand the amyloid and Tau doctrines, for example, the inflammatory hypothesis [39]. Since 1990 several studies have demonstrate that the use of anti-inflammatory treatments had also protective effects against AD [40]. Studies have demonstrated that neuroinflammation promotes APP production, Aβ deposition and Tau hyperphosphorylation. Neuroinflammation is now considered as a central mechanism that must be studied to better understand AD pathology [39].

1.3.1 The APP protein

One of the main hallmarks of AD is the accumulation and aggregation of amyloid β-peptides, ultimately forming Aβ plaques (Figure 4). The accumulation of amyloid plaques in AD is less predictable than the NFT and three stages can be detected during the amyloid accumulation. During the first stage there is the involvement of isocortical regions then at the second stage allocortical or limbic structures and the last stage is characterised by the deposition in subcortical regions [41]. β-amyloid accumulation is also founded in Down's syndrome, head injury and in some healthy individuals [42]. Extracellular aggregates of amyloid-β peptides are generated by the cleavage of the large transmembrane protein

amyloid-β protein precursor (APP) [43]. These aggregates are found in the brain parenchyma but also in the walls of cerebral and meningeal blood vessels [44]. The APP protein is ubiquitously expressed in several types of cells. It is a transmembrane protein type I characterised by a large extracellular amino-terminus domain, a single transmembrane segment and a short cytoplasmic carboxyl terminus region [45, 46]. In non-pathological condition, the APP protein seems to be involved in neurite outgrowth and synaptogenesis, neuronal protein trafficking through the axon, signal transduction, cellular adhesion and calcium metabolism [47]. The APP protein is a member of a related family of proteins: the amyloid precursor-like proteins (APLP1 and APLP2) [48] but only the APP contains the Aβ sequence [49]. The gene encoding for the APP protein is located on chromosome 21 and alternative slicing of APP gene produces different APP isoforms [45] varying in size from 695 to 770 amino acids [50]. The most expressed isoforms are APP695 mainly in CNS by neurons, APP751 and 770 containing the Kunitz serine protease inhibitor domain (KPI), expressed ubiquitously [48] and by astrocytes and microglia in the brain [51].

1.3.1.1 The APP protein processing, aggregation and trafficking

The APP protein is synthetized in the endoplasmic reticulum (ER), transported by the Golgi apparatus to the trans-Golgi-network (TGN) and then to the plasma membrane (PM) by the TGN vesicles. APP can be cleaved at the PM or re-internalized via endosomal/lysosomal degradation pathway [47]. After synthesis, the APP protein undergoes different modifications such as O- and N-glycosylation, phosphorylation and sulphonation at tyrosine motifs in the Golgi apparatus and only a small amount of APP reaches the PM, most of it remains in the Golgi and TGN [52]. The APP protein can be cut by two different pathways: the non-amyloidogenic pathway by the action of α- and γ-secretases and the amyloidogenic-pathway through processing by β- and γ-secretase. In the amyloidogenic pathway, two different forms of Aβ are produced: Aβ40 and Aβ42. Aβ42 is able to aggregate more rapidly than Aβ40 and it is the most abundant form found in amyloid plaques. Most of Aβ is secreted out the cells but different intracellular compartments are involved in the production of pathological amyloid: the Golgi apparatus, the endosomal/lysosomal system and the ER [53]; Aβ can also be re-internalized by cells to be degraded [47]. Aβ plaques formation is characterised by the acquisition of a folded state β-sheet. Folded monomers associate each other thought hydrophobic and hydrogen interactions forming protofibrils

that are self-assembled and that are able to form long fibrillar aggregates [54]. The fibrils formation have oligomers as intermediate state and oligomers are particularly important because they are more toxic than the mature fibrils; the oligomers concentration is positively correlated with the neuropathology [55]. Oligomers are also responsible of synaptic dysfunction, due to the ability to bind some glutamate and cholinergic receptors such as NMDA, mGluR5, α7-nicotinic a receptor, that are essential in the acquisition of memory [56].

Amyloid can also bind directly to membranes through two types of interaction: insertion in membrane with formation of pore-like structures and binding at the surface membrane. The insertion in the membrane causes the formation of channels that changes the homeostasis and promotes the activation of apoptotic pathways and therefore cellular death [57, 58]. Binding at the membrane surface promotes amyloidogenesis and different membrane elements can influence this process: peptide composition, charge, fluidity and hydrophobic of the membrane [57].

1.3.1.2 α-secretase processing

α-secretase is involved in the non-amyloidogenic pathway which is predominant in the healthy brain [59]. The α-secretase is a zinc metalloproteinase and different metalloproteinases are part of the α-secretase constitutively: in particular ADAM9, ADAM10 and ADAM17 which are part of the ADAM (A Disintegrin And Metalloprotease) family [60]. ADAM 10 seems to be the most essential constitutive part of α-secretase in neurons [61]. α-secretase can cut the APP protein in two different ways: constitutively or regulated [62]. The regulated cleavage occurs mainly in the Golgi apparatus under the control of protein kinase C (PKC) and the constitutive at the plasma membrane [63]. The α-secretase cleavage starts at the Lys16 and Leu17 in the Aβ domain; after the first cut a large soluble ectodomain called sAPPα is released, which has an important role in regulation of synaptic plasticity and protection against excitotoxicity [47]. The C-terminal membrane bound fragment (CTFα) becomes the substrate for the γ-secretase activity which leads to the production of the small extracellular peptide P3 and a cytosolic APP intracellular domain (AICD), which has different roles in transcription and as adapter proteins [49] (Figure 4).

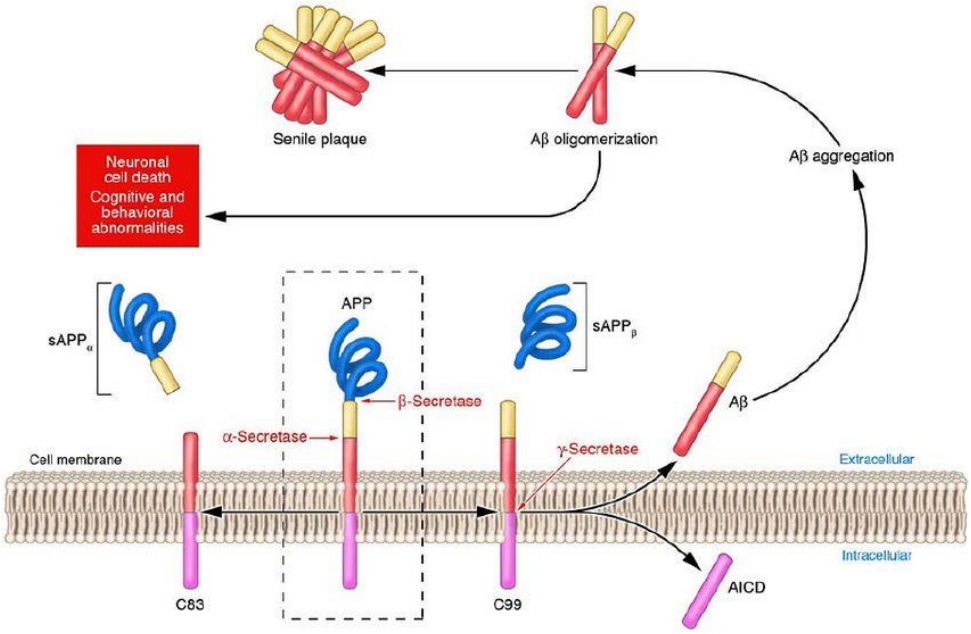

Figure 4: The amyloidogenic and non-amyloidogenic pathways of APP. The non-amyloidogenic pathway is characterised by the α-secretase cut that generates the sAPP-α and C83 fragment. β-secretase cleavage promotes the amyloidogenic pathway and the production of sAPP-β and the fragment C99. C99 and C83 are then cleaved by γ-secretase producing ACID and p3 fragments (non-amyloidogenic pathway) (not shown in figure) and ACID and Aβ peptide (amyloidogenic pathway). The amyloid peptide can aggregate and forms oligomers and senile plaques [64].

1.3.1.3 β-secretase processing

β-secretase is a transmembrane aspartyl protease of 501 amino acids, expressed in neurons. It is modified by glycosylation, phosphorylation, and palmitoylation after translation and is transported to the PM, internalised via the di-leucine motif at the C-terminus by endosomes or Trans-Golgi Network (TGN) [65]. BACE1 and his homologous BACE 2 differ in tissue expression, BACE1 is widely expressed in brain tissue whereas BACE-2 is abundant in peripheral tissues [66]. β-secretase is mainly found in endosomes, lysosome and Golgi complex in soma, dendrites and axons [65] which have an acidic environment essential for β-secretase optimal activity [61]. β-secretase is also found at the cellular surface [67] in a specific zone called lipid raft [65] which is a membrane domain rich in cholesterol and glycosphingolipids. The β-secretase cleaves the APP protein at the N-terminus of Aβ about 16 residues down to the α-secretase domain between methionine 671 and aspartic acid 672. This results in the production of a small extracellular fragment called sAPPβ and the formation of a large membrane C-terminus domain called C99 [68]. The C99 fragment, characterised by the complete Aβ attached domain, is then cleaved by a membrane complex

of γ-secretase (Figure 4). The trim by γ-secretase at the trans membrane domain causes the release of Aβ and the intracellular APP domain (AICD) able to translocate in the nucleus and induce the transcription of various genes such as APP, BACE1, the Aβ-degrading protease neprilysin (NEP) and the glycogen-synthase-kinase3 (GSK-3), known to be responsible of tau hyper phosphorylation. This also triggers the expression of several enzymes involved in lipid metabolism [69], such as dihydroxyacetonephosphate-synthase (AGPS), which regulates the expression of lipids in brain, and serine-palmitoyl transferase (SPT) which regulates the *de novo* synthesis of sphingolipid [69, 70]. Due to the multiple γ-secretase cutting domains, Aβ can vary in length [69]. The activity of BACE1 is fully related to the cellular localization; for example, the retention of BACE1 in the ER with a neutral pH reduces its activity; proteins such as reticulon/Nogo are able to bind BACE1 and increase its retention in the ER compartment. Instead Golgi-localized *γ*-ear-containing ARF-binding (GGA) proteins are able to interact with BACE1 and regulate its tracking between late Golgi and endosomes. In AD patients, GGA3 seems to be reduced, this protein seems to be important to regulate the BACE1 localization in early endosome but also, when reduced, it blocks BACE1 degradation in lysosomes [71]. BACE1 has different substrates other than the APP protein, such as Golgi-localized membrane-bound α2,6-sialyltransferase, P-selectin glycoprotein ligand-1 (PSLG-1), the APP homolog proteins APLP1 and APLP2, low-density lipoprotein receptor-related protein (LRP), the voltage-gated sodium channel β2 subunit (Navβ2), neuregulin-1 (NRG1), and neuregulin-3 (NRG3) [71]. The knowledge of other substrates is essential for the development of new therapies because the inhibition of BACE1 could potentially be beneficial in AD while increasing the undesirable effects due to the BACE1 activity on other substrates.

1.3.1.4 γ-secretase cleavage

γ-secretase is a multiple protease complex able to cut membrane proteins defined as type I single pass transmembrane, meaning able to span through the membrane only once. The γ-secretase complex has different subunits: presenilin (PS), nicastrin, anterior pharynx-defective 1 and presenilin enhancer 2. The catalytic parts of the secretase are the presenilin sites while the others regions are involved mainly in the maturation and stability of the γ-secretase complex [72]. Different sites of APP, separated by three amino acids, are cut by γ-secretase: ε, γ and δ [73]. In the amyloidogenic pathway APP is cleaved by BACE1 first,

producing an N-terminal β-APP and a C-terminus fragment C99. C99 is then cut by the presenilin complex that induces the production of different size of Aβ released into the extracellular space and the AICD domain into the cytosol. The first cleavage by the presenilin complex is at the residue 49 relative to the BACE1 cut site, called ε-site, then at the residue 46 of the δ-site and at the end at residue 40 of the γ site. Other cuts can occur, producing cut at Aβ48 (ε site), Aβ45 (δ site) and Aβ42 (γ site) [74]. The Aβ42 fragment is more toxic than the Aβ40 one. The γ-secretase complex has also other substrates and one of them is Notch, which becomes activated post-cleavage. Notch is a proto-oncogene and tumour suppressor in some cancer types. Notch after its cleavage is involved in cell survival and differentiation but its most important role is the ability to induce the differentiation of neuronal stem cells into adult neurons, this has been shown to play an important role during the improvement of spatial memory [75]. Other substrates are DCC receptors (Netrin receptor), involved in the axon guidance of neuronal growth, and ephrinB and its receptor which are both important in synaptogenesis and spine maturation [75].

1.3.2 Tau

The modification of Tau is another hallmark in AD. Neurons morphology is characterised by dendrites and axons and is essential for optimal cellular functions. Rearrangements of cytoskeleton proteins are involved in the maintenance of the correct cell shape. The cytoskeleton is composed mainly by microtubules, microfilaments, and intermediate filaments [76]. Tau is a microtubule-associated protein, involved in the dynamic of microtubule assembly along with axonal transport of proteins, vesicles and organelles [77]. The Tau gene is localised on the chromosome 17 and the gene is characterised by 16 exons and after nuclear transcription of the mRNA, different splicing processes induce the production of six isoforms of Tau protein that differ by the number of exons. The constitutive exons are the 1, 4, 5, 7, 9, 11, 12, and 13 and the alternatives spliced are the exons 2, 3 and 10 (Figure 5). The six isoforms differ in their C-terminal region that can have three or four binding domains (R); the number of R repetitions determine the strength of the binding to microtubules; the N-terminal region is essential for signal transduction because it interacts with molecules involved in synaptic signalling, energy metabolism, and cytoskeletal function [78].

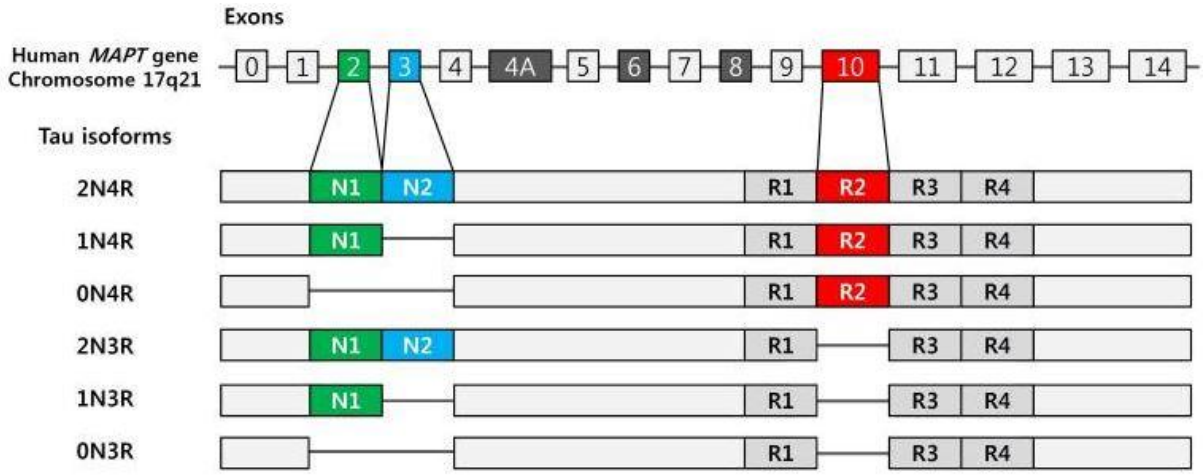

Figure 5: Tau isoforms in human brain. Different splicing of exons 2, 3 and 10 induce the production of six isoforms that differ for the C-terminal regions and the N-terminal region and therefore changing of microtubles R domain at C-terminal and the binding at neural plasma N domain at the N-terminal. Exons 4A, 6 nad 8 are not transcribed in brain [78].

The Tau protein is subjected to different modifications such as: phosphorylation, glycosylation, ubiquitination, de-amidation, oxidation, nitration, cross-linking, or glycation [76], and normal level of phosphorylation is essential to regulate the microtubules binding and their assembly [79]. The three amino acids involved in the phosphorylation processes are serine, threonine and tyrosine and there are about 85 putative sites for phosphorylation [80]. Phosphorylation processes are regulated by different kinases and phosphatases. Kinases are involved in the induction of phosphorylation and they are divided in three classes: proline directed protein kinases (PDPKs), protein kinases non-PDPKs and protein kinases acting on tyrosine sites. The main protein kinases involved in the hyperphosphorylation of Tau in AD are GSK3β, cyclin-dependent protein kinase 5 (CDK5), cAMP-dependent protein kinase (PKA), MAPKs, casein kinase 1 (CK1) and DYRK1A [80]. GSK3β plays a central role in AD, it is expressed abundantly in brain and it is able to phosphorylate tau in unprimed and primed sites; a primed site is defined when a residue of serine or threonine is placed four amino acids at the C-terminal before the target Ser/Thr site, is phosphorylated first [81]. GSK3β is involved in different roles such as glycogen metabolism, gene transcription, apoptosis and microtubules stability [82]. The activity of GSK3β is regulated by the phosphorylation processes mainly on tyrosine 216 that induces increase in its activity and serine 9 that promotes the inhibition of GSK3β [83]. The activity of GSK3β is regulated by growth factors, such as insulin and also by proteins that are part of the mitogen-activated protein kinase (MAPK) signalling [82]. An hyperphosphorylation of Tau

can also be due to an alteration in protein phosphatases function, that are unable to maintain the right level of Tau phosphorylation. Different types of protein phosphatases have been reported to be reduced in AD such as protein phosphatase PP2A , PP5 [80].

There are also other modifications that can promote the acquisition of pathological form of Tau. Glycosylation is the attachment of sugar on specific residues and the glycosylation process reduce Tau phosphorylation by PKA, CDK5 and GSK3β. Glycation is a non-enzymatic glycosylation; the glycation causes the accumulation of Tau in cells and the over-production of free radical and oxidation process, therefore contributing to stop Tau degradation and causing neuronal death. The prolyl-isomerization, a rearrangement of disulfide bonds that promote a conformational change, also contribute to Tau pathology [80]. The truncation of Tau also occurs in AD patients reducing its ability to bind to and stabilize microtubules. The truncation promotes the acquisition of specific tangle-associated conformations, self-assembling into filaments, and inducing apoptosis [84]. The nitration of Tau consists in the addition of nitrogen dioxide on tyrosine residues which facilitates Tau aggregation [80].

In pathological conditions, Tau aggregates in the cytosol and then is released either freely or inside vesicles by cells even when there is no cellular death [85]. Extracellular low molecular weight Tau oligomers and short fibrils, but not monomers or long fibrils, can be internalised by neurons and promote tauopathies [86]. During the formation of NFT, altered Tau unable to bind microtubules, aggregate forming first low molecular weight oligomers (dimers and trimers) and then fibrils. Fibrils are the main structures involved in the formation of aggregates such as paired-helical filaments (PHF) that upon assembling form NFTs [80, 86]. The progression in the formation of NFTs is predictable and the spreading of NFTs can be divided in 6 different stages according to the cerebral areas that are involved in AD. During stage I, the trans-entorhinal cortex is involved, then, in stage II, the entorhinal cortex proper and the CA1 hippocampal region. The stage III is characterised by the accumulation of NFT in limbic system, in stage IV in amygdala, *thalamus* and *claustrum*. The last two stages, V and VI, are characterized by NFT in the isocortical areas (isocortical stage), with the associative areas being affected prior and more severely than the primary sensory, motor and visual areas [41].

1.3.3 Alterations in neurotransmission system

Changes in acetylcholine neurons and synapses in the cerebral cortex and hippocampus are the main alterations in neurotransmission in AD. In brain there are two main innervating acetylcholine pathways originating from the brainstem and the magnocellular basal forebrain-cholinergic systems [87]. The cholinergic system undergoes degenerative changes that have been related to the progression of memory deficits with aging (Figure 6). In AD, the *nucleus basalis* of Meynert, which provides the major cholinergic input to the neocortex [88], is affected by a profound loss of neurons, whereas in normal aging the cholinergic system undergoes mainly alterations of dendrites, synapses and axons with much less cellular loss [89].

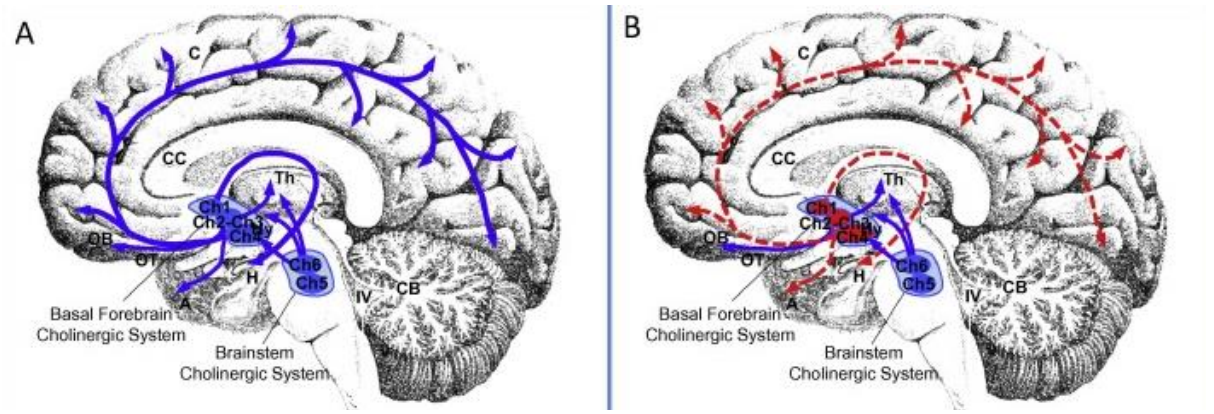

Figure 6: Representation of the main central cholinergic pathways in healthy brain (A) and AD brain (B). Blue arrows are the normal pathway and red arrows the degenerated pathways in Alzheimer's disease. Brain regions CC: corpus callosum; CB: cerebellum; C: cortex; H: hippocampus; Th: *thalamus*; OB: olfactory bulb; OT: olfactory tract; A: amygdala. Ch1: medial septum; Ch2: ascending diagonal band of Broca; Ch3: horizontal limb diagonal band of Broca, Ch4: *nucleus basalis* of Meynert; Ch5: *peduncolo-pontine nucleus* ; Ch6: dorsolateral tegmental *nucleus*. IV: 4th ventricle. The cholinergic system not involved in neurodegeneration is not shown in this picture [90].

Acetylcholine is an essential neurotransmitter which is involved in different functions such as learning and memory but also stress response, wakefulness and sleep, and sensory information processing [91]. Synthesis of acetylcholine (ACh) requires Acetyl Coenzyme A (AcetylCoA) generated during the glycolysis by the metabolism of glucose in mitochondria; therefore cholinergic cells seems to be more susceptible to glucose levels [89]. As shown in Figure 7, the synthesis of ACh starts in cytoplasm with the enzyme choline acetyltransferase (ChAT). The transport in synapses is operated by the vesicular acetylcholine transporter (VAChT). After depolarization of cholinergic neurons there is the release of ACh which can activate two different types of receptors: muscarinic which are G protein coupled receptors

and nicotinic which are ion gated receptor channels. The nicotinic receptors are composed by α, β, δ and γ (foetal) or ε (adult) subunits and different combinations of them form different subtypes of these receptors [92]. They are characterized by their permeability to different ions such as $K^{+,}$ Na^{+} and Ca^{2+}. The nicotinic receptors in CNS have a high permeability for Ca^{2+}. Activation of these receptors provokes the release of different neurotransmitters such as glutamate, GABA, dopamine, serotonin, norepinephrine, as well as acetylcholine. Five types of muscarinic receptors are present and are coupled to different G-proteins. M1, M3, and M5 bind $G_{\alpha q}$ and M2 and M4 bind $G_{\alpha i}$. These G-proteins have different pathways, in particular $G_{\alpha q}$ which facilitates the excitability, whereas $G_{\alpha i}$ decreases cell excitability [91].

α7nAchR has been found to be implicated with AD; indeed it is highly expressed in the cholinergic target areas affected in AD [93]. $A\beta_{42}$ is able to interact with the nicotinic receptor and activate the MAPK pathway and the downstream cAMP-regulatory element binding (CREB) protein that are both important for memory formation [94]. The prolonged exposure activation could lead to a deregulation of α7, ERK MAPK, and CREB and learning and memory impairments [95]. $A\beta_{42}$ seems also able to promote the Tau phosphorylation via α7nAchR [96] through the MAPK pathway [97]. Another nicotinic receptor is the α4β2 subtype. This receptor plays an important role in cognitive functions such as attention, learning and memory. PET studies showed a relatively reduced availability of α4β2 nAChRs in mild AD patients compared with healthy controls in basal forebrain and fronto-temporo-parietal cortices [98].

ACh is catabolised into choline and acetate by the acetylcholinesterase (AChE); the choline is then re-up-taken from an active transport system, the high-affinity sodium-dependent HC-3-sensitive choline transporter (CH1), expressed on neurons in early endosomes and synaptic vesicles [91]. Autopsy brain samples of patients with AD showed a significantly reduced activity of choline acetyltransferase in the temporal lobe [99] and a comparison between no cognitive impairment, mild cognitive impairment, and early-stage Alzheimer's disease showed that the choline acetyltransferase is preserved during the early stages of AD [100].

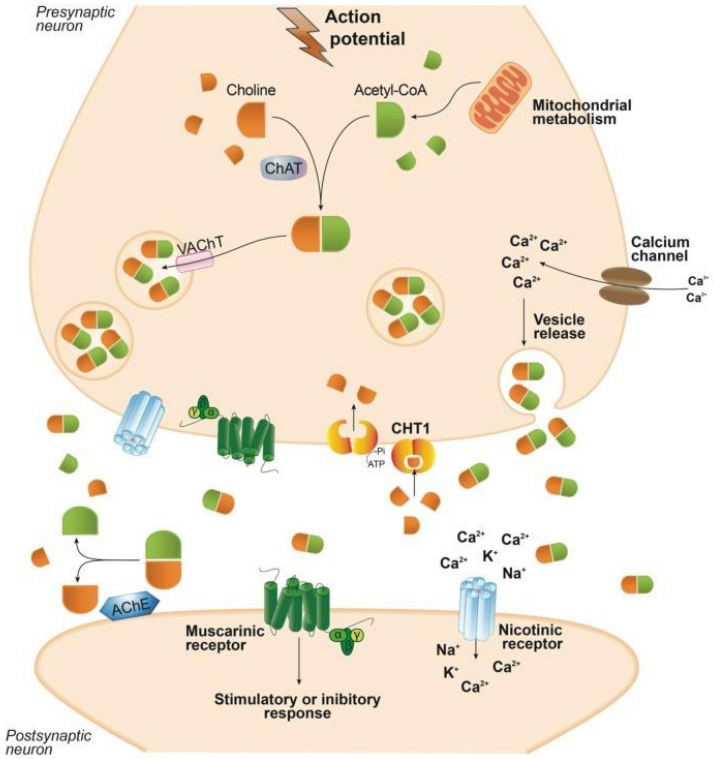

Figure 7: Acetylcholine synthesis and degradation. Acetylcholine (ACh) is synthesized in neurons from choline and acetyl-coenzyme A by the enzyme acetyltransferase. ACh is then packed in synaptic vesicles and released into the synaptic cleft where it binds muscarinic and nicotinic receptors. Released Ach is degraded into choline and acetate by the enzyme acetylcholinesterase (AChE) and choline is recycled back into neurons [91].

Beside alterations of the cholinergic system, alteration in other neurotransmitters, notably glutamate, GABA and dopamine, have also been observed in AD. Glutamate is the most abundant excitatory neurotransmitter in CNS, mainly involved in synaptic plasticity and therefore in memory formation processes. Glutamate is produced trough different metabolic pathways [101]. Upon release, glutamate binds to two types of receptors: ionotropic and G-protein-coupled metabotropic receptors. Ionotropic receptors are permeable to different ions, Ca^{2+} ions for the N-methyl-d-aspartate receptors (NMDAR) and Na^{+} and K^{+} ions for the α-amino-3-hydroxyl-5-methyl-4-isoxazole-propionate (AMPA) receptors. There are eight subtypes of metabotropic receptors and they can be grouped in three families, mGluRI, mGluRII and mGluRIII, based on the sequence homology, G-protein coupling, and ligand selectivity [102]. The activation can induces a wide variety of cells signalling; in general mGluRII and mGluRIII promote mainly an inhibition of intracellular release of Ca^{2+} and therefore an inhibition of neurotransmitters release whereas activation of mGluRI provokes the release of intracellular stores of Ca^{2+} and increase the NMDAR activity [103]. The ionotropic receptors are mainly post-synaptic whereas the metabotropic

are present in pre- and post-synaptic space and are present on both neurons and glial cells [104]. Glutamate is removed from the synaptic space by glial cells using the excitatory amino acids transporters (EAAT). In glial cells, glutamate is converted into glutamine and transported back to presynaptic terminals where it is transformed back into glutamate by the glutaminase enzyme and goes into vesicles through the vesicular transporters VGLUT1 and 2 [104]. NMDAR and AMPAR are the main glutamate receptors involved in learning processes because their activation promotes long-term potentiation (LTP) and long-term depression (LTD), both crucial events in synaptic plasticity. During LTP the strong and prolonged release of glutamate causes the activation of AMPARs and a strong depolarization which removes Mg^{2+} that block the NMDAR channel and allows the influx of Ca^{2+} ions into neurons. This strong activation of NMDARs provokes an enhanced synaptic strength. A weak activation of NMDARs causes a low increase in post-synaptic Ca^{2+} and triggers phosphatases which instead promote LTD [101] (Figure 8).

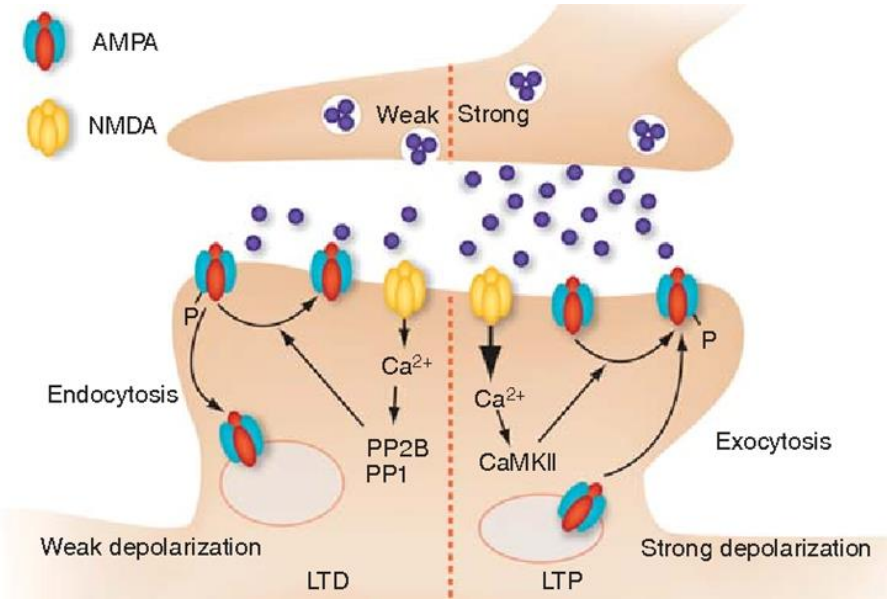

Figure 8: LTP and LTD effect on post-synaptic neurons. A weak activation in presynaptic neurons induces a moderate calcium influx through NMDA receptors. This event leads the activation of phosphatases that dephosphorylate AMPA receptors and induce the receptor endocytosis. A strong activation causes a strong depolarization that is able to trig LTP and activate the CaMKII, receptor phosphorylation, and exocytosis [105].

NMDAR are also important because they are able to activate expression of survival genes by activating Ca^{2+}-dependent transcription factors such as cyclic-AMP response element binding protein (CREB) and suppresses caspases and apoptotic pathway [101]. Pathological level of Ca^{2+} influx can cause excitotoxicity processes that lead to synapses loss and neuronal death. Therefore, regulation of glutamate availability in synaptic space is

essential to neuronal survival. Studies in AD patients have shown a decrease in the glutamate transporter capacity and a selective loss of vesicular glutamate transporter (VGluT) as well as reduction in EAAT type 1 and 2 in AD. Aβ oligomers are also able to induce an aberrant release of glutamate from astrocytes, these alterations in recycling of glutamate provokes its accumulation in the extra-synaptic space causing an over-activation of NMDA receptors leading to excess of intracellular Ca^{2+} and synaptic excitotoxicity [106]. In AD there is also a strong alteration in glutamate receptors. Aβ can enhance the activity of NMDARs in favour of LTD instead of LTP. Aβ promotes an excessive influx of Ca^{2+} and the activation of MAPK signalling pathway and protein phosphatases that promote the AMPAR endocytosis and again the promotion of LTD [107]. The internalization of AMPAR can also be modulated by GSK3β, an important protein involved in Tau phosphorylation (see §1.3.2). GSK3β appears to be essential for LTD. GSK-3β can phosphorylate the synaptic density protein 95 (PSD-95) and promote the destabilization of PSD-95 at the dendritic spines, reducing its association with the membrane [108]. PSD-95 is essential to determine the synaptic strength by controlling the AMPAR trafficking [109].

Another neurotransmitter altered in AD is the neurotransmitter γ-aminobutyric acid (GABA). GABA is involved in the control of anxiety, pain, anticonvulsive activity, cardiovascular regulation and depression [110]. GABA synthesis occurs from glutamate by the enzyme glutamic acid decarboxylase (GAD), through an irreversible reaction dependent on the availability of the cofactor pyridoxal-5'-phosphate (a vitamer of vitamin B_6) [111] and then it is transported into vesicles by the vesicular GABA transporter (vGAT). GABA acts on three different receptors $GABA_A$, $GABA_B$ and $GABA_C$ which are divided into ionotropic $GABA_{A/C}$ and metabotropic $GABA_B$ [111]. The re-uptake of GABA is mainly due to the action of transporter proteins GAT present in presynaptic neurons and in glial cells [112]. GABA re-up-taken by glial cell is converted to succinic semi-aldehyde by GABA transaminase (GABA-T) and then converted in glutamine that is transported back to neurons and convert again in glutamate [113]. Post-mortem studies have shown a reduction in GABA and GAD activity in cortical regions of AD patients [114]. GABAergic terminals have been shown to be diminished in both AD patients and APP/PS1 transgenic mice by immunocytochemistry, mainly on cortical neurons adjacent to amyloid plaques [115]. Post-mortem IHC study on AD shows an up-regulation of α1 and γ subunits of $GABA_A$ receptors [115].

The serotoninergic system plays also a fundamental role in memory acquisition and therefore a perturbation of it has been implicated in memory decline in AD. Serotonin (5-hydroxytryptamine, 5-HT) is synthetized in the *raphe nuclei* (brainstem) that has many afferent and efferent projections through the brain [116]. There are seven type of receptors (5-HT_1 to 5-HT_7) with each having different subtypes; most of them are coupled with G proteins and one is an ion channel, 5-HT_3 [116]. The main 5-HT receptors involved in learning are: 5-HT_{1A}, 5-$HT_{2A,}$ 5-HT_3, 5-$HT_{4,}$ 5-HT_6 [117]. Studies have shown that the inhibition of 5-HT_{1A} promotes the activation of molecular cascades involved in memory formation and positive effects on memory seem to happen when the 5-HT_3 receptors are inhibited; the inhibition promotes the enhancement of LTP induction, memory retention and spatial memory in normal rats. Conversely, activation 5-HT_{2A} receptor seems to be able to enhance the memory consolidation and this role seem to be due to the ability to enhance the release of other neurotransmitters such as ACh and glutamate. [117]. *In-vivo* and *in-vitro* studies have shown that 5-HT_4 receptor agonists promote the release of sAPPα fragment; therefore this receptor seems to be able to promote the non–amyloidogenic pathway of APP [118, 119]. The receptor 5-HT_6 has a very restricted expression in brain; studies on rat brain have shown that 5-HT_6 receptor is localised in the striatal, hippocampal and cortical areas of the brain, brain areas closely associated with memory and learning. Even if this receptor function seems to be strictly related to pro-cognitive effects, the exact role in AD upon activation or inhibition is still not very well established [120].

Dopamine (DA) is well known to be the neurotransmitter affected the most in Parkinson disease, but it has also be shown to be altered in AD [121]. Dopamine neurons are localized in retrorubral field, the *substantia nigra pars compacta* and the Ventral Tegmental Area (VTA); each area containing dopamine neurons interacts with different brain regions, specifically *substantia nigra pars compacta* targets the medium spiny projection neurons of the caudate and putamen nuclei and Ventral Tegmental Area targets the hippocampus, cerebral cortex and the *nucleus accumbens* [122]. DA plays an important role in control of locomotion, learning, working memory, cognition, and emotion. There are five types of DA receptors and they can be classified in D1-like and D2-like and are associated to G proteins. D1 receptor activation increases cyclic adenosine monophosphate (cAMP) concentration and D2 decreases it [123]. The ventral tegmental area is connected with the hippocampus, the main brain structure involved in memory, and the release of DA on hippocampus promotes

the synaptic plasticity and the long term memory [124]. The VTA is also connected with *nucleus accumbens* and cerebral cortex and it modulates the motivation and reward circuits in brain [125]. Based on these observations, a strong correlation of AD and DA dysfunction was hypothesised. Studies on human AD brains have shown that DA level are significantly reduced in AD [126] and a decrease in DA receptors is also related to AD [127] and the severity of cognitive dysfunctions [128]. Animal model for AD, mice Tg257 overexpressing the APP695, have a degeneration of VTA neurons and a reduction in connection coming from this brain regions; the administration of DA precursor is able to restore the impairment in food reward processing and dendritic spine density [121].

1.3.4 Neuroinflammation

Neuroinflammation is an important process that occurs during the development of AD and localised neuroinflammation occurs already in the early stages of AD. *In-vitro* and *in-vivo* studies have shown an activation of different neuroinflammation pathways induced by the accumulation of amyloid and NTF [129]. Astrocytes, microglia cells and cytokines regulate neuroinflammation and cell signalling [130]. Chronic neuroinflammation is the main characteristic that is present during AD and is characterised by a prolonged activation of immune cells which promotes neuronal injury and death due to the production of oxygen species (ROS) and nitric oxide (NO). The chronic neuroinflammation is also characterised by microglial cells able to phagocyte neurons due to expression of “eat-me” signals such as phosphatidylserine or calreticulin, activation of the complement system, activation of reactive astrocytes that secrete neurotoxic factors, loss of neurotrophic functions and activation of the inflammasome [131].

1.3.4.1 Microglial activation in AD

Microglial cells represent the 5-20% of glial population in brain [132]. The main role of microglial cells is to control and eliminate pathogens and cellular debris but they also provide factors responsible for supporting neurons and therefore to protect and maintain synapses [133]. Microglia cells are characterised by a small soma and a lot of ramified processes, in healthy condition the soma remain stable on its location and the processes elongate to explore the environment with no overlapping with other microglia processes. In pathological condition, activation of different receptors on microglia promotes the retraction of processes and their ability to move [134]. Historically microglia cells have been

classified in two different phenotypes M1 and M2 that were respectively a pro and anti-inflammatory state [135]. However recently has been demonstrated that the M1 and M2 classification is not correct and many microglia subtypes can be detected under disease conditions [136]. The classical pro-inflammatory (M1) status is characterised by the release of TNFα, interleukin-1, interleukin-6, interleukin-12, and interleukin-18. The classical anti-inflammatory status (M2) is characterised by the secretion of anti-inflammatory cytokines such as interleukin-4, interleukin-10, interleukin-13 and TGFβ [133]. In neurodegenerative diseases microglia cells are able to express both neurotoxic and neuroprotective factors and they have characteristics that seem to be specific of the disease, therefore the classification of the microglia activation status has been refined [136]. The M2 phenotype can be sub classified in: M2a alternative activation; type II alternative activation M2b and acquired deactivation M2c. Classical activation M1 is due to pro-inflammatory agents such as lipopolysaccharide (LPS) and interferon gamma (IFN-γ) [137]. The M1 activation promotes the production of reactive oxygen species, pro-inflammatory cytokines that can lead the tissue damage. M2a responds to IL-4 or IL-13 and they are mainly involved in phagocytic processes and the activation promotes the production of anti-inflammatory cytokines and growth factors [137]. M2b is activated by the exposure to immune complexes and agonists of Toll-like receptors or IL-1R and M2c by IL-10 and glucocorticoid hormones [138]. Different receptors are involved in the activation of microglia cells. CD200 is expressed by neurons, oligodendrocytes and astrocytes and is able to bind its receptor (CD200R) on microglial cells and their interaction promotes the resting state of microglia. Another essential receptor able to regulate the activation state of microglia cells is the G-protein-coupled seven-transmembrane chemokine receptor CX_3CR1, also called fractalkine receptor, that binds the ligand CX_3CL1 expressed by neurons [134]. There are also receptors that regulate the microglia phenotype. CD47 is a transmembrane immunoglobulin family protein expressed mainly on synapses and inhibits phagocytic processes after binding to its receptor SIRPα expressed on microglia cells [139]. Another important receptors on microglia cells is TREM2 which binds different molecules such as bacterial lipopolysaccharide, phospholipids, lipoproteins (HDL and LDL), and TREM2 ligands expressed on apoptotic neurons [140]. After the ligand binding with TREM2 receptor, the adaptor proteins DNAX-activation protein 12 (DAP12; also known as TYRO protein tyrosine kinase-binding protein) and DAP10, also called haematopoietic cell signal transducer, induces the activation of downstream signalling

molecules that cause different processes such as new expression of TREM2 on the cellular surface, Ca^{2+} mobilization, cytoskeleton rearrangement, the activation of the mechanistic target of rapamycin (mTOR) and of the mitogen-activated protein kinase (MAPK) signalling [141]. An up-regulation of TREM2 has also been found in AD [142]. Microglial cells also express Toll-like receptors (TLR) that are important to define cellular survival or death. TLR are widely expressed on different cellular type in CNS such as neurons, astrocytes, oligodendrocytes and microglia and the main role of these receptors is to detect pathogen-associated molecular patterns to activate pro-inflammatory pathways [135]. Microglia have a protective role based on the acute immune response against harmful stimuli such as misfolded proteins, if the response do not resolve, the activation of microglia becomes chronic reducing the beneficial functions and increasing the pathology [143]. In AD, microglia cells are able to bind the Aβ fibrils and oligomers using different receptors: the scavenger receptor A1, CD36, CD14, α6β1 integrin, CD47 and toll like receptors (TLR2, TLR4, TLR6 and TLR9), all able to promote the pro-inflammatory pathways. In different brain regions of post-mortem AD patients, toll-like receptors expressed on microglia cells have been founded up-regulated mainly around senile plaques [135]. The subtype of microglia associated with aging process, chronic stress and AD has been described as “dark microglia” as they present a condensed, electron-dense cytoplasm and nucleoplasm, accompanied by cytoplasmic shrinkage, Golgi apparatus and endoplasmic reticulum dilation, as well as mitochondrial alteration and sign of oxidative stress. They are able to phagocyte dendritic spines, axon terminals, and entire synapses, so they seem to be essential in maintaining and remodelling of neurons circuits and they are extremely active. Dark microglia express myeloid cell marker ionized calcium-binding protein (IBA1) and high level of CD11b, which is a critical component of phagocytic receptor CR3 and TREM2 when associate with amyloid plaques. Dark microglia are mainly localised close to the vasculature, with processes around the blood vessels they are found very close to the amyloid plaques with increased phagocytosis of amyloid β and surrounding dystrophic neurites [144].

1.3.4.2 Astrogliosis in AD

Astrocytes cells are important in the maintenance of brain integrity and homeostasis. They represent 20%–40% of human non-neuronal cells and are essential for tropic and metabolic support for neurons [145]. Astrocytes cells are involved in different roles and they

provide essential nutritional and growth support to neurons. They also regulate ions and neurotransmitters concentration to regulate synaptic activity and are therefore essential in synapsis plasticity and synaptic transmission [131]. Astrocytes cells are involved in the clearance of amyloid plaques by receptors advanced glycation end products (RAGE) and lipoprotein receptor-related protein 1 (LRP1) that control respectively the influx of circulating Aβ into the brain and the efflux of brain Aβ into the circulation through blood brain barrier (BBB) [146]. Astrocytes cells can be divided in two main subtypes of cells: fibrous and protoplasmic. The fibrous astrocytes are mainly present in the white matter and possess straight and long processes whereas the protoplasmic astrocytes are localised mainly in the grey matter with many short and thick ramification processes [146]. In pathological condition, the activation of astrocytes cells induces the release of cytokines such as IL-1, IL-6, and TNF-α which promote the neurodegenerative processes [147], release of nitric oxide (NO) and reactive oxygen species. This change into a reactive state is called astrogliosis and it is characterised by an increase in the expression of their main intermediate filament glial fibrillary acidic protein (GFAP), by morphological alterations (hypertrophy) and by functional changes such as control over ions in the synaptic cleft, uptake of neurotransmitters [148]. Dysfunction of astrocytes activity can lead to alteration in clearance of amyloid plaques, metabolic and energy dysfunctions and increase in neuroinflammation processes that contribute to the progression of AD.

1.3.4.3 Chemokines

As mentioned above, cytokines (interleukins, TNF, etc.) are produced by microglia and astrocytes and strongly contribute to the neuroinflammation; another family of important molecules involved in inflammation are the chemokines. Chemokines are essential for the recruitment of immune cells into the site of injury. There are four groups of chemokines in relation with their protein structure and the number of amino acids that separate two cysteine residues: α (CXC), β (CC), γ (CX3C) and δ (C). Chemokines are produced by different cellular types: microglia, astrocytes, oligodendrocytes, endothelial cells of the brain microvasculature and neurons; also their receptors are expressed in CNS on neurons, microglia cells and astrocytes [149]. CXCL8 (previously called IL-8) is produced by macrophages and endothelial cells and has been found elevated in AD with amyloid seemingly increasing their expression [150]. CCL2 or monocyte chemoattractant protein 1

(MCP-1) is a chemoattractant molecule involved in monocytes migration, CCL2 regulates the expression of IL-1 and IL-6 and experiments in the Tg2576 animal model of AD revealed that deficiency in CCL2 receptor is correlated with an early deposit of Aβ soluble [151]. CXCL10 (or IP-10) seems to be involved in neuroprotection and in Tg2576 co-localises with amyloid plaques and its expression is increased. CX3CL1 (fractalkine) and its receptor regulate the microglia activation and are up-regulated in AD [151].

1.3.5 The Blood Brain Barrier

1.3.5.1 Structure and functions

The microvasculature in the CNS is characterised by the blood brain barrier which controls the passage of molecules and cells into the brain parenchyma. The brain vasculature is characterised by continuous non-fenestrated vessels and is essentially responsible for protecting the brain from pathogens and toxins. The BBB is also essential in mediating the communications between the peripheral immune cells and controlling their possible infiltration as well as maintaining the homeostasis of the brain. The BBB is composed of endothelial cells, pericytes, the basement membrane and astrocytes end feet [152]. Endothelial cells are highly polarised, characterised by a luminal and abluminal compartment and in the brain are united by tight junctions (TJs) and adherens junctions (AJs). Different proteins are involved in the construction of TJs such as claudins, occludins, and junctional adhesion molecules (JAM) while vascular endothelial (VE)-cadherin and N-cadherin are specific molecules expressed at the adherens junction [153]. Different transporters and metabolic enzymes are expressed by endothelial cells. Transporters such as Glucose transporter 1 for glucose and LAT1 systems for large neutral amino acid; receptors such as transferrin receptor and ionic pumps that carry Na^+, K^+, Cl^-, Ca^{2+}, and other ions are responsible for the transport of their substrates from the blood to the brain while ATP pumps such as ABC transporters that carries lipid-soluble molecules, mainly move substrates from the brain to the blood [154]. Endothelial cells in BBB are also characterised by a low expression of leukocytes adhesion molecules [153]. The basement membrane is mainly characterised by molecules that are produced by endothelial cells, astrocytes and pericytes. It is composed primarily by collagen IV, laminin, nidogen, perlecan, fibronectin, agrin, osteonectin and glycosaminoglycans. The basement membrane has an important role in controlling the redistribution of junctional proteins and transporters [153]. Pericytes cover

mainly the abluminal surface of micro vessels and are incorporated into the basement membrane. They are linked to the endothelial cells by gap junctions and have a contractile function that is important to regulate blood flow [155]. Around vessels, astrocytes, beyond their roles describes above, are able to modify the TJs and change the expression and localization of transporters and enzymes [154]. Astrocytes end-feet are closely applied to the microvessels wall and they are enriched in transmembrane dystrophin–dystroglycan complex that are essential to create binds and interaction with the agrin, a component of the extracellular matrix. The end-feet are also characterised by the high density of orthogonal arrays of particles (OAPs); the water channel aquaporin 4 (AQP4) and the Kir4.1 are part of OAPs. The exact localization of these high density sites on the astrocytes end-feet is strongly regulated by the extracellular membrane through agrin; confirming the strong relation between endothelium and astrocytes cells [154]. The exchange of water and K^+ are essentials in the modulation of neuronal activity [153]. They are critical in improving energy to neurons by up-taking glucose, metabolising it anaerobically and producing lactate that is then transferred to neurons for their metabolism [156]. The BBB has also the role to modulate the infiltration of peripheral immune cells in brain which plays an important role in neuroinflammation. During neuroinflammation, perivascular macrophages expressing low major histocompatibility complex (MHC) class II become active promoting the recruitment of lymphocytes through increased endothelium permeability which helps cellular infiltration [153]; the role of circulating immune system cells in AD-related brain damage is still unclear even if a migration of immune cells have been observed in AD [157].

1.3.5.2 The BBB in AD

In AD, the BBB undergoes different changes and alterations. For example, the expression of GLUT1 endothelial cells is decreased when compared with age matched controls [158]. In AD, there is also a reduction in expression of the Aβ transporters LRP1 which is involved in the efflux of amyloid at the BBB, while higher levels of RAGE, which causes an influx of Aβ from the blood, have also been shown [159-161]. As described above, higher level of inflammatory molecules, such as nitric oxide, pro-inflammatory cytokines, chemokines prostaglandins, metalloproteases (MMP) promote disruption of the BBB [162, 163]. The basement membrane is also profoundly altered in its compositions with the production of MMP causing also degradation of the basement membrane while the number of pericytes

seem to be reduced during the developing of the pathology in the cortex and hippocampus [164]. An index of BBB breakdown is the micro bleeds (micro haemorrhages) that in AD patients has been detected in lobar regions instead of basal ganglia/thalamus and infratentorial regions [165] and micro bleeds are strongly associated with amyloid depositions detected with [^{18}F]florbetapir PET in MCI and AD [166]. TJ also appear altered in their function in subject with AD. Indeed studies *in-vitro* have shown that the permeability increases due to a reduction in the expression of ZO-1, claudin-5 and occluding that are component of TJ and the increase in MMP-2 and MMP-9 production [167, 168]. At the membrane basement of frontal and temporal cortex, the expression of collagen IV, perlecan and fibronectin seem to be increased in subclinical and clinical AD patients [169]. Astrocytes end-feet appear to undergo changes in their polarization and a study using the Arc/SweAβ animal model of AD has shown that the localization of AQP4 changes. The redistribution of AQP4 from end-feet to the non-end-feet membranes and close to the Aβ deposition potentially causes astrocyte depolarization and alteration in their functions [170].

1.4 Memory deficits in AD

Memory is defined as an adaptation to the past, the ability to store and maintain information over time. There are different types of memories and their classification can be done according to the duration (short vs. long term memory) and evaluation of the content, (declarative or explicit and procedural or implicit) [171]. In term of formation, the main difference between short (STM) and long term memory (LTM) is the mechanisms involved. Short term memory is characterised by the post-translation modification of pre-existing proteins and has a duration of seconds, whereas the long term memory requires new gene expression and protein synthesis and requires minutes to hours to be formed [172]. Different neuroanatomical systems are also involved in different forms of learning and memory [173] (Figure 9).

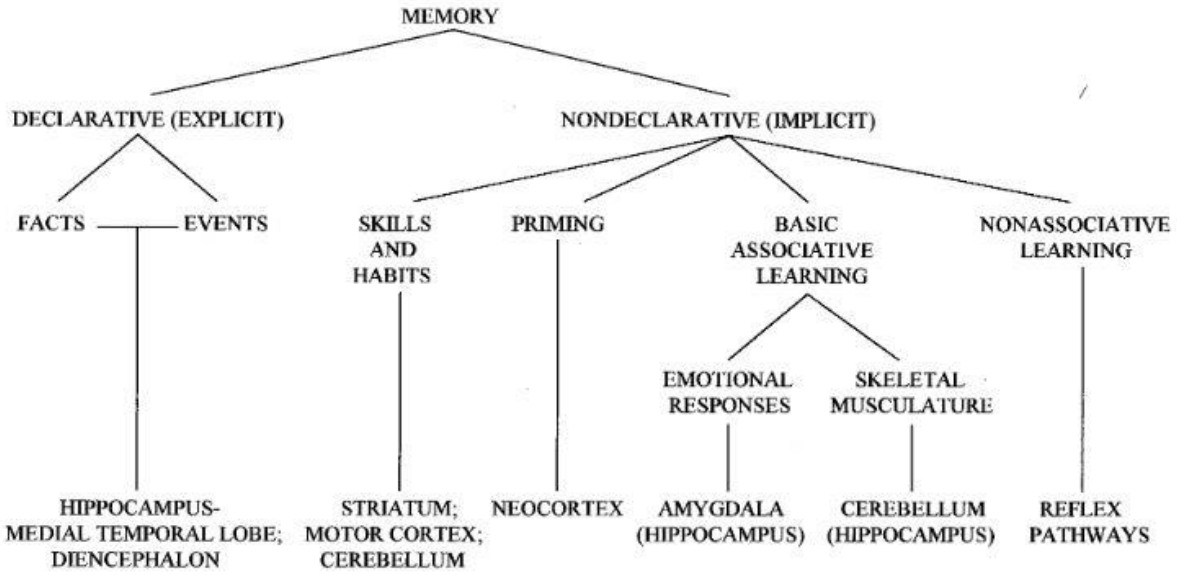

Figure 9: Brain regions involved in the formation and storage of memory. Memory can be devided in two types declarative and non delarative. Declarative memory is the explicit long term memory acquired by expiriences. The implicit long term memory, also called procedural is acquired by unconscius memories such as skills [173].

The hippocampus is a fundamental area of the brain, involved in learning and memory. Hippocampus communicates with different brain regions through interconnections with the medial temporal lobe. The hippocampus is characterised by a tri-synaptic circuit formed by the *gyrus dentatus*, the *cornu ammonis* (CA) fields and the *subiculum* (Figure 10). Two pathways coming from the entorhinal cortex, called perforant pathways, send inputs to the hippocampus. One input project to the *dentate gyrus* and CA3 and the second to the CA1 region and the *subiculum* [174]. The tri-synaptic excitatory pathway in the hippocampus starts from the *dentate gyrus* and connects to the CA3 pyramidal cells; the CA3 pyramidal cells, through the Schaffer collateral projection connect to the CA1 region which then projects to the subiculum and the deep layers of entorhinal cortex; from here projections go back to the cortical sensory areas that projected originally to the entorhinal cortex [175]. Acquisition of memory is mainly due to synaptic changes that need to be stabilized and consolidate to be persistent. The main synapses involved are the excitatory and inhibitory synapses, namely glutamate and GABAergic synapses which are involved in the long term potentiation and long term depolarization necessary to long term synaptic plasticity [176]. Action potentials cause the activation of presynaptic cyclic AMP (cAMP)-dependent kinases (protein kinase A, PKA, and protein kinase C, PKC) and the activation of those induce the release of glutamate. Different neurotransmitters promote the activation of cAMP-dependent signalling. The release of glutamate induces the activation of its receptors and

the influx of Ca^{2+} in post-synaptic neuronal cells. The high level of intracellular Ca^{2+} promotes cytoskeleton alterations and remodelling of membrane, therefore structural changes in synaptic buttons and activation of kinases namely: Ca^{2+}/calmodulin-dependent II, PKA/PKC and tyrosine kinase fyn. These processes cause different intracellular changes such as the activation of transcription factors cAMP response element binding protein 1 (CREB-1) triggering *de novo* protein synthesis to reinforce synaptic strength [176].

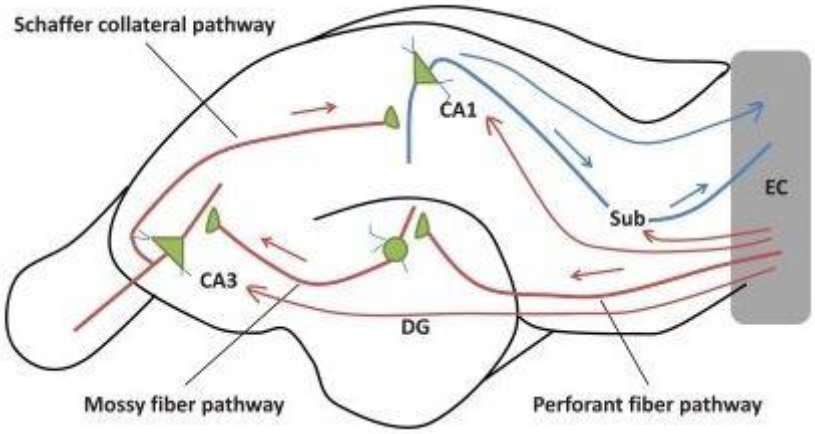

Figure 10: Hippocampal circuits. Information coming from the entorhinal cortex reach the hippocampus through the perforant pathways. The perforant pathway can project directly to the CA1 regions or starts the tri-synaptic excitatory pathway. In the tri-synaptic excitatory pathway, the *gyrus dentatus* is excited by the perforant pathway, then the *gyrus dentatus* projects excitatory synapses to the pyramidal cells in the CA3 region through the mossy fibre pathway. CA3 project to CA1 through the Schaffer collateral pathway and from there the projections go back to the cortical sensory area from which the input has started [177].

1.5 Protein synthesis

As mentioned above (see §1.4), in the CNS, appropriate protein synthesis is essential to stabilize the formation of long term memory [178]. Memory consolidation and reconsolidation require transcription processes. Protein synthesis requires the copy of encoded information in the DNA to mRNA. The RNA production involves mainly three steps: initiation, elongation and termination. The initiation steps requires the binding of RNA polymerase at the promoter region; during the elongation process nucleotides are added to the 3' end and for the termination phase termination sequences are recognised and the RNA polymerase is released [179]. RNA polymerases work with transcription factors to produce RNA molecules. The main transcription factors activated during memory formation and causing synaptic changes are:

- cAMP response element binding protein (CREB)

- CCAAT enhancer binding protein (C/EBP)
- activating protein 1 (AP-1)
- early growth response factor (Egc)
- Rel/Nuclear factor kB (Rel/NF-kB) [179].

The first step of translation is the initiation phase. During this step there is formation of the 43S pre-initiation complex that is made of ribosome 40S, initiator methionyl-tRNA and a GTP bound form of eIF2 and other translation factors. This complex binds the 5' end of the mRNA by recognizing the 5' cap which was added in the nucleus. This assembling is promoted by eIF3, the poly(A)-binding protein (PABP) and eIF4F. eIF4F is composed of eIF4E, eIF4A and eIF4G. eIF4G binds eIF3 and brings the 40S ribosome to the 5'-mRNA. eIF4G binds also PABP that promote the circularization of the mRNA. The formation of this complex triggers the scan of the mRNA until the recognition of the AUG start codon and form the 48S complex. After the match between AUG and the Met-tRNA, the elongation phase begins; it is characterized by arresting of the ribosome scanning, hydrolysis of eIF2 by eIF5B and formation of the ribosome 80S [180]. The translation processes is highly controlled by the regulation of the factor eIF2 and the eIF4E–binding proteins (4E-BPs) target of the rapamycin complex 1 (mTORC1).

1.5.1 eIF2 and the UPR pathway

The eIF2 factor is a 95 kDa protein and is a member of the G-protein super family, therefore able to bind guanosine-triphosphate (GTP) and guanosine-diphosphate (GDP) during its activation/inactivation state respectively. The protein eIF2 is composed by three subunits α, β and γ and during the translation phase binds GTP and the Met-tRNAi (initiator methionyl-tRNA). This activated complex is essential to deliver the t-RNA to the 40S subunits ribosome [181]. With the AUG codon and the t-RNA-mRNA matching, the elongation phase starts and the eIF2 bound GTP is hydrolysed by the GTPase accelerating protein (GAP) activity of eIF5 and a Pi (phosphate) is released. The release of a Pi induces a reduction in affinity of the Met-tRNA$_i$ for eIF2 and eIF5 are both released and in turn induce the formation of a ribosome 80S. The eIF2-GDP is now in its inactive form and the reactivation of eIF2 by GTP binding is mediated by the guanine nucleotide exchange factor (GEF) eIF2B [182]. The exchange GDP/GTP is controlled by phosphorylation state; the phosphorylation of

Serine 51 of the subunit α blocks the GDP/GTP exchange, causing the inability of the factor eIF2 to bind eIF2B [183].

The phosphorylation of the α subunit is regulated by different kinases that are activated by cellular stress conditions. The subunit α of eIF2 can be phosphorylated by different kinases that are activated in various stress condition. The general control non-derepressible 2 (CN2) kinase is able to phosphorylate *i)* the eIF2α subunit in case of amino acid deficiency, *ii)* PERK (PKR-like endoplasmic reticulum kinase) when there are perturbation of endoplasmic reticulum homeostasis (see below), *iii)* HRI (heme-regulated eIF2α kinase inhibitor) when there is heme deprivation in erythroid cells and *iv)* the protein kinase R (PKR) which phosphorylates the α subunits of eIF2 during viral infection [184]. These phosphorylation processes are important not only because they control the translation of newly synthetized proteins but also because phospho-eIF2 promotes the translation of several mRNAs, including the transcriptional modulator activating transcription factor 4 (ATF4). ATF4 is a repressor of cyclic-AMP response element binding protein (CREB) and therefore reduces synaptic plasticity and memory (see §1.5) [185]. Another gene that is translated after phosphorylation of eIF2α is β-secretase [181] which is one of the main secretase involved in AD pathophysiology (see §1.3.1 & 1.3.1.3).

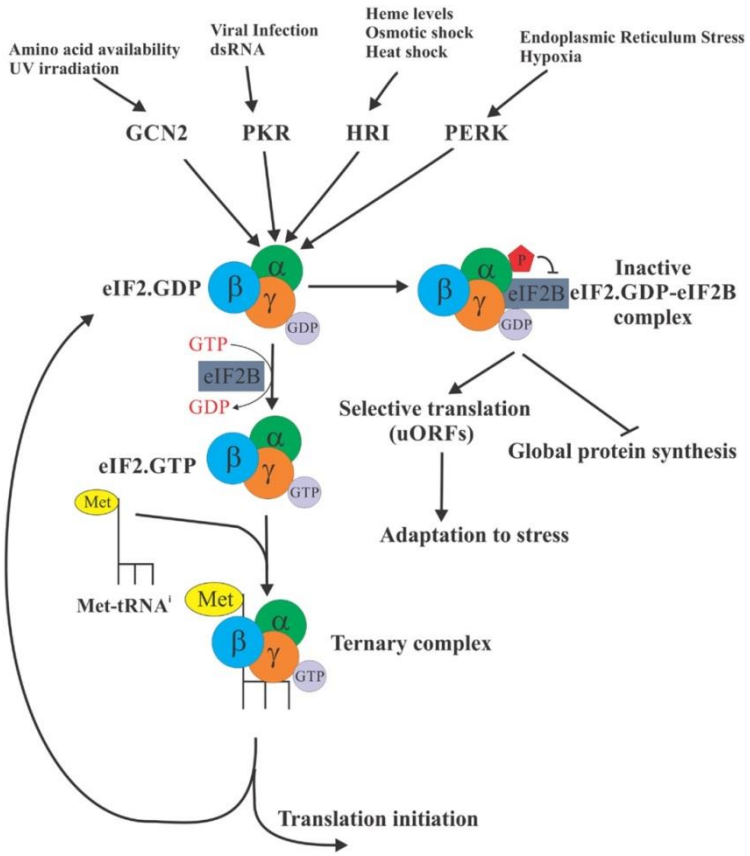

Figure 11: Attenuation of protein synthesis due to the phosphorylation of α-subunit by different kinases. The eukaryotic initiation factor 2 (eIF2) is a ternary complex consisting of α, β, and γ subunits. eIF2 can bind the GDP (inactive) and GTP (active), but only the active form can bind Met-tRNA$_i$. The active form promotes the delivery of the initiator Met-tRNA$_i$ to the 40S ribosomal subunit and induce the initiation of translation. Stress condition can induce the activation of kinases that phosphorylate the α subunit of eIF2 locking eIF2 in an inactive eIF2 complex with eIF2B [186].

Decrease in proteins translation can happen during different cellular stress conditions (Figure 12), therefore maintaining cellular homeostasis is essential. The endoplasmic reticulum has important roles in many cellular processes; it is important to maintain Ca^{2+} cellular concentration, protein synthesis and transport and apoptotic signals; all these mechanisms are altered or involved in AD [52]. ER alteration due to accumulation of misfolded pathological proteins or ER stress prevents the normal ER protein maturation and promotes the activation of the unfolded protein response (UPR) causing a temporally attenuation of protein synthesis [187]. When the UPR pathway fails, affected cells undergo dysfunction and cellular death. Normal cells respond to ER stress condition, increasing the transcription of ER-resident chaperones such as GRP78/BiP, GRP94 and protein disulfide isomerase (PDI) [188]. In the ER, there are three stress sensors: IRE1 (inositol-requiring enzyme-1), PKR-like ER kinase (PERK) and activating transcription factor 6 (ATF6). The

dissociation of GRP78 from PERK, ATF6 and IREα triggers the activation of the UPR pathways. Short term activation of the UPR pathways leads to restoration whereas prolonged perturbation of cellular homeostasis triggers apoptosis [189] (Figure 12).

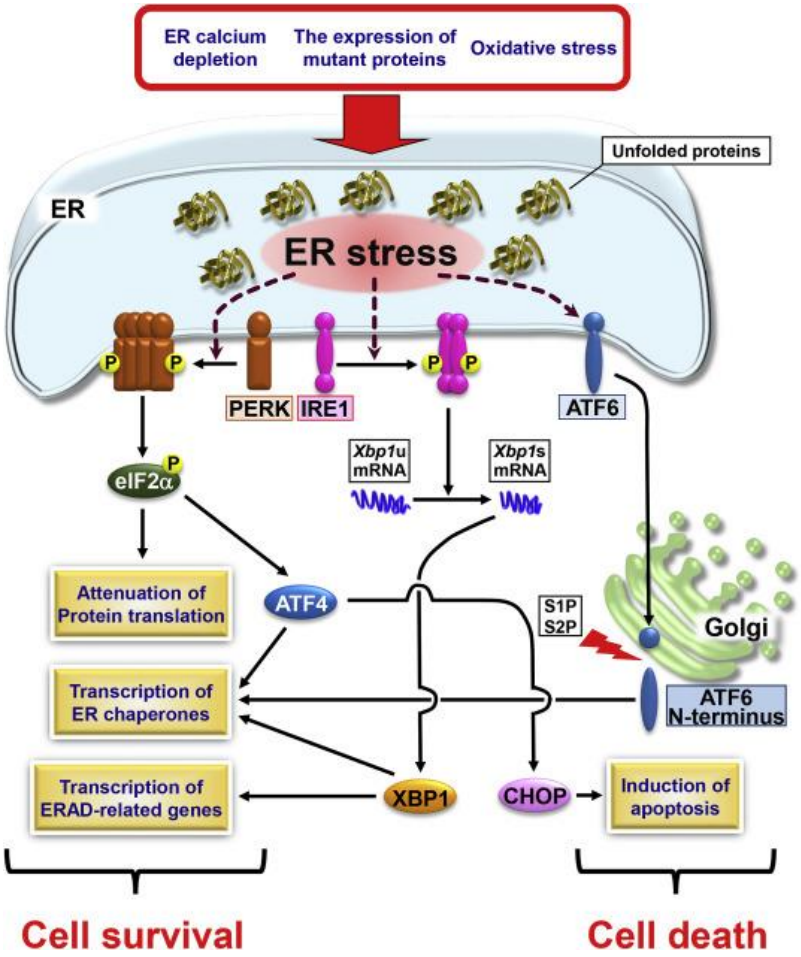

Figure 12: Activation of UPR pathway during stress condition. Alteration in cellular homeostasis promote the activation of three stress ER sensors, PERK, IRE-1 and ATF6. Different response can be induced: attenuation of protein synthesis, pro-survival mechanisms such as ERAD but the prolonged activity can also promotes the cellular death, therefore the apoptotic processes [190].

IRE1 exists in two different isoforms α and β. The dissociation of GRP78 from IREα promotes its auto phosphorylation and the activation of its RNAse activity [189]. IREα has the ability to bind different adaptor proteins that are involved in the activation of autophagy, apoptosis and inflammatory processes [52]. Activated IREα promotes the splicing of mRNA encoding for the transcription factor Xbox binding protein-1 (XBP1). XBP1 is able to regulate different UPR target genes such as genes for chaperones proteins, proteins involved in the degradation pathways (ER-associated degradation, ERAD) and phospholipid synthesis machinery, all important for the induction of ER membrane expansion during ER stress conditions [191]. The ERAD pathway, in which misfolded proteins present in cytosol undergo

an ubiquitination process, induces the degradation of protein by the proteasome [192]. The ubiquitination process is a post-translation modification that happens in cytosol and nucleoplasm; it is an ATP dependent process involving the enzymes E1, E2 and E3. Ubiquitination of a protein is a signal to the proteasome for protein degradation. If in the ER the protein is not correctly folded, the degradation-enhancing α-mannosidase-like lectins (EDEMs) bring the protein to a retrotranslocon, a pore in the ER membrane that promotes the exit of the protein to the cytosol, the ubiquitination from E enzymes promotes the degradation of the protein by the proteasome [193]. The dissociation of GRP78 from ATF6 induces its translocation in the Golgi where it is cleaved by two proteases site-1 and site-2. The activated ATF6 enhances a proper protein folding via increased production of ER chaperones and increased degradation of misfolded proteins [52, 194]. The other stress sensor is PERK. PERK is a type I transmembrane ER protein, its activation triggers the phosphorylation of the Ser51 of eIF2α. This phosphorylation provokes a temporary inhibition of protein synthesis, inactivating the formation of ribosome 80S [191]. The phosphorylation of eIF2α subunits promotes the expression of ATF4. ATF4 is a member of the ATF/CREB transcription factor family. The expression of ATF4 increases during stress conditions such as hypoxia, anoxia, ER stress, oxidative stress, amino acid deprivation and during development [195]. ATF4 acts as an activator but also as a repressor of transcription depending on the conditions. ATF4 is able to promotes the inhibition of CREB-dependent gene expression [181], hence inhibiting the synaptic plasticity and memory consolidation. ATF4 can also modulate metabolic and oxidative stress through modulation of different genes involved in mitochondrial function, amino acids metabolism and transport. ATF4 also regulates protein synthesis attenuation because it promotes the GADD34 transcription which is involved in dephosphorisation (=de-inhibition) of eIF2α [196]; ATF4 can also regulate apoptotic processes (intrinsic pathway) by the transcription of stimulate genes of CCAAT-enhancer-binding protein homologous protein (CHOP) [197]. Activation of PERK signalling has been shown to induce the activation of GSK-3β, one of the kinases involved in the processes of hyperphosphorylation of Tau protein [198] (see §1.3.2).

1.5.2 mTORC

mTORC (mechanistic target of rapamycin complex) is a ubiquitously expressed protein complexes that belongs to the family of phosphatidylinositol 3-kinase-related kinase

(PIKK) [199] and that can be found in 2 form: mTORC1 and mTORC2. mTORC1 is composed of various proteins: mTOR, raptor, the mammalian lethal with sec-18 protein 8 (mLSTR8), the DEP domain–containing mTOR-interacting protein (Deptor), the Tti1/Tel2 complex and the proline-rich Akt substrate 40 kDa (PRAS40). mTORC2 is composed of mTOR, rictor, mLSTR8, deptor, Tti1/Tel2 and mammalian stress-activated MAP kinase-interacting protein 1. mTORC1 and mTORC2 have different roles; mTORC1 regulates proliferation, mortality, survival and protein synthesis; mTORC2 main role is in cytoskeleton assembly [200] (Figure 13). mTORC1 is activated by different signals such as growth factors, amino acids availability and energy cellular level [199]. mTORC1 controls protein synthesis by the phosphorylation of eIF4E–binding proteins (4E-BPs) and p70 S6 kinases (S6K1/2) [180]. The 4E-BPs are able to bind the factor eIF4E. eIF4E is a subunit of eIF4F translation initiation complex that facilitates the binding of mRNA to the ribosomes. A strong phosphorylation by mTORC1 to the 4E-BPs proteins promotes the release of the binding proteins 4E-BPs from the factor eIF4E, eIF4E is then able to bind other proteins and form the active eIF4F complex for the translation [201]. The protein synthesis is also regulated by the phosphorylation of SK6 that is able to phosphorylate and activate substrates that promote the initiation of mRNA translation, including eIF4B, a cofactor of eIF4A involved in the regulation of the 5’ cap binding eIF4F complex [202], and the elongation factor 2 that is responsible for the elongation step [203]. mTORC1 has an important role in inhibiting autophagy. Autophagy is a mechanism in which macromolecules are trapped in a double membrane and then bound to the auto phagosomes. The fusion of auto phagosomes with lysosomes induces the degradation of organelle and proteins in cells [204]. mTORC1 also regulates mitochondrial function, not only for its role in autophagy but also because mTORC1 regulates the transcription of mRNAs coding for nuclear mitochondria proteins and mitochondria ribosomes; most important is the regulation of transcription of mitochondria proteins involved in fission processes [205]. Fission and fusion of mitochondria are essential processes that restore the mitochondria by e elimination or compensation of mitochondria damage. Failure of these processes can lead to neuronal death and also activation of apoptotic processes [206].

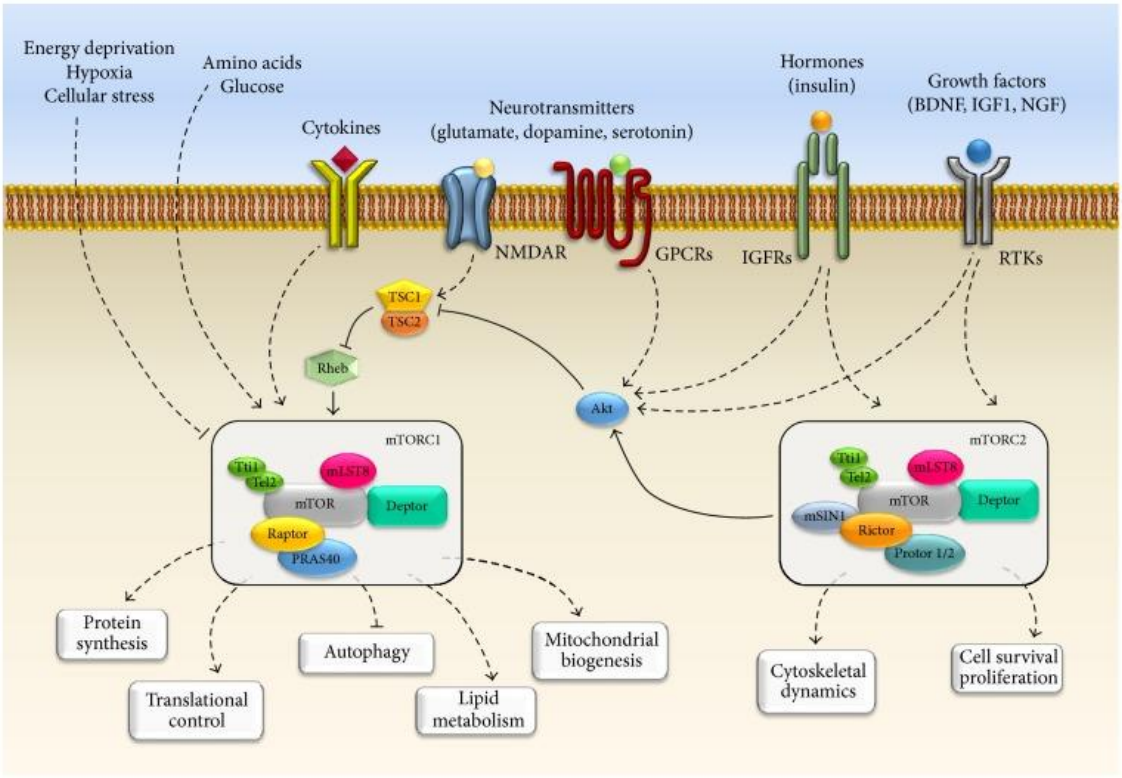

Figure 13: mTORC signalling in neurons. Different stimuli can promote the activation of mTORC1 and mTORC2 such as nutrients, cytokines and hormones. The activation of these factors induces different cellular responses. mTORC1 is mainly involved in the regulation of protein synthesis, autophagy, lipid metabolism and control of mitochondria; mTORC2 has the role to control cytoskeletal functions and cellular proliferation [207].

1.6 Apoptosis and organelles involvement

Prolonged ER stress condition can activate apoptotic processes by activation and deactivation of ATF6, PERK and IRE1-α (Figure 14). Apoptosis differs from necrosis as necrosis is a toxic cellular death, energy independent and in which the cells are passive victims of the process [208] whereas apoptosis is a highly regulated, energy and proteins dependent mechanism. Two different pathways are induced in apoptosis: extrinsic (death receptor) and intrinsic (mitochondrial). The extrinsic pathway involves the activation of receptors, member of the tumour necrosis factor (TNF). TNF receptors are mainly characterised by a cytoplasmic death domain and after activation the adaptor FADD (associated death domain) is recruited, causing the formation of a death-inducing signalling complex (DISC) [208]. Activated DISC leads to the autocatalytic activation of caspase 8, caspase 8 activates caspase 3 by cleavage or cleaves BH3-interacting-domain death agonist (Bid), a pro-apoptotic Bcl2 family member. The Bid fragment promotes the release of

cytochrome-C by mitochondria which activates caspases 9 and 3, inducing DNA fragmentation and cell death [209].

The intrinsic pathway is regulated by Bcl-2 family members that can be pro- or anti-apoptotic. They are characterised by at least one to four α-helical BH domains. The anti-apoptotic members have all four BH domains: Bcl-xL, Bcl-w, Bcl-2, Mcl-1 and A1. The pro-apoptotic can be divided in two groups based on their BH domains; Bak, Bax and Bok, contain BH domains 1–3 while Bim, Bad, Bik, Bid, Bmf, Hrk, Puma and Noxa contain only the BH domain 3. The main proteins involved in the intrinsic pro-apoptotic pathway are Bax and Bak which, when they homo-oligomerize, induce the permeabilization of the outer mitochondrial membrane, facilitating cytochrome-C release. When cytochrome-C is released by mitochondria, an apoptosome is formed by binding of cytochrome-C with procaspase-9 and apoptotic protease activating factor 1 (APAF-1). Activation of caspase-9 promotes the sub-sequential activation of caspase-3 and therefore the death pathway [210]. Under prolonged stress condition, PERK is able to induce the transcription of ATF4 that promotes transcription of CHOP and pro-apoptotic family members; CHOP is a transcription factors that coordinate the expression of different genes involved in intrinsic apoptotic pathway [211, 212]. Prolonged activation of IRE1α is able to bind TNF receptor-associated factor 2 (TRAF2) that promote the activation of caspases-12. Caspase-12 (murine or caspase-4 in human) that triggers the direct activation of caspase-9 [213]. IRE1α and TRAF2 are able to active c-Jun-N-terminal inhibitory kinase (JIK) that induces the transcription of CHOP [52]. Alteration in Ca^{2+} levels in the ER can also activate apoptosis; Ca^{2+} is transferred from ER to mitochondria, causing ATP production and mitochondrial respiration. Excessive transfer of ER Ca^{2+} provokes the opening of the permeability transition pore (PTP), which leads to mitochondrial dysfunction and therefore apoptosis [210]. The pore formation can also be induced by the oligomerization of BAX, which translocate to mitochondrial membrane causing the pore formation and release of cytochrome-C [214].

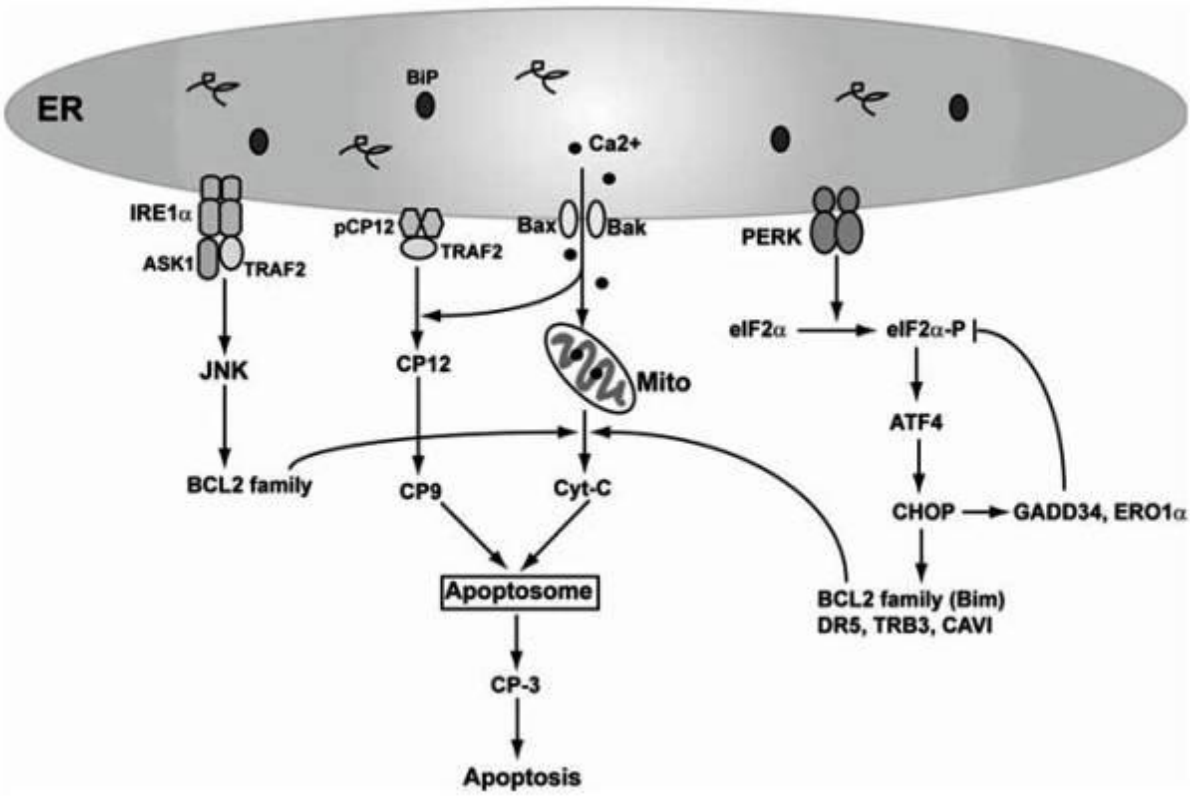

Figure 14: Regulation of apoptosis during ER stress condition. ER alteration can induce the activation of PERK and IRE1α. Upon activation PERK proteins can induces the transcription of genes involved in apoptosis. On the other hand IRE1α serves as a scaffold protein to form a complex with TRAF2 that promotes also the extrinsic apoptotic pathway. Excessive transfer of Ca^{2+} from ER causes the opening of the permeability transition pore (PTP), which leads to mitochondrial dysfunction and the activation of intrinsic apoptosis pathway [206].

Mitochondria are closely associated with ER, they control cellular energy and apoptotic processes. The physical interaction ER and mitochondria is mediated by a specific region called mitochondria-associated membranes (MAM) region. MAM region is enriched in cholesterol and other lipids and has a lipid raft-like structure. The MAM region is involved in cholesterol and phospholipid metabolism, in Ca^{2+} homeostasis, and in mitochondrial function and dynamics [215]. The role of mitochondria in neurons is essential in particular at the synapses because they control the production of ATP and the Ca^{2+} homeostasis, both essential for the neurotransmission and the generation of membrane potential [216]. Dysfunction in mitochondria promote oxidative stress in which reactive species of oxygen lead damage in lipids, proteins and DNA [217], dysfunction in synthesis and storage of neurotransmitters, all processes that lead neurons impairment and neuronal death [218].

1.7 PSR and Alzheimer's disease

Misfolded proteins and protein aggregates are one of the main characteristics of neurodegenerative disease such as AD or Parkinson disease (PD), while oxidative stress, ER and mitochondrial dysfunction are also well described in such diseases [219]. Pathological forms of proteins can be due to genetic mutations, alteration during transcription and/or translation due to cellular stress. As described above (see §1.5.1 &1.5.2), the attenuation of protein synthesis is one of the first steps activated during cellular stress conditions. Different studies have shown alterations in pathways activated by ER stress in AD patients but also in animal models. Bip/GRP78 proteins are expressed in ER with a dual role such as folding and assembly of proteins and ER stress sensor (see §1.5.1). Level of Bip/GRP78 have been found by Western Blot (WB) to be elevated in the hippocampus and temporal cortex in AD when compared with healthy brain. The analysis of Bip/GRP78 protein by immunohistochemistry showed strong staining in CA1 and CA2 areas of the hippocampus in AD when compared to control cases [220]. Also in the 3×Tg-AD animal model, immunostaining showed an increase in GRP78 levels when compared with controls [221].

The main factor involved in regulation of protein synthesis is eIF2α which promotes the attenuation of protein transcription when phosphorylated. Studies of human brains and in animal model of AD have demonstrate an increase in the phosphorylation of eIF2α. WB analysis of 10-12 months old APP/PS1 mouse brains and in 5XFAD mice have shown an increase in eIF2α phosphorylation in hippocampus but no in cerebellum and similar data were found in human AD brains and case controls by WB and IHC [222]. The elevated phosphorylation of eIF2α is accompanied by an elevated activation of PERK proteins evaluated by WB in 5XFAD when compared to WT. In the same study, mice having PERK haplo-insufficiency and AD ($PERK^{+/-}$/5XFAD) have a significant reduction in eIF2α phosphorylation when compared to 5XFAD and higher levels of phospho-eIF2α when compared to WT; even if levels of eIF2α remains unchanged between WT, $PERK^{+/-}$/5XFAD and 5XFAD. Comparison of WB from WT and $PERK^{+/-}$ showed no change in phosphorylated eIF2α. These data confirm that PERK is the main kinase involved in the phosphorylation of eIF2α and that the PERK activation happens mainly in AD [223]. Over stimulated PERK pathway can promote cellular death, and evaluation by IHC of the medial septum and the vertical limb of the diagonal band in 5XFAD, $PERK^{+/-}$/5XFAD and WT brains showed that choline acetyltransferase staining was lower (i.e. neuronal loss) in 5XFAD whereas the

number of cholinergic neurons in PERK$^{+/-}$/5XFAD was respectively higher and nearly equivalent to the number in WT [223].

mTORC controls the balance between protein synthesis and degradation and a relation between mTORC and AD has been established. Mice hAPP(J20) treated with rapamycin (inhibitor of mTORC1) showed an improvement in their performance in behaviour tests and strong activation of autophagic processes that promote the reduction in $A\beta_{42}$ levels [224]. This data has also been shown in 3×Tg-AD mice in which has been found also a reduction in Tau protein [225]. Similarly, treatments with temsirolimus (inhibitor of mTORC1) also showed an increase in clearance of Aβ in HEK293-APP_{695} cells and in brain of APP/PS1 mice [226].

1.8 The synaptic vesicles SV2A

The connections between neurons is mediated by the release of neurotransmitters. Neurons receive chemical input from other neurons from dendrites and transfer their information to others through axons. The transmission is mediated through the release of neurotransmitters in the synaptic cleft, able to bind receptors on the post–synaptic neurons hence transmitting the neuronal activity. At the axonal terminal, specialised structures called vesicles (synaptic vesicles, SV) are filled with neurotransmitters and when an action potential reaches the axon terminal, it induces the release of neurotransmitters by an increase in calcium that cause the fusion of the SV with the cellular membrane [227] (Figure 15).

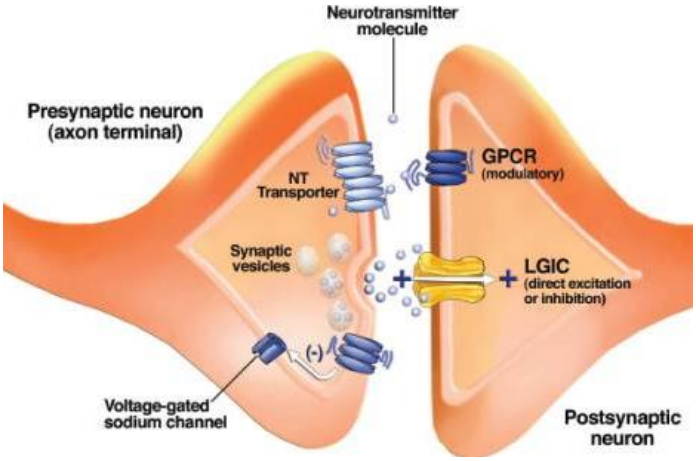

Figure 15: Representation of communication between two neurons. When an action potential reaches the presynaptic neuron terminal, it induces the fusion of synaptic vesicles with the membrane, stimulating the release of neurotransmitters. The neurotransmitters in the synaptic cleft is able to bind receptors expressed on the post-synaptic neurons, promoting their action. LGIC = ligand-gated ion channels and GPCR = G-protein–coupled receptors [227].

SV2A is a glycoprotein present in the membrane of synaptic vesicles and is part of the SV2 family. SV2 vesicles are highly conserved proteins in vertebrates and three isoforms are part of this family: SV2A, SV2B and SV2C. SV2 family proteins are characterised by 12 transmembrane regions and N- and C- cytoplasmic terminal-sequences, a large N-glycosylated intraluminal loop. The N terminal and the luminal loops have less homology between the isoforms while the cytoplasmic loops connecting the transmembrane sequences are highly conserved [228]. The levels of expression of these three isoforms vary in brain; SV2A is ubiquitously expressed in neurons, the expression of SV2B is restricted to some brain areas such as in the trigeminal and motor nuclei and low expression in *globus pallidus*, *dentate gyrus* of the hippocampus, cerebellum, and *substantia nigra pars reticulata* [229] and SV2C is present only in some neurons in basal forebrain and brainstem [228]. The exact role of the synaptic vesicle SV2A is still not clear; it seems to be involved in the modulation of neurotransmitters exocytosis through the regulation of Ca^{2+} sensor proteins and their sensitivity to Ca^{2+} [230]. SV2A dysfunction has been associate with many disorders such as epilepsy, schizophrenia and Alzheimer's disease. A decrease in SV2A expression has been found in post-mortem brain of AD patients [231] and the use of levetiracetam, a drug used for epilepsy able to bind selectively SV2A, has been shown to improve memory, behaviour abnormalities and synaptic alteration in AD mouse models [232]. Synaptic loss is one of the main alterations that happens in neocortex and hippocampus of AD [233, 234] and synaptic loss is very well correlated with cognitive decline in AD [235]. The plasticity of hippocampal synapses changes during the development of AD and before synaptic loss starts, a neuroplastic compensatory response happens in the first stages [236, 237].

1.9 Animal model of Alzheimer's disease

1.9.1 Mice

Different animal models, invertebrates (e.g. *Drosophila melanogaster* and *Caenorhabditis elegans*) and vertebrates (e.g. zebrafish, mice and rats, non-human primates) have been used to better understand the AD pathology and to assess novel therapies [238]. Each animal model is not able to reproduce all the pathophysiological changes that characterise AD and therefore there are limitations associated with all of them. Most of the animal models used to study AD are mice. The APP (695) protein in mice has a 97% homology with the human APP and the Tau protein has 88% homology [238]. The first generation of mouse models were characterised by the over-expression of APP protein with or without familial mutations, and various promoters such as platelet-derived growth factor-β (PDGF-β), prion protein (PrP) and the thymocite differentiation antigen-1 (Thy1), have also been used to generate transgenic mice. The most used APP models are PDAPP, Tg2576, APP23, J20, and TgCRND8 (Table 1). The transgene can carry more than one mutation and the most used is the Swedish (K670N/M671L) mutation in which two amino acids lysine (K) and methionine (M) are substituted with asparagine (N) and leucine (L) [239]. APP-Tg mice are able to reproduce only some aspect of AD pathology indeed, even if they are able to reproduce the memory dysfunction before the amyloid deposition in many cases, they do not present NFT and neuronal loss. To reproduce better the AD pathology several mutations of the γ-secretase gene have been incorporated to increase the ratio of $A\beta_{42}$ such as: the Indiana (Ind, V717F), London (Lon, V717I), Florida (Flo, I716V) and the Iberian Peninsula (Ibe, I716F) or mutations in PSEN1 such as M146V, M146L, L166P , L286V, or exon 9 deletion (dE9) [240]. In efforts to replicate the NFT pathology, mutant Tau mice with APP-Tg have been generated. APP-Tau-Tg mice present amyloid deposition, NTF, gliosis, synaptic damage and memory impairment but the mutation on the MAPT gene encoding for Tau are not cause of AD but fronto-temporal dementia with parkinsonism (FTPD) [239].

Table 1: transgenic mouse model of AD. Table adapted from [240].

APP transgenic	
Model	**Transgene**
PDAPP	huAPP770 (Ind) minigene (cDNA + introns 6–8)
Tg2576	huAPP695 (Swe)
C3-3	mo/huAPP695 (Swe)
APP23	huAPP751 (Swe)
J20	huAPP770 (Swe/Ind) minigene (cDNA + introns 6–8) huAPP695 (Swe/Ind)
TgCRND8	huAPP770 (Swe/Dutch/Iowa)
APP/PS1 Transgenic	
APP/PS1	mo/huAPP695 (Swe); Tg huPSEN1 (ΔE9)
APPPS1	huAPP695 (Swe); huPSEN1 (L166P)
5XFAD	huAPP695 (Swe/Flo/Lon); huPSEN1
Tg6799	M146 L/L286 V
Tau Transgenic	
Tau Tg	huMAPT3R0N (wt)
JNPL3	huMAPT4R0N (P301L) huMAPT4R0N (P301S)
PS19	huMAPT4R1N (P301S)
APP/PS1/Tau Transgenic	
3xTg-AD	huAPP695 (Swe); MAPT4R0N (P301L); Psen1 M146V knock-in

1.9.2 Rats

Mice were preferred to rats for technical reasons such as higher availability of pro-nuclei and survival of embryos after injection or better availability of stem cells. However, rats have other advantages, indeed their large body facilitates drugs administrations, neurosurgical and neuroimaging procedures they are generally better in behaviour analysis [241]. Different rat AD models have been created to mimic better the various aspects of AD pathology (Table 2). The first transgenic rat model for Alzheimer's disease appeared only in 2000s, since then single and multi-transgenic rat models of AD have been developed. Due to the recent availability of AD rat models, they are not as well characterised as the many mouse models [242].

Table 2: Transgenic rat models of Alzheimer's disease and the pathology that each mutation induces in the rats. Table adapted from [241].

Name	Transgene	Background	Amyloid pathology	Tau pathology
UKUR28	hAPP751 Swe, IndPDGF promoter	Wistar (outbred)	iAβ in cortex and hippocampus from 6 m. No plaques	N/A
UKUR25	hAPP751 Swe, Ind Human PS1 (M146L) PDGF promoter	Wistar (outbred)	iAβ in cortex and hippocampus from 6m. No plaques	Increased ptau (PHF-1) at 9m, no tangles
TgAPPswe	hAPP751 Swe, PDGF promoter	Fisher-344 (inbred)	Increased APP mRNA (56%) and Aβ-40 and Aβ-42 peptides, no plaques	N/A
Tg6590	hAPP695 Swe, UbiquitinC promoter	Sprague-Dawley (outbred)	Increased APP products Cerebrovascular deposits at 15 m. Few diffuse plaques	Increased pTau (PHF-1) at 15m, no tangles.
hAPP695	hAPP695 wild-type, UbiquitinC promoter	Wistar (outbred)	Increased APP/ Aβ levels (2 fold) in cortex and hippocampus	N/A

			no plaques	
PSAPPTg478/ Tg1116/ Tg11587	hAPP695 Swe, Rat synapsin I promoterhAPP695 Swe, Lon, PDGFβ promoter Human PS1 (M146V), Rat synapsin I promoter	Sprague-Dawley (inbred)	Mostly diffuse plaques Few compact plaques in hippocampus. No vascular Aβ depositsAβ load confirmed with (F-18) FDDNP microPET	Increased ptau (AT8, PHF-1), no tangles
McGill-R-Thy1-APP	hAPP751 Swe, Ind, Mouse Thy1.2 promoter	Wistar (outbred)	Progressive accumulation of iAβ in cortex and hippocampus from 1 week post-natalAβ plaques starting at 6-9 m.	N/A
TgF344-AD	hAPP695 Swe, Human PS1ΔE9 Mouse PrP promoter	Fisher-344 (inbred)	Progressive accumulation of iAβ, Aβ-40 and Aβ-42 and Aβ plaques	Increased ptau (CP-13, pTau-PADRE and others) and Gallyas-positive NFT
SHR72 and SHR318 Human tau truncated (151-391, 4R)	Mouse Thy1 promoter	SHR (inbred)	N/A	Increased ptau (AT8) Tangles in brainstem
SHR24	Human tau truncated (151-391, 3R) Mouse Thy1 promoter	SHR (inbred)	N/A	Increased ptau (DC11 and others) Tangles in cortex

1.9.3 TgF344-AD rat model used in this work

TgF344-AD and the associated background WT (Fischer-344) was the model selected for use in my PhD studies. TgF344-AD have a Fischer-344 background and two AD human mutations in a single transgene: The Swedish APP (APPswe) and the Δ9 exon of the presenilin-1 (PS1ΔE9 or PS1dE9), which cause familial early onset AD. The AD pathology in

this rat model is characterised by increased levels of soluble amyloid β and p-Tau as detected by WB already present from 6 months of age and increasing with age. This is accompanied by increasing amyloid β plaque deposition neuroinflammation as well as neuronal loss and cognitive dysfunction [243-247] from 6 months of age onward and neurofibrillary tangles (NTF) at 16 months of age. A neurovascular dysfunction is also present in TgF344-AD rats at 9 months of age with a significant amount of vascular Aβ deposits and arteriolar mural cells that undergo structural remodelling, leading to vascular changes [244]. Reduced basal transmission in entorhinal-hippocampal (medial perforant path to dentate gyrus) synapses is present already at 6 months of age in TgF344-AD and the transmission between CA3-CA1 remain unchanged at 6 months but a significant deficit appears at 9 months in male TgF344-AD and at 12 months in female TgF344-AD [248]. MRI techniques have also identified a decrease in functional connectivity already present at 6 months and a hypo-connectivity at 10 months of age [246] and structural brain networks was found altered since the earliest age getting worse with age [249]. Transgenic rats also showed an early *locus coeruleus* dysfunction that lead to a decrease *locus coeruleus* innervation in the medial entorhinal cortex and reduced norepinephrine levels in the hippocampus already present at 6 months of age [250]. Increased anxiety-like behaviours were found present in TgF344-AD rats at 4 months of age [251]. Working memory was found impaired in old TgF344-AD rats (24 months) by novel object recognition test [243]. Morris water maze test on WT and TG rats at 4-5, 7-8 and 10-11 months of age, showed that at 10-11 months of age TG rats had spatial impairment using less precise trajectories to reach the platform [252]. No deficit in learning or memory was detectable at 15 months of age by using the Barnes maze and reversal Morris water maze showed a hippocampal-dependent spatial memory impairment in TgF344-AD rats at 24 months with an improvement of performances in TG rats when treated with the neuro-protective compound (-)-P7C3-S243. (-)-P7C3-S243 promotes the proliferation or survival of new born hippocampal neurons in the *dentate gyrus* of the hippocampus mitigating the cognitive decline in aging rats [245]. Behaviour tests in this animal model showed quite inconsistent data. Indeed, in the first publication Choen *et al.* [243] described an alteration of spatial memory that start at 15 months of age and increased at 24 months in the initial learning and in the reversal phase during the Barnes maze; in another study TG rats performed worse than WT only in the reversal phase of MWM at 24 months of age [245]. These data show

that TgF344-AD could be used as a good model for AD, having most of brain alterations present in patients affected by Alzheimer's disease but this strain seems to be not suitable for behavioural tests.

Table 3: AD-like pathology in TgF344-AD.

AD-like pathophysiological characteristics			
Amyloid pathology	Tau pathology	Neuroinflammation	Neurodegeneration
Progressive accumulation of $A\beta_{40}$ and $A\beta_{42}$ and Aβ plaques	Increased pTau (CP-13, AT8, pTau-PADRE) and Gallyas-positive NFT	Age-dependent increase in astrogliosis (IHC) and microgliosis (PET and IHC)	Neuronal loss Alteration in NAA (MRS) Loss WM Decreased functional connectivity

1.10 PET imaging

1.10.1 PET imaging physics

The AD brain is characterised by histopathological, structural and functional alterations that precede the clinical manifestations of Alzheimer's disease. These modifications can all be assessed using *in-vivo* brain imaging [253]. Positron emission tomography (PET) is used to measure quantitatively metabolic and pharmacological processes dynamically (along time) and in 3D. The radionuclides that are used in PET imaging emit β^+ (or e^+) particles (positron emission decay) and have a half-life of 2mins for [^{15}O], 20mins for [^{11}C] and 109mins for [^{18}F]. The β^+ emitted is an antiparticle of the electron (same mass but opposite charge). The β^+ decay is described by:

$$\boldsymbol{p = n + \beta^+ + \nu} \qquad \textbf{(Equation 1)}$$

p is a proton, *n* is the neutron and *v* is a neutrino.

The annihilation of the β^+ with an e^- produces two γ photons of 511 keV in opposite direction (180°) (Figure 16) [254].

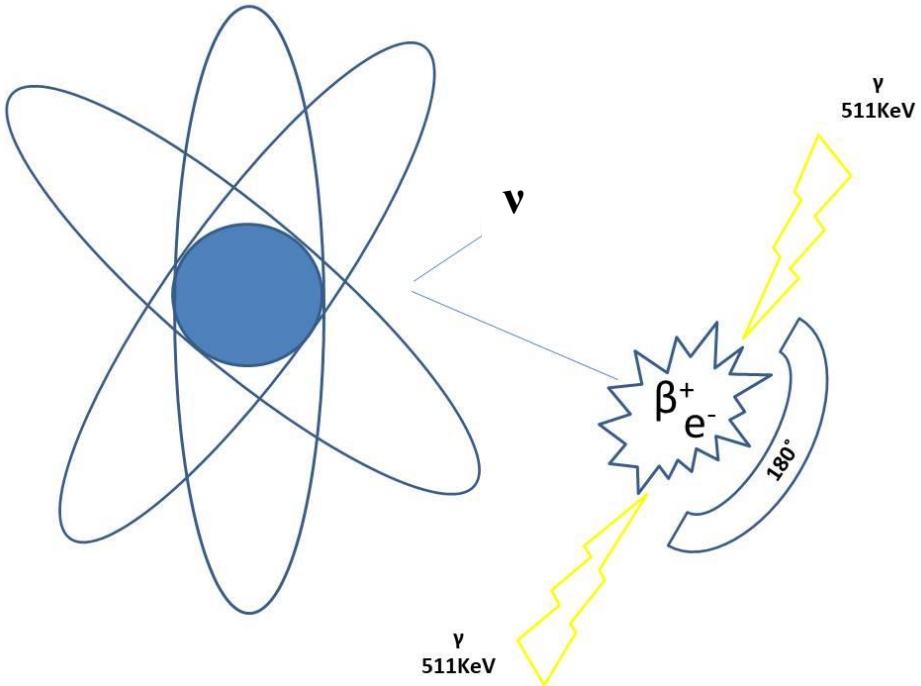

Figure 16: Representation of annihilation process of a positron and an electron. When the annihilation happens 2 photons 511KeV, are emitted in opposite direction (180˚).

1.10.2 Data correction Inveon PET/CT

After annihilation the two γ-rays of 511 KeV hit two scintillation detectors. There are different types of scintillation material and the one implemented in the Inveon PET/CT small

animal scanner used in this study are scintillation detectors using LSO (Lutetium oxy-orthosilicate) crystals. The LSO detectors show almost all the characteristic of an ideal detector, having high atomic number and density and short decay after scintillation [255]. The scintillation lights is converted into an electrical pulse by a photomultiplier tube and the signal is then amplified and processed by pulse height analyser able to discriminate the photon energy and register as counts [256]. A list-mode file containing coincidence data recorded with time and space information is generated for each event and sorted into a 3D sinogram [257]. In our study the 3D data were corrected for several effects such as normalisation, attenuation, radioactivity decay and scatter and random events, as part of the image reconstruction using the OP-OSEM3D-MAP. Correction for these parameters is essential for the quantitative accuracy PET images.

Normalisation is the correction of errors coming from the heterogeneity of detectors. To measure this, a normalization scan is performed to evaluate the detection sensitivity of each detector. Normalization is obtained by exposing uniformly all detector pairs to a 511keV photon source using a phantom filled with a known amount of activity (^{68}Ge). A normalisation map is then calculated dividing the average of counts of all detector pairs (line of response, LORs) by the individual detector pair count and is then applied to all detectors to correct for any variation between detectors and guarantee that measurements are truly accurate and quantitative.

After annihilation three different types of coincidences can be detected by PET, scattered, random and true coincidences (Figure 17). Only true events give an accurate information about the emission sources the others need to be corrected to obtain quantitative PET images.

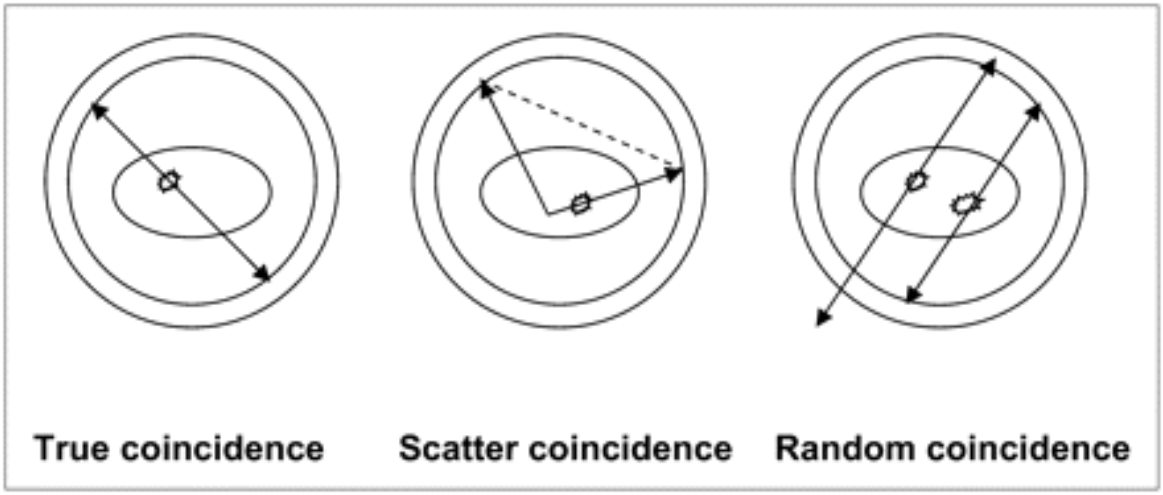

Figure 17: Different types of coincidences detected by PET scan [258]. Scattered coincidence are caused when two photons are directed to false locations on the detector and random coincidence can also be detected from two separate annihilations that hit detectors within the coincidence timing window of the detector.

Random events happen when two uncorrelated single events occurring sufficiently close together in time can be mistakenly identified as a true coincidence events arising from the same annihilation event. To reduce random events, LSO detectors with low scintillation decay are used.

Compton scattering happens when the annihilation γ-photons passes through the body and are deflected in a different directions than the other co-incident γ-photon; the radiations can be scattered in any direction [256]. The scattered events are the most complicated correction in PET analysis as the only way to truly discriminate true and scattered events is the quantity of energy. However, γ-photon that are scattered only once do not lose much energy and can be detected by a pair of detectors with the same coincidence time window as if they were true co-incident photons. To correct the scattered events, the simulation method is used [259]. The simulation is based on the reconstruction of the images without scatter correction and then using an attenuation map; the scatter is simulated by using different methods such as Monte Carlo that are algorithms used to study and solve any problem having a probabilistic interpretation [259].

Attenuation is defined as the loss of true events due to scatter and absorption. The method used to correct for attenuation is to use the CT scan of a PET/CT scanner to produce the attenuation map. The attenuation factor μ depends on the energy of the photons and the atomic number of the material [260]. The attenuation factor from the CT scan must be converted to an attenuation map correcting for the high energy of the 511 keV γ-photons

emitted in PET. The attenuation correction factor is then calculated for each pixel and applied to the PET data.

Dead time is another physical parameter that needs to be corrected for in PET acquisition. Dead time is the time required to record a signal and during which no other event can be recorded; it can be reduced by using detectors with shorter scintillation decay time and faster electronics components in PET scanners [254] but overall it is best to keep dead-time as minimal as possible and this can be easily achieved by keeping the injected dose within the range of activity for which the PET scanner does not suffer dead-time, i.e. for which the PET scanner can acquire events proportionally to the injected dose.

Partial volume effect is defined as a dilution of the signal with the surrounding structures, due to the relatively low image resolution (1.4 mm for Inveon small animal PET) and the limited size of ROI. There are different methods that can be used to correct for partial volume effect. One method based on anatomical imaging data is The LMA (Local Means Analysis) geometric transfer matrix (GTM) method is implemented in the BrainVisa software (version 4.1.1) [261, 262] used in this thesis. This method is a region based method characterized by an algorithm able to measure the temporal variation in the PET signal, and segments (ROI) are determined by presenting homogeneous Time Activity Curves (TACs). Therefore, the ROI/VOI are segmented based on the drug's pharmaco-distribution in the PET image. The algorithm calculates the average uptake in the inner of the structures and the percentage of pixel considered is a parameter of the method. 100% pixels is equal to the standard GTM method [262].

1.10.3 Use of PET in Alzheimer's disease

Different PET radiotracers have been used to characterise and study the progression of Alzheimer' disease. They can be used to detect Aβ and Tau aggregation, metabolic abnormalities and neuroinflammation. The first PET tracer developed to image Aβ aggregation is the carbon-11 labelled thioflavin T derivative 2-(4'-methylaminophenyl)-6-hydroxybenzothiazole, also called [^{11}C]Pittsburgh Compound-B (Figure 18). Due to the short half-life of ^{11}C other compounds with ^{18}F have been developed such as [^{18}F]Flutemetamol [263], [^{18}F]Florbetapir [264] and [^{18}F]Florbetaben [265]. Amyloid scans are used to discriminate AD patients from age-matched healthy individuals and other form of dementia [266].

Another PET tracer widely used for AD is [^{18}F]FDG. 2-[^{18}F]fluoro-deoxy-D-glucose ([^{18}F]FDG) is a glucose analogue and it is used to monitor the brain glucose metabolism. In AD, [^{18}F]FDG uptake is reduced (Figure 18) and this reduced uptake can be detected years before the clinical symptoms. The most affected brain regions with low [^{18}F]FDG uptake are the parieto-temporal, frontal and posterior cingulate cortices and the sensitivity of [^{18}F]FDG PET to distinguish the development of AD in the early stage is around the 90% [266].

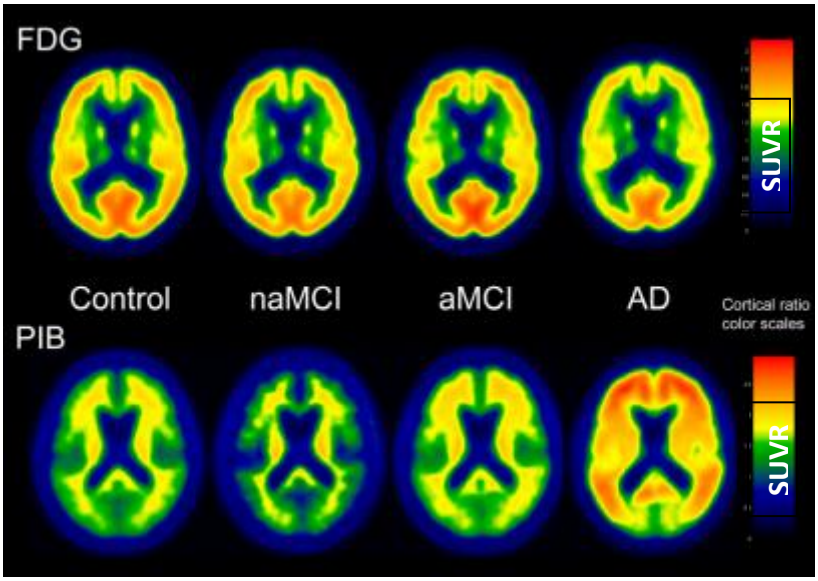

Figure 18: Brain uptake of [^{18}F]FDG and PIB. Evaluation of [^{18}F]FDG and PIB. in control, non-amnestic MCI, amnestic MCI and patients affected by AD. Regions with greater uptake are shown in yellow and red [267].

Different compounds can also be used in PET to detect the progressive accumulation of hyper-phosphorylate Tau protein. Tau in AD, coexist with amyloid and both proteins have a β-sheet structure; therefore, the radiotracers developed to study Tau accumulation need to be highly selective and with much higher affinity/selectivity for Tau than for Aβ. Several radiotracers have been developed such as: [^{11}C]PBB3, the arylquinolines THK family, [^{18}F]T807 and [^{18}F]T808 [268]. The tracer [^{11}C]PBB3 is able to bind NFT and therefore to discriminate AD patients from healthy controls but it is not able to discriminate AD from other tauopathies, suggesting an ability to recognize multiple isoforms of the tau protein [268]. A tracer highly selective for Tau fibrils is [^{18}F]THK523, but *in-vivo* studies have demonstrated a high retention in white matter so it is not used in research or clinical studies. [^{18}F]T807 seems to be the most promising tracer for Tau (Figure 19) with a strong affinity and selectivity for Tau but no data are available on the use of this radiotracer on non-AD-tauopaties [269].

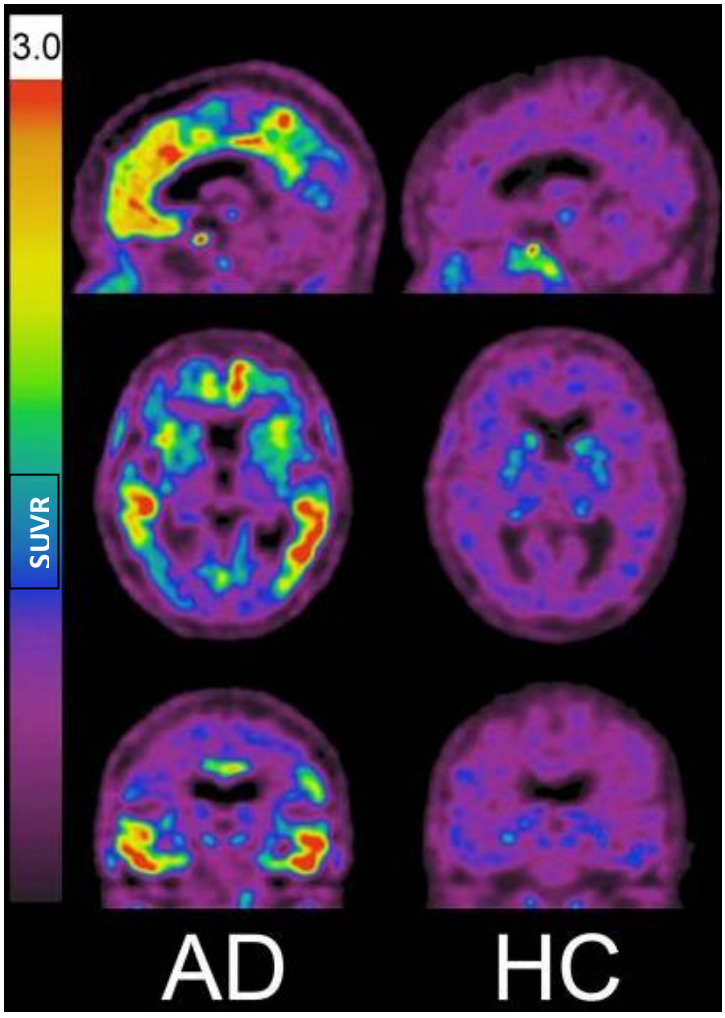

Figure 19: AD patients and healthy controls (HC) PET scan by using [^{18}F]Flortaucipir also known as [^{18}F]T807. The radiotracer [^{18}F]T807 shows a high specificity for paired helical filaments of Tau. Patients affected by AD have a high uptake mainly in neocortex regions [270].

The cholinergic system is one of the neurotransmitter systems strongly altered in AD (see §1.3.3). A variety of PET tracers have been developed to study the degeneration of cholinergic pathways in AD. [^{11}C]PMP and [^{11}C]MP4A are two PET tracers used to measure the activity of acetylcholinesterase (AChE), where their uptake was shown to be reduced in AD when compared with healthy controls [266]. The reduced uptake has been also found in MCI patients in cortical areas [271].

PET has also been used to study neuroinflammation in various brain conditions including AD. So far the most used biomarker targeted by molecular imaging for neuroinflammation is the 18kDa translocator protein (TSPO), which is over-expressed mainly by activated microglia [272]. However different studies have shown that the astrocyte are also able to express TSPO [273, 274] whereas under basal conditions the expression of TSPO

in CNS has been shown to be low. The first-generation radiotracer for TSPO was [^{11}C]PK11195. [^{11}C]PK11195 showed some limitations due to a high level of non-specific binding [275] and hence a low signal to noise ratio [276], relatively poor penetration of BBB and low brain uptake indeed the first study in AD showed no differences between mild to moderate dementia patients and healthy controls [277]. Later on, the use of the R enantiomer, [^{11}C]-(R)-PK11195, showed an increased uptake detected in entorhinal, temporoparietal, and cingulate cortex of mild and early AD patients vs. healthy control [278, 279]. More recently, other radiotracers have also been developed with the aim to improve the specificity for TSPO and signal-to-noise ratio, and are classed as second-generation TSPO PET tracers such as the [^{18}F]FEDAA1106, [^{11}C]AC5216, [^{11}C]DAA1106 and [^{18} F]FEDAA1106 with improved pharmacokinetics and specificity [280]. The main limitation for the use of these tracers for the TSPO is the genetic polymorphism in the gene, in which alanine is substituted by threonine. This polymorphism strongly affect the binding affinity of radiotracers to the TSPO [280-282]. The most used TSPO tracers in clinical studies are the [^{11}C]PBR28 and [^{18}F]DPA-714. An increased uptake of [^{11}C]PBR28 in parietal and temporal cortices and by using [^{18}F]DPA-714 in the frontal, temporal, and parietal cortex was determined in AD patients when are compared to healthy controls and this increased uptake by using [^{18}F]DPA-714, was also detected in the early stages of AD characterised by amnesic MCI associated with positive amyloid PET [283]. Hamelin *et al.* showed also higher level of neuroinflammation in MCI-AD than demented AD, confirming the idea of the involvement of neuroinflammation mainly during the early stages of pathology [284].

1.11 [^{11}C]Leucine and [^{18}F]UCBH: new tracers for Alzheimer's disease?

Neuroimaging techniques have played an important role in the dementia diagnosis promoting a novel approach for an early diagnosis and the possibility to discriminate between different types of dementia, detecting pathological and functional neuronal changes, even before the clinical symptoms. The development of new tracers to image key pathways or mechanisms are essential to provide a more comprehensive understanding of the molecular basis of neurodegeneration in AD and avoid costly, inadequately prescribed, and potentially harmful treatments and identifying therapeutic strategies for the treatment of AD. Preclinical animal models make valuable contributions to improve the understanding of human diseases and imaging studies represent a connection between the discovery at the molecular level and the clinical use for diagnosis and therapies. Preclinical PET gives a unique

opportunity to study a disease in real time, in a quantitative way, at the molecular level, and monitoring the progression or response to treatment, repeatedly and non-invasively. The greatest advantages of preclinical imaging techniques is the possibility to acquire many data during the disease progression without interfering with the biological process under study and reduce the number of animals required for a particular study. Despite the brain imaging has many difficulties due to the small size of brain structures different imaging studies have been validated and measured. Biomarkers provide insight into underlying mechanisms, disease progression, prognosis, regression, response to therapy, and accurate early diagnosis for early treatment. It is well established that no single biomarker can accurately diagnose a heterogeneous disorder such as AD. A combination of several biomarkers yields the highest diagnostic power to discriminate between AD and cognitively healthy controls with sensitivity and specificity values. For example, FDG-PET has a high sensitivity and specificity (>90 %) for discriminating AD from healthy elderly controls; but the percentage for discrimination between AD and other types of dementia (including MCI) decreases to 78%. Furthermore, biomarkers actually used for diagnosis of AD are based on detecting neuronal degeneration, therefore when the brain damage is already present. Synapses loss and alteration of protein synthesis are processes that precede cellular degeneration in most cases, therefore [^{18}F]UCB-H and [^{11}C]leucine could be used potentially to determine initial phases of AD before degeneration (brain damage) is apparent but also used in combination with others for the prognosis and evaluation of therapeutic effects. The aim of this work was not only for the validation of these tracers for diagnosis of AD but also to study the prognosis and the possibility to measure therapeutic approach in restoring alterations in these parameters in AD.

1.11.1 Amino acids PET tracer : [^{11}C]leucine

As described in previous chapters (see §1.5 & 1.7), protein synthesis is altered in AD. Amino acid PET (AA-PET) is a good methodology for diagnosis and prognosis information about the alteration in protein synthesis (PS) in many fields such as oncology, neurology and psychiatry. The incorporation of L-amino acids into proteins reflects the protein synthesis activity of a tissue [285], although the use of labelled amino acids will reflect the protein synthesis coming from exogenous amino acids only. After being transported in cells, the labelled amino acid is converted into amino-acyl-tRNA by the enzyme amino-acyl RNA

synthetase and then used in the incorporation for protein synthesis [285]. To be suitable as a tracer for protein synthesis rate PSR, an amino acid needs to meet several criteria [285, 286]:

- High blood brain barrier penetrance of the labelled amino acid
- High incorporation of the labelled amino acid in proteins
- No parallel (i.e. other than incorporation in protein) or complex catabolic pathways of the labelled amino acid
- Rapid clearance of the labelled amino acid from the plasma
- Rapid turnover of the tissue precursor pool
- The amino acid needs to be supplied only from plasma, so that the incorporation of radio-labelled (i.e. exogenous) AA can be measured by PET while the endogenous incorporation rate from the breakdown of proteins will account only for a very small fraction of the amino acids pool
- Radio-labelling sufficiently easy to be compatible with short half-life of PET radio-isotopes such as [^{11}C]

Amino acids are classified as essential and non-essential AA. This classification relates to the ability of the cells to produce them. Cells are only able to use the L-isomers of the amino acids. There are nine essential amino acids and each amino acid has a different uptake in brain as described by Oldendorf *et al.* [287]. The amino acids with high uptake are: L-phenylalanine, L-leucine, L-tyrosine and L-methionine [287]. To study alterations in PSR, different essential amino acids or analogues have been used. The main problems in the use of amino acid as tracer for PS are associated with the production, complex multistep syntheses and/or low radiochemical yields, complex purification methods and the need to isolate the L-enantiomer [285]. Amino acids have a formula [R-CH-(NH2)-COOH], where -COOH is the carboxylic acid group, -NH_2 the amino group, an alpha-carbon atom -CH- and a branched-chain group (-R) (Figure 20). [^{11}C] and [^{18}F] can be used to label amino acids at each of the 4 groups and they can be natural or unnatural (non proteinogenic amino acid) [288]. 1-^{11}C have the labelling at the carboxylic acid group and these amino acids tracers such as L-[1-^{11}C]-leucine (^{11}CLeu), L-[1-^{11}C]tyrosine (^{11}CTyr), L-[1-^{11}C]phenylalanine (^{11}CPhe) and L-[1-^{11}C]methionine (^{11}CMet) are used to study PSR because they are incorporated into proteins. 1-^{11}C non-natural AA such as carboxyl-^{11}C-1-α-aminoisobutyric acid (^{11}C-AIB), carboxyl-^{11}C-1-aminocyclopentanecarboxylic acid (^{11}C-ACPC), and carboxyl-^{11}C-1-

aminocyclopentane carboxylic acid (^{11}C-ACBC) cannot be incorporated into proteins, but these tracers can be still used to measure AA transport in tumour. Similarly alpha carbon labelled AA such as α-[^{11}C-methyl]-L-tryptophan (^{11}C-AMT) and α-[^{11}C-methyl]-aminoisobutyric acid ($^{11}CH_3$-AIB) are rarely used and are not suitable for PS but only for tumours AA uptake; the same applies to amino acids labelled at the R group or when they have the substitution of the amino group [288].

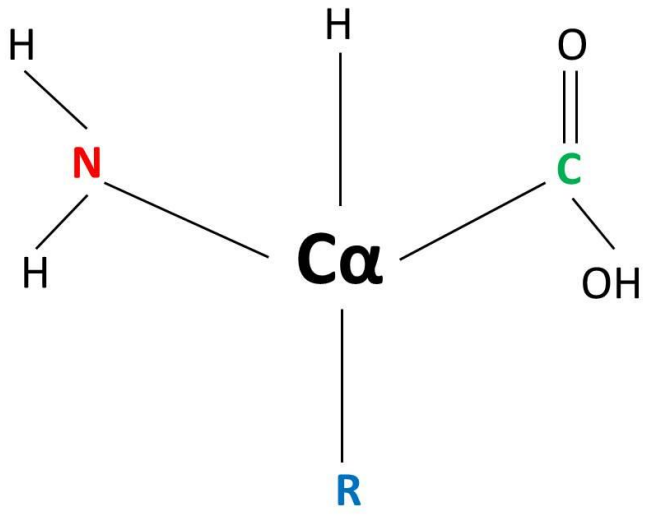

Figure 20: Amino acid structure. COOH is the carboxylic acid group (1-C, green), -NH2 the amino group (red), an alpha-carbon atom -C- and a branched-chain group (R, blue).

In general, amino acids labelled in the carboxyl position are preferred to study PS because the labelling at the carboxyl group does not induce change in the AA structure. Another advance in the use of AA labelled into the carboxylic group for PS is the low production of labelled metabolites; indeed, the main non-protein metabolite is the labelled carbon dioxide, derived from decarboxylation process. The carbon dioxide is then removed by the diffusion and blood flow from the tissues and removed from the plasma by ventilation in lungs [285].

[^{11}C]leucine is a good tracer for the evaluation of PSR by PET imaging, because leucine has a good uptake at the blood brain barrier, the amount of metabolites produced during its catabolism is negligible and it is incorporated well in proteins [289]. Leucine is an essential amino acid and as other large neutral amino acids it is transported across the blood brain barrier by using the L-system, large neutral amino acid transporter (LAT) [290]. LAT is

sodium-independent, binding with high affinity for zwitterionic (with an equal number of positively- and negatively-charged functional groups) amino acids with “large neutral” side chains, including L-leucine, L-phenylalanine, L-tryptophan, L-tyrosine, L-isoleucine, L-methionine, L-valine and L-histidine [291]. The transport of these amino acid from plasma to brain by LAT transporters follows the Michaelis-Menten kinetics where:

$$\boldsymbol{influx = Vmax[C]/(Km + [C])}$$ **(Equation 2)**

therefore any increase in concentration of one amino acid in plasma will reduce the influx of the others that remain constant in plasma [292]. In cells, carboxyl-labelled leucine is either incorporated in proteins but also metabolised by a transamination reaction causing the transfer of the α-amino group to a keto acceptor α-ketoglutarate (α-KIC) which ultimately will lead to the decarboxylation reaction producing CO_2 and CO_2 products of fixation [293]. The α-KIC labelled in brain is very low [294] and the amount of $^{11}CO_2$ in brain is also low, i.e. less than 10% of radioactivity at 10 minutes after injection [293]. These values are also very low in blood and the labelled CO_2 was estimated to reach the peak at 25-30 minutes to 13% [289] of the total blood activity; it also considered an equilibrium between brain:blood, therefore the radioactivity coming from these metabolites are not accounted for PET quantification. The absolute model of leucine incorporation in tissue, protein and catabolism, has been described by complex *ex-vivo* experiments using [^{14}C]leucine using the model below [293] (Figure 21).

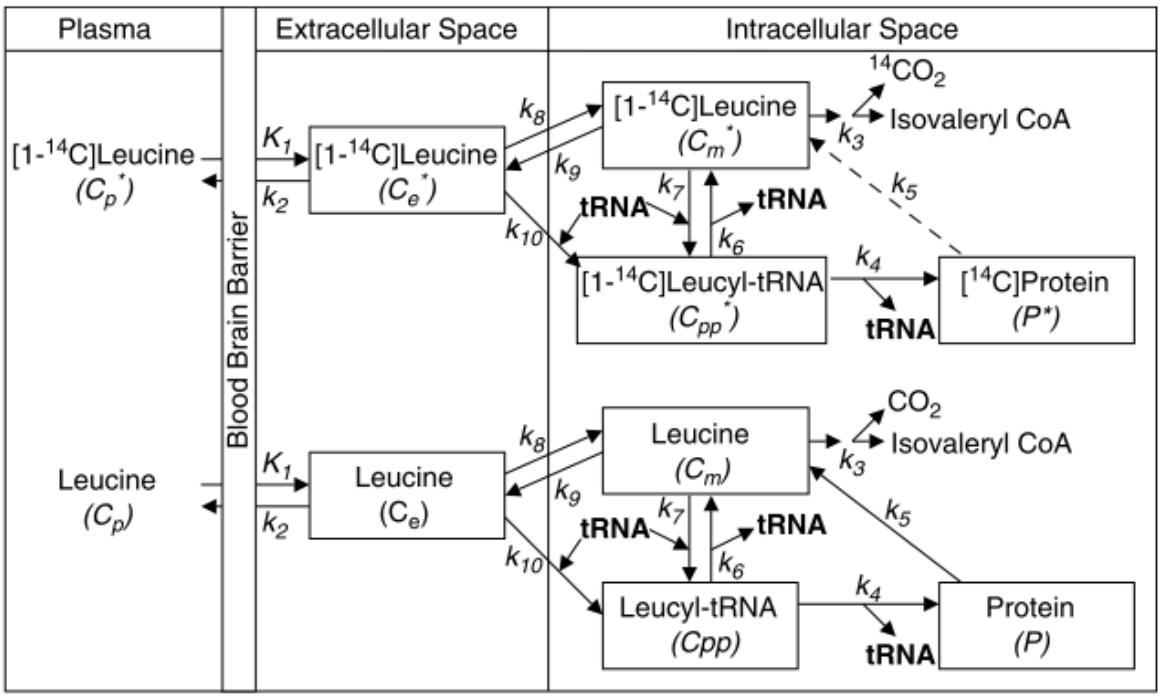

Figure 21: Full model of leucine in brain. Cp is the concentration of leucine from plasma to tissue; Ce the concentration in the extracellular space, and Cm intracellular. Cp, Ce, and Cm * are the concentration of labelled leucine. The contribution of leucine RNAt are shown as Cpp and Cpp* respectively when is leucine unlabelled and labelled by ^{14}C. K are the rate constants: K_1 from plasma to tissue; K_2 from tissue to plasma; K_3 for leucine catabolism; K_4 for leucine incorporated into proteins; K_5 free leucine coming from the degradation of proteins; K_6 and K_7 for the production of RNA_t and vice versa; K_8 and K_9 are respectively for the transport of leucine from the extracellular space to the intracellular space and vice versa [293].

The kinetic modelling of [^{11}C]leucine is fundamental during the analysis to define the amount of tracer, its distribution in tissues and to truly obtain quantitative data expressed as Protein Synthesis Rate (PSR) from the PET data. Compartmental models are used to describe physiological processes as dynamic systems in tissues. In PET imaging, the knowledge of the diffusion of the tracer across the BBB, its transport and uptake is important to evaluate where and how much tracer is in brain, how it is delivered, if it is able to diffuse in the parenchyma or if it is actively transported. Different compartmental models have been proposed to describe the pharmacokinetic and bio distribution of tracers. The number of compartments is due to the biological features of the tracers which implies different models for different types of tracers to describe their biological and/or pharmacological properties. The two-compartment model is the simplest model, in which one compartment represents the amount of free tracer in plasma measured by the plasma and blood time-activity curve and the second compartment represents the amount of tracer in tissue. The three

compartments model (commonly called confusingly 2 ***tissue*** compartments model) is used for [^{18}F]FDG in which the tracer is transported in the extra/intracellular space and then trapped and accumulates in cells. Three- or four-compartments models are more complex and used when the injected tracer is metabolised and the metabolites are detected by PET and the compartmental need to take in account also the kinetic of metabolites [295]. Due to the characteristics of leucine and its metabolism, the simplified compartmental model to study PSR is a 2-tissue-compartmental model (Figure 22), in which the intra- and extra-cellular spaces are pooled, the contribution of $^{11}CO_2$ is considered negligible and it is assumed that the activity of [^{11}C]leucine-RNAt is very low [296]. The compartmental model take also in count the contribution of endogenous recycling by proteolysis that is estimate to be 40% of leucine in the precursor pool [296]. To account for the contribution of endogenous leucine recycling, Schmidt *et al.* have introduced a new parameter named λ [293]. λ is defined as the fraction of leucine in the precursor pool derived from plasma and therefore the leucine coming from proteolysis in brain will be 1-λ [297].

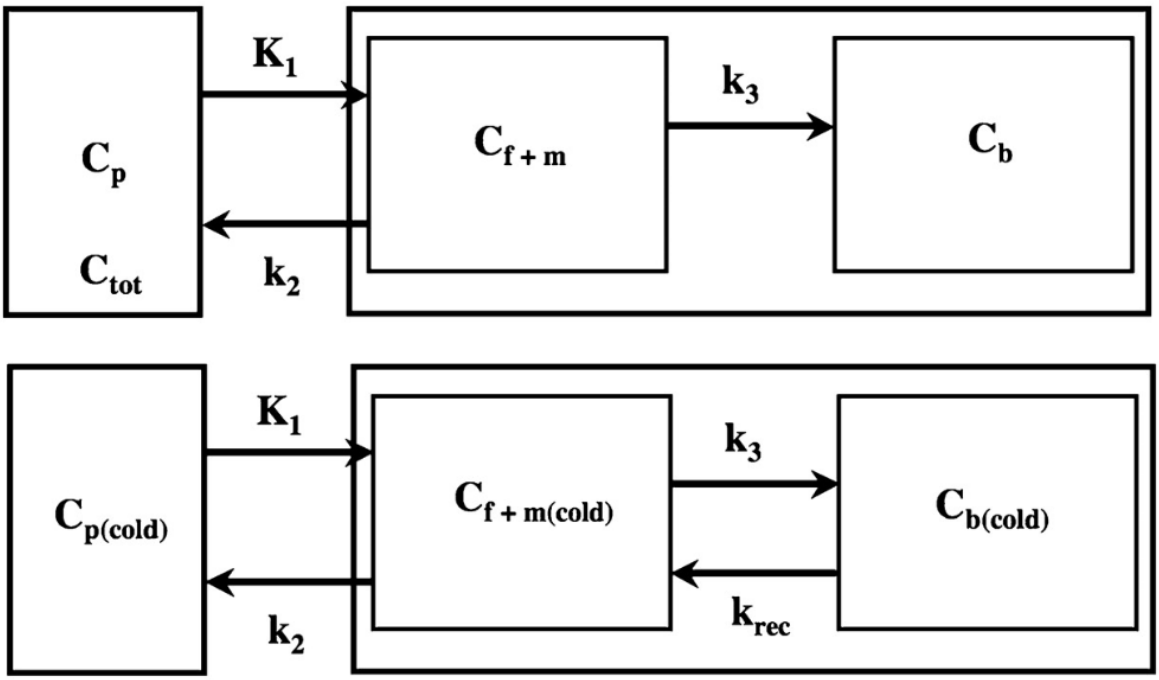

Figure 22: simplified compartmental model to measure the PSR by using [^{11}C]leucine. K_1 is the rate constant for leucine uptake in brain, K_2 the loss of the leucine from the brain and K_3 is the rate constant representing the effective leucine incorporation in proteins. Cp is the concentration of leucine in blood, Cf+m is the concentration of free and metabolised leucine in brain and Cb the concentration of leucine in proteins [297].

λ is defined as:

$$\lim_{t\to\infty}\left[\frac{\frac{Cf}{Cf(cold)}}{\frac{Cp}{Cp(cold)}}\right] \quad \textbf{(Equation 3)}$$

C*f* is the concentration of leucine in free precursor pool in tissue, and C*p* is the concentrations of leucine in plasma (cold=unlabelled leucine). Unlabelled leucine is in steady state in tissue and:

$$\boldsymbol{dCf(cold)/dt = dCp(cold)/dt = 0} \quad \textbf{(Equation 4)}$$

and because C*f* for labelled leucine is equal to:

$$\boldsymbol{K1 \times Cp/(k2 + k3)} \quad \textbf{(Equation 5)}$$

and $Cf_{(cold)}$ is equal to:

$$\boldsymbol{Cf(cold) = \frac{K1}{K2}\, Cp\,(cold)} \quad \textbf{(Equation 6)}$$

λ will be [297]:

$$\boldsymbol{\lambda = \frac{K_2}{K_2+K_3}} \quad \textbf{(Equation 7)}$$

For labelled leucine, it is assumed that no recycling from radioactive proteins occurs and therefore K_{rec}=0 during the experimental time of 60 minutes. PSR can be estimated by the mathematical formula:

$$\boldsymbol{PSR = K_{cplx} \times \frac{leucine\ [C]}{\lambda}} \quad \textbf{(Equation 8)}$$

In which PSR is in μM/min and K_{cplx} in min^{-1} and Leucine[C] is the concentration of unlabelled leucine in arterial plasma n.mole/ml [297]. The factor K_{cplx} is defined as unidirectional uptake rate of plasma leucine into tissue and it is calculated:

$$\boldsymbol{K_{cplx} = \frac{K_1K_3}{(K_1+K_3)}} \quad \textbf{(Equation 9)}$$

1.11.2 PET tracer for synaptic vesicles

SV2A is ubiquitously expressed in presynaptic neurons and therefore is a good biomarker to study synaptic density; consequently, specific radioligands that can bind to SV2A have been developed. One of the first radiotracers used to study SV2A was levetiracetam labelled with [^{11}C] but the binding affinity was very low and therefore [^{11}C]levetiracetam was deemed not suitable for the study of synaptic density [298]. Other ligands with higher affinity for SV2A have been developed: [^{11}C]UCB-A, [^{18}F]UCB-H, [^{11}C]UCB-J, [^{11}C]UCB-J from UCB Pharma and others produced by Invicro such as [^{18}F]MNI-1038 (racemate), [^{18}F]MNI-1126 (*(R)*-enantiomer) and [^{18}F]MNI-1128 (*(S)*-enantiomer) and others from Yale ([^{18}F]SDM-2 and [^{18}F]SDM-8) (Figure 23) [299].

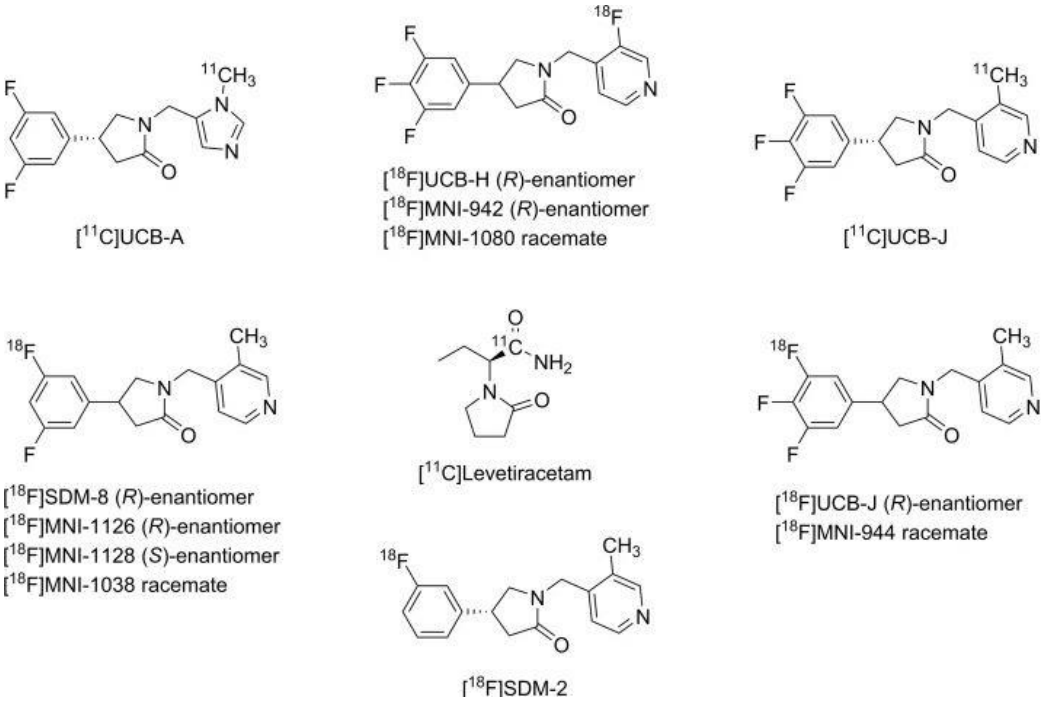

Figure 23: Tracers developed to study the synaptic density [299].

The radiotracer [^{11}C]UCB-J was he first PET tracer developed with a nanomolar affinity for SV2A, and its homolog [^{18}F]UCB-H has also been used in PET studies. Despite the higher affinity of [^{11}C]UCB-J, the short half-life of ^{11}C limits the use of this tracer for clinical studies. Studies using [^{18}F]UCB-H in animal models and humans have established the suitability of this tracer to measure *in-vivo* SV2A [300]. *In-vivo* propriety of [^{18}F]UCB-H have been validate by Becker *et al.* [300] in which it has been shown that [^{18}F]UCB-H has a rapid uptake in brain, with a peak at 5 minutes after injection and characterised then by fast wash-out. The affinity for SV2A depends on the chirality of [^{18}F]UCB-H; indeed the *(R)*-enantiomer has a higher affinity than the *(S)*-enantiomer. The metabolism of [^{18}F]UCB-H is characterised

by the production of three metabolites N-oxide hydroxylated metabolites, and N-dealkylation of the pyrrolidinone ring. The major metabolite is the N-oxide that represents the 90.2% of formed metabolites and it is unable to cross the BBB; the amount of metabolites in brain and plasma were always low and therefore considered negligible for PET analysis [300]. In this study, the use of a population-based input function was also validated for the quantification of PET images due to the very low variability between population based IF and the activity measured in blood samples and low variability of the volume distribution with both methods [300]. A human study with [^{18}F]UCB-H showed a strong reduction in the number of synapses in hippocampus, thalamus and cortex in patients with AD [301], in agreement with other studies by using [^{11}C]UCB-J [302] confirming the suitability of this tracer to measure SV2A *in-vivo*.

2 Aims of project

Alteration in memory is the main feature of Alzheimer's disease and consolidation of memory requires the synthesis of new proteins and the growth of new synaptic connections. Based on this observations, [^{11}C]leucine and [^{18}F]UCB-H are important imaging tools that could provide important information to define changes in PSR and synaptic density, help to better understand the disease during the early stage of AD by PET and potentially measure therapeutic efficiency in restoring alterations in these parameters in AD.

The aims of the leucine project were to:

- Validate the use of [^{11}C]leucine as a tracer to measure the protein synthesis rate (PSR) and determine the best approach to study *in-vivo* PSR by using [^{11}C]leucine for a clinical study.
- Test whether protein synthesis was altered in TgF344-AD and WT rats based on the hypothesis that AD-like pathology is inducing a progressive decline in protein synthesis due to the age and a more prominent decline in TgF344-AD due to the development of AD.

For the validation of [^{11}C]leucine as a tracer to measure PSR, we used anisomycin, an antibiotic able to inhibit the formation of 80S system and the protein synthesis of about 85%, in Wistar rats. We also planned to measure an Arterial Input Function (AIF) in Wistar rats and to determine the concentration of unlabelled leucine in plasma. This was done in order to develop a method to determine and validate an image-derived input function to be applied to the Fischer-344 strain (WT and TG) at different ages in a longitudinal study in which arterial blood measurements were not possible.

The aims of the synaptic density investigation were to:

- Develop a method allowing for quantification of the [^{18}F]UCB-H binding in absence of a reference region and without blood sampling by measuring non-specific binding using scans in blocking condition (pre-saturation with and excess of cold UCB-J).
- Study in WT and TG rats at 2 different age to study the effect of both ageing and AD-like pathology on synaptic density.

To correlate any potential changes in PSR or synaptic density, a behavioural study was also planned to assess memory impairment at 6, 12 and 18 months of age. To achieve this, we used the following behavioural tests:

- Morris Water Maze (MWM) and reversal MWM (RMWM) for spatial memory
- Open field to determine stress conditions
- Smell tests to evaluate the olfactory memory

For a full analysis, measurements of the expression of different proteins were planned to be tested by using *ex-vivo* techniques:

- eIF2α and its phosphorylation for the attenuation of protein synthesis
- ATF4 for its involvement in memory
- SV2A for the study of synapses

3 Materials and methods

3.1 Animals

Male Wistar rats (Charles River, Margate, Kent, UK) and male Fischer-344 strain WT and TG were used in this study. All procedures were carried out in accordance with the Animals (Scientific Procedures) Act 1986 and the project was approved by the UK Home Office. Animals were kept under a 12-hour light-dark cycle with free access to food and water at each age. Studies utilising two different radiotracers were performed, one with [^{11}C]leucine (Figure 24) and the other with [^{18}F]UCB-H (Figure 25). The power calculations were based on previous PET results with other tracers and *ex-vivo* results of PSR in other models; in which the difference between genotypes was of 10% and the variability approximatively 5-6%.

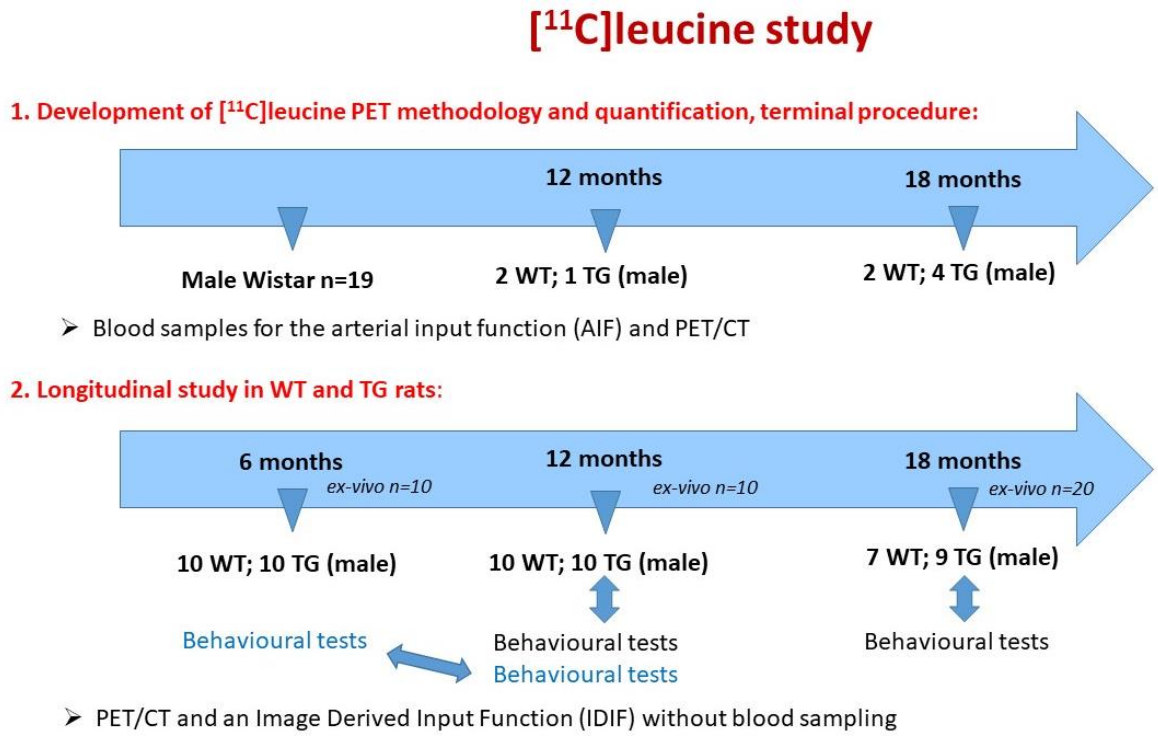

Figure 24: [^{11}C]leucine study plan. The study was performed with the aim to develop a methodology for PET quantification and implement the data acquired for the longitudinal study. To determine the first step, Wistar rats and some WT and TG at 12 and 18 months of age had a PET/CT scan but also a terminal procedure to determine the arterial input function (top). For the longitudinal study, the same rats were used at 6, 12 and 18 months of age and had a PET/CT scan and the determination of the Image Derived Input Function (IDIF) without blood sampling. The same rats used for PET, were tested behaviourally at 12 and 18 months of age. A second group of rats was added for behavioural tests at 6 months and also at 12 months. *Ex-vivo* analysis on other WT and TG were performed at each time point.

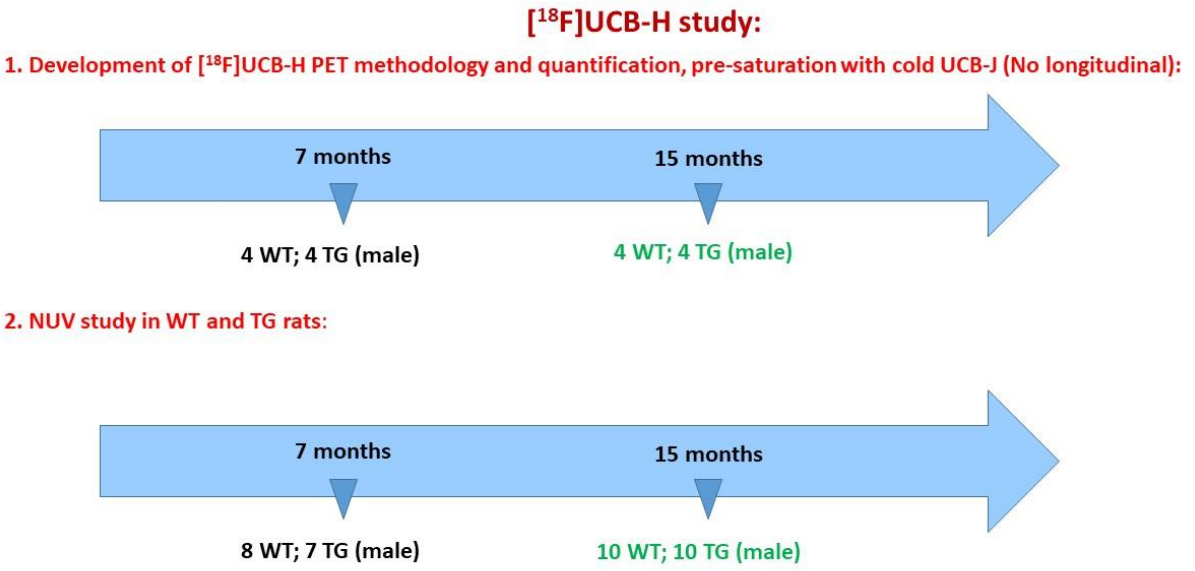

Figure 25: [^{18}F]UCB-H study plan. To quantify PET images for [^{18}F]UCB-H some WT and TG rats at 7 and 15 months of age were injected with cold UCB-J (blocking scans) to determine the non-specific binding (top). The blocking scans (one per group) were used to quantify PET images in WT and TG rats at 7 and 15 months through the calculation of the Normalised Uptake value (NUV).

For the [^{11}C]leucine study Wistar rats were scanned with a weight of 434.10g ± 59.77gr; WT and TgF344-AD were used for a longitudinal study, therefore the same animal was scanned at different ages. At 6-7 months with a weight 432.25g ± 26.88g, at 12 months with a weight 481.17g ± 23.39g and at 18-19 months of age with a weight of 479.62g ± 32.43g. The injected dose of [^{11}C]leucine was 37.42MBq ± 7.14MBq and the specific activity was 47.2MBq/nmole ± 27.26 MBq/nmole. At each time point rats were tested for behavioural analysis.

For the [^{18}F]UCB-H analysis, we didn't perform a longitudinal study, therefore two different groups at 7 and 15 months of age were used. WT and TgF344-AD at 7-8 months of age with a weight 438.38g ± 30.36g and 15-16 months of age with a weight 479.24g ± 22.44g were scanned for [^{18}F]UCB-H study and the injected dose applied was 28.70MBq ± 4.58MBq and the specific activity was 87.97MBq/nmole ± 33.16 MBq/nmole. All data are expressed as mean±SD.

3.2 Scanning protocol

All animals were anaesthetised by isoflurane inhalation (induction 5% and thereafter 2-2.5%) in O_2/NO_2 (30%/70%). For all scans, 300µl of tracer in saline followed by a 300µl

saline flush were injected using Cole-Parmer Syringe® Touchscreen Control pumps at a rate of 1.2ml/min in a single bolus over 30sec to ensure steady delivery of the tracer.

For [^{11}C]leucine study, three Wistar rats were also injected 10 minutes before starting the [^{11}C]leucine PET acquisition with 60mg/kg of anisomycin in saline (pH adjusted at 7 by addition of few drops of 37% HCl).

For [^{18}F]UCB-H study, some WT and TG rats at 7 and 15 months of age were also injected with 1mg/Kg cold UCB-J in saline, 10 minutes before starting PET acquisition.

Rats were scanned on a Siemens Inveon® small animal PET-CT [303, 304]. The following data acquisition protocol was used: a CT scan was performed immediately prior to the PET scan for each animal to acquire attenuation correction factors. The time coincidence window was set to 3.432 ns and levels of energy discrimination to 350 keV and 650 keV. List mode data from emission scans were histogrammed into 25 (14 × 5 sec; 3 × 15 sec; 3 × 1 min; 2 × 5 mins; 3 × 15 mins) and 36 (16 ×15 sec; 4 × 30 sec; 4 × 1 min; 4 × 2.5 mins; 8 × 5 mins) dynamic frames for analysis of the heart and brain time activity curves, respectively. Emission sinograms were normalised, corrected for attenuation, scatter along with radioactivity decay and reconstructed using OP-OSEM3D-MAP (16 subsets, 2 iterations of OP-OSEM3D followed by 18 iterations of MAP) into images of 128 × 128 × 159 voxels with 0.776 × 0.776 × 0.796 mm voxel size. Respiration and temperature were monitored throughout the scans using a pressure sensitive pad and rectal probe (BioVet, m2m Imaging Corp., USA). Body temperature was maintained using a heating and fan module controlled by the rectal probe via interfacing with of the BioVet system.

3.3 [^{11}C]Leucine study and measurement of the Arterial Input Function (AIF)

In 7 Wistar and 9 WT/TG rats (1 WT and 2 TG at 12 months, and 2 WT and 4 TG at 18 months), the femoral vein and artery were cannulated with a 26G catheter (Terumo® Surflo®-W) and connected to a fine-bore polyethylene tubing (inner diameter: 0.58mm, outer diameter: 0.96mm) going through a Twilite Swisstrace™ blood sampler (Swisstrace GmbH, Switzerland) [305] in an arterio-venous shunt of 80cm length in total. This sampler contains a dual LYSO detector system (detector head), with tubing carrying arterial blood running between the two crystals. Blood flow was maintained by a peristaltic pump (350 µl.min^{-1}). Discrete blood samples of approximately 350µl were collected from the shunt between the peristaltic pump and the venous catheter at 2, 5, 10, 20, 30, 40, and 60 minutes during the scan. A photo of the setup is shown (Figure 26). These samples were collected in

heparinised Eppendorf tubes and placed immediately on ice. A 50 or 100µl aliquot of whole blood was counted using a γ-counter (1470 Wizard Automatic Gamma Counter from Perkin Elmer (UK)) and the remaining was centrifuged at 8050×g for 3 minutes at 4°C to obtain plasma. A 50 or 100µl aliquot of plasma was subsequently counted using the γ-counter. An aliquot of the remaining plasma from each sample was mixed with 5% percholoric acid (PCA) or 70% of PCA to precipitate proteins and centrifuged at 8050 ×g for 5 minutes at 4°C. The supernatant was counted on the γ-counter to measure the amount of free [^{11}C]leucine in plasma. Free and bound [^{11}C]leucine (incorporated in proteins) were determined in the PCA supernatant and total plasma respectively, the amount of [^{11}C]leucine incorporated in proteins was calculated from the difference between plasma (total [^{11}C]leucine) and supernatant (free [^{11}C]leucine). A last aliquot of plasma was then stored at -80°C for measurement of the total leucine concentration by the company Alta Bioscience. The Alta Bioscience (https://altabioscience.com/) through the use of post column detection, quantified the concentration of individual amino acids in plasma expressed in n.mole/ml. The injected leucine was measured to be 0.5µg ± 0.2 µg, calculated from the injected dose and the specific activity, and the total leucine in plasma was measured to be 770.9µg ± 171.15 µg, calculated by from the measurements done by Alta Bioscience and the rat blood volume of 60ml/Kg [306]. A foot switch was used to record the timings of the discrete blood samples.

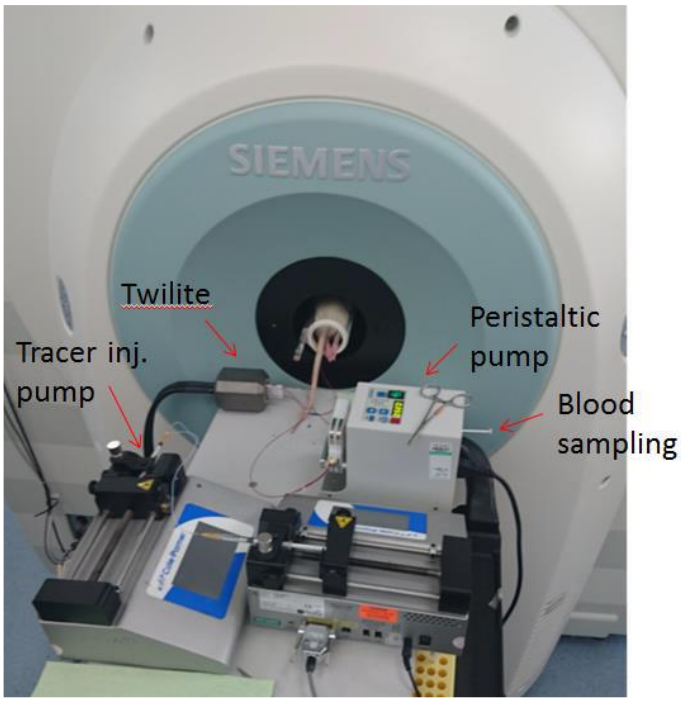

Figure 26: Experimental setup to determine the Input Function (IF). During the PET/CT scan the Twilite detector was used to determine the radioactivity in whole blood. Two pumps for the injection of radiotracer and saline flush; a peristaltic pump to move the blood from the artery to the vein and a syringe for the discrete blood sampling. In the background is the Siemens Inveon PET/CT scanner.

At the end of the PET scan, rats were rapidly decapitated and the brain removed for dissection into different regions: whole cortex, hippocampus, striatum, cerebellum and rest of the brain. All brain regions were counted in a γ-counter.

WT and TG rats used for the longitudinal study were scanned without arterial input function and an aliquot of plasma (100µl) coming from the tail vein was taken before each PET acquisition to correct the image derived input function.

3.4 [^{18}F]UCB-H Study

Under isoflurane anaesthesia WT and TG rats at 7 months (WT, n= 8; TG, n=7;) and 15 months (WT, n=10; TG, n=10) of age were injected i.v. with [^{18}F]UCB-H at the beginning of PET scan. Some WT (n= 4 at 7m and 15m) and TG (n=4 at 7m and 15m) rats were injected 10 minutes before PET acquisition with cold UCB-J (1mg/kg) [307] for the evaluation of non-specific binding (blocking scan). The blocking scans were used to determine the normalised uptake values (NUV) of the ratio of SUV without blocking to SUV with blocking scan between 9 and 20 minutes after injection of [^{18}F]UCB-H.

3.5 Image analysis

For the image-derived input function in the [^{11}C]leucine study, images were segmented automatically using local means analysis (LMA) in the BrainVisa/Anatomist framework (http://brainvisa.info,[261, 262, 308]). Automatic segmentation was preferred to manually drawn regions of interest (ROIs), which can introduce a user-dependent bias. In short, the LMA algorithm first extracts the whole body of the rodent from the background, before identifying voxels in the core of organs based on the notion that their variation in PET signal should be lower than those voxels at the organ borders, which are more subject to variations driven by physiological movement and spill-over from neighbouring organs/vessels. Neighbouring voxels are then identified based on the similarity of their kinetics to these organ 'cores'. Ultimately, the implementation in BrainVisa segments the whole-body image into a maximum of 200 regions based on the similarity of kinetics of the voxels contained within them. Within the heart, the segmented ROI of the heart left ventricle was manually defined as well as a manually defined ROI over the vena-cava.

[^{11}C]leucine and [^{18}F]UCB-H uptake in the brain were quantified using BrainVisa and Anatomist software (http://brainvisa.info/web/index.html) and a rat brain atlas [309]. An MRI rat brain template one for Fischer-344 rats and one for Wistar rats, were used to create 28 brain ROIs large enough to be accurately quantified based on the spatial resolution of the PET scanner (Figure 27). Data are expressed as standardised uptake values (SUVs).

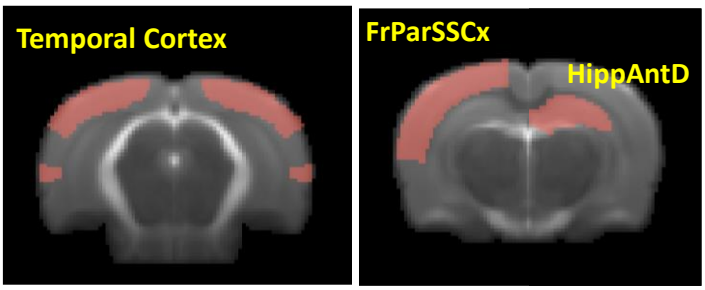

Figure 27: MR template with example of ROIs used for quantification

3.6 Modelling of [^{11}C]leucine uptake to determine PSR using MICK software

Kinetic modelling is used for the quantitative analysis of dynamic PET data. MICK (Modelling, Input functions and Compartmental Kinetics) is an in-house software based on Matlab used for PET Kinetic analysis.

The tracer kinetics in tissue can be described by compartmental models, that are separate regions in which the tracer can be transferred. Each compartment is defined by the

rate constant K_i, that represent the transfer of the tracer from a compartment to another. Starting from the assumption about the knowledge of the number of compartment and K_i, a software as MICK is used to try to find a set of coefficients K_i such that the prediction about the tracer kinetics optimally matches the measurements, changing the K_i values until the best match is found. In order to run the MICK software the brain Time Activity Curves (TAC) and the Arterial Input Function (AIF), defined as total radioactivity in arterial plasma across the time, need to be loaded (Figure 28).

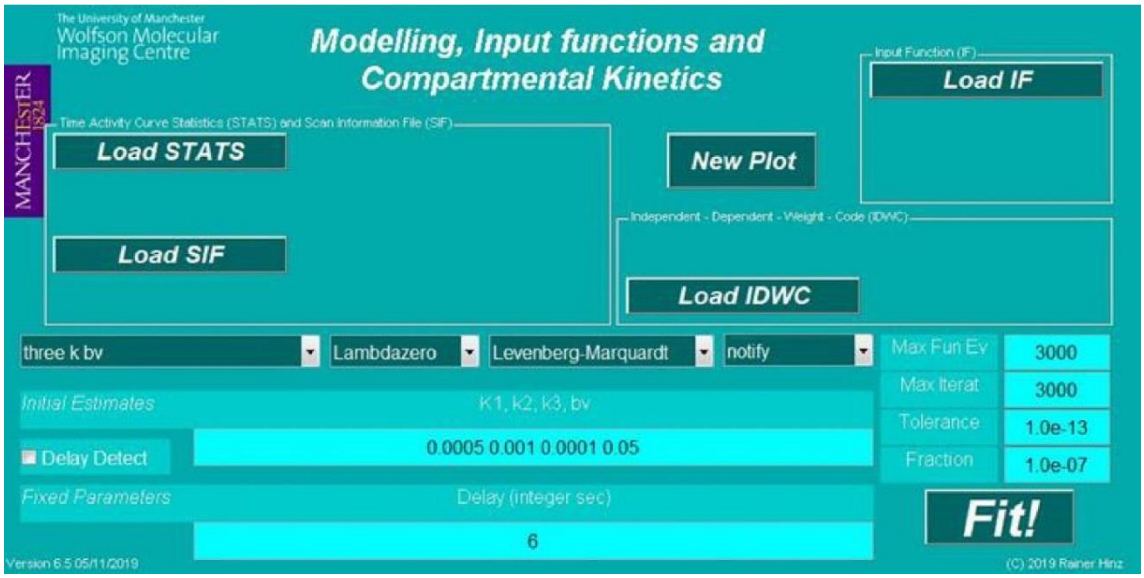

Figure 28: Screenshot of the MICK software, used to determine the rate constants.

The compartmental model used to describe leucine metabolism in brain is characterised by three rate constant; in which K_1 and k_2 are the rate constant for the transfer of leucine from blood to the brain and vice versa and K_3 represents the rate constant for leucine incorporation in proteins (Figure 29). In the estimation of PSR it is essential to estimate other parameter as K_{cplx}, defined as the net uptake rate constant for [^{11}C]leucine; λ, defined as the fraction of [^{11}C]leucine in the precursor pool for protein synthesis derived from plasma and C that represents the concentration of unlabelled leucine in plasma (Figure 29).

One of the aims of this study was to identify and validate an Image Derived Input Function (IDIF) to be used as IF for the longitudinal study, in which rats had no blood measurements. There are three steps to validate an IDIF:

1. identify a blood pool large enough on the PET image by using a co-registered anatomical images (CT) or segmented PET image

2. determine the whole blood time-activity curve from this blood ROI
3. correct the radioactivity values detected by PET using *ex-vivo* measurements of parent radioligand [310].

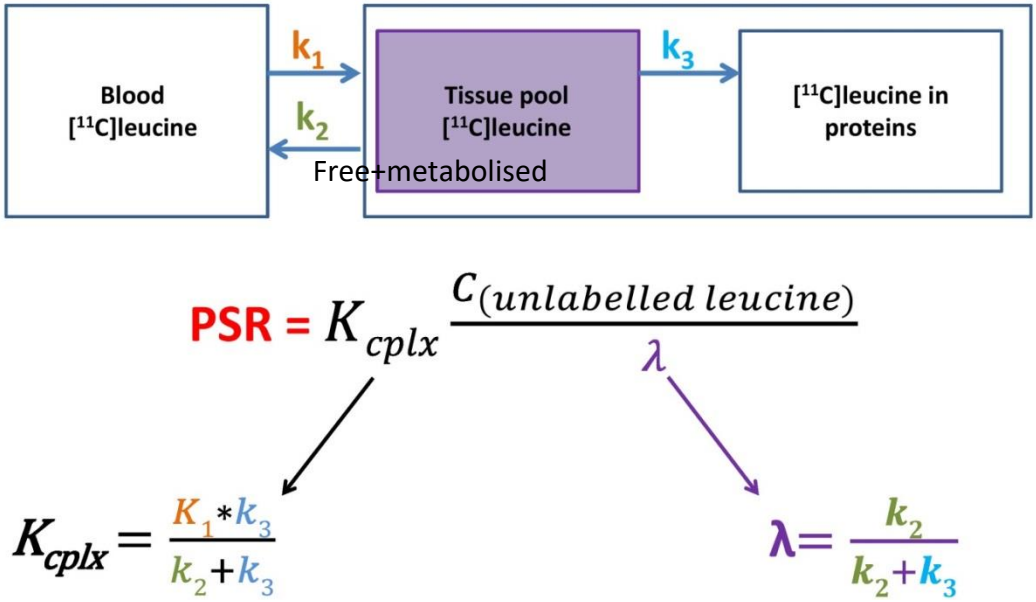

Figure 29: Simplified compartmental model of leucine metabolism in brain [297]. It is a two-tissue compartmental model. The rate constants K_1 and K_2 represent the transfer of leucine across the blood-brain barrier from blood to the brain and vice versa. K_3 is defined for the incorporation of leucine in proteins. The mathematical formula for the estimation of PSR = Protein Synthesis Rate is calculated from: K*cplx* is the net uptake rate constant; C is the concentration of unlabelled leucine in plasma and λ is the fraction of [^{11}C]leucine in the precursor pool derived from plasma.

3.7 Behaviour tests

All rats had a habituation period for a minimum of 20 minutes before starting each test. Two batches of rats were used one were tested at 6-7 months and then at 12-13 months and the other group at 12-13 months of age and then again at 18 months of age. Each test was run in a space where the light was blocked using black curtains and was always performed after 5pm until 9pm.

3.7.1 Morris water maze and reversal Morris water Maze

Morris water maze (MWM) is a test used to evaluate spatial learning. Rats were placed in a swimming pool and using distal clues, they had to navigate from the starting point and try to find a submerged escape platform. Spatial learning was acquired through the repeated trials and the spatial memory acquisition was determined on the last day when the platform was removed from the water. During the reversal phase, the platform was

moved to another quadrant and the rats trained again. The reversal phase was used to determine how the rat reacts to the change and how quickly the rat was able to memorise the new platform position.

To perform the MWM, a large black circular swimming pool with 175 cm diameter was used. The pool was filled with water at around 25˚C, changed every day after the test and few drops of water-soluble black paint were added to hide the platform. The top surface of the platform was 15×15 cm and it was under 1-2 cm of water. 2D distal clues, two per wall during the MWM and one per wall during the reversal MWM, were placed around the pool to help the rat during the navigation and to learn the platform position (Figure 30). A heat mat was used to warm the rat after the test. A video camera placed above the pool was used to record the animal performance and all videos were analysed using the ANYMAZE software.

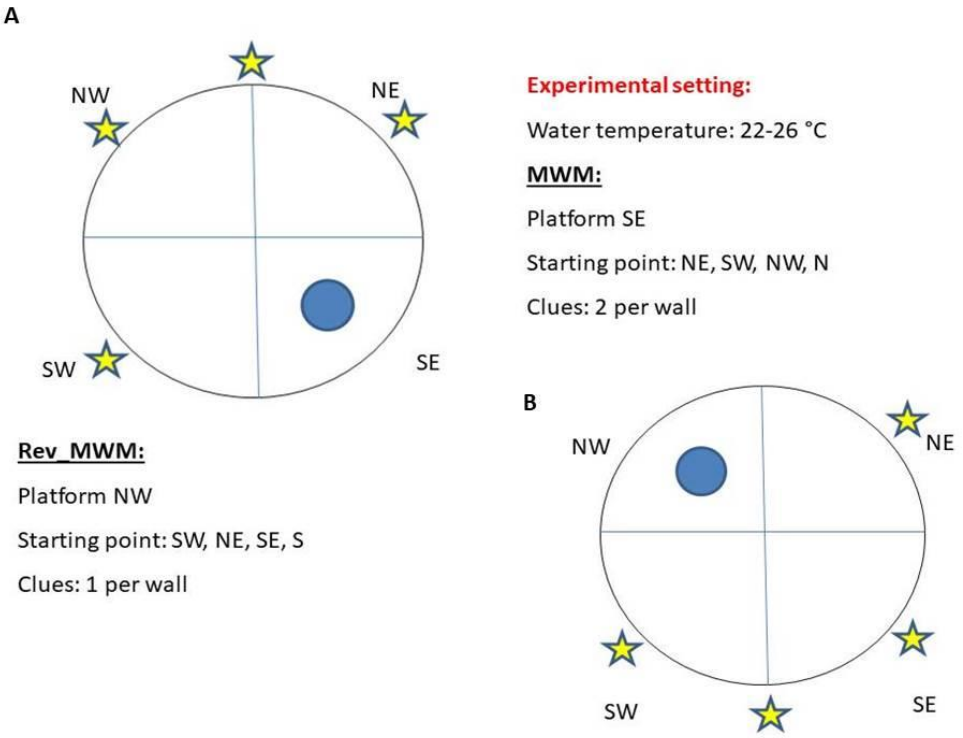

Figure 30: (A) Experimental setup of Morris water maze (MWM) and (B) reversal MWM. Stars indicate the starting point from which the rat was released into the pool. The blue circle is the platform position during the test.

The full test (MWM and reversal MWM) had a duration of 9 days. Before starting the test, each rat had one day of habituation. During the habituation each rat was placed on the platform for 15 seconds 4 times to teach the rat that an escape platform was present in the

pool. Then to habituate the rat to the test, the rat was released in the pool 4 times from different starting points and the platform was highlighted by a small bottle placed on it.

The acquisition was performed for 4 days during the MWM and 3 days for the reversal MWM. Each rat had 4 trials per day and the platform was always placed in the same quadrant, South East (SE) during the MWM and North West (NW) during the reversal MWM (Figure 30). The rat was released in the pool from North-East (NE), South-East (SE), North-West (NW) and North (N) during the MWM and South-West (SW), NW, SE and South (S) during reversal MWM. The maximum swimming time allowed was 60 seconds. The camera was switched off after 60 seconds or when the rat reached the platform. If the rat was not able to reach the platform after 60 seconds, it was helped and left on it for 15 seconds.

During the probe test, the platform was removed from the pool and the swimming time allowed was 60 seconds. The starting point was N during the MWM probe test and S during the reversal MWM.

The software ANYMAZE was used to analyse the video files. The software was set to recognise the rat and discriminate the animal from the background. Different parameters were determined during the acquisition and the probe days. Time to reach the platform, time spent in each quadrant, time to getting close the platform, speed, path efficiency and the distance travelled. All data were then analysed by using GraphPad Prism 8.4.1. and 2-way ANOVA and/or Mixed effect analysis and Sidak multiple comparison post-hoc test.

3.7.2 Open Field

The open field test was used to evaluate the rat behaviours, anxiety and stress condition. The open field consisted of a square wall-enclosed (52cm × 52cm) area high enough to avoid the rat escape (Figure 31). At the end of each test, the chamber was cleaned with 70% ethanol or fragrance-free cleaner. A video camera placed on top of the chamber was used to record the rat behaviour. Each test had a duration of 10 minutes and the ANYMAZE software was used to analyse the video files. The software was set to discriminate the rat and parameters evaluated were the time spent in moving and not moving and also the time spent close to the wall or in the centre of arena. All data acquired were analysed by using GraphPad Prism 8.4.1 and Mixed effect analysis and Sidak post-hoc test.

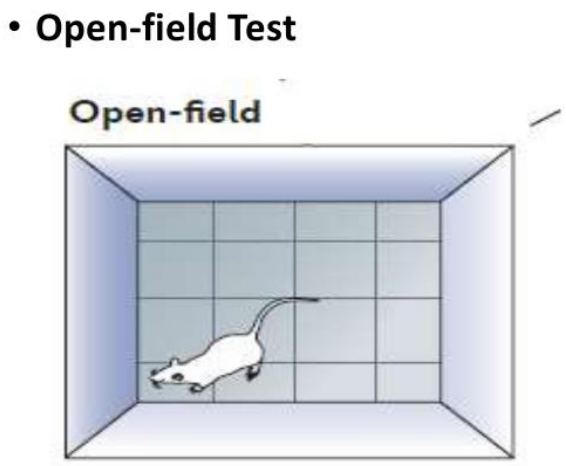

Figure 31: Images of the arena used to perform open field and smell tests. The box was black 52×52 cm.

3.7.3 Smell tests

Two different smell tests were performed on these rats. For both tests, cotton wool was used and the amount of fragrance was defined based on the rat ability to sense/detect the smell. The first test was based on the memory retention of an odour after one-time exposure. Three different fragrances were used: strawberry, vanilla and green tea oils and they were placed in the middle of the square arena, same environment used for the open field test. Each fragrance was presented twice by using different delay time 30 minutes, 1 hour and 4 hours. A single time interval was tested on each day to avoid cross interference of olfactory detection and memory. At the end of each test the box was cleaned using 70% ethanol or fragrance-free cleaner. Rat performance was recorded for 10 minutes using a video camera placed on top.

For the second smell test, a two arms maze with either predator (fox) or non-predator (rabbit) urine at the end of each arm were used to assess general olfactory ability in 12- and 18-months old rats. Each rat had 1 day of habituation at the new maze and at the end of each test the maze was cleaned using 70% ethanol or fragrances free cleaner. A video camera placed on the maze has been used to record rats for 10 minutes.

For both smell tests, the video files acquired were analysed with ANYMAZE software. The software was set to discriminate the rat and manually, the time spent by each rat in smelling was determined. GraphPad Prism 8.4.1 with Two-way ANOVA with Sidak post hoc-test and Paired t-test were used to analyse the data.

3.8 Immunohistochemistry (IHC)

Immunohistochemistry was done on WT and TG rat brains at different ages 6, 12 and 18 months, with antibodies for Aβ (6E10) and GFAP (astrocyte marker) to test the presence of amyloid deposition and the increase in astrogliosis, respectively. Animals were culled by isoflurane overdose and the death was confirmed by cervical dislocation. The brains were rapidly collected, snap frozen using isopentane on dry ice and stored at -80°C. Fifteen sets of 4 sagittal brain sections (20µm thick) were taken on SuperFrost Plus glass slides using a cryostat (Leica CM3050s, Leica Biosystems Nussloch GmbH, Germany) from 1, 1.62, 2.24 and 2.86mm lateral of Bregma and stored at -80°C. Brain sections were fixed in 4% paraformaldehyde for 10 minutes at room temperature; then washed 6 × 5 minutes in PBS. To avoid the non-specific binding, sections were incubated in 2% normal donkey serum for 30 minutes. Primary antibodies: 6E10 BioLegend (803001, 1:1000) and GFAP (Dako Z0334, 1:1000) were incubated overnight at 4°C with serum. Before starting the incubation for 2 hours with secondary antibodies at room temperature, sections were washed 3 × 10 minutes in PBS. A few drops of Prolong anti-fade kit (Molecular Probes, Invitrogen) with DAPI, to stain the nucleus, were used as mounting medium. Other factors involved in the attenuation of protein synthesis and in memory consolidation were evaluated by immunohistochemistry using the following antibodies: eIF2α (Santa Cruz, 133132), phospho-eIF2α (abcam, 32157) and ATF4 (Proteintech, 10835-1-AP). All primary antibodies were tested at different concentration 1:500 and 1:1000. Standard protocol, antigen retrieval, sodium borohydride and DAB (3,3'-Diaminobenzidine) staining were tested. The antigen retrieval and the sodium borohydride have few more steps compared to the standard protocol. In the antigen retrieval slides were incubated for 20 minutes at 95˚C in citrate buffer at pH=6 before the blocking step while during the sodium borohydride protocol, slides were incubated 3 times for 10 minutes in sodium borohydride after the citrate buffer. For immunofluorescence, the secondary antibodies used were Alexa Fluor 594nm Donkey anti-mouse IgG (1:500) for eIF2α and 6E10 and Alexa Fluor 488nm Donkey anti-rabbit IgG (1:500) for GFAP, phospho-eIF2α and ATF4. (see §10.4.1)

3.8.1 DAB staining protocol

3,3'-Diaminobenzidine (DAB) is a derivate of benzene, an organic compound that is used in the staining of nucleic acids and proteins, and when oxidised it forms water insoluble

brown precipitates. Slides were dehydrated by washes in Xylene and then several washes in ethanol at different concentration: ethanol 100%, ethanol 90% and 70%. Distillate water was then used for 5 minutes before the incubation in citrate buffer PH=6, at 95˚C for 25 minutes. Slides were subsequently washed 3 times over 5 minutes in dH_2O and before being incubated in 0.3% Peroxide in Methanol at room temp for 30 minutes. After washes in dH_2O and PBS, slides were incubated overnight in Blocking Buffer at 4˚C (from Vector Laboratories kit). The primary antibody was added for 1 hour at room temperature and the biotinylated secondary antibody (from Vector kit) was added for 30 minutes. The prepared ABC solution (from Vector Kit) was added for another 30 minutes with the final step being the introduction of the DAB solution. Haematoxylin was used few second before starting the hydration process by using again ethanol from 70% to 100% and Xylene. Glue was used to mount a glass on slides. (see §10.4.1).

3.8.2 Western blot analysis

3.8.2.1 Homogenisation

Brain hemispheres were dissected into 5 different brain regions: hippocampus, cortex, cerebellum, striatum and rest of the brain. Dissected regions were stored in -80˚C and used for Western Blot (WB) analysis. The same antibodies used for IHC were tested for Western Blot: eIF2α (Santa Cruz, 133132), phospho-eIF2α (abcam, 32157) and ATF4 (Proteintech, 10835-1-AP) but also 2 more antibodies: PSD95 (abcam 2723) and SNAP25 (abcam 5666). Dissected brains were homogenised by using a homogenisation solution and a pestel. Samples were centrifuged for 15 minutes at 3,200rpm (+4°C) and the pellet discarded. The supernatant (S1) was centrifuged for a further 20 minutes at 12,200rpm (+4°C) and the subsequent supernatant (S2) stored at -20˚ and used for Western Blot analysis. (see §10.4.3).

3.8.2.2 Protein concentration

The Bradford protein assay was used to determine the protein concentration in individual samples for these studies. This assay is based on the absorbance shift of the dye reagent. Hydrophobic and ionic interactions stabilize the anionic form of the dye, causing a visible colour change. A protein concentration of Bovine Serum Albumins (BSA) is used 2 mg/ml (Sigma-Aldrich) at different concentrations ranging from 0 to 1 mg/ml is used to generate a standard curve. The protein concentration from this standard curve and

individual assay samples were determined by using a plate reader spectrophotometer (BioTek µQuant microplate spectrophotometer) at 595 nM. (see §10.4.4).

3.8.2.3 Western Blot

The automated Western (Protein Simple, Wes) was used to perform the Western Blot (WB) analysis. The main characteristic of the automated Wes is the absence of gels, transfer devices, film, etc. The advances in using the automated Wes is the possibility to process in 1 plate 25 samples and different antibodies at the same time. Quantitative data are available after few hours and the immunoassay happens in a capillary in which samples are separated by size. The immobilized proteins are detected by a primary antibody and an HRP-conjugated secondary antibody and a chemiluminescent substrate will be than used to generate a chemiluminescent signal, detected and quantified. β-actin (Aldrich A5441) was used as a housekeeping gene to normalise the signal. After defining the samples concentration, 1 part of 5× fluorescent master mix was combined with 4 part of lysate. Samples were then heat-denaturated and then vortexed. Finally, samples were loaded on the plate (Figure 32). (see §10.4.5)

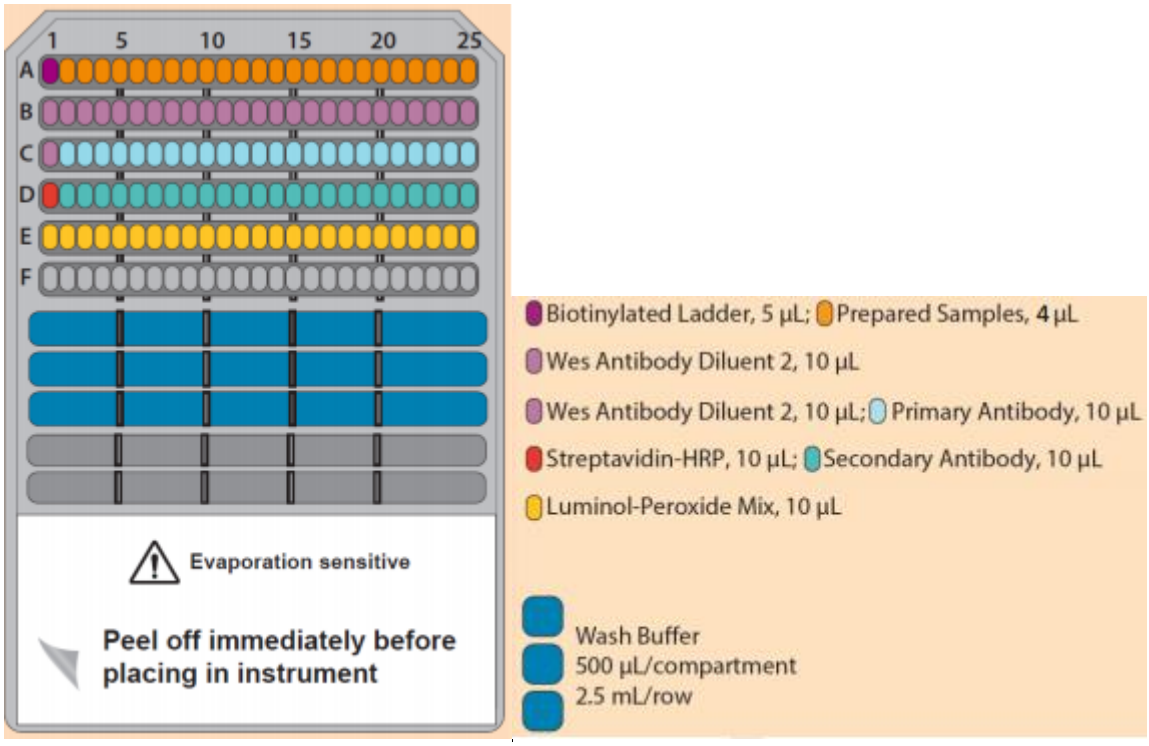

Figure 32: Plate used for WES analysis and µl of each reagent.

3.9 Statistical analysis of PET data

All data were analysed by using GraphPad Prism 8.4.1 and expressed as mean ± SD. The analysis of unlabelled leucine in arterial vs. venous blood samples in WT and TG rats was conducted by using Two-way ANOVA and Sidak post-hoc test. The evaluation of unlabelled leucine in arterial plasma between WT and TG was done by using Unpaired t-test. The comparison of unlabelled leucine and LNAA in arterial plasma between Wistar, WT and TG was done by using One-way ANOVA. The analysis of [^{11}C]leucine free in plasma between 70% and 5% PCA was done by using Two-way ANOVA and Sidak post-hoc test. PSR analysis in rats with all individual blood measurements were done by using Choen's d effect size. PSR, K_{cplx} and the SUV uptake for the longitudinal study were analysed by using Mixed effect analysis and Sidak post-hoc test and only at 18 months of age the Unpaired t-test was used for the PSR and K_{cplx}. Unpaired t-test was also used to study the K_{cplx} and PSR differences in Wistar rats with and without anisomycin injection.

Behavioural data were analysed by using Two-way ANOVA and Mixed effect with Sidak post-hoc test for MWM and Reversal MWM. Mixed effect with Sidak post-hoc test was used for Open field. Both smell tests were analysed by using Two-way ANOVA with Sidak post-hoc test and Paired t-test,

For the [^{18}F]UCB-H was used Two-way ANOVA with Sidak post-hoc test for the SUV and NUV analysis.

4 Results of the PET studies

4.1 [^{11}C]leucine

The analysis of protein synthesis was first reached by using a semi-quantitative method based on the evaluation of the standard uptake value (SUV) between WT and TG rats at different ages. This method does not take into account the biochemical processes involved in [^{11}C]leucine metabolism in brain and it is expressed as a tissue radioactivity concentration at a specific time (20-60 minutes after injection) (Ct) and the administered dose (ID) multiplied by body weight (BW).

$$\boldsymbol{SUV = \frac{Ct}{ID} * BW} \quad \textbf{(Equation 10)}$$

The Figure 33 shows the SUV PET images in WT and TG rats at 6, 12 and 18 months highlighting a gradual increase of SUV with age. The SUV values showed an age effects and genotype × age interaction in two of the brain regions tested: hippocampus and temporal cortex (Figure 34), with a p value in the hippocampus of p=0.0013 and p=0.0321 and in temporal cortex p=0.0014 and p=0.0169. The SUV increased in both genotypes, more specifically at 18 months in WT rats and earlier, at 12 months of age, in TG rats. The higher SUV values in WT rats were statistically significant between 6 months and 18 months (p=0.0123) in hippocampus. In TG rats the SUV increase was statistically significant between 6 and 18 months (p=0.0060) in the hippocampus. In temporal cortex TG, a statistical difference was measured between 6 and 12 months (p=0.0391) and 6 months and 18 months (0.0031). The comparison between WT and TG showed a statistical difference only in temporal cortex at 12 months of age (p=0.0239).

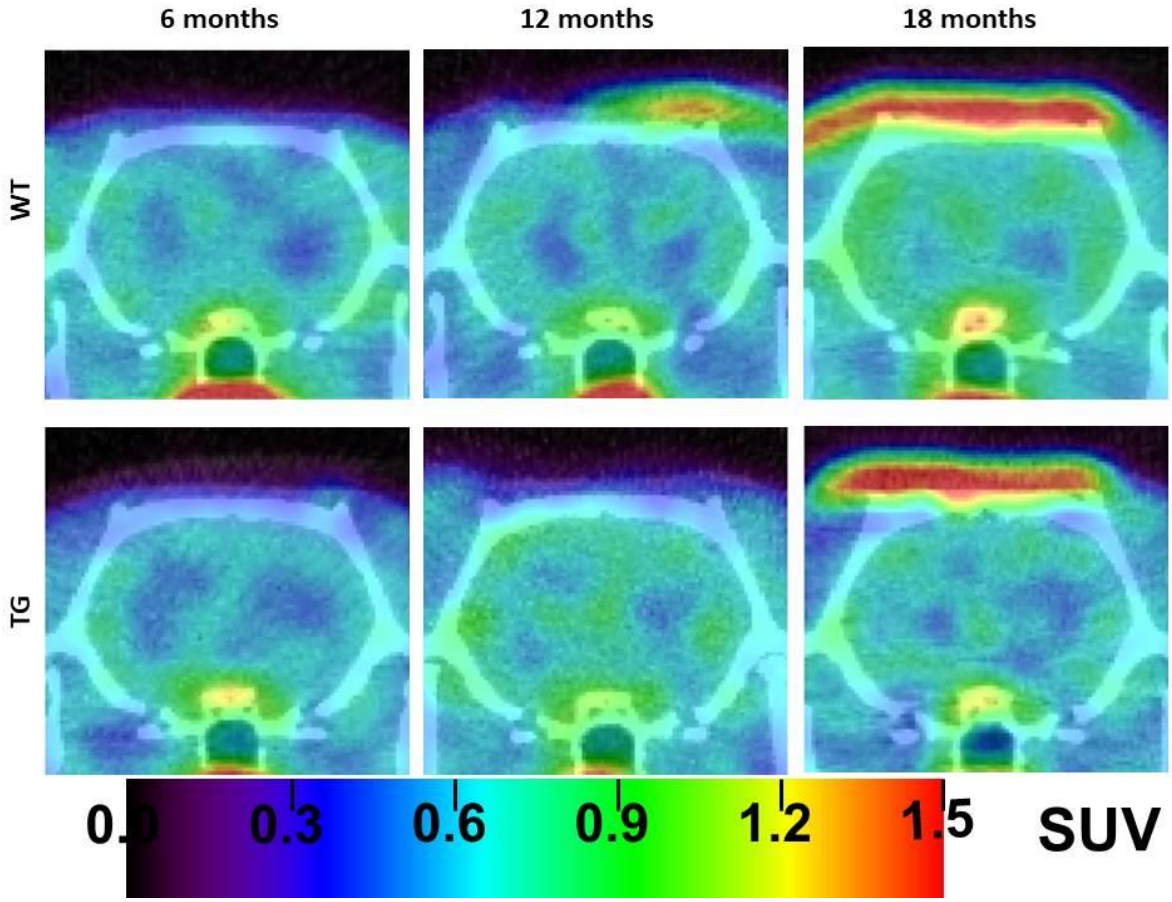

Figure 33: Representative sum 20-60min PET images of [^{11}C]leucine uptake (shown as SUV) in the brain of a WT (top) and TG (bottom) rats at 6, 12 and 18 months of age.

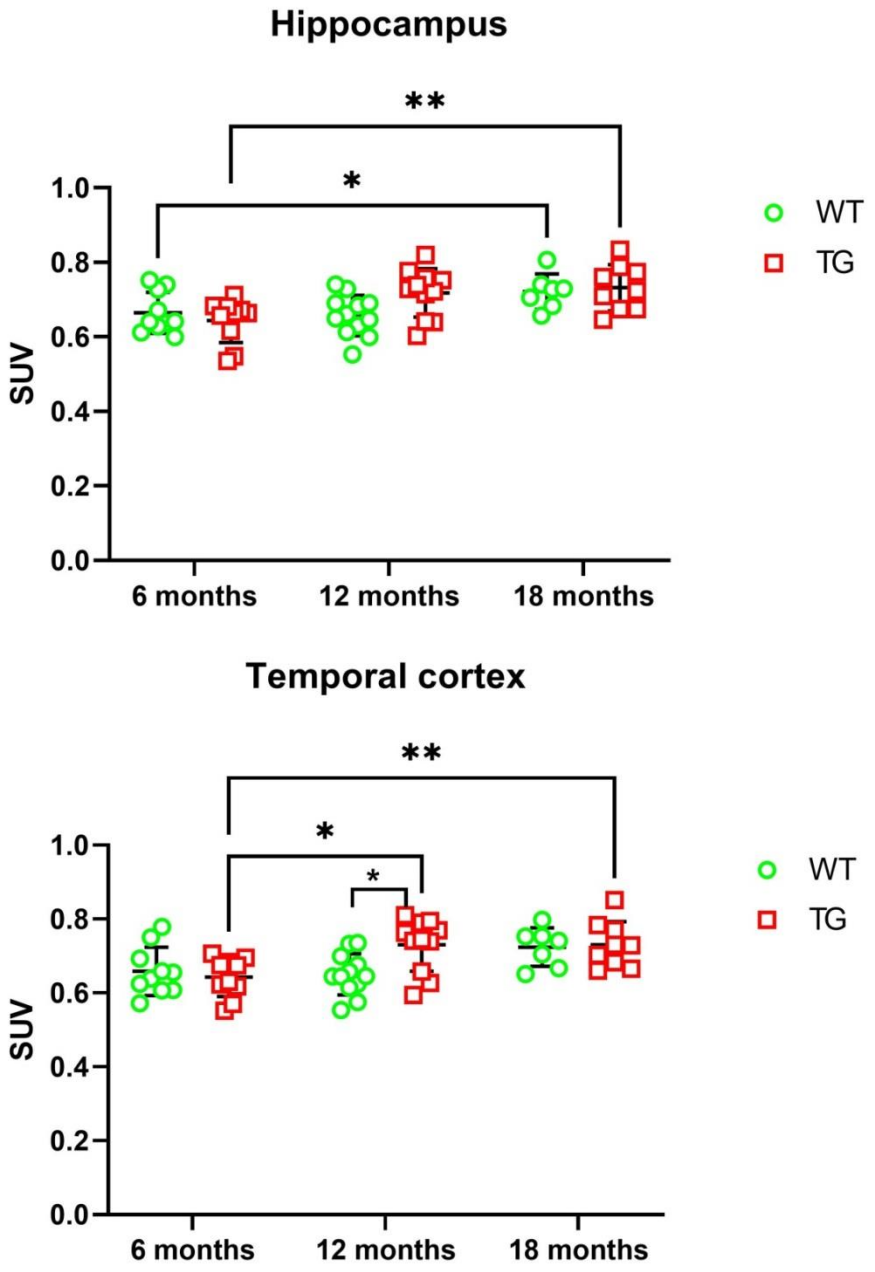

Figure 34: SUV graphs of [^{11}C]leucine brain uptake in hippocampus (top) and temporal cortex (bottom) at 6, 12 and 18 months of age. The statistical analysis showed an age effect and genotype × age interaction in both brain regions; hippocampus: p=0.0013 and p=0.0321 and in temporal cortex: p=0.0014 and p=0.0169. An age increase of SUV values was evaluated in both genotypes, with p values in WT hippocampus of 0.0123 between 6 and 18 months. The TG rats were statistically different between 6 and 18 months of age (p=0.0060) in hippocampus. In Temporal cortex WT rats showed no statistical difference whereas TG were evaluated statistically different between 6 months and 12 months (p=0.0391) and 6 months and 18 months (p=0.0031). A genotype difference was revealed at 12 months of age in hippocampus (p=0.0239). All data were analysed by using Mixed model effect and Sidak post-hoc test. Data were expressed as mean±SD. *p≤0.05; **p≤0.01.

To better understand and characterised the kinetic of the radiotracer in the tissues, the compartmental model approach was applied for the quantification of PET images. The compartmental model describes the physiological processes in which the tracer is involved. The compartmental model is characterised by mathematical functions that describe the system, exchanges between compartments and it allows a full understanding of the physiological system [311]. The compartmental model requires the dynamic PET images and the tracer and cold amino acids concentration in arterial plasma for the estimation of the model parameters such as the rate constants describing the kinetic of the tracer in blood, plasma and tissue. The measurement of PSR is determined by the formula:

$$\boldsymbol{PSR = K_{cplx} \times \frac{leucine\ [C]}{\lambda}} \quad \textbf{(Equation 11)}$$

Were K_{cplx} is the net [^{11}C]leucine uptake in brain, λ is the fraction of [^{11}C]leucine in the precursor pool derived from arterial plasma and [C] is the concentration of unlabelled leucine in arterial plasma

4.1.1 [^{11}C]leucine as a tool to measure the protein synthesis rate in brain

The table below (Table 4) summarises the rats utilised in this study. One of the aims of this study was to determine a population-based arterial input function (AIF) by using a full blood analysis from Wistar rats. The AIF requires the use of a terminal procedure; therefore, the AIF measurement was not possible to apply for the longitudinal study in Fischer-344 strain. As explained later in section 4.1.2, because we could not extrapolate a population-based IF from the Wistar rats representative of the Fisher 344 strain, we later added two WT rats and 1 TgF344-AD rat at 12 months of age and 2 WT rats and 4 TgF344-AD rats at 18 months of age that had complete blood measurements and were used to determine the AIF for Fischer-344 strain.

Table 4: Summary of rats used for the [^{11}C]leucine. Most of Wistar rats were used to determine the AIF, 5 of 19 Wistar rats had only blood evaluation without PET/CT scan, to better characterise the concentration of free leucine in plasma. 4 Wistar rats were used without blood sampling and therefore they had only PET/CT scan. 3 Wistar rats with full analysis were used to study the protein synthesis after injection of an inhibitor. The other Wistar rats (n=7) had a complete analysis with PET/CT and blood measurements. Two WT and 1 TG at 12 months of age and 2 WT and 4 TG at 18 months of age were used for the AIF. The other Fischer-344 rats, 10 WT and 10 TG at 6 months and 12 months and 6 WT and 9 TG at 18 months were used for the longitudinal study with only a PET/CT acquisition and without blood measurements.

	With blood samples	**Without blood sampling**
Wistar	**15**	**4**
WT 7m	**N/A**	**10**
TG 7m	**0**	**10**
WT 12m	**2**	**10**
TG 12m	**1**	**10**
WT 18m	**2**	**7**
TG 18m	**4**	**9**

4.1.2 Measurement of unlabelled leucine in plasma

As described in the section 1.11.1, an essential factor in the calculation of PSR is the measurement of unlabelled leucine in plasma. To know the concentration of unlabelled leucine in plasma, 200µl of arterial and venous plasma from each animal were sent to Alta Bioscience UK (Table 5).

Table 5: Summary of blood samples analysed. Blood was taken from the femoral artery (red) and/or tail vein (blue). N is the number of samples analysed. Blood samples from Wistar rats were all arterial. Concentration: n.mole/ml

	WT		TG		Wistar
Age	Arterial blood (n. mole/ml)	Venous blood (n. mole/ml)	Arterial blood (n. mole/ml)	Venous Blood (n. mole/ml)	Arterial blood (n. mole/ml)
6 months	n=0	183.03±18.12 (n=3)	n=0	192.94±18.50 (n=3)	163.65±27.62 (n=5)
12 months	241.64±0.06 (n=2)	160.39±0.44 (n=2)	210.66 (n=1)	162.61±6.43 (n=3)	
18 months	203.25±8.67 (n=2)	157.81 (n=1)	235.26±19.07 (n=4)	177.08±6.15 (n=2)	

Leucine is an essential amino acid and can be transported across the BBB through the LAT-system. LAT system is also used by other amino acids and the transport follows the Michaelis-Menten kinetics; therefore the increased concentration of one amino acid in plasma, reduce the influx of the others that remain constant [292]. Histidine, methionine, leucine, isoleucine, valine, phenylalanine, tyrosine and tryptophan are the main Large Neutral Amino Acids (LNAA) using this transport [312]. The concentration of unlabelled leucine and the other LNAA were analysed in both types of blood samples, arterial and venous (Figure 35).

The analysis of unlabelled leucine showed a difference between arterial and venous plasma samples in WT and TG. As indicated in Figure 35A, a statistical difference in the concentration of unlabelled leucine was detected when arterial and venous plasma were compared at 12 and 18 months of age. Specifically, the arterial concentration of unlabelled leucine at 12 months was 231.31±17.89 n.mole/ml and in venous plasma was 161.72±4.71 n.mole/ml with an increase of arterial plasma values of 43% when compared to the venous blood samples. 18 months old WT and TG had arterial values of unlabelled leucine of 224.59±22.50 n.mole/ml and the venous concentration was 170.65±11.94 n.mole/ml with an increase of arterial plasma values of 31.6% when compared to the venous blood. Since the concentration of unlabelled leucine had different values in arterial and venous plasma, it was decided to take this aspect into account for the calculation of PSR, and hence only the cold leucine concentrations taken from arterial plasma were used in further analysis.

The comparison of unlabelled leucine taken from arterial blood revealed Wistar rats had a lower (-28%) concentration of cold leucine than both Fischer-344 WT and TG rats at both 12 and 18 months (Figure 35, B). No difference was observed in the cold leucine when the two genotypes were compared (Figure 35, C). The concentration of the 8 LNAA was evaluated in Wistar and Fischer-344 strain (Figure 35, D). The analysis showed that Fischer-344 strain WT and TG, had higher values of arterial 8 LNAA (1039.92±40.26 n.mole/ml) at 12 months and at 18 months (1042.23±82.95n.mole/ml) when compared to Wistar (779.58±107.18 n.mole/ml). Because the difference of unlabelled leucine (-29%) and 8 LNAA (-25%) in arterial plasma were much lower in Wistar when compared to Fischer-344 strain at 12 and 18 months of age the use of blood measurements from Wistar rats could not be applied to the analysis of the longitudinal study of WT and TG rats as initially planned.

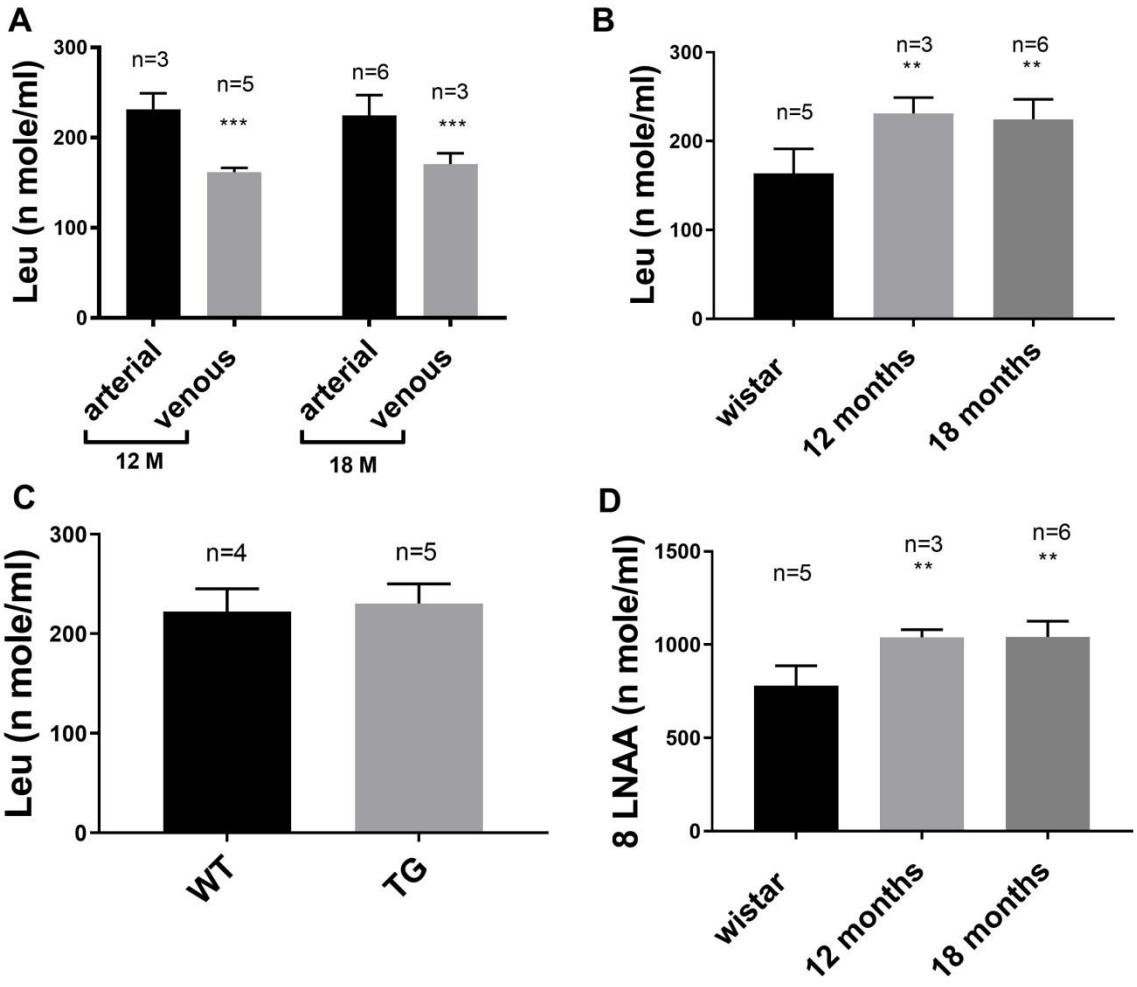

Figure 35: Analysis of unlabelled leucine and a range of 8 large amino acids (LNAA) in plasma. (A) The evaluation of cold leucine in arterial and venous plasma samples from WT and TG rats at 12 and 18 months of age. Data analysed by using Two-way ANOVA and Sidak post hoc test show a statistical difference between the 2 types of plasma samples (p=0.0001 at 12 months and p=0.0010 at 18 months of age). (B) Unlabelled leucine concentration between Wistar, WT and TG rats at 12 and 18 months of age using One-way ANOVA. (C) The concentration of unlabelled leucine remained unchanged between the WT and TG rat genotypes, data analysed by using Unpaired t-test. (D) shows the concentration of the 8 LNAA in arterial plasma samples in Wistar and Fischer-344 strain (WT and TG polled together) at 12 and 18 months of age. The 8 LNAA are: Histidine, methionine, leucine, isoleucine, valine, phenylalanine, tyrosine and tryptophan. Data analysed by One-way ANOVA showed a statistical difference in 8 LNAA concentration, with a p values of p=0.0054 between Wistar and Fischer-344 (WT and TG) 12 months and p<0.0013 between Wistar and Fischer-344 (WT and TG) 18 months. **p≤0.01; ***p≤0.001. Data were expressed as mean±SD.

4.1.3 [^{11}C]leucine free fraction in plasma

For the evaluation of the AIF, the percentage of free [^{11}C]leucine was estimated by using a plasma aliquots, mixed with 5% or 70% perchloric acid (PCA) (Table 6). The more concentrated PCA was used by mistake in the protocol and after realising that other studies used lower concentrated acids to precipitate proteins. Therefore, the values obtained at 70% were converted into 5% even if in literatures is not specify very well the effect of more concentrated PCA on protein precipitation.

Table 6: Wistar and Fischer-344 rats were both used for blood measurements. Fifteen Wistar rats were used for blood measurements, of which 7 had their blood tested with 5% and 70% PCA simultaneously. Blood of WT and TG rats were always tested by using 70% PCA.

Strain	**5% PCA**	**70% PCA**
Wistar	8	15
Fischer-344 (WT & TG)	0	9

Blood samples were taken from the femoral artery of 7 Wistar rats and were tested by using 5% and 70% of PCA. From 2 minutes after injection until 20 minutes most of [^{11}C]leucine was free in plasma and therefore the use of 5% PCA and 70% PCA did not change significantly the measurements of free [^{11}C]leucine. However, from 30 minutes post-injection onward, the amount of free [^{11}C]leucine increased significantly with the 70% PCA precipitation. From 30min post-injection onward, the amount of free leucine extracted with 5% PCA was significantly lower than with 70% PCA (-42%, -62% and -74% at 30, 40 and 60min post-injection respectively).

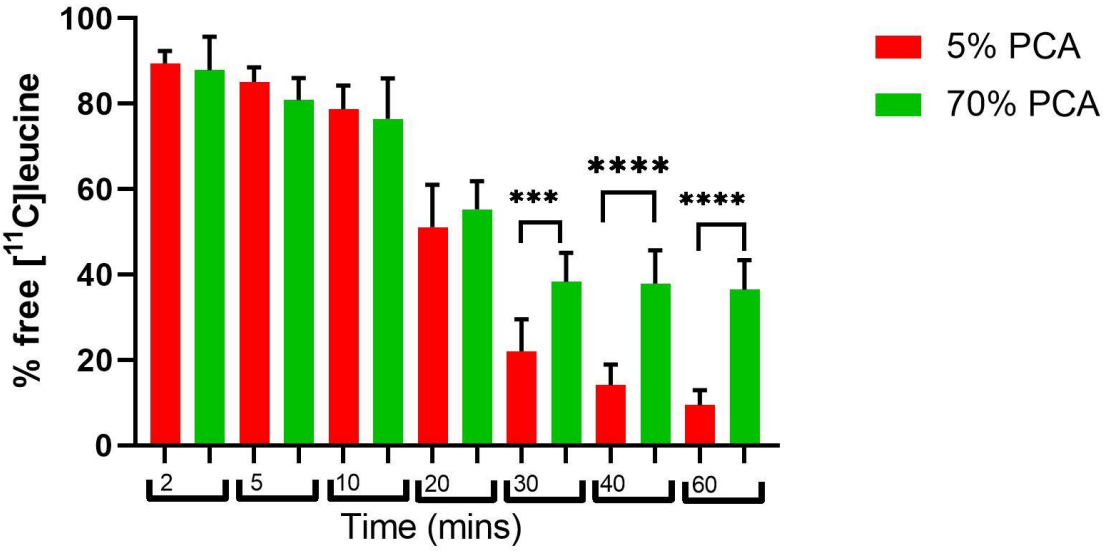

Figure 36: Evaluation of free [^{11}C]leucine in plasma in 7 Wistar rats using 5% and 70% PCA. Data show that from 2 to 20 minutes the values of free [^{11}C]leucine were similar and increased at 30 minutes onwards. Two-way ANOVA and Sidak post-hoc test showed a statistical difference at 30 minutes (p=0.0001) and at 40 and 60 minutes (p<0.0001). *** p≤0.001 and **** p<0.0001. Data were expressed as mean±SD.

As all blood samples from the Fischer-344 WT and TG were analysed using 70% PCA, a calibration study was done with the aim of finding a mathematical function to calibrate the free [^{11}C]leucine values achieved by using 70% PCA with those obtained with 5% PCA (Figure 37) .

$$[\mathbf{11}\boldsymbol{C}]\boldsymbol{Leu}_{(\boldsymbol{free@5\%})} = -(-\mathbf{1} - \mathbf{0.05} \times [\mathbf{11}\boldsymbol{C}]\boldsymbol{Leu}_{(\boldsymbol{free@70\%})}) \div (\mathbf{0.55} \div [\mathbf{11}\boldsymbol{C}]\boldsymbol{Leu}_{(\boldsymbol{free@70\%})})^{\mathbf{5}} + \mathbf{1}).$$

(Equation 12)

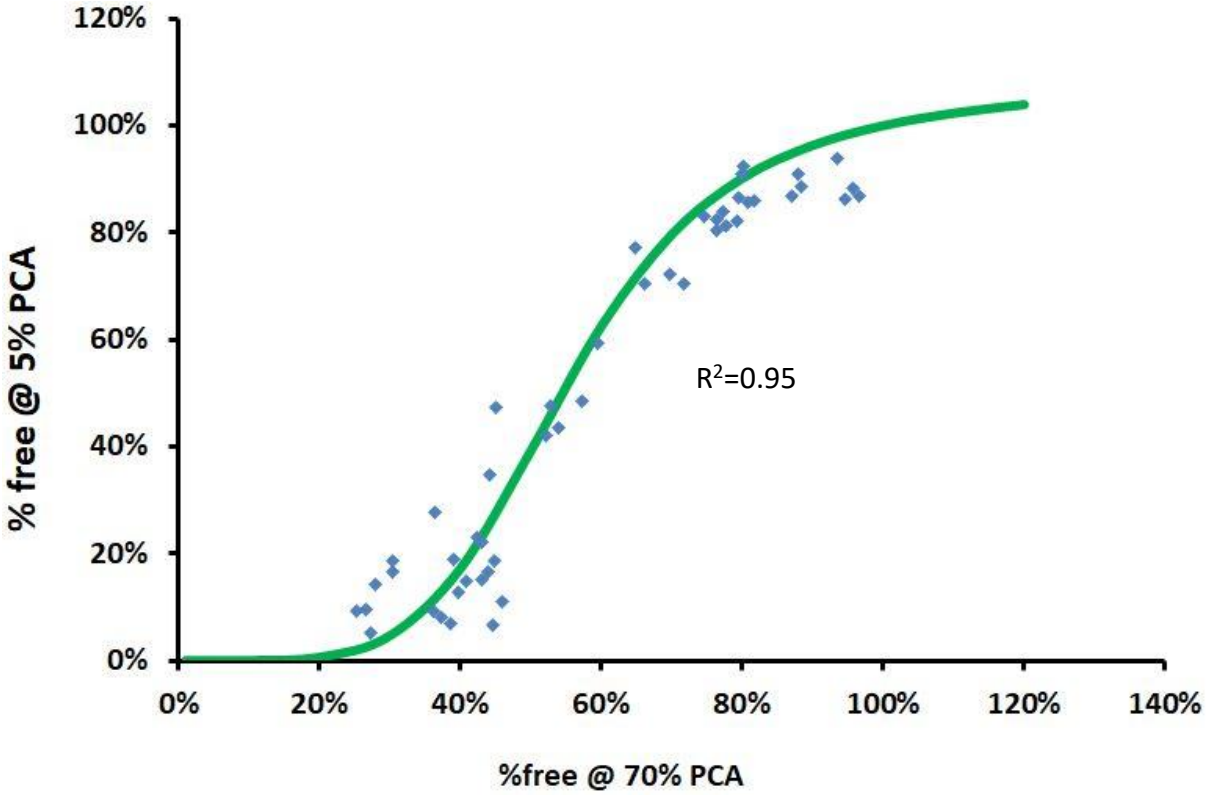

Figure 37: Values of free [^{11}C]leucine in plasma in Wistar rats acquired by using 5% (Y axis) and 70% (X axis) PCA and plotted on an XY graph to determine a calibration curve. The curve-fit indicates the mathematical function describing this calibration.

To validate if the use of the mathematical function for the conversion of blood did not change the AIF, two Wistar rats had full analysis PET/CT scan and indivudual blood measurements tested with 5% and 70% PCA. The values of free [^{11}C]leucine measured when using 70% PCA were converted by using the mathematical formula ($[\mathbf{11}\boldsymbol{C}]\boldsymbol{Leu}_{(\boldsymbol{free@5\%})} = -(-\mathbf{1} - \mathbf{0.05} \times [\mathbf{11}\boldsymbol{C}]\boldsymbol{Leu}_{(\boldsymbol{free@70\%})}) \div (\mathbf{0.55} \div [\mathbf{11}\boldsymbol{C}]\boldsymbol{Leufree@70}\%\square\square)\square\mathbf{5}\square + \mathbf{1})\square.\square$ (Equation 12) and two AIF were determined; one coming from the blood measurement with 5% PCA and another coming from the converted values. The parameters K_{cplx} and PSR were then compared. Despite the low n-number of Wistar analysed (n=2), K_{cplx} and PSR showed similar values when AIF was estimated by using 5% PCA or converted to 5% PCA (Figure 38) and subsequently the mathematical function was applied to all WT and TG rats.

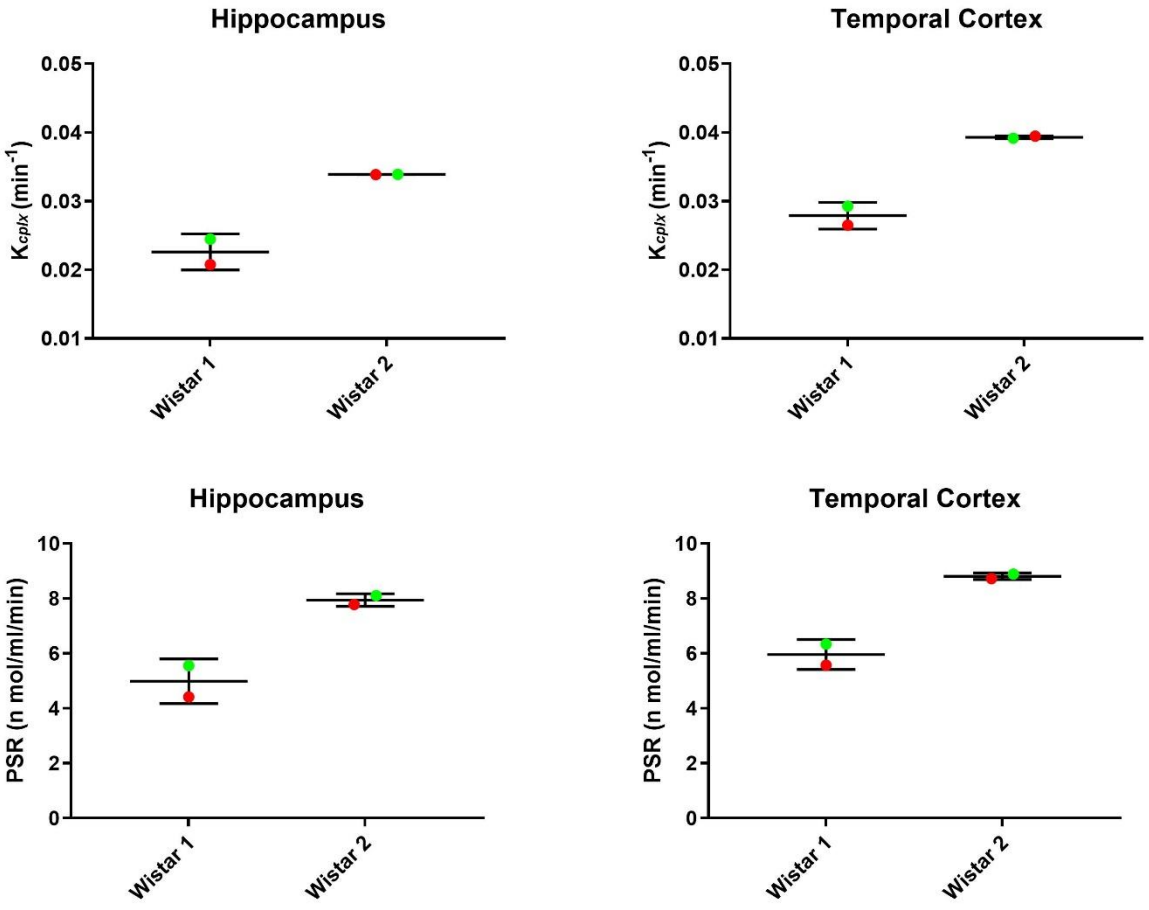

Figure 38: Evaluation of two parameters k_{cplx} and PSR in hippocampus and temporal cortex in two Wistar rats by using two different AIF. One AIF was measured by using 5% PCA for the evaluation of free [^{11}C]leucine (red dot) and the other AIF was measured by using 70% PCA and corrected by using the conversion formula (green dot). To determine the PSR, averaged values of unlabelled leucine in arterial plasma of Wistar rats were used.

4.1.4 PSR analysis by using individual IF and individual unlabelled leucine concentration in arterial plasma

The blood measurements revealed differences in the concentration of unlabelled leucine and 8LNAA between strains (see §4.1.2), therefore we could not use a Wistar population-based IF for the study of PSR in WT and TG rats. Before determining an image derived input function (IDIF) for the longitudinal study, by using the AIF measured in 4 WT and 5 TG, the PSR was evaluated in Fischer-344 rats WT and TG that had the full blood measurements of free [^{11}C]leucine and unlabelled leucine in arterial plasma (2 WT and 1 TG at 12 months of age and 2 WT and 4 TG at 18 months of age). Different brain regions were

analysed and the results showed a similar trend in which the PSR values remain constant at 12 months with no differences between genotype observed, however at the 18 month age, WT animals exhibited an increase in PSR compared to the TG animals but also compared to WT at younger age (12 months)(Figure 39). Despite the low n-number per group, at 18 months of age WT rats have higher PSR values than TG in temporal cortex, hippocampus, cerebellum and in somatosensory cortex.

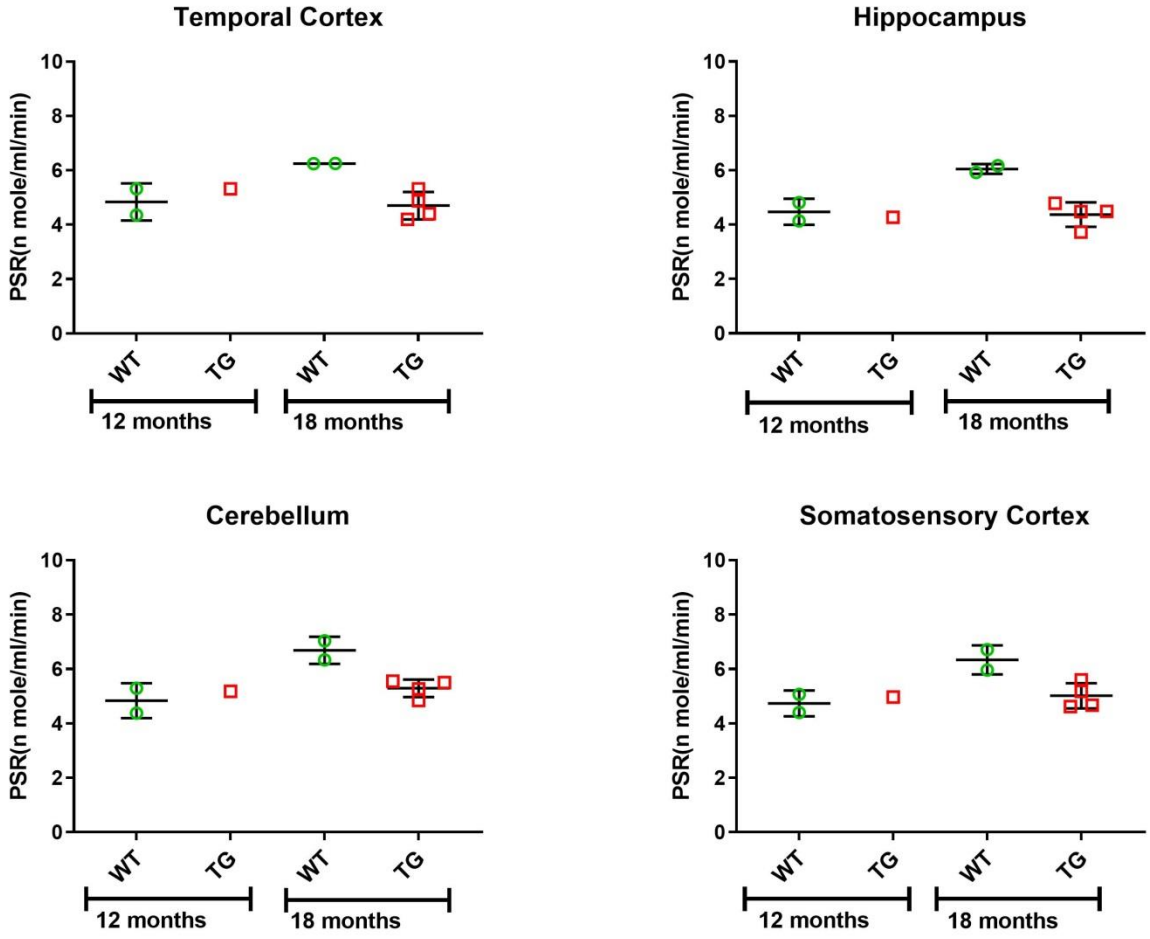

Figure 39: PSR study in WT and TG rats at 12 and 18 months by using individual AIF and individual values of unlabelled leucine in arterial plasma. Data showed that at 18 months, WT had higher values of [^{11}C]leucine PSR in the 4 brain regions analysed compared to TG at the same age; the effect size at 18 months of age was >0.80 by using the Choen's d test. Data were expressed as mean±SD.

4.1.5 Validation of [^{11}C]leucine as a tracer to measure PSR

Anisomycin is an antibiotic that inhibits protein synthesis through inhibition of 80S ribosome. Anisomycin was used in this study for the validation of [^{11}C]leucine as a tracer to

measure brain PSR. Three Wistar rats were injected with anisomycin, 60mg/kg, 10 minutes before starting the [^{11}C]leucine PET acquisition. K_{cplx} and PSR values acquired in 3 anisomycin treated Wistar rats were compared with 6 Wistar rats without anisomycin injection (baseline). Different brain regions were analysed and in all brain regions of all animals pre-treated with anisomycin there was a large (min. 77% max. 89%) inhibition of the net uptake (K_{cplx}) of [^{11}C]leucine and PSR when compared to the non-treated rats (Figure 40). This inhibition of PSR by anisomycin confirmed the sensitivity of [^{11}C]leucine to measure brain PSR following an experimental challenge inhibiting protein synthesis. The inhibition of PSR after injection of anisomycin was also clearly observed on PET images of Wistar rats with and without pre-treatment (Figure 41).

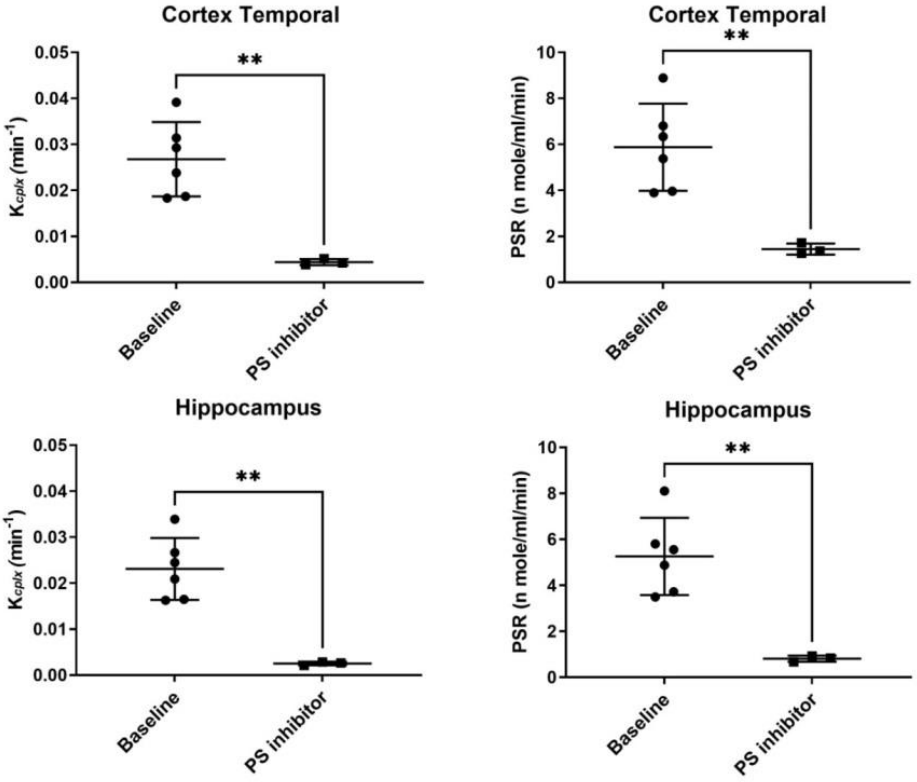

Figure 40: Comparison of K_{cplx} and PSR of Wistar rats with (n=3) and without (baseline, n=6) anisomycin injection, 60 mg/Kg, 10 minutes before the [^{11}C]leucine PET acquisition. Unpaired *t*-test showed a big difference between baseline and protein synthesis inhibitor. p=0.0024 and p=0.0059 in temporal cortex K_{cplx} and PSR respectively and p=0.0014 and p=0.0030 in hippocampus K_{cplx} and PSR. **p≤0.01. Data were expressed as mean±SD.

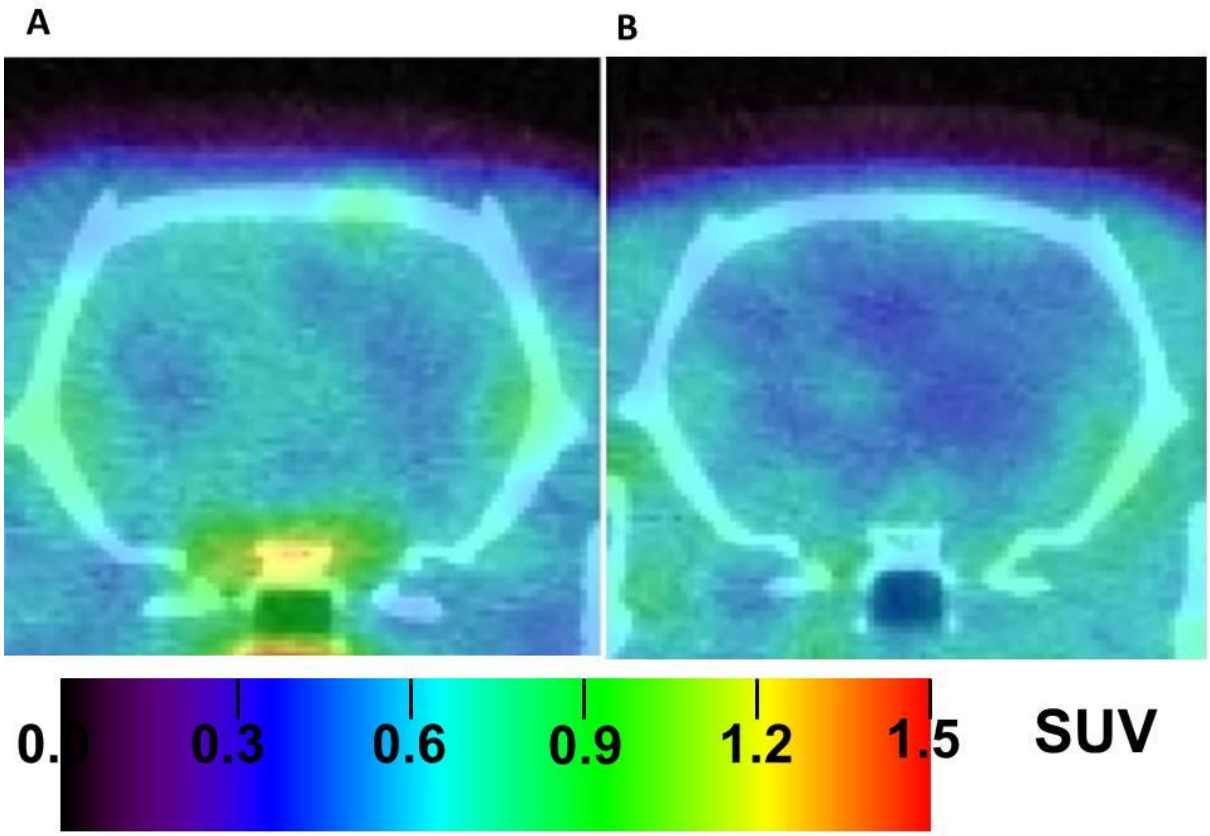

Figure 41: Representative sum 20-60min PET images of [^{11}C]Leucine uptake (shown as SUV) in the brain (A) without and (B) with injection of anisomycin (PSR inhibitor) @ 60mg/kg i.v.

4.1.6 Input Function measurement for longitudinal study

For the longitudinal study, permanent arterial canulation for individual arterial blood sampling was not feasible under Home Office licence regulation (i.e. femoral canulation is a terminal procedure), and hence an averaged population-based whole-blood and plasma input function (AIF) was validated and used to calculate K_{cplx} together with an averaged population-based arterial cold leucine concentration to calculate the PSR in the longitudinal study in WT and TG rats.

The first step, for validation of the IDIF, was to align time-wise and average the individual arterial input function (AIF) obtained in the 4 WT and 5 TG rats together because no differences in heart TAC and AIF were evaluated between genotype. For each animal, a ROI over the left heart ventricles was manually drawn in order to determine a heart time activity curve (TAC). A specific time-point with similar SUV values between the averaged heart TAC and the averaged blood measurement obtained by γ-counter (starting frame 180 seconds and 240 seconds) was identified to calculate the ratio between individual heart TAC

and the averaged AIF hence producing a scaling factor between TAC and AIF (Equation 13). The individual ratio was then applied to the averaged AIF to generate a scaled IDIF, in which the averaged AIF was scaled up to the individual Heart TAC. Figure 42 shows the averaged AIF (purple) and the individual Heart TAC (orange) in one rat and Figure 43 shows the application of the individual ratio to generate an individual IDIF.

(Equation 13):

$$Scaling\ Factor = \frac{Individual\ Heart\ TAC}{Averaged\ AIF}$$

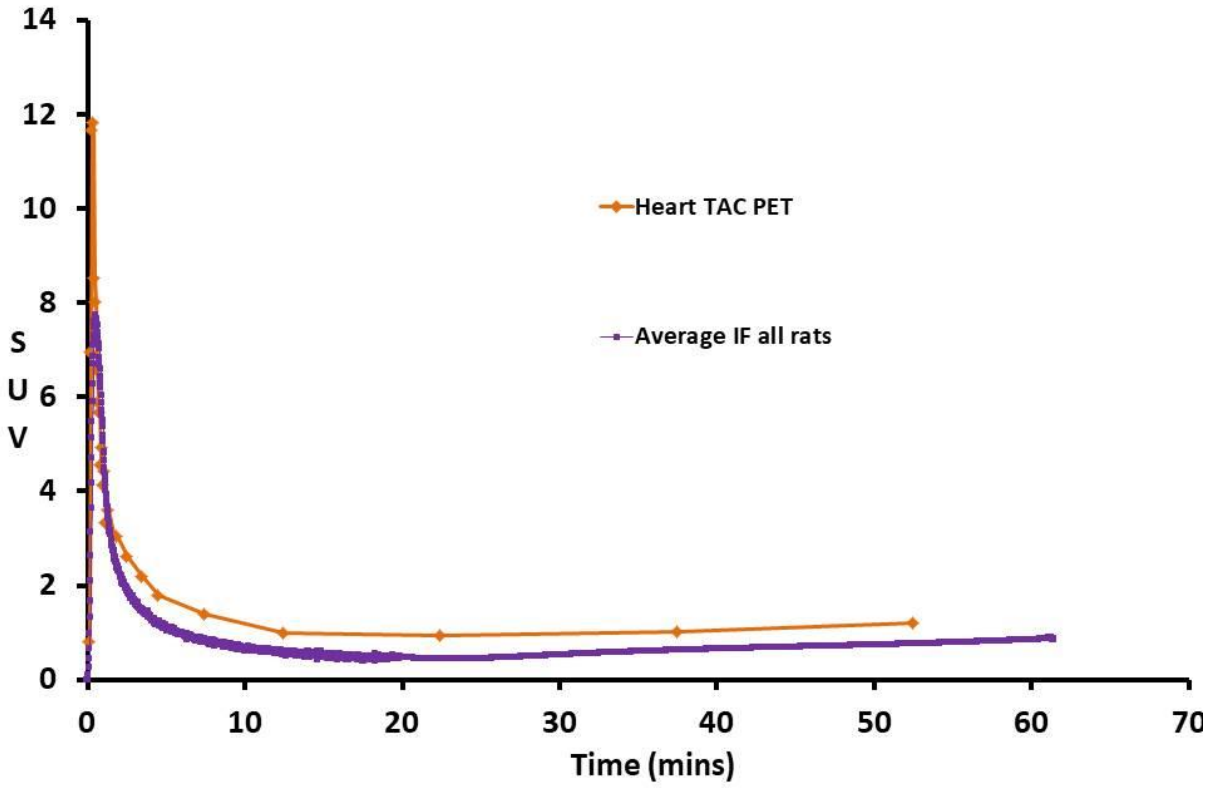

Figure 42: Heart TAC (orange) from one rat and the averaged AIF obtained by the average of blood measurements from 4 WT and 5 TG rats, before applying the ratio to generate a scaled IDIF.

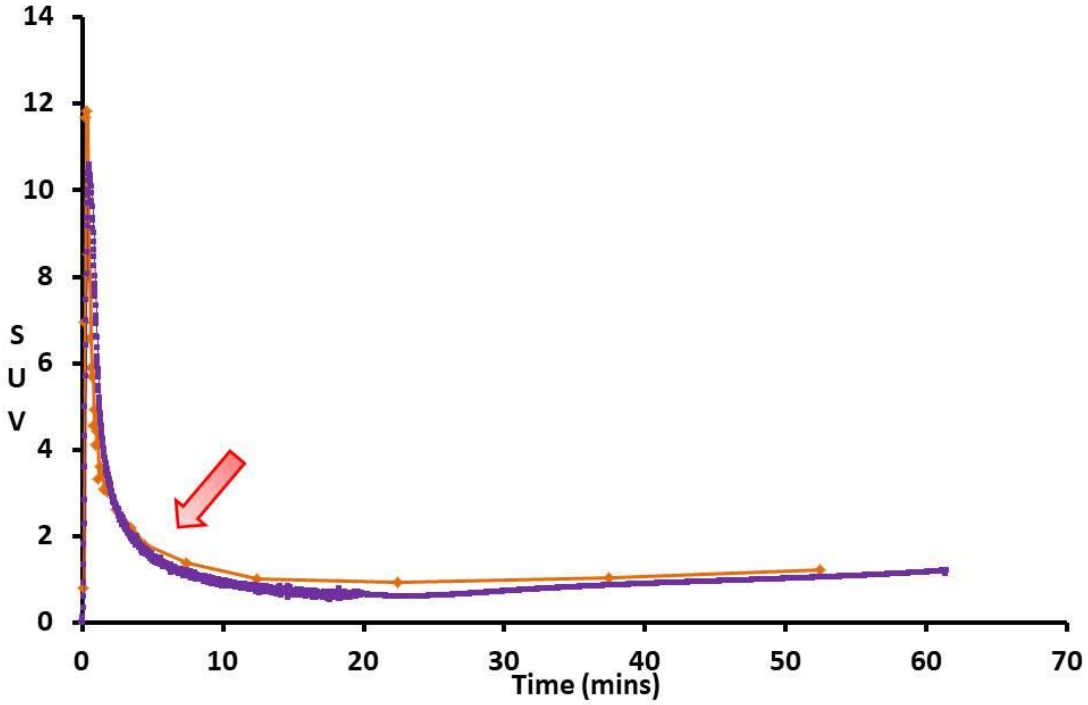

Figure 43: Heart TAC of an individual rat (orange curve) and the scaled AIF (IDIF; Purple curve) obtained after the calculation of the ratio between frames 180sec and 240 sec, of TAC and average AIF. The applied ratio calculated by dividing the Individual Heart TAC (frame 180-240 seconds) and the Averaged AIF (frame 180-240 seconds) obtained from the 4 WT and 5 TG rats with blood measurements scaled up the Averaged AIF to the individual heart TAC.

4.1.7 K_{cplx} and PSR in longitudinal study

The individual IDIF and the individual brain TAC were loaded in the MICK software (developed in-house at Manchester) and then used to determine K_{cplx} and PSR for the longitudinal study. To determine the PSR, averaged values of unlabelled arterial leucine obtained from 4 WT and 5 TG rats at 12 and 18 months of age were used.

The analysis of K_{cplx} showed a significant genotype effect with slightly higher K_{cplx} values in WT than TG in four of the brain regions studied, i.e. the hippocampus (p=0.0442), whole brain (p=0.0448), *globus pallidus* (p=0.0325) and the *caudate putamen* (p=0.0423) (Figure 44).

The PSR remained unchanged between WT and TG or by age in all brain regions analysed (hippocampus, temporal cortex, cerebellum, cortex somatosensory, frontal cortex, *thalamus*, cortex cingulate/anterior, *globus pallidus*, *caudate putamen* and whole brain (Figure 45)), with the exception of the *globus pallidus* which exhibited a significant genotype

effect on PSR (p=0.0295) (Figure 46, A). Specifically, at 18 months of age the [^{11}C]leucine K_{cplx} in the *globus pallidus* and the PSR were decreased significantly (-15% Figure 46 B,C).

Taken together these data show a trend in PSR and K_{cplx} where the TG animals appeared to have a decreased [^{11}C]leucine K_{cplx} and PSR when compared to WT at 18 months, also shown on PET images (Figure 47). The significant genotype difference for K_{cplx} was present in most of the brain regions studied. The apparent loss of this genotype effect for PSR measurements could be due to the use of a population-based input function and averaged cold unlabelled leucine concentration instead of individual measurements and hence have led to an averaging of the PSR.

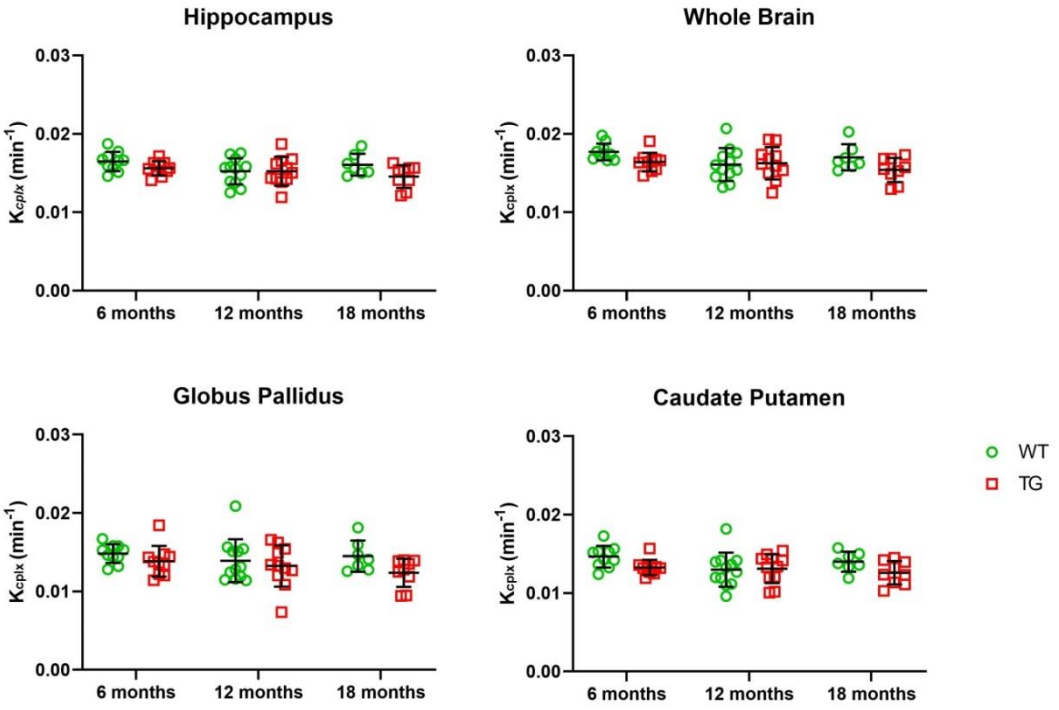

Figure 44: K*cplx* analysis in WT and TG rats at 6, 12 and 18 months by using averaged and scaled IF (IDIF) and averaged values of unlabelled leucine measured from arterial plasma samples of WT and TG at 12 and 18 months of age. Mixed model analysis shows a significant genotype effect in K*cplx* in hippocampus (p=0.0442), whole brain (p=0.0448), *globus pallidus* (p=0.0325) and the *caudate putamen* (p=0.0423). Sidak post-hoc test showed any statistically relevant differences between genotypes or age. Data expressed as mean±SD.

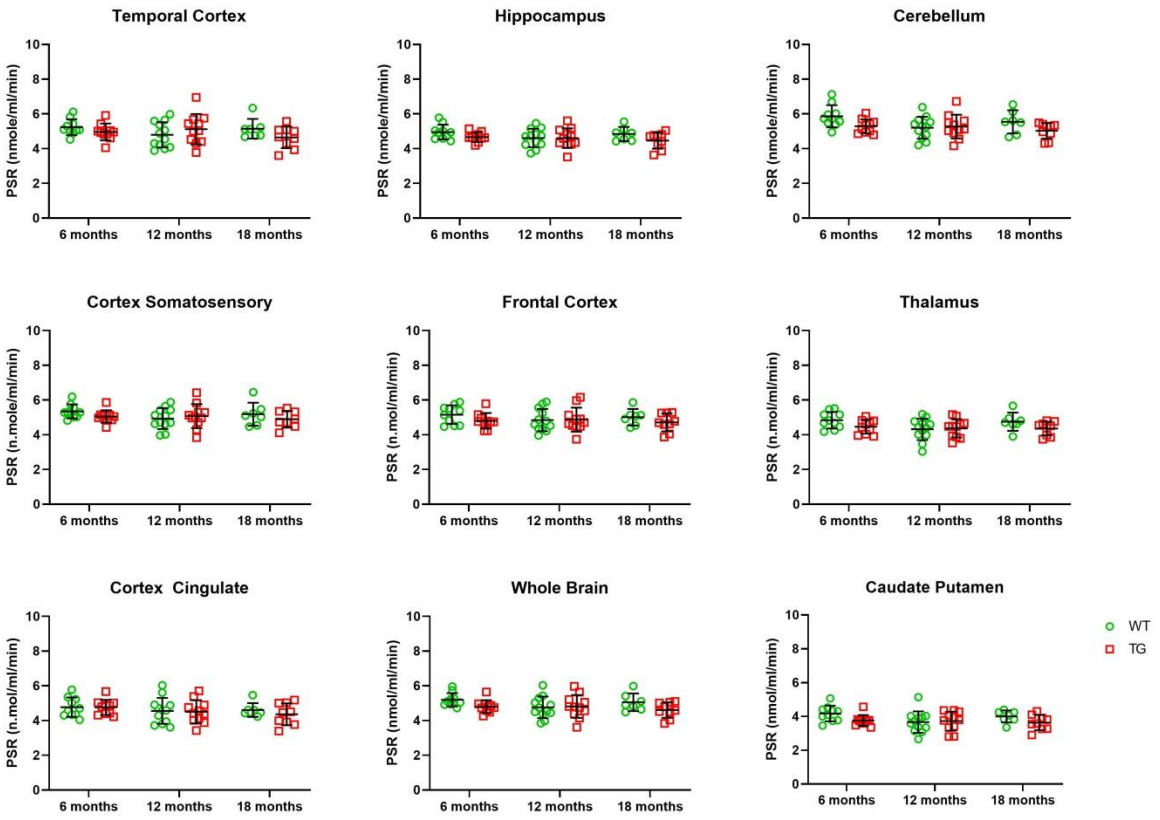

Figure 45: PSR evaluation at 6, 12 and 18 months of age, in different brain regions: temporal cortex, hippocampus, cerebellum, cortex somatosensory, frontal cortex, thalamus, cortex cingulate whole brain and caudate putamen by using averaged and scaled IF (IDIF) and averaged values of unlabelled leucine obtained from arterial plasma samples at 12 and 18 months of age in WT and TG. Mixed model effect and Sidak post-hoc test did not show any statistically relevant differences between genotypes and age. Data were expressed as mean±SD.

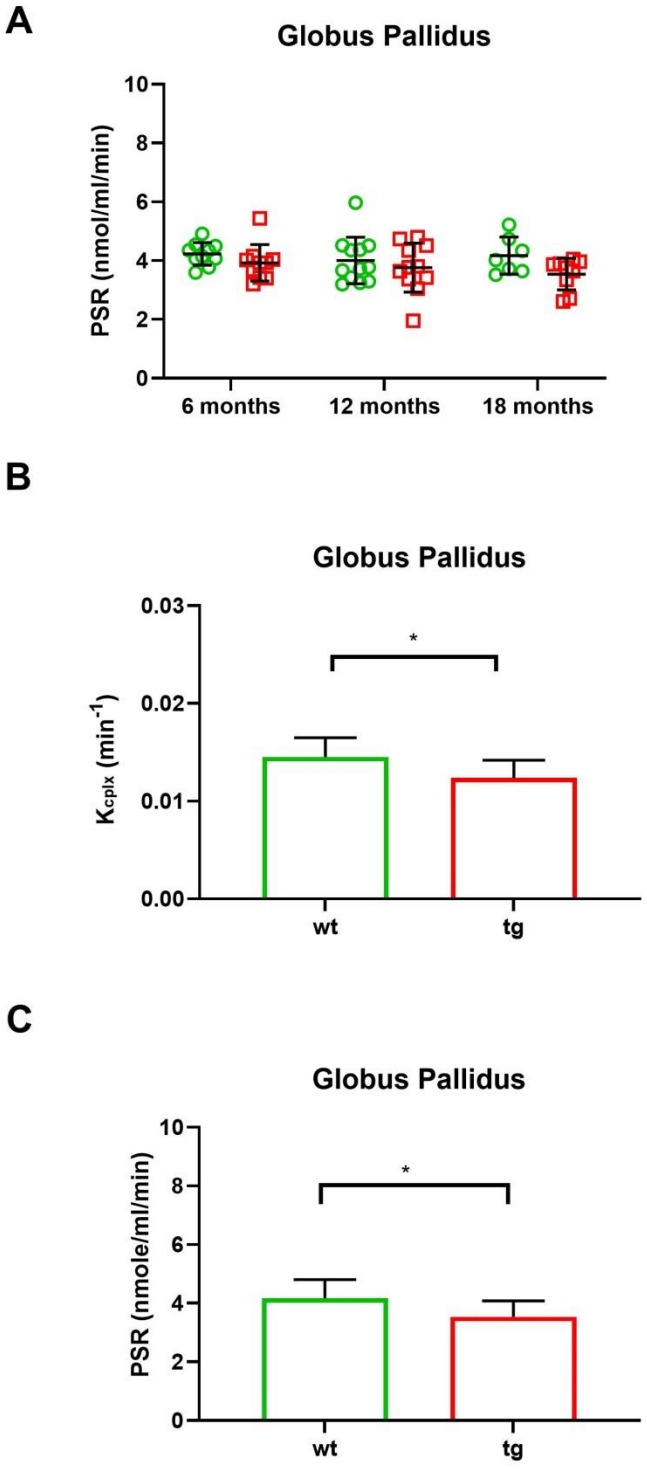

Figure 46: PSR and K_{cplx} analysis by using averaged and scaled IF (IDIF) and averaged values of unlabelled leucine coming from arterial plasma samples at 12 and 18 months of age in WT and TG. Mixed model effect and Sidak post-hoc analysis in WT and Tg rats at 6, 12 and 18 months of age, shows a significant genotype effect in PSR (top graph, A) in *globus pallidus* (p=0.0295). Unpaired t-test performed at 18 months (graph B and C) show a decrease (-14% for K_{cplx} and -15% for PSR) in K_{cplx} and PSR in TG rats statistically relevant (p=0.0427 and p=0.0488, respectively). *p≤0.05. Data expressed as mean±SD.

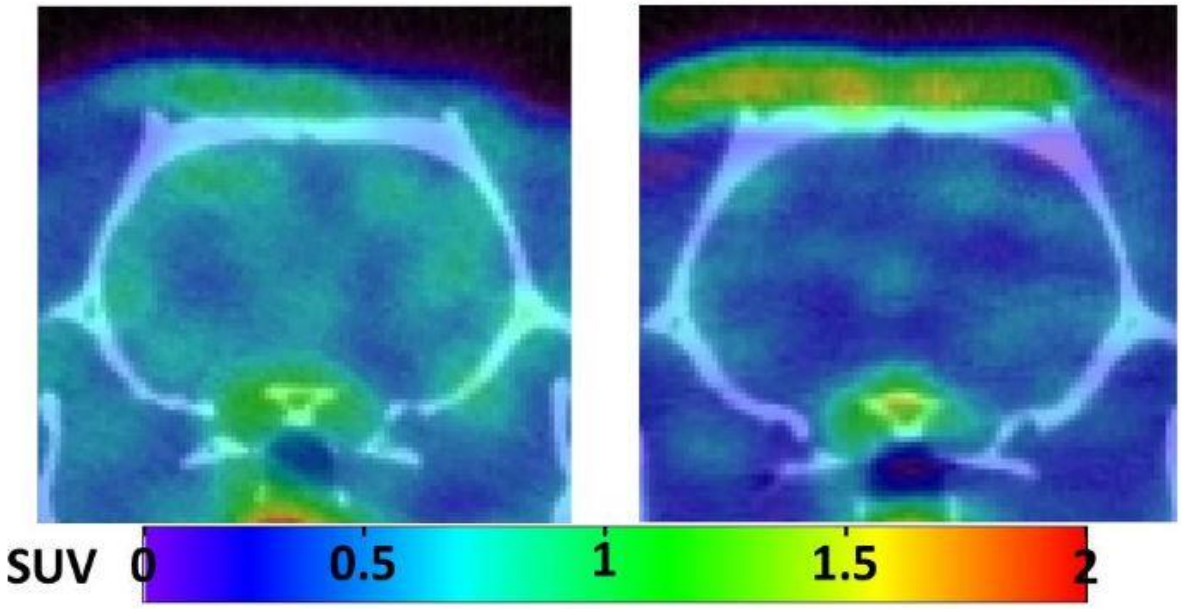

Figure 47: Representative summed PET image (20-60min) of [^{11}C]Leucine uptake (shown as SUV) in the brain of a WT (left) and TG (right) rats at 18 months of age.

4.2 [^{18}F]UCB-H study

Protein synthesis and local protein synthesis at the synapses are essential for the synaptic plasticity and for memory consolidation [313]. Therefore, WT and TG rats were also used for another PET study, in which we evaluated the synaptic density by [^{18}F]UCB-H PET, a tracer able to bind the synaptic glycoprotein SV2A.

8 WT and 7 TG rats at 7 months of age, and 10 WT and 10 TG at 15 months of age were injected i.v. with [^{18}F]UCB-H (baseline). 4 WT and 4 TG at 7 and 15 months were injected before staring the [^{18}F]UCB-H PET acquisition with 1mg/Kg of UCB-J (block scans) and theses scans were used to quantify PET images (Figure 48). Data were analysed between 9 and 20 minutes post-injection as at these time-points, the biggest difference in SUV between baseline and blocked scans was observed. This is likely to be due to the rapid brain pharmacokinetic of [^{18}F]UCB-H resulting in a rapid wash-out and a small difference between baseline and blocked scans at later time-points (>20-30min) (Figure 49).

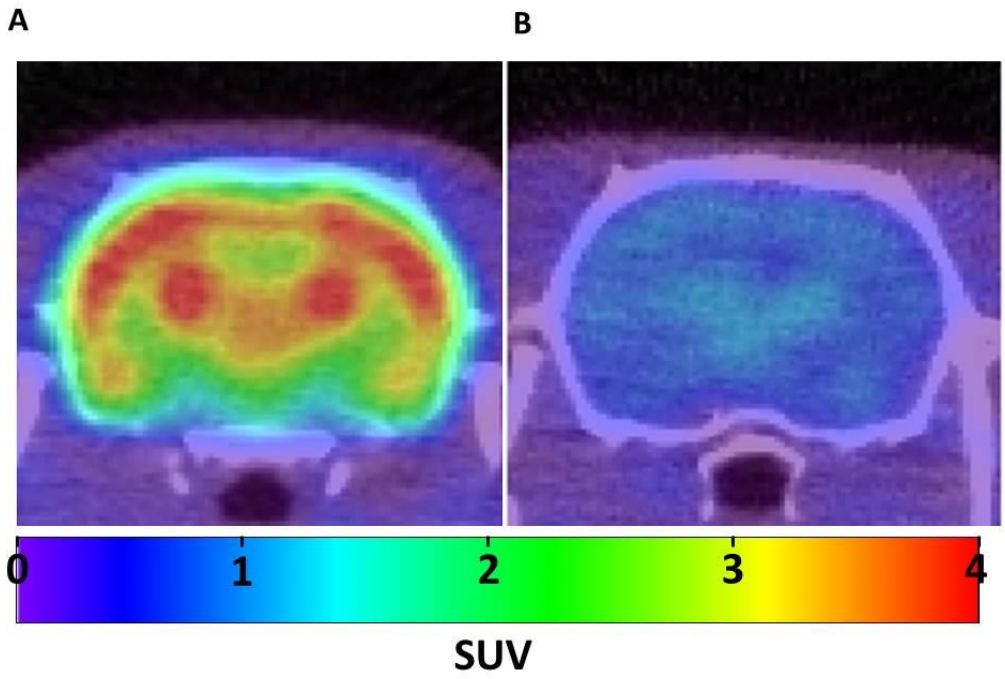

Figure 48: Representative coronal section sum 9-20min PET images of [^{18}F]UCB-H uptake (shown as SUV) in the brain of a WT 7 months without (left, baseline) and with (right, block scan) injection of 1mg/kg of UCB-J before starting the [^{18}F]UCB-H.

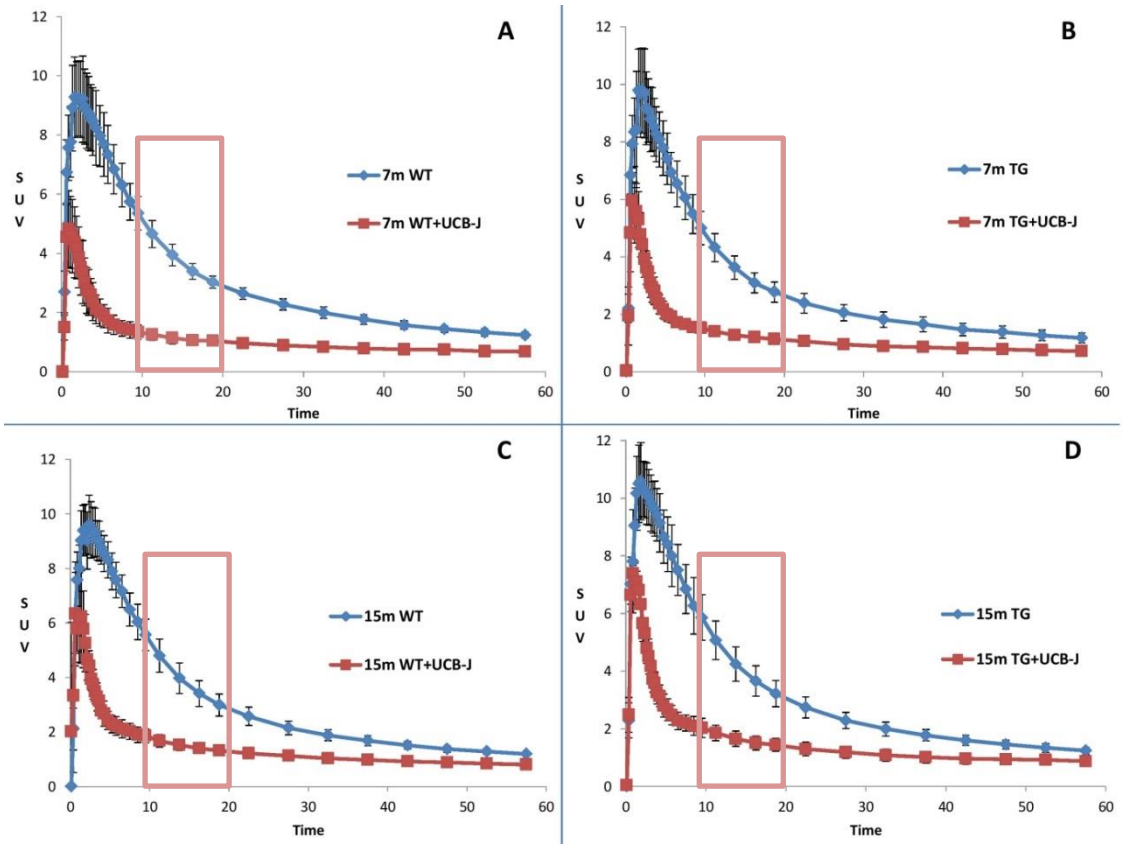

Figure 49: Baseline brain SUV Time Activity Curves (TAC) of [^{18}F]UCB-H (blue) and TAC blocking scan after injection of UCB-J (red) in frontal cortex. Curves show a peak during the first second then followed by a rapid wash-out. Big difference between blocking (red) and non-blocking (blue) scan was shown between 9 and 20 minutes in all groups (shadow). The pre-saturation study (red curves) was developed by using 4 rats per group injected with 1mg/Kg of UCB-J. The blue curves represented the values of averaged TAC of [^{18}F]UCB-H in rats without pre-saturation: 8 WT at 7 months WT (A); 7 TG at 7 months TG (B); 10 WT at 15 months (C) WT and 10 TG at 15 months (D).

The SUV values in different brain regions are shown in Figure 50, and the graphs show that in almost all brain regions the blocking values were similar between WT and TG at 7 months of age but at 15 months, TG rats had an increase of non-specific binding when compared to WT at the same age and the increase happened also in WT and TG due to the age. Few brain regions frontal cortex, frontoparietal motor cortex, hippocampus and thalamus were analysed and the analysis showed a statistically significant decrease of SUV in all groups due to the injection of UCB-J when compared to the baseline ($p \leq 0.0001$), and no statistical differences were determined between genotypes or age detailed in the baseline group with the exception of frontal cortex in which TG rats showed a statistical increase between 7 and 15 months of age ($p=0.0264$) (Figure 51).

In the blocking study, TG rats presented higher values when compared to WT and this increase was statistically significant ($p \leq 0.05$) between 7 and 15 months for both genotype in frontal cortex and in the other brain regions only for TG rats (Figure 51).

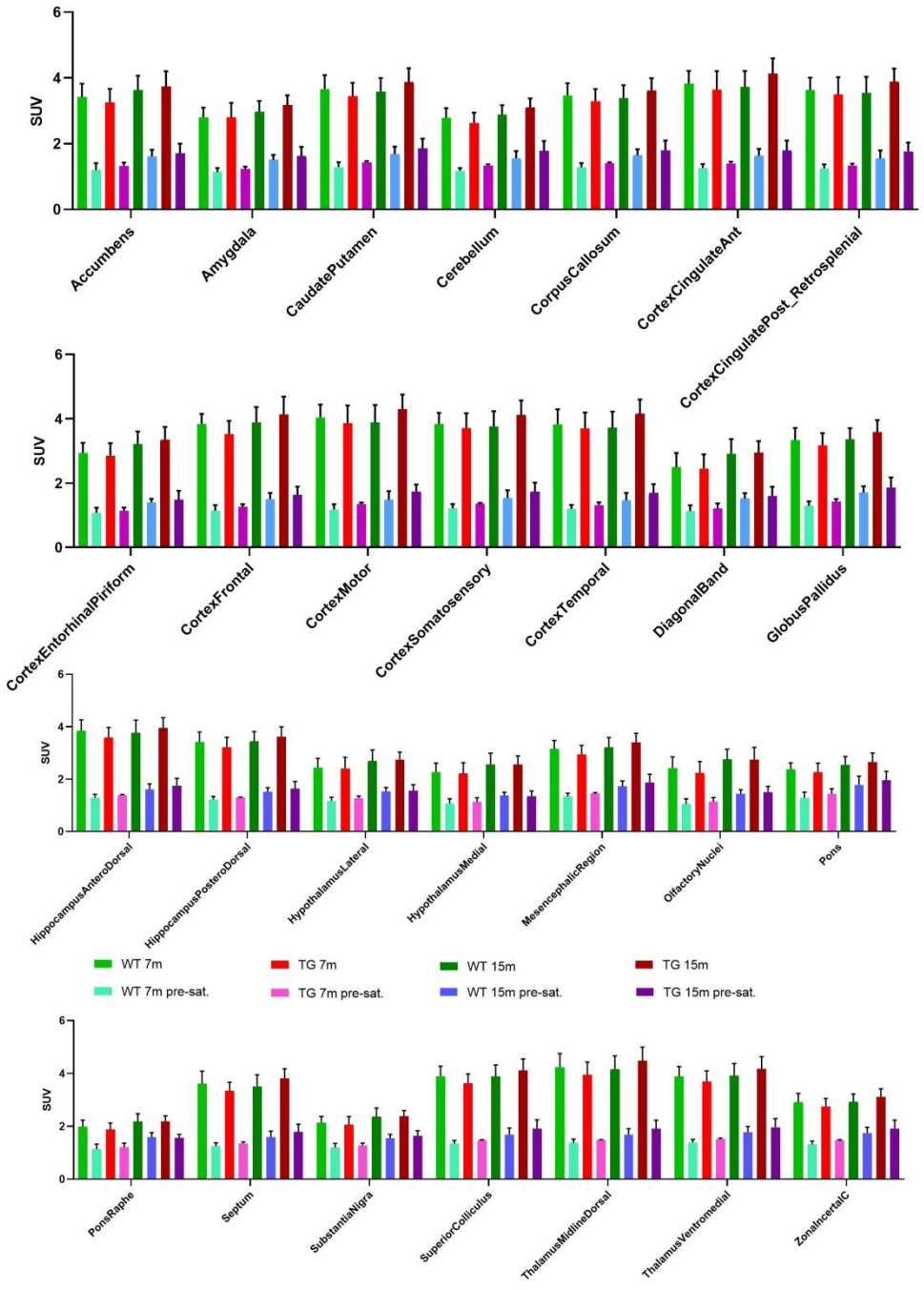

Figure 50: Averaged values of [^{18}F]UCB-H brain uptake in WT and TG rats at 7 and 15 months of age without and with a prior injection with cold UCB-J (1mg/kg). The [^{18}F]UCB-H uptake after blocking study increase with age in both genotypes and is higher in TG in all brain regions analysed. Data were expressed as mean±SD.

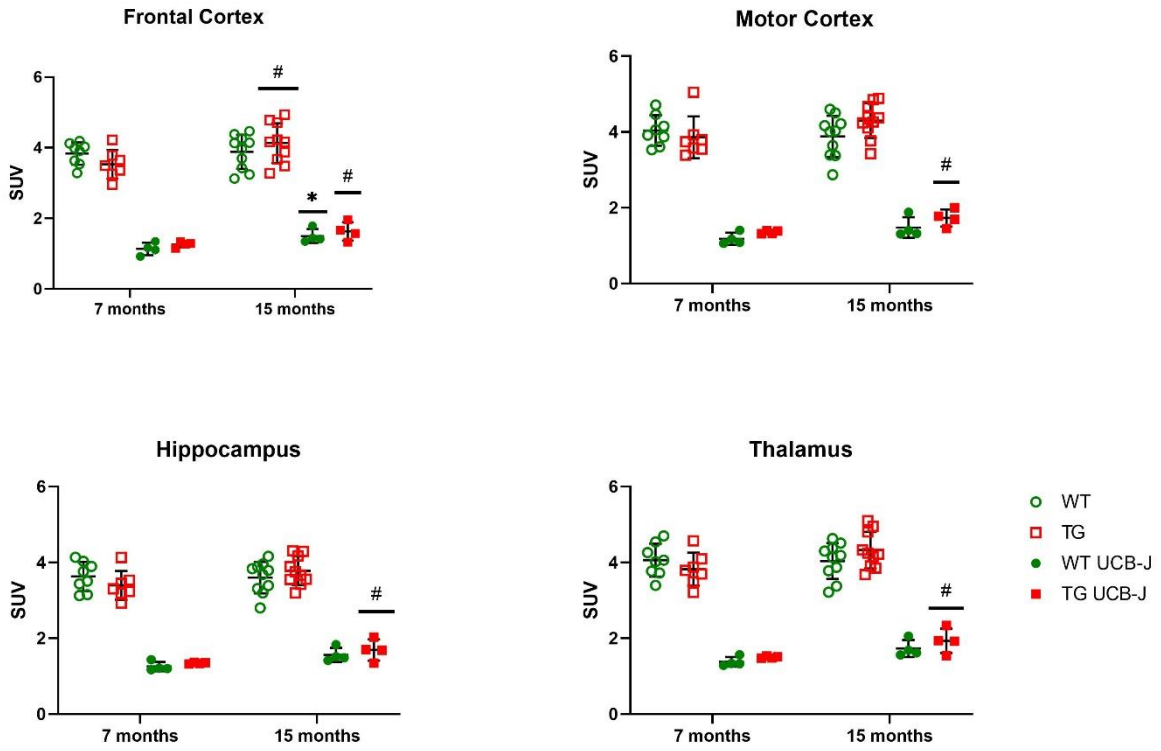

Figure 51: SUV study in some brain regions: frontal cortex, motor cortex, hippocampus and thalamus, in WT and TG rats at 7 and 15 months of age with (blocked scan, UCB-J) and without (baseline) pre-injection with UCB-J (1mg/Kg) 10 minutes before starting the [^{18}F]UCB-H acquisition. The analysis by using Two-way ANOVA showed no statistical differences between genotype and age in baseline scans. Only in frontal cortex TG rats, showed a significant increase due to the age between 7 and 15 months of age (p=0.0264). The blocking scans showed statistically differences in TG rats at 7 and 15 months; specifically, in frontal cortex p=0.0353; motor cortex p=0.0369; hippocampus p=0.0349 and thalamus p=0.0241. In frontal cortex (blocking scans) WT at 7 months were statistically lower than WT at 15 months of age p=0.0382. # means statistical differences between rats same genotype but different age. * and # p≤0.05. Data were tested between 9 and 20 minutes after injection and expressed as mean±SD.

The brain SUV data of [^{18}F]UCB-H showed an over-estimation of the synaptic density due to the increase of the non-specific binding with age and this increase was more prominent in TG than WT rats, highlighting that SUV quantification might not be ideal for this tracer. Blocking scans, performed via the use of unlabelled UCB-J (1mg/kg) 10min before [^{18}F]UCB-H PET scan acquisition, were used to normalise PET images. Because the blocking scans showed an increase of SUV due to the age and more prominent in TG, four averaged blocking scans were used per each group of age and genotype.

The individual brain SUV (9-20minutes) were normalised to the averaged values of blocking scans (9-20 minutes) at the same age and genotype, defining a Normalised Uptake Value (NUV) (Equation 14).

(Equation 14):

$$NUV = \frac{Ind\_SUV_{(9-20\,mins)}}{Averaged_{SUVblocked\ (9-20mins)}}$$

The difference of [^{18}F]UCB-H uptake in WT and TG and at different ages can be clearly observed on the PET image (Figure 52). At 7 months of age, TG rats showed diminution in the uptake (NUV) in many brain regions for example, frontal cortex, motor cortex, hippocampus, thalamus, cerebellum, *caudate putamen*, *globus pallidus* and but not in the temporal cortex (Figure 53) and at 15 months of age no statistical difference was measured between WT and TG (Figure 53). Importantly, a statically age-dependent decrease in [^{18}F]UCB-H uptake was evaluated in WT rats and not in TG with the exception of *caudate putamen* and *globus pallidus* (Figure 53).

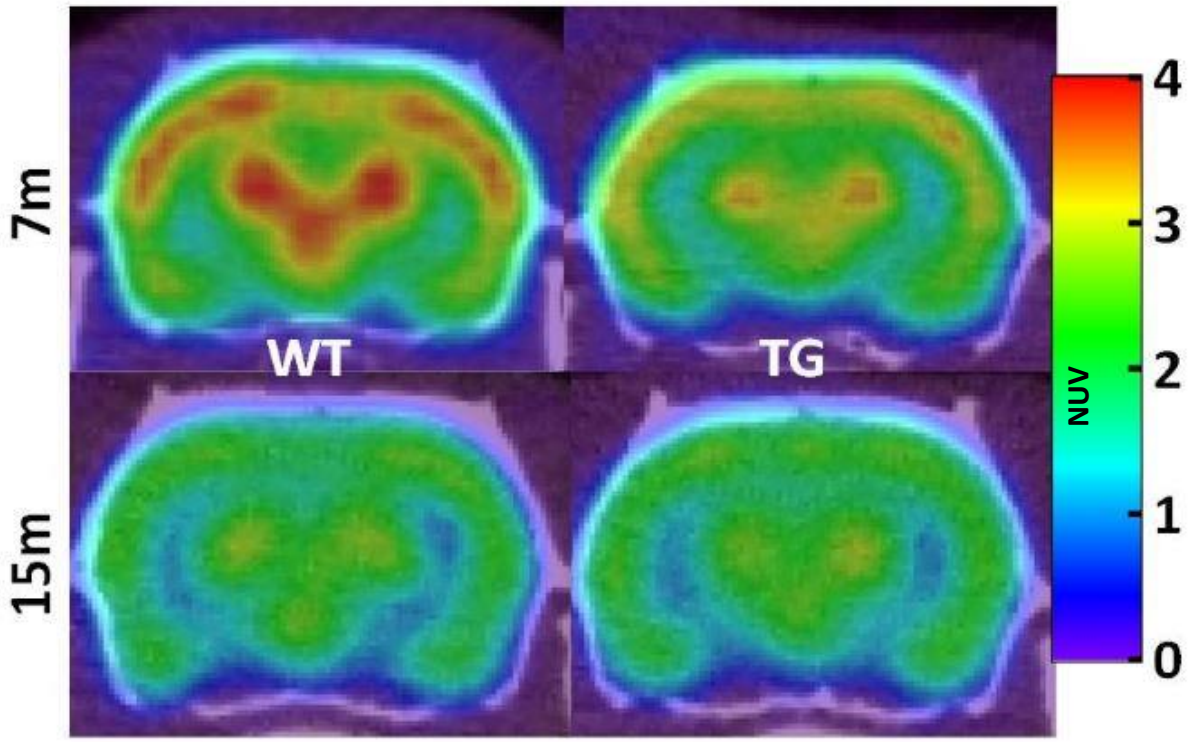

Figure 52: Representative sum 9-20min PET images of [^{18}F]UCB-H uptake (shown as NUV) in the brain of a WT (left) and TG (right) rats at 7 months (top) and 15 months of age (bottom).

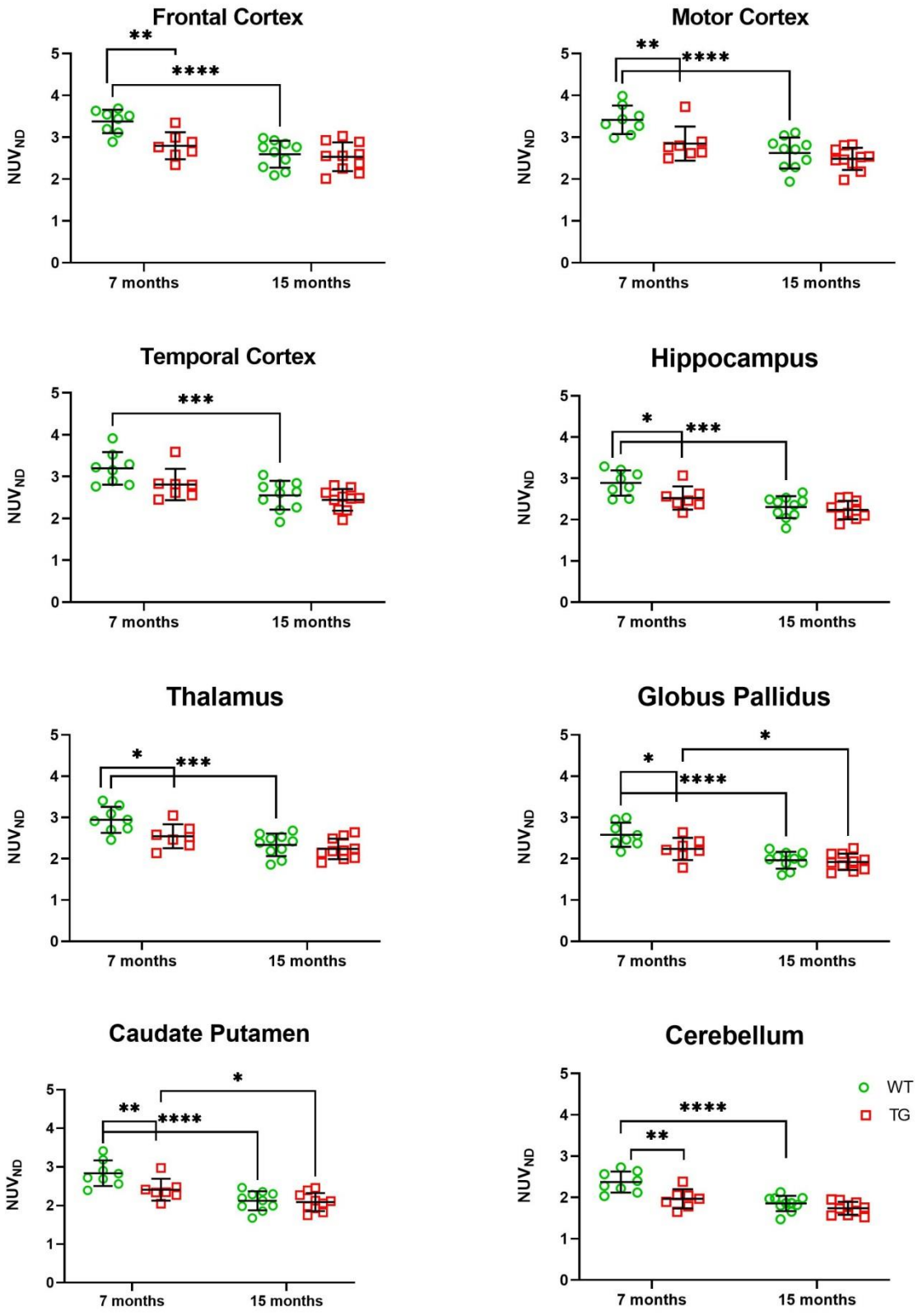

Figure 53: [^{18}F]UCB-H normalised uptake values (NUV_{ND}) analysis in different brain regions at 7 and 15 months of age. Data were analysed with Two-way ANOVA and Sidak post-hoc test. *, ** and ** indicate significant difference between WT and TG and between age as p≤0.05, p≤0.01 and p≤0.0001 respectively. Data were expressed as mean±SD.**

5 Behaviour

5.1 Morris water maze and reversal MWM

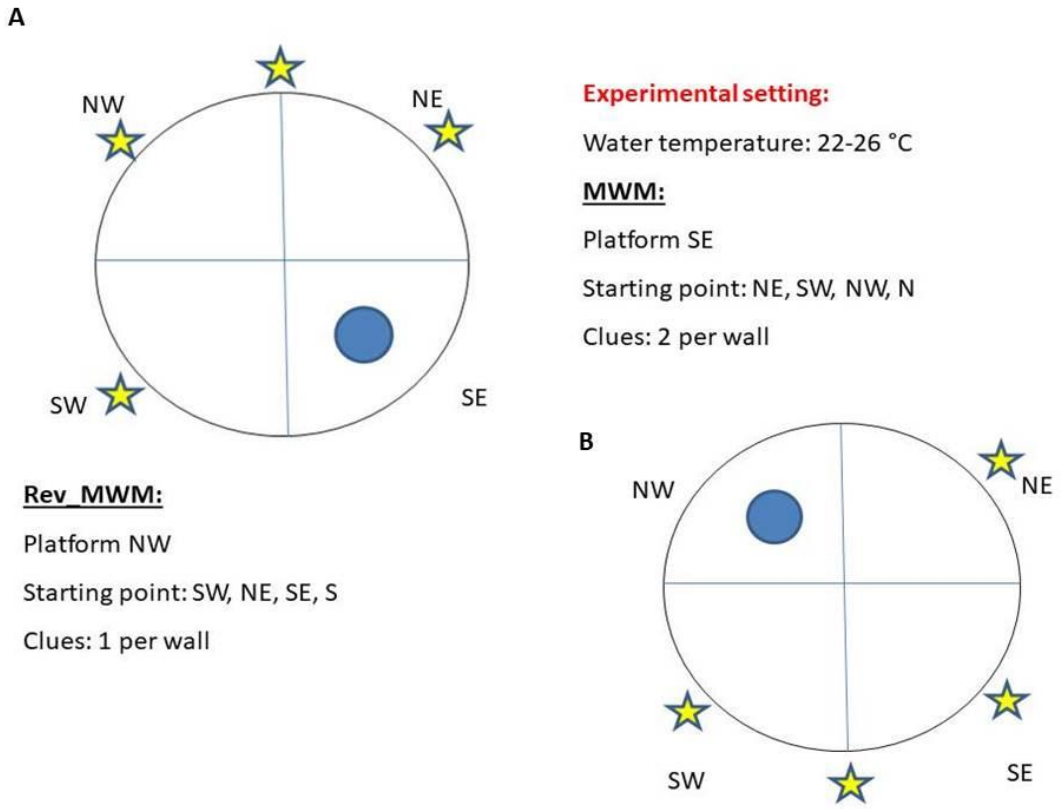

Figure 54: experimental setup of MWM (A) and reversal MWM (B). During the training days of MWM platform was placed in south east (SE) quadrant and rats were released in the pool from 4 different starting point. During the probe test the platform was removed from the tank and rats were released in the pool from the North. During the reversal MWM the platform was moved and the platform was placed to the opposite quadrant, North West (NW). During the probe test after removing the platform, the rat was released from the South. Clues and platform position were always the same during MWM and reversal MWM at each age tested.

MWM is a behavioural test used to assess the spatial memory of rats. The concept behind this test is the necessity of the rat to learn a platform position and escape from the water by using distal visual clues. The reversal MWM has the aim of determining if the rat is able to memorise a new platform position and distinguish the initial learning with the new one. Each rat was released in the tank from four different starting point and the maximum swimming time was 60 seconds.

For the MWM, the platform was placed in SE quadrant and in the opposite position (NW) for the reversal MWM (Figure 54). Each rat was tested for 4 days (acquisition) and 1

day of probe test, in which the platform was removed, for the MWM. The reversal MWM was conducted with 3 days of acquisition and 1 day for the probe test. Different parameters were tested to determine spatial learning. Duration (in seconds) represents the time spent performing the test, the total time to reach the platform. A reduction of the time across days means the ability to remember the platform position. Overall, at each age all rats had a gradually reduced test time. Specifically, WT showed a learning effect ($p=0.0107$) and by comparing all WT across days, a statistical difference was found between days 1 and 2 at 6 months of age ($p=0.0355$) and between 6 months and 18 months of age day 1 ($p=0.0034$). In TG rats also a learning effect ($p=0.0010$) was determined and at 6 months of age a statistically significant difference was found between days 1 and 4 ($p=0.0368$) and between 6 and 18 months of age of the first day of training ($p=0.0273$); no genotype difference was found between WT and TG at each age in MWM (Figure 55). During the probe test of MWM the platform was removed from the tank and the time spent in each quadrant was analysed over 60 seconds. All rats, WT and TG and at each age, spent more time in the South quadrants (SE and SW) (Figure 56, A), and the time spent in South quadrants were statistically significant when compared to North quadrants at 6, 12 and 18 months of age in WT and TG. This result seems to indicate the ability of rats WT and TG to memorise at each age the platform position.

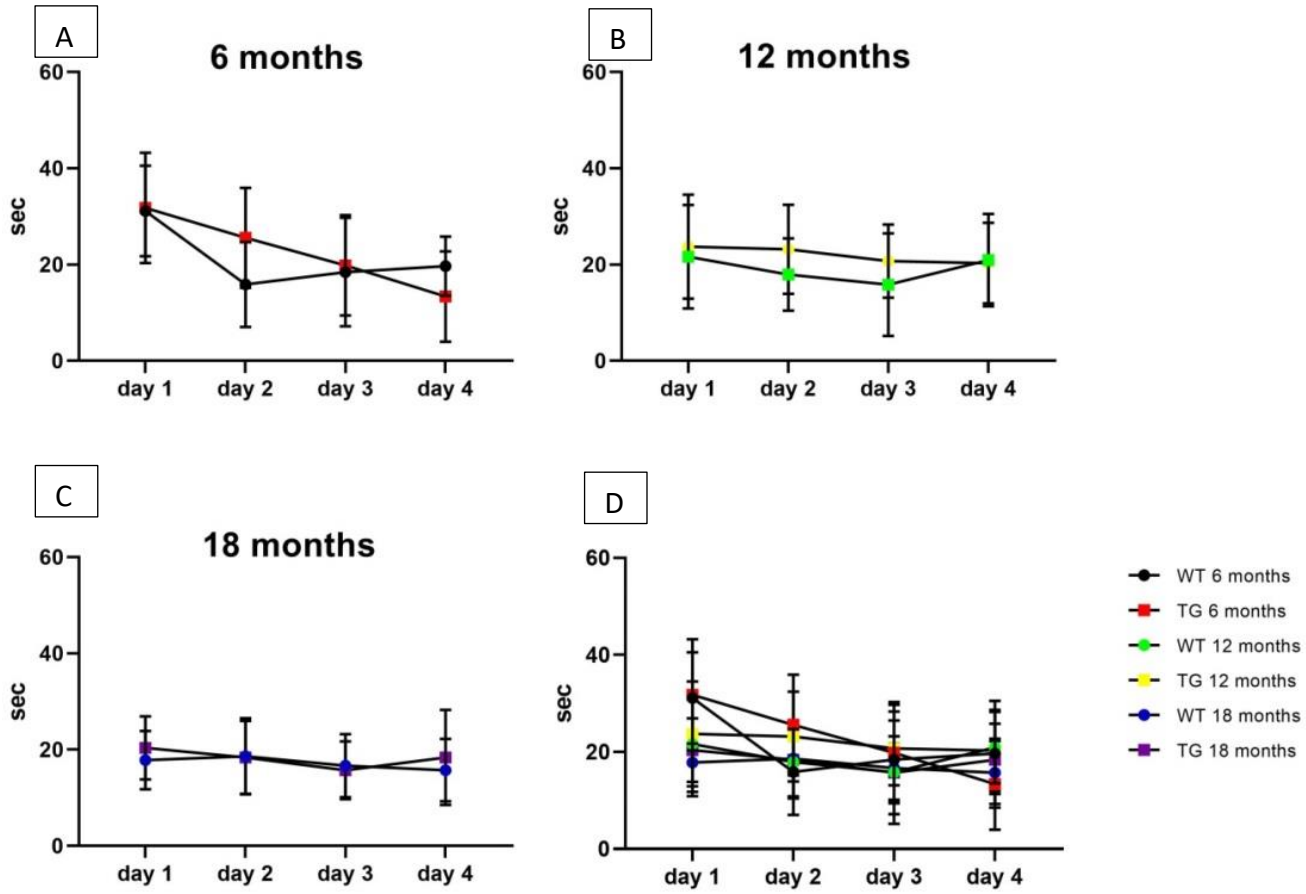

Figure 55: Time spent to find the platform during the training period of MWM at 6 (A), 12 (B) and 18(C) months. Data were analysed by using Two-way ANOVA and Sidak post-hoc test and showed a statistical difference between days 1 and 2 (p=0.0355) in WT 6 months and between 6 and 18 months WT (p=0.0034) day 1. In TG rats a statistical difference was evaluated at 6 months of age, days 1 and 4 (p=0.0368) and between 6 and 18 months of age day 1 (p=0.0273). The bottom right panel (D) shows all data on the same graph. For the MWM were used 11 WT and 12 TG at 6 months of age, 17 WT and 18 TG at 12 months of age and 10 WT and 10 TG at 18 months of age. Data were expressed as mean±SD.

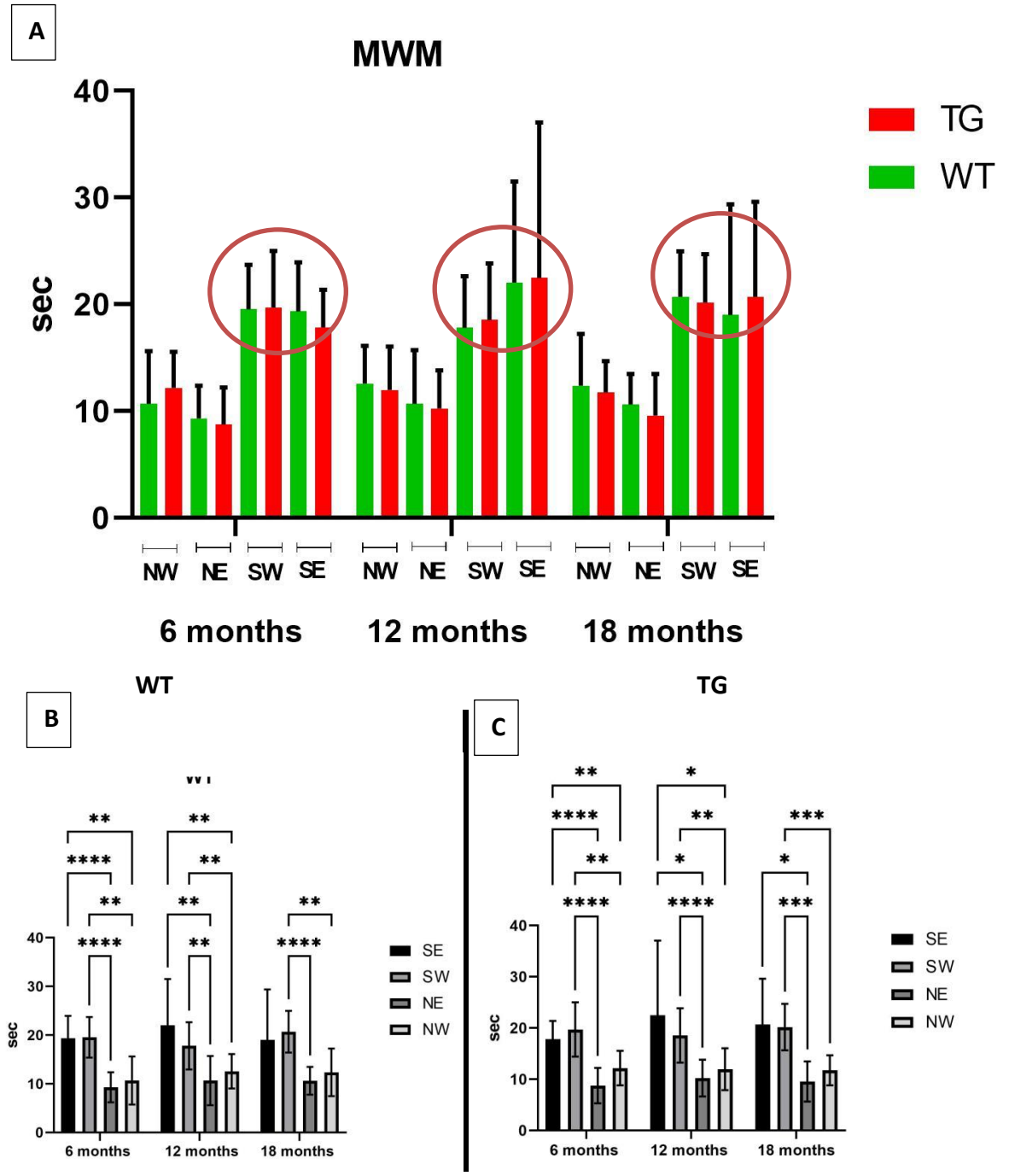

Figure 56: Evaluation of the time spent in each quadrant during the probe test of MWM (A). Graphs B and C show the evaluation of the time spent in each quadrant in WT and TG rats respectively. Data were analysed by using Mixed model and Two-way ANOVA with Sidak post-hoc test. Circles in graph A show the preference of South quadrants in WT and TG rats at each age. *p≤0.05; **p≤0.01; ***p≤0.001 and ****p≤0.0001. The number of rats tested was: n=11 WT, n=12 TG rats at 6 months of age, n=17 WT and n=18 TG at 12 months of age, n= 10 WT and n=10 TG at 18 months of age. Data were expressed as mean±SD.

The analysis of duration during the reversal MWM showed no learning or genotype effects during the training days (Figure 57). The inability to memorise a new platform

position was also confirmed in the probe test of reversal MWM, in which rats did not show a preference for the quadrant in which was placed the platform during the training (NW) (Figure 58).

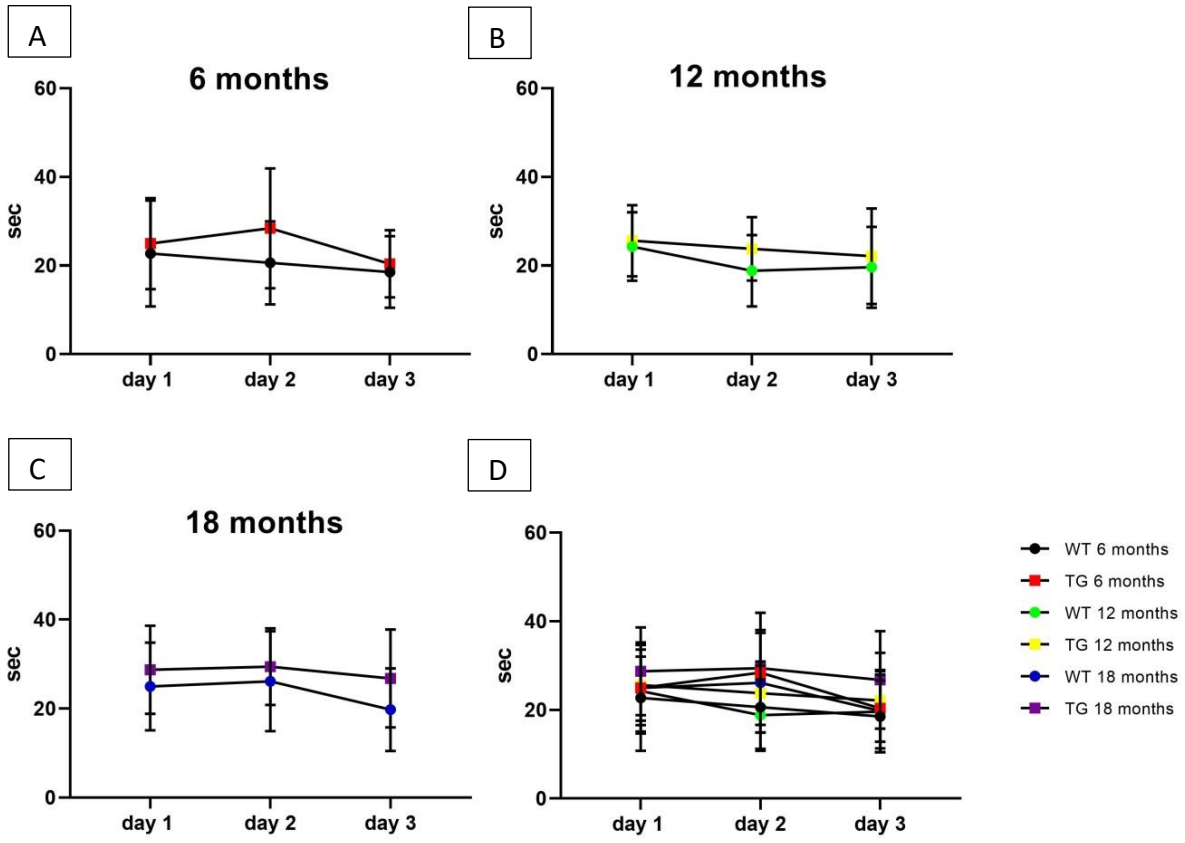

Figure 57: Time spent to find the platform during the training period of reversal MWM. Graphs showed data at 6 (A), 12 (B) and 18 (C) months and n=11 WT, n=12 TG rats at 6 months of age, n=17 WT and n=18 TG at 12 months of age, n= 10 WT and n=10 TG at 18 months of age were tested. Data were analysed by using Two-way ANOVA and Sidak post-hoc test showed any statistical difference between groups. Data were expressed as mean±SD.

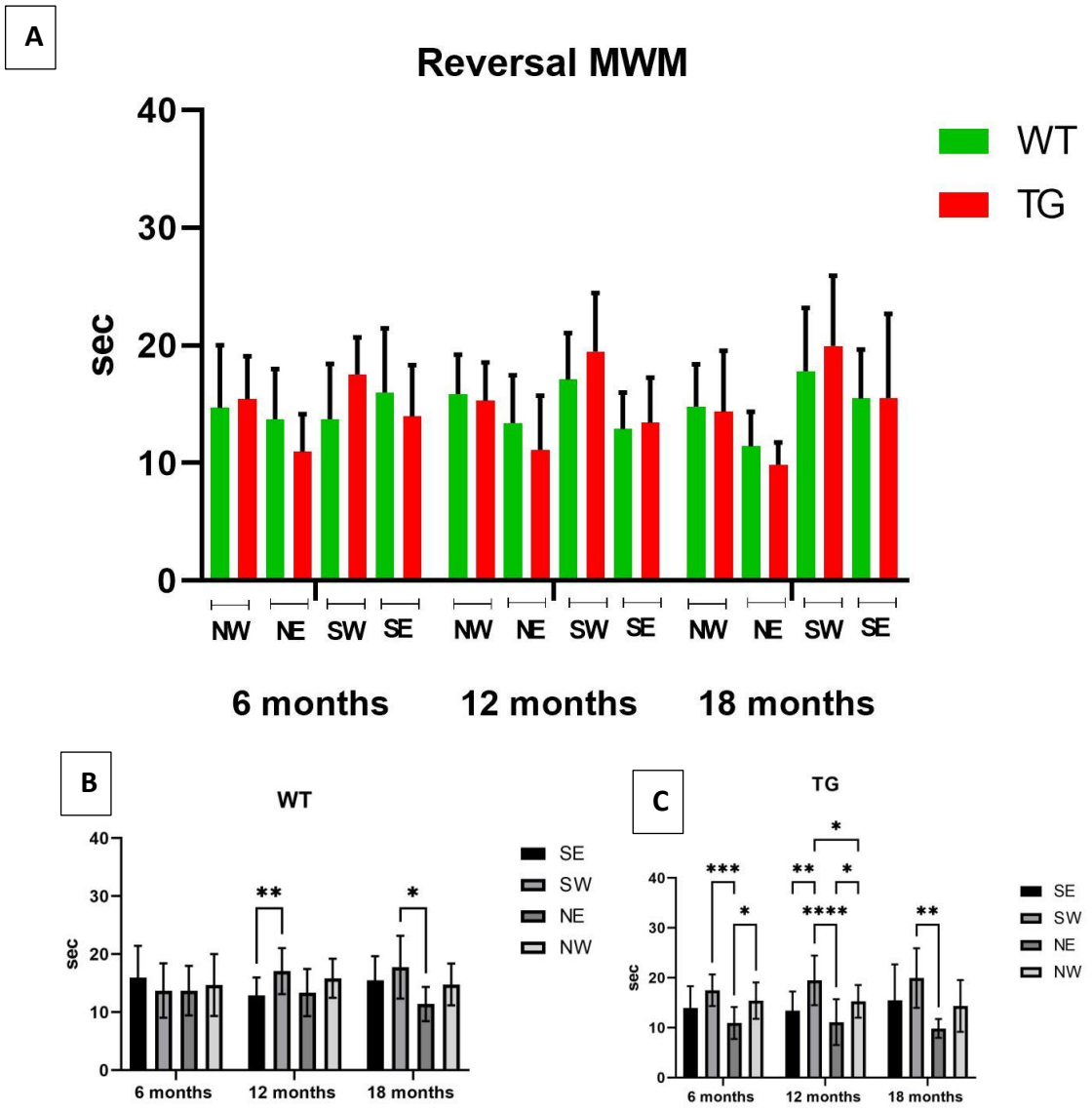

Figure 58: Evaluation of the time spent in each quadrant during the reversal MWM graph A shows all rats together, while B and C showed WT and TG respectively. The analysis showed the inability of rats to remember the new platform position and mainly TG rats tended to spent more time in South quadrant (SW) but no in the old platform position (SE). Data were analysed by using Mixed model, Two-way ANOVA and Sidak post-hoc test. The number of rats tested was: n=11 WT, n=12 TG rats at 6 months of age, n=17 WT and n=18 TG at 12 months of age, n= 10 WT and n=10 TG at 18 months of age. Data were expressed as mean±SD. *p≤0.05; **p≤0.01; ***p≤0.001 and ****p≤0.0001.

Time spent to get closer to the platform area is another parameter used to evaluate how much time a rat has spent before approaching the platform area during the probe test. This parameter can be used to discriminate if a rat appears able to remember the platform position. During the probe test of MWM (Figure 59,A) and reversal MWM (Figure 59,B), rats at each age and genotype spent the same amount of time to get closer the platform.

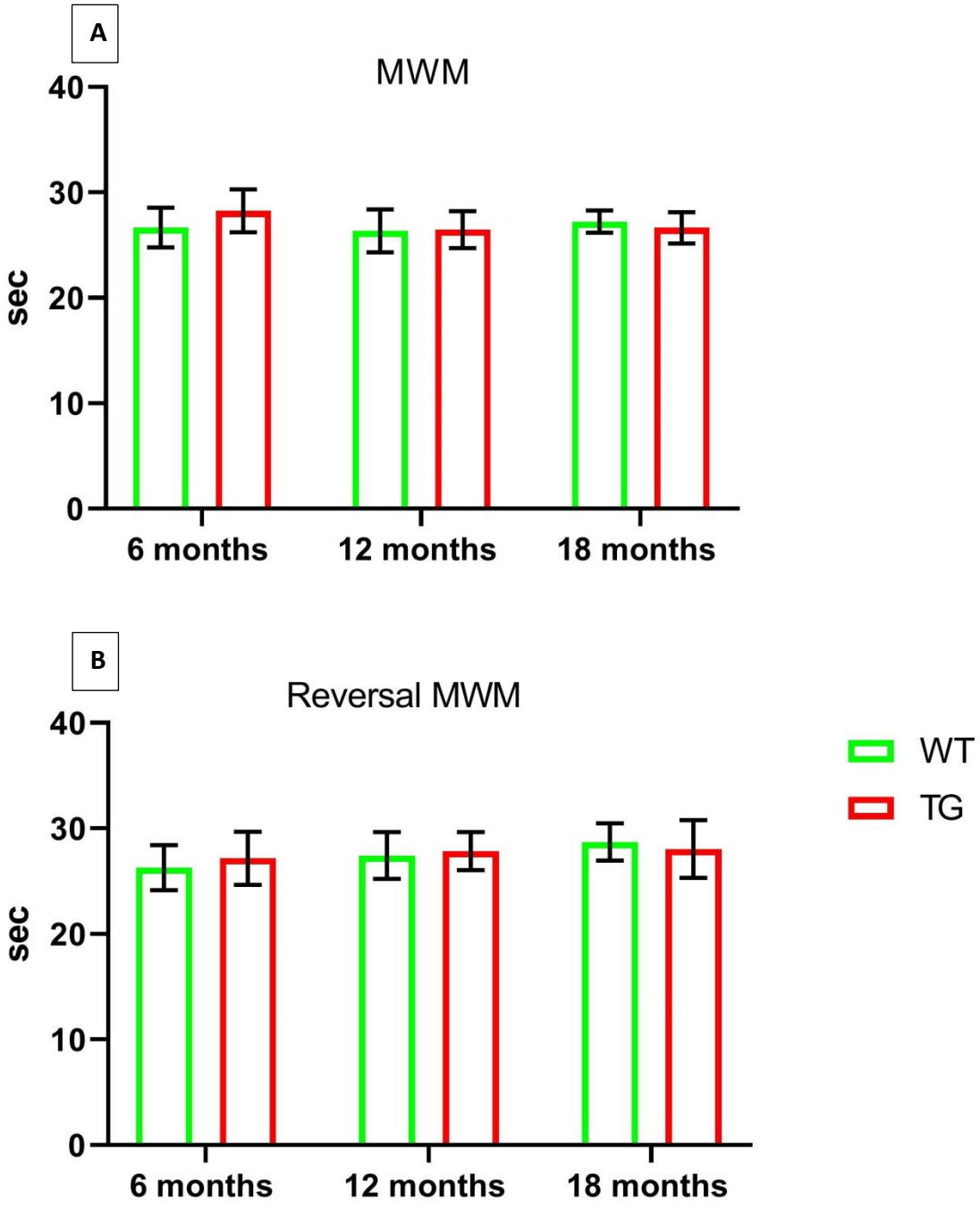

Figure 59: Analysis of the time spent by rats to approach to the platform area during the probe test of MWM (A) and reversal MWM (B). Data tested by Mixed model and Sidak post-hoc test show no difference in both probe tests between age and genotype. N=11 WT and n=12 TG at 6 months of age, n=17 WT and n=18 TG at 12 months of age, n=10 WT and n=10 TG at 18 months of age were used for both tests. Data were expressed as mean±SD.

Path efficiency is an index with values ranging from 0 to 1. The value of 1 means perfect efficiency, meaning the rat is moving in a straight line from the start-point to the endpoint (platform). Values less than 1 and closer to the value 0 correspond to the rat taking

a more complicated pathway to the platform and therefore an inefficient path. To calculate the path efficiency, the straight line between first and last position is divided by the distance travelled.

The analysis of this parameter showed very low values in each group which does not improve with trial number, during the MWM (Figure 60) and the reversal MWM (Figure 61). The very low values indicate that during the acquisition days, rats were not improving their ability to find the platform. These results indicate that "finding the platform" could not be due to a real spatial memory acquisition but to coincidences, such as accidentally touching the platform with the tail.

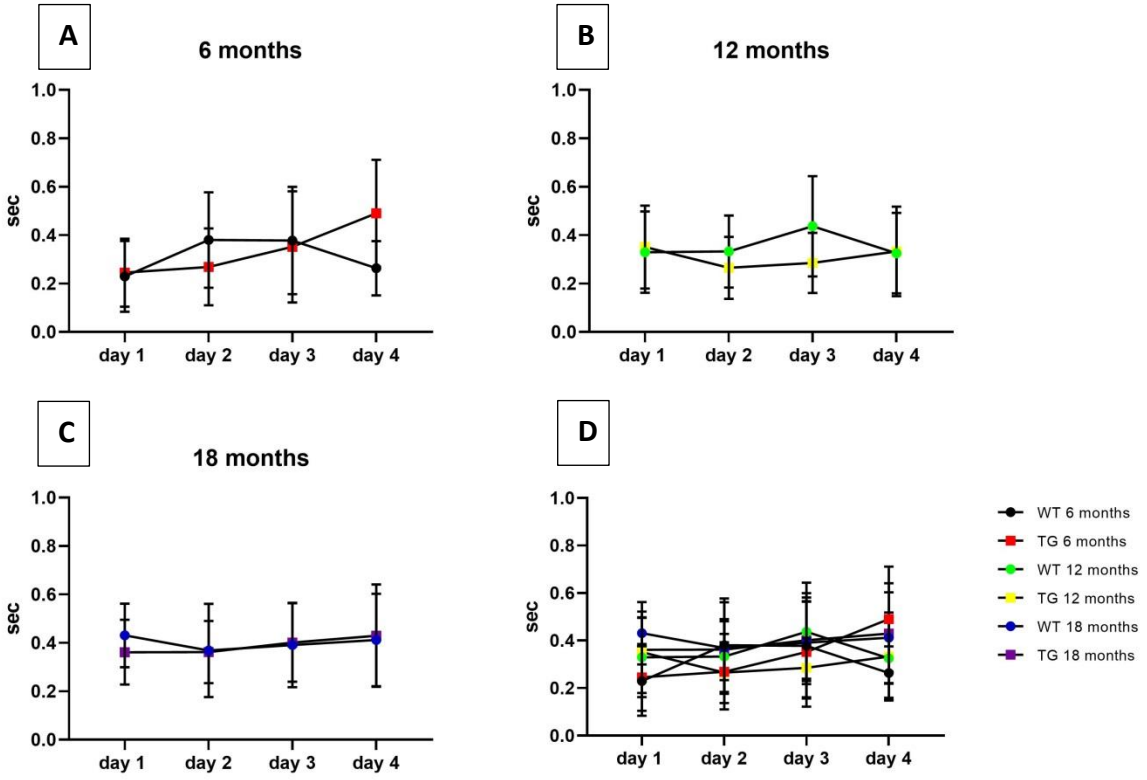

Figure 60: Path efficiency analysed during the MWM at 6 (A), 12 (B) and 18 (C) months of age. The graph D show all age and genotype together. The values of path efficiency were very low highlighting the inability of rats to follow a trajectory as a straight line. Data were analysed by using Two-way ANOVA and Sidak post-hoc test, determining a training effect p=0.0092 in TG rats and a statistically significant increase of values between days 2 and 4 in TG rats (p=0.0307). A genotype effect was found at 6 months day 4 (p=0.0241), with TG performing better than WT. N=11 WT and n=12 TG at 6 months of age, n=17 WT and n=18 TG at 12 months of age, n=10 WT and n=10 TG at 18 months of age were used for the test. Data were expressed as mean±SD.

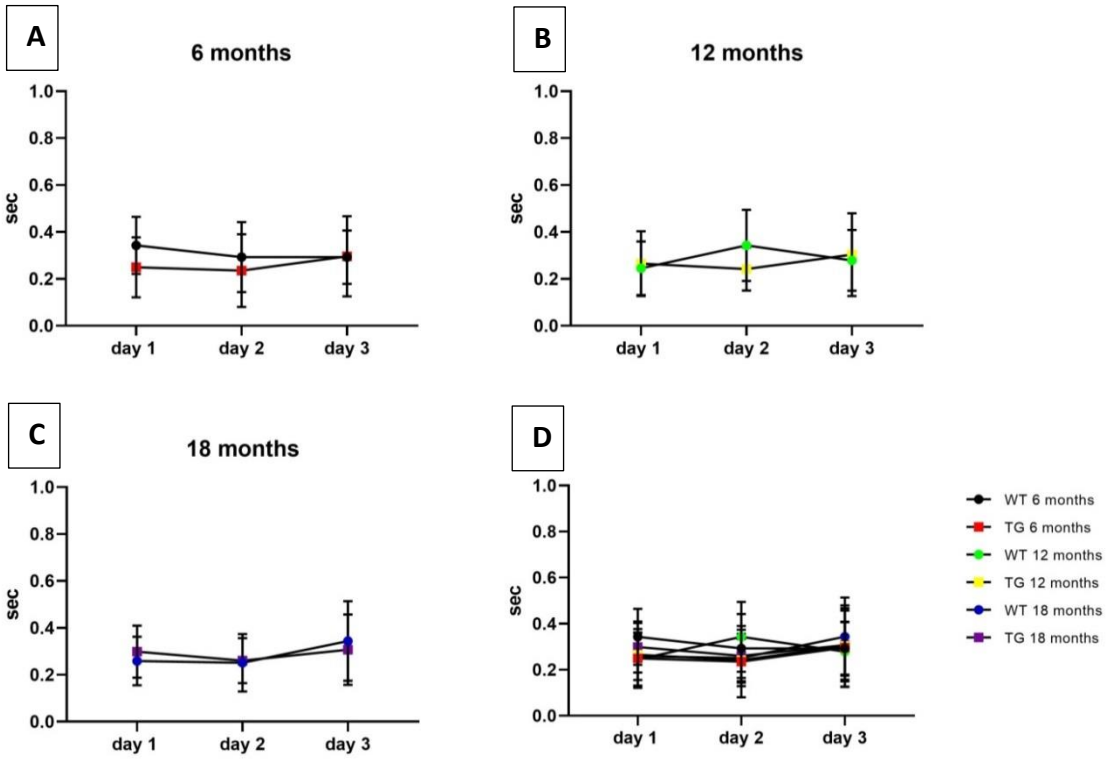

Figure 61: Path efficiency in reversal MWM at 6 (A), 12 (B) and 18 (C) months of age. The graph D show all age and genotype together. Also in reversal MWM rats showed very low values for path efficiency. No statistical differences were found between age or genotype. Data were analysed by using Two-way ANOVA and Sidak post-hoc test. N=11 WT and n=12 TG at 6 months of age, n=17 WT and n=18 TG at 12 months of age, n=10 WT and n=10 TG at 18 months of age were used for the test. Data were expressed as mean±SD.

Other parameters were analysed such as swimming speed during acquisition days (Figure 62, A and B) and probe test (Figure 62, C). The analysis of speed showed an age effect in WT rats ($p \leq 0.0001$), with a decrease of speed from young age to the older age and quite constant values during the training days; the post hoc test showed a statistically differences between 6 and 18 months day 1 values in WT ($p=0.0033$) and an age effect was found also in TG rats ($p=0.0122$) and a statistical differences were found in TG rats only between 6 and 18 months ($p=0.0056$) day 1 and at 12 months TG between days 2 and 4 ($p=0.0077$). During the probe test (Figure 62, C) of the MWM the speed values were similar with no statistical differences between WT and TG or age.

An age effect was found during the reversal MWM in WT rats (Figure 62, D) ($p=0.0062$) and post-hoc test showed a statistically differences on day 2 between 6 and 12 months ($p=0.0253$) and day 3, between 6 and 18 months of age ($p=0.0149$). 6 months WT showed a gradual increase of speed between days 1 and 2 ($p=0.0317$) and between days 1 and 3 ($p=0.0145$) and at 6 months a training effect was determined between both genotypes ($p=0.0052$). Same as in MWM no significant speed differences were found in TG rats (Figure 62,E) and during the probe test (Figure 62,F) in both genotypes and at each age.

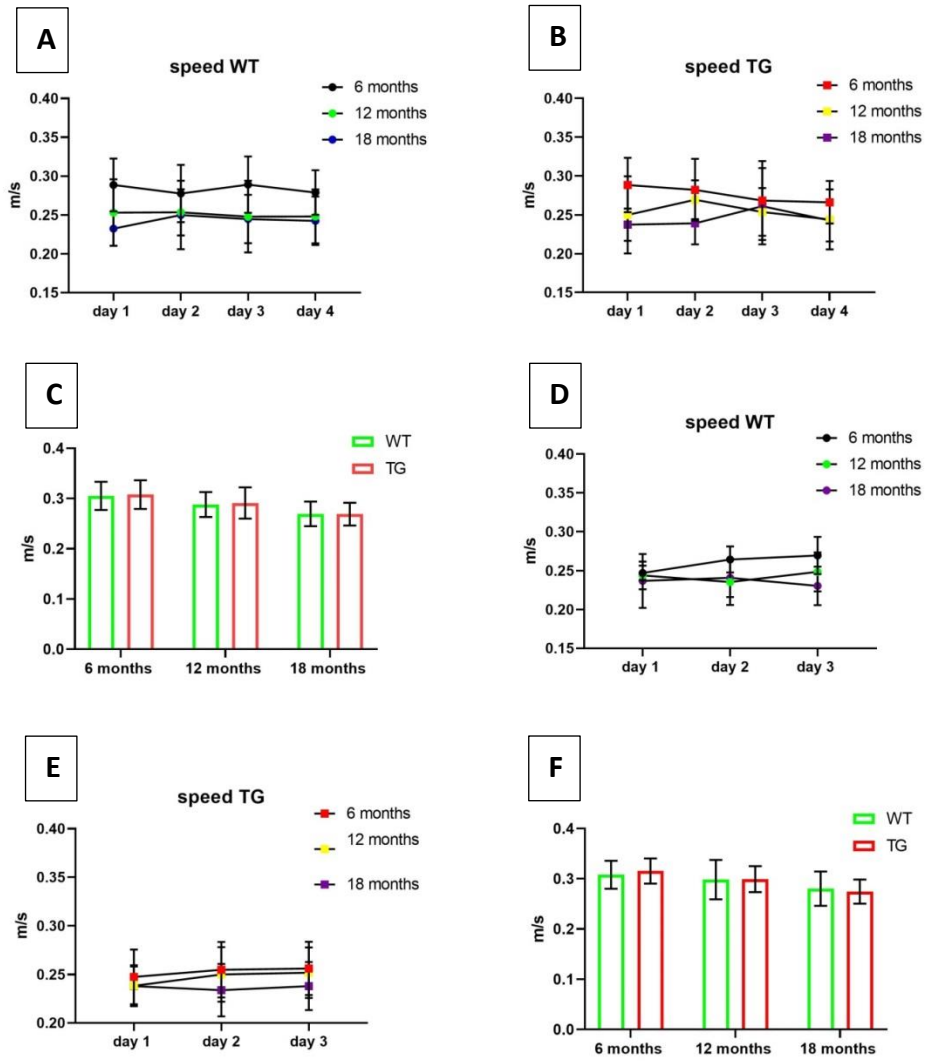

Figure 62: speed analysis during the MWM acquisition (A,B) and probe test (C) and reversal MWM acquisition (D, E) and probe test (F). Data were analysed by using Two-way ANOVA and Mixed model with Sidak post-hoc test. In WT rats the analysis of speed showed an age effect (p≤0.0001) and by using post-hoc test a statistical difference was evaluated on day 1 between 6 and 18 months of age, in which 18 months had lower values (p=0.0033). in TG rats was also determined an age effect (p=0.0122) and a statistical decrease was determined on day 1 between 6 and 18 months of age (p=0.0056). At 12 months of age TG rats had a statistical decrease of speed between day 2 and day 4 (p=0.0077); while the probe test showed similar values between genotypes and age. In reversal MWM an age effect was determined in WT rats (p=0.0062) and on day 2 and 3, 6 months had statistically significant higher values when compared to 12 months (day 2; p=0.0253) and 18 months (day 3; p=0.0149). 6 months WT had a statistically significant difference between days 1 and 2 (p=0.0317) and between days 1 and 3 (p=0.0145) and at 6 months a training effect was determined between both genotypes (p=0.0052). In probe test of RMWM no statistically differences were determined between age or genotype. N=11 WT and n=12 TG at 6 months of age, n=17 WT and n=18 TG at 12 months of age, n=10 WT and n=10 TG at 18 months of age were used for tests. Data were expressed as mean±SD.

The distance travelled by the rats during all test days was also analysed between age and genotype. The analysis revealed a training ($p=0.0357$) and age ($p=0.0059$) effects in WT rats. Specifically a statistical difference in WT rats day 1, between 6 and 18 months of age ($p=0.0034$) and at 6 months between days 1 and 2 ($p=0.0487$) (Figure 63,A). In TG rats the analysis showed learning (training) x age ($p=0.0183$) interaction, training ($p=0.0013$) and age ($p= 0.0058$) effects. A statistical difference was evaluated during the day 1 between 6 and 18 months of age ($p=0.0028$) and at 6 months between days 1 and 4 ($p=0.0093$) (Figure 63,B). For the reversal MWM (Figure 63D,E) and probe tests, no statistical differences were detected between age, days or genotype (Figure 63,C,F).

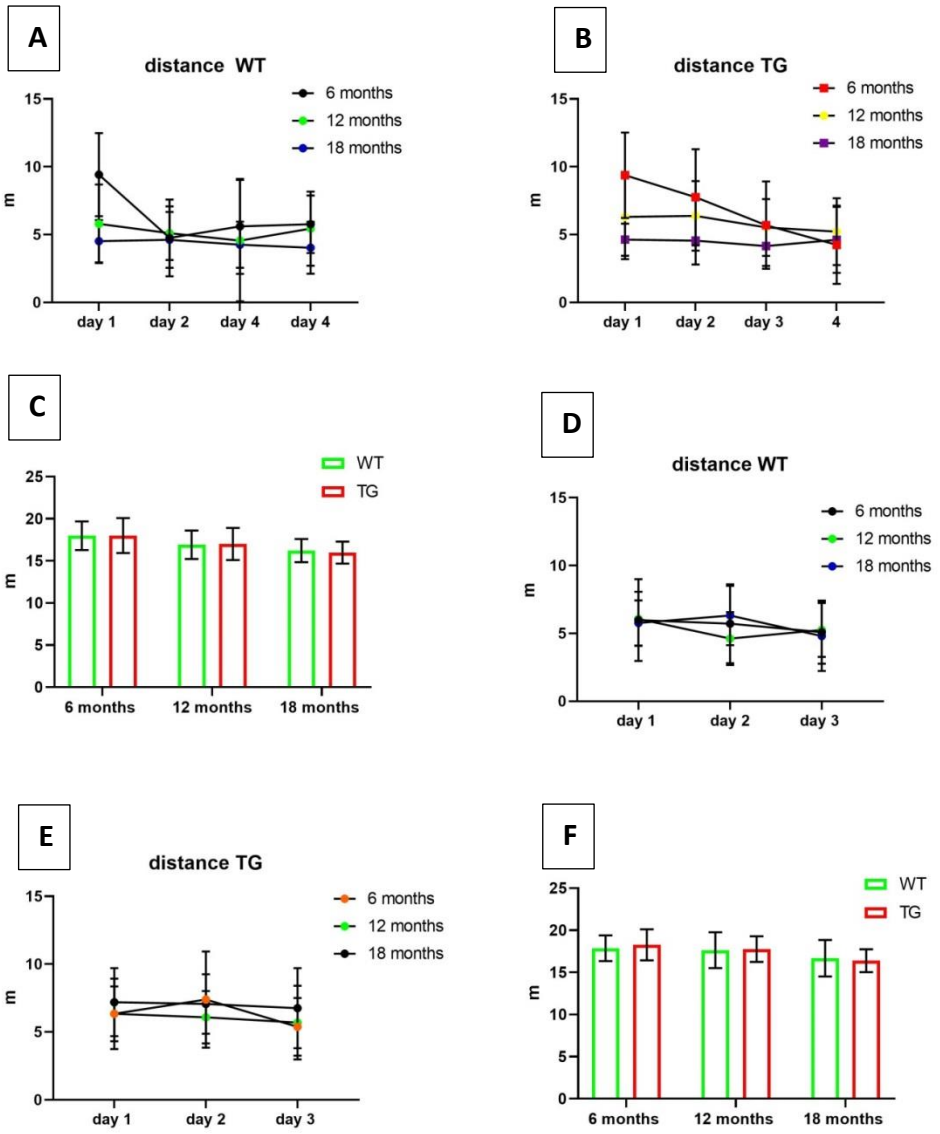

Figure 63: Analysis of distance travelled during MWM acquisition (A, B) and probe test (C) and during the RMWM acquisition (D,E) and probe test (F) in WT and TG rats. Data were analysed by using Two-way ANOVA and the Mixed model, both with Sidak post-hoc test showing a training (p=0.0357) and age (p=0.0059) effects in WT rats. Statistical difference in WT rats was found on day 1, between 6 and 18 months of age (p=0.0034) and at 6 months between days 1 and 2 (p=0.0487) (Figure 63,A). TG rats showed leaning x age (p=0.0183), training (p=0.0013) and age (p= 0.0058) effects. A statistical difference in TG was evaluated during the day 1 between 6 and 18 months of age (p=0.0028) and at 6 months between days 1 and 4 (p=0.0093). In RMWM and in both probe tests the analysis of duration showed no statistically significant differences between age or genotype. The number of rats implemented for all tests was: n=11 WT and n=12 TG at 6 months of age, n=17 WT and n=18 TG at 12 months of age, n=10 WT and n=10 TG at 18 months of age. Data were expressed as mean±SD.

5.2 Open Field

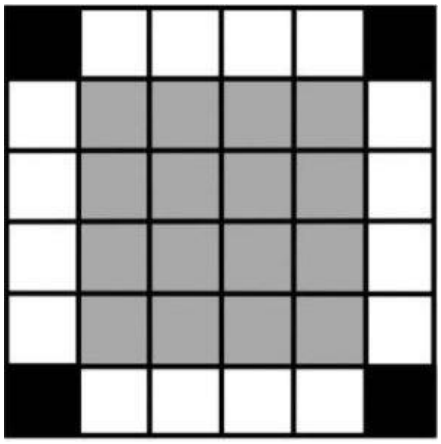

Figure 64: Open field arena. The arena was divided for the analysis in 3 specific parts: corners (black), centre (grey) borders (white). For the analysis corners and borders were took together.

The open field test is used to determine stress and willingness to explore a new environment. A stressed status is determined by less locomotion and by the preference to not explore the arena and stay close to the walls or corners (Figure 64).

As expected based on the MWM performance and the literatures about the Fisher-344 strain, during the test rats spent only few seconds in the exploration of the new environment (Figure 65,A) and were almost all the time immobile (Figure 65,B) and close to the wall (Figure 65,C) the analysis showed no statistically significant differences between WT and TG and also between ages.

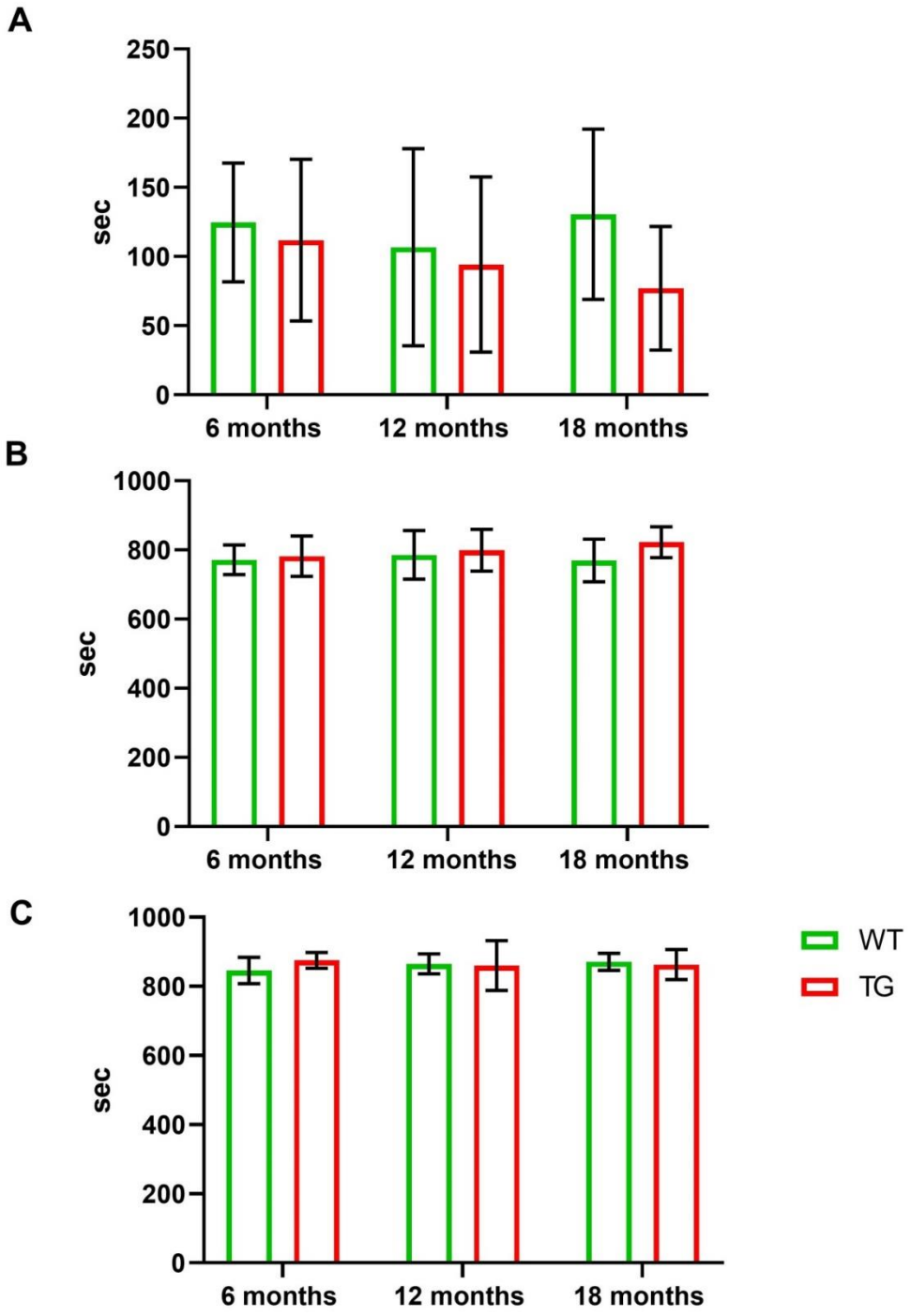

Figure 65: Evaluation of the time spent in exploring a new environment (A), immobile (B) or close to the wall (C) in n=11 WT and n=12 TG at 6 months of age, n=17 WT and n=18 TG at 12 months of age, n=10 WT and n=10 TG at 18 months of age. Data were analysed by using Mixed model effect revealing no statistical differences between groups. Data were expressed as mean±SD.

5.3 Smell tests

Two different smell tests were performed in WT and TG rats at 12 and 18 months of age. During the first test three different fragrances, tested on three separate days, were presented to the rat twice daily with different, but consistent, delay times (30 minutes, 1 hour and 4 hours).

This test is used mainly to evaluate the ability of rats to remember an odour and to see for how long rats are able to remember a specific fragrance. The rat is presented to a fragrance twice for 10 minutes each with an interval between the two presentations of 30 minutes, 60 minutes and 4 hours. Different fragrances were used when were tested different intervals.

Even if the time spent in smelling a fragrance was very low, just few seconds (≤20 seconds), WT rats at 12 and 18 months perform better than TG during the test with a 30 minutes' delay, as the amount of the time spent smelling each fragrance decreased during the second presentation. After a delay of 1 hour and 4 hours, both genotypes did not appear able to memorise the fragrances and the time spent smelling during the second and third days were even lower than the first day (Figure 66).

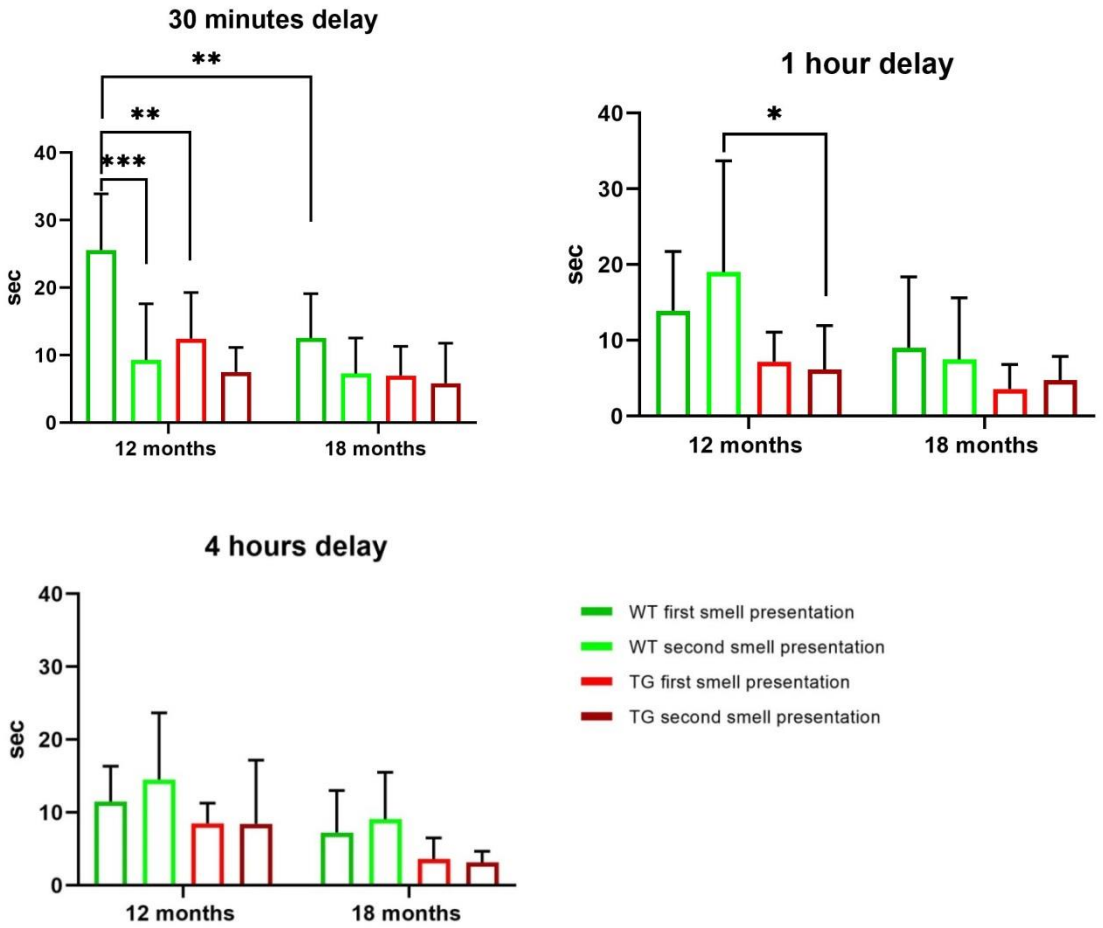

Figure 66: Time spent in smelling during the first and second presentation of an odour at different delay time: 30 minutes (A), 1 hour (B) and 4 hours (C). N=7 WT and n=7 TG at 12 months and n=10 WT and n=10 TG at 18 months were tested and analysed. Data analysed by using Two-way ANOVA and Sidak post-hoc test showed a statistical difference at 12 months between the first and second presentation. During the first presentation at 12 months WT rats showed statistically significant higher values of sniffing when compared to TG. *p≤0.05; **p≤0.01 and ***p≤0.001. Paired t-test at 18 months WT showed a statistically significant differences between the first and second presentation when the two fragrances were presented after an interval of 30 minutes (p=0.0265). Data were expressed as mean±SD.

To better characterise the olfactory ability of these rats, the urine test was performed. In general rats should be able to recognise a predator urine (fox) and therefore they should spend less time in smelling. The analysis showed that over the experimental time (10 minutes) only few seconds were used by rats to perform the test (Figure 67). Two-way ANOVA between each age and genotype showed no statistical differences between WT and TG at 12 months. At 18 months of age TG rats were statistically different in the time spent in smelling fox and rabbit urine when compared to WT. Overall these data showed the inability of rats to recognise the predator, because rats spent more time in smelling fox urine

instead of rabbit urine in almost all groups analysed and the low values of time to smell highlights the low ability of these rats to smell.

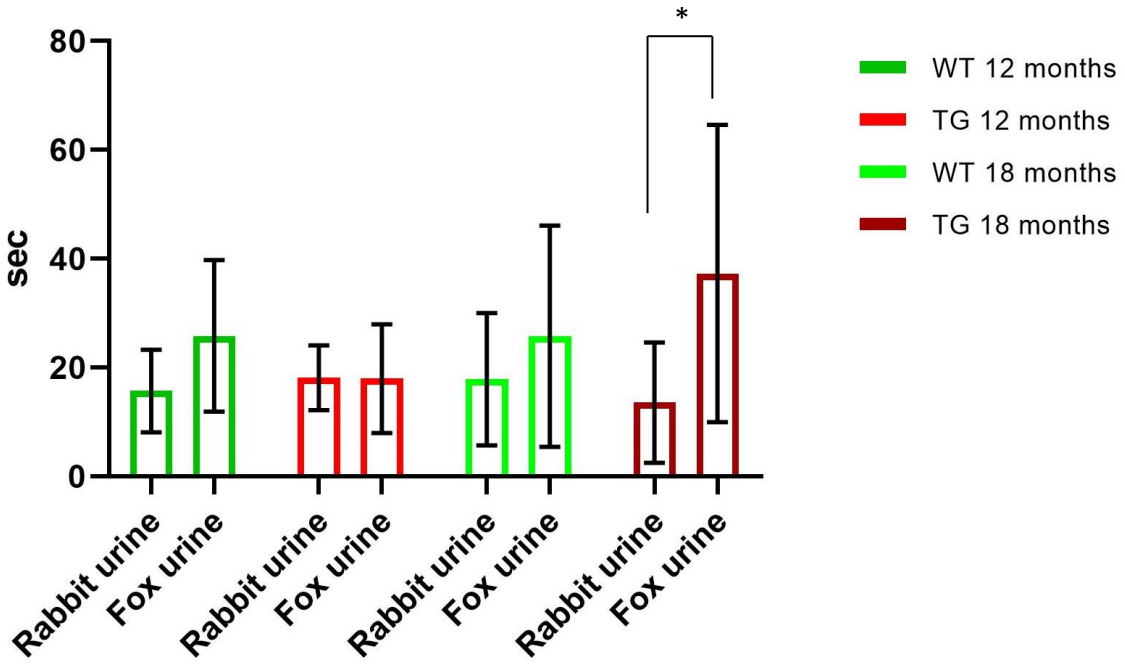

Figure 67: Time spending in smelling two different odour simultaneously, fox and rabbit urine. Data analysed by using Two-way ANOVA and Sidak post-hoc test showed a statistical difference at 18 months TG (p=0.0210) between fox and rabbit urine. The time smelling the fox urine between 12 and 18 months was statistically different (p=0.0287). N=7 WT and n=9 TG at 12 months; n=10 WT and n=10 TG at 18 months were used for the test. Data were expressed as mean±SD.

6 Ex-vivo analysis

6.1 Immunohistochemistry (IHC)

Despite the Fischer-344 strain being a difficult strain to assess by behavioural tests, the alterations in AD-like pathophysiology do bear a similarity to the human AD. For example, deposition of amyloid and increase of neuroinflammation had been already showed in other studies [243] but I also assessed this parameters in the rats used in these studies.

IHC analysis showed a progressive increase of amyloid deposition from a modest Aβ load at 6 months of age to a severe Aβ load at 12 and even more at 18 months of age. In parallel, a progressive increase of neuroinflammation by GFAP (astrocytes) staining was detected (Figure 68).

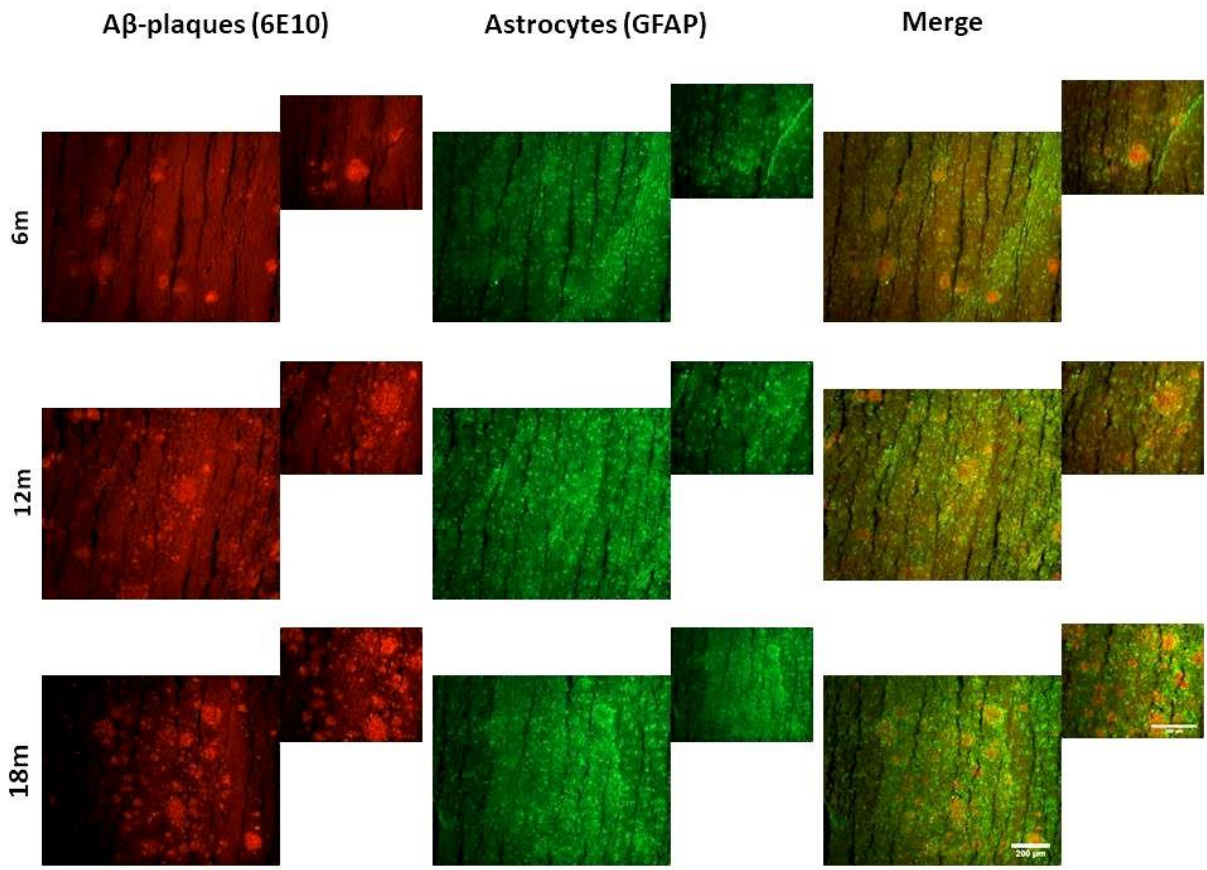

Figure 68: IHC fluorescent staining of amyloid deposition (red) and neuroinflammation (green) detected by the antibodies 6E10 and GFAP respectively in transgenic rat at 6, 12, and 18 months of age. All images have been taken by using a magnification 10X and 20X.

One of the aims of this project was to test an alteration by *ex-vivo* measurements, of different factors involved in the attenuation of PS. The proteins tested were the factor eIF2α and its phosphorylation, phosphor-eIF2α that regulates the PS during stress condition, along with the protein ATF4 which is a memory repressor (see §1.5.1) with the role to block the expression of genes required for memory formation. The IHC, either using fluorescence or DAB staining showed a high degree of background that led at the inability to discriminate between background and specific stains. Different protocols were tested to optimise to and quantify better signals but due to time restrictions of the PhD, these optimised protocols were not completed, and the analysis by IHC will be probably conducted by Herve Boutin's laboratory.

6.2 Western Blot

Another *ex-vivo* measurement tested was the Western Blot (WB). For WB, dissected brain regions (hippocampus, striatum, cortex, cerebellum and the remain) were tested for the factors eIF2α, its phosphorylated form phospho-eIF2α and ATF4. More related to the synaptic density study, PSD95 and SNAP25 were also tested. To optimise protocols, 0.1 and 0.2 mg/ml of sample proteins were incubated with different primary antibody dilution. The right dilution of antibodies was determined: Phosphor-eIF2α, 1:200; ATF4, 1:200; PSD95, 1:200 and SNAP25, 1:200. Even though many protocols were tested it was not possible to determine a specific protein concentration and primary antibody dilution for eIF2α.

For WB analysis it is essential to use a housekeeping protein. The signal from housekeeping protein is used to normalise the signals from the proteins of interest. The housekeeping protein should be stable among the samples and have a different molecular weight from the protein of interest. The proteins used are constitutively expressed and necessary for basic cell functions such as β-actin.

For ATF4 and phosphor-eIF2α, β-actin was not suitable to use due to the similar molecular weight of both proteins, whereas the two proteins PSD95 and SNAP25 had different molecular weights. Before quantifying the proteins of interest, the expression of β-actin was tested. Few experiments in WT and TG rats at 18 months, hippocampus and cerebellum, revealed changes in the expression of β-actin >10% in WT and TG, tested at 18 months in cerebellum and hippocampus. To better understand if the variability was due to the sensibility of the WES instrument, it was planned and started an analysis by using the standard Western Blot and the testing of new housekeeping genes but due to the time still

available in my PhD, I could not complete this part of the study and probably the study will be pursuit in future in our laboratory.

7 Discussion

7.1 [^{11}C]leucine PET

Plasticity and consolidation of memory in the central nervous system (CNS), are regulated by many processes that promote the reorganisation of structures at synaptic level and synthesis of new proteins is an essential mechanism of learning and memory [179, 314].

Learned information are stored and consolidated into the brain through the *de novo* synthesis of proteins. Therefore the balance of synthesis and degradation of proteins are essential to guarantee the memory stabilisation [315]. Several proteins undergo folding, maturation, quality control and degradation in the endoplasmic reticulum (ER) [316]. Alteration of cellular homeostasis due to extrinsic or intrinsic factors such as disease-related mutant proteins, high secretory demands, loss of calcium homeostasis, altered lipid homeostasis, viral infection, changing of energy level and other insults can induce an alteration of proteostasis in ER. The unfolded proteins response (UPR) pathways are activated by the ER with the objective to re-store the cellular homeostasis (see §1.5.1). The activation of UPR can induce gene expression to regulate the protein synthesis and attenuate the protein synthesis but during prolonged stress condition, the apoptosis processes can also be activated (see §1.6) [317]. ER stress and the consequent activation of UPR pathways are implicated in various pathological condition such as neurodegeneration, heart disease, diabetes, and cancer [318]. In Alzheimer's disease the activation of UPR and ER stress are thought to happen in the early stage of the disease and the different studies have already shown these activations during the development of AD [319] (see §1.7) .

To study the protein synthesis *in-vivo*, different amino acids were used and tested [287, 320, 321]. In general, the most suitable amino acids to study the protein synthesis are labelled at the carboxyl groups, because the labelling in this position results in very low production of radiolabelled metabolites and therefore an easiest quantification of PET images [285]. Moreover, an amino acid to be used as a PET tracer to measure protein synthesis rate (PSR) needs to have a high brain uptake and from the study of Oldendorf *et al.*, the L-phenyl- alanine, L-leucine, L-tyrosine and L-methionine have the highest brain

uptake [287]. An important parameter to be considered to choose an amino acid for the measurement of PSR is its metabolism, having the simplest as possible metabolism in brain allows accurate modelling and quantification. The ideal amino acid should only be incorporated into proteins and not be involved in other complex catabolic pathways. Comparing leucine with phenylalanine, tyrosine and methionine, leucine is the only amino acid used exclusively for protein incorporation, the others have more complicated pathways in brain. These alternative pathways could lead to a lower ability of the tracer to measure PSR even if for some amino acids, such as tyrosine, the amount of metabolites is very low [294, 320, 321].

The aims of this study were to:

1. Identify the best approach to study PSR *in-vivo* in rats using [^{11}C]leucine PET;
2. Measure longitudinally potential changes in PSR in TgF344-AD rats, an animal model of AD;
3. Compare the results obtained in rats with a human study which started contemporarily of my PhD.

For the set of studies included in this thesis, two different rat strains were used: Wistar and Fischer-344 (WT and TG). The Wistar rats for the modelling and refine the methodology to study PSR and the Fischer-344 (WT and TG) to evaluate the alteration of protein synthesis in Alzheimer's disease.

To validate the use of [^{11}C]leucine as a PET tracer to measure the PSR *in-vivo*, three Wistar rats were injected with anisomycin, a protein synthesis inhibitor, at a dose of 60mg/kg 10 minutes before the PET scan. This dose was established based on a rat study in which the incorporation of 5-[H^3]lysine was evaluated by using 30, 60 and 120 mg/kg of anisomycin [322]. This study showed that the inhibition was dose dependent and no toxic side effects were observed. The dose of 60 mg/kg was able to induce an inhibition of PS of 80% [322]. Our results are consistent with the published data, where we found that injection of anisomycin provoked inhibition of [^{11}C]leucine uptake and PSR by ~86% (PSR hippocampus with anisomycin 0.81±0.13nmol/ml/min and PSR without anisomycin 5.25±1.67nmol/ml/min in all brain regions analysed (Figure 40)). These results confirm the ability of [^{11}C]leucine to measure protein synthesis *in-vivo* in rodents.

The [^{11}C]leucine study using WT and TG rats was conducted at three time points: 6, 12 and 18 months of age. These three stages represent the initial phase of AD-like pathology to the more advanced stage. For example, between 6 and 12m brain alterations start with a progressive increase in Aβ deposition and development of neuroinflammation, whereas by 18m these animals demonstrate a more advanced form of AD in which the accumulation of Aβ is very elevated in all brain regions, together with phospho-Tau deposition and strong increase in astrocytosis, microglyosis and neuronal loss. The study in WT and TG was planned to be longitudinal, with the objective to use the same rat at each time point, hence increasing the power of the statistical analysis while reducing the number of rats for the experiments. Since the determination of Arterial Input function (AIF) was a terminal procedure based on the cannulation of femoral artery and vein (see §3.3), it was subsequently decided to use Wistar rats for the determination of the AIF and the validation of a population-based IF to implement for the longitudinal study.

The first evaluation of PSR in WT and TG was conducted by using a semi-quantitative method, the analysis of SUV. This analysis showed a statistical difference only at 12 months of age between genotypes, WT and TG and with a gradual increase due to the age, data opposite to the original hypothesis (Figure 33; Figure 34).

As described in other publications [293, 323] using [^{11}C]leucine to measure PSR in brain, quantification of the PET image is deemed the best approach with full kinetic analysis using a plasma input function compartmental model. This is because the SUV does not take into account the physiological processes, bio-distribution and pharmacokinetics of the tracer in plasma and brain. Leucine in brain is used for protein synthesis and the metabolism of the carboxyl-group produce α-ketoglutarate (α-KIC) which is converted into CO_2 through a decarboxylation reaction; labelled CO_2, products derived by CO_2 fixation and α-KIC are very low in brain [293].

Based on the leucine metabolism in the brain, the compartmental model used for leucine uptake is generally a 3K (rate constants) compartmental model, in which there is no distinction between intra and extra-cellular space, and metabolites were not accounted because are considered negligible [293, 297]; indeed $^{11}CO_2$ fixation and the amount of $^{11}CO_2$ in brain are low and at equilibrium with blood, therefore the contribution of $^{11}CO_2$ was not

measured. In the estimation of PSR with leucine, the endogenous fraction of leucine deriving from the recycling of proteins was also taken into account through the introduction of the factor λ (see §1.11.1), and a full PSR quantification requires also the measurement of unlabelled leucine in plasma (leucine [C]).

$$\boldsymbol{PSR = K_{cplx} \times \frac{leucine\ [C]}{\lambda}}$$

To determine the concentration of unlabelled leucine in plasma, blood samples were taken in Wistar rats from femoral artery and in WT and TG rats from femoral artery and/or tail vein. The comparison of arterial and venous blood measurements in WT and TG showed a significant difference in the concentration of unlabelled leucine between arterial and venous blood. These data were the opposite to the human results reported by Tomasi *et al.* [324]. Indeed in human, the values of unlabelled leucine between arterial and venous blood samples were similar. The differences found in rats between arterial and venous samples could be due to the fact that we used the same site for the tracer injection and venous samples withdrawn (tail vein), in which phenomena of extravasation can happens leading an alteration of the tracer clearance [325]. Based on the difference between arterial and venous unlabelled leucine concentration, the concentration of unlabelled leucine in arterial plasma was compared in Wistar and Fischer-344 WT and TG. This analysis showed a statistical difference of unlabelled leucine between the two different strains but not between genotypes (Figure 35). Not only leucine but also the concentration of the other unlabelled large neutral amino acids was found statistically different between strains but not between WT and TG (Figure 35). In my study, the concentrations of unlabelled leucine in arterial plasma averaged between WT and TG were 226.83±20.19 n.mole/ml, comparing the values obtained we found differences with other strains and animal. Indeed, the concentration of unlabelled leucine was reported to be 154±9 n.mole/ml in Sprague Dawley rats [326], 184.6±59.4 n.mole/ml in monkeys [327], and around 110 n.mole/ml in humans [289, 327, 328]. In Sundaram *et al.* [297], the values of unlabelled leucine in humans were much lower when compared to the other human studies, because the measurements were conducted after infusion of glucose, a procedure designed to lower the concentration of circulating amino acids to increase the brain uptake of [^{11}C]leucine [297]. Indeed studies demonstrate that the infusion of glucose and exogenous insulin increased the large neutral

amino acids uptake in brain [329]. These data indicate that the concentration of unlabelled leucine changes between animal species and therefore for an accurate measure of PSR, it is essential to conduct the analysis of cold leucine in each group of the study.

As a result of my studies, since the comparisons between Wistar, WT and TG rats revealed differences between the strains in terms of the concentration of unlabelled leucine, Wistar rats were not used to determine the population-based or image-derived IF applied in the longitudinal study in WT and TG rats (Figure 69).

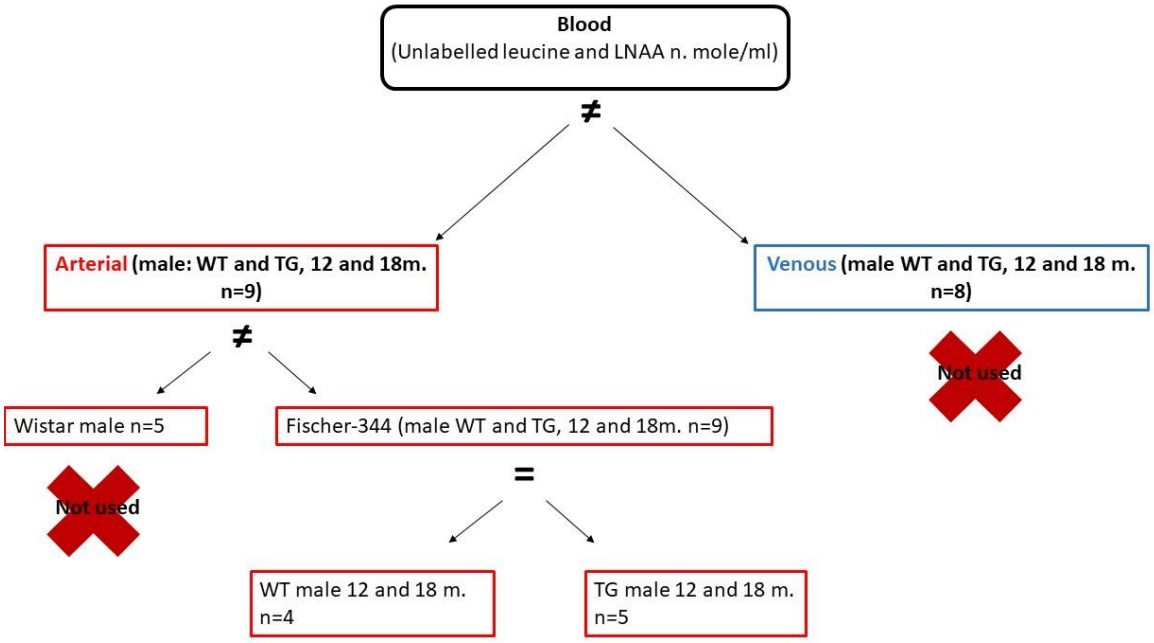

Figure 69: Summary of the blood data decision tree. Analysis of unlabelled leucine and LNAA in plasma showed significantly different values between venous and arterial blood samples in WT and TG rats. Therefore, it was established that venous blood was not a reliable proxy of arterial plasma values for the calculation of PSR. The arterial blood values were also different between Wistar and Fischer-344 but not between WT and TG. Therefore, it was decided to pool together the values of WT and TG for the estimation of PSR.

For the modelling of PSR using [^{11}C]leucine, it was necessary to determine an Input Function (IF) that represents the availability of free radiotracer in arterial plasma. To determine the arterial input function (AIF), it is essential to know the concentration of radiotracer in plasma, because only the radiotracer in plasma is available to tissue extraction. The evaluation of the free fraction in plasma can be obtained through protein precipitation. This analysis is based on the use of arterial plasma and in our pre-clinical study

required the implementation of an arterial-venous shunt which is unfortunately a terminal procedure. This evaluation was conducted initially in Wistar rats and then, considering the blood results mentioned above which prevented the use of venous or Wistar data, it was also performed in a subset of Fischer-344, WT and TG.

Blood samples were tested by using different perchloric acids concentration although people classically use 5% PCA, there is no or little evidence what is the best percentage to use [327]. The analysis in Fischer-344 (4 WT and 5 TG) was carried out by using 70% perchloric acid (PCA) while in Wistar, some rats had the evaluation with 5% PCA and others with 70% PCA or with both. The estimation of free labelled leucine with both concentrations of PCA showed similar values between 2 minutes until 20 minutes after injection, but from 30 minutes until the end of scan, the values differed significantly. The amount of free [^{11}C]leucine increased with higher concentration of perchloric acid (see §4.1.3; Figure 36) with the concentrations of free [^{11}C]leucine in 5% PCA (plasma/PCA v/v, 2.5% final concentration) being 42%, 62% and 74% lower than with 70% PCA (plasma/PCA v/v, 35% final concentration of PCA) at 30, 40 and 60 minutes, respectively. The blood measurements analysis in Wistar rats with 70% and 5% PCA were used to determine a mathematical function, through a calibration experiment, with the aim to convert the 70% values into 5% at each time point (see §4.1.3; Figure 37).

To precipitate proteins, there are different methods such as acid, salt or alcohol. The acidic precipitation is characterised by changing the pH of the solution which causes the proteins to become denatured, changing their conformational, hence inducing protein precipitation. Centrifugation is then used to create a supernatant containing free AA. The most used acids for protein precipitation are the perchloric acid (PCA) and the trichloroacetic acid (TCA). There are only few studies describing the effect of acids concentration on protein precipitation. For example, Rajalingam *et al*. 2009 studied the different TCA concentrations from 0 (no acid) to 90% (w/v) on four proteins: lysozyme, acidic fibroblast growth factor (aFGF), carbonic anhydrase, and bovine serum albumin. The amount of precipitated proteins was evaluated after centrifugation by SDS-PAGE gel for the precipitated proteins (pellet) and by absorptiometry at 280nm for the free AA (supernatant). The analysis showed that increased acid concentration promotes a gradual increase in precipitated proteins until reaching a plateau between 5% and 45% w/v, above 45% the amount of proteins

precipitated decreases; in parallel, the analysis of supernatant showed, as expected, that the amount of un-precipitated proteins increases with acid concentration with acid concentration above 45% w/v [330]. Based on these results, the authors determined that the best range for the maximum precipitation was at 5% w/v in which a plateau was reached [330]. TCA and PCA are both acids and despite that the protein precipitation should be similar, there are no studies showing the effect of different PCA concentration on proteins precipitation. To better understand the results obtained in my study with 70% and 5% PCA, the evaluation of [^{11}C]leucine free in plasma could be measured by radio-HPLC. The main limitation in using this procedure is the short half-life of [^{11}C] (20 minutes) and the need of high volume of plasma to circumvent this problem. This analysis could lead to the specific determination of [^{11}C]leucine free fraction and proteins when different acids concentrations are used and therefore determine which is the best procedure for an accurate quantification.

As previously discussed, the absolute quantification of PET images requires the measurement of the AIF. The measurement of the blood radioactivity concentration can be obtained from samples withdrawn through a catheter from the femoral artery, or can be derived on a quantitative dynamic PET image, if a large artery or the left ventricle heart cavity is in the field of view (i.e. to generate an image-derived blood curve). When an image-derived blood curve is used, blood samples can also be used to scale and correct some bias due to partial volume effect (Figure 70).

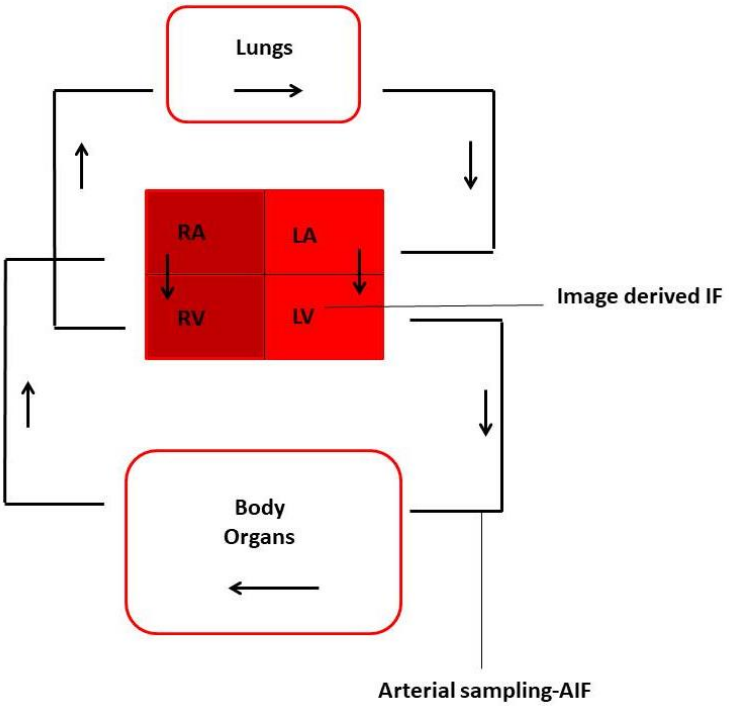

Figure 70: Scheme describing the blood circulation in mammals. The Input Function (IF) describes the quantity of radioactivity in arterial plasma during the time. For the AIF blood samples are taken from an artery and in rat the femoral artery was used. The Image derived Input function (IDIF) do not require blood samples to be taken but the estimation of radioactivity can be reached by drawing a ROI over the left ventricle of the heart.

The initial aim of this project was to use the AIF coming from Wistar rats and define a population-based input function; then use the population-based IF to scale and fit the image-derived input function for WT and TG rats, in which no blood measurements were planned to be taken. Due to the strain differences of unlabelled leucine values in arterial plasma described above, some Fischer-344 rats, 4 WT and 5 TG, were added to the study and were scanned with blood sampling to determine the AIF.

To validate and scale the individual heart TAC to the blood measurements by γ-counting, we determined a time-point at which the radioactivity concentrations in both measurements were almost equal. For each rat, a ratio between the individual Heart TAC and the averaged AIF at that specific time-point was calculated. This ratio was then applied to scale the population based IF to the individual image-derived IF. The new scaled IF, calculated for each rat, was used in a Matlab-based software for PET kinetic analysis (MICK), to determine the macro parameters K_{cplx} (net uptake rate constant) and λ, and all rate constants K_1, K_2 and K_3 that were used to describe the kinetic of [^{11}C]leucine in brain.

This kinetic model for PSR measurements with [^{11}C]leucine is based on the assumption that the levels of [^{11}C]CO_2 in brain are negligible and in equilibrium with those in blood, therefore the contribution of this metabolite was not taken into account as described by Bishu *et al.* [289]. Most papers using [^{11}C]leucine measured level of [^{11}C]CO_2 in blood by a γ-counter to estimate the time course of [^{11}C]CO_2 concentrations in brain; in that case, K_{cplx} and λ were not calculated by using 3K (rate constants) modelling as we did, but using a 4K model. The additional rate constant k_4 describes the first step of leucine catabolism into [^{11}C]CO_2 [289].

In the studies reported in this thesis, a first evaluation of the PSR was performed in rats which had individual AIF and individual blood measurements of unlabelled leucine. In this initial analysis, despite the low number of rats per group a difference in PSR was found at 18 months of age between WT and TG, in 4 brain regions analysed: hippocampus, temporal cortex, somatosensory cortex and cerebellum (Figure 39). WT rats, showed also an increase in PSR with age, in hippocampus, cerebellum, somatosensory and temporal cortex as an aging effect and this process could be disrupted in TG rats due to neuronal dysfunction. The calculation of PSR and K_{cplx} was also done for the longitudinal study using the scaled population-based IF and different brain regions were analysed: temporal cortex, hippocampus, cerebellum, somatosensory cortex, frontal cortex, *thalamus*, cingulate cortex, *caudate putamen*, *globus pallidus* and whole brain. The analysis showed a genotype effect for K_{cplx} in hippocampus, *caudate putamen*, whole brain and *globus pallidus*; but this difference was not big enough to be significant in the post-hoc analysis (Figure 44). Also, in the measurement of PSR, no significant differences were found between age or genotype (Figure 45). The only brain region showing a significant decrease in PSR and K_{cplx} in TG vs. WT at 18 months was the *globus pallidus* (Figure 46). The ROI for the *globus pallidus* is immediately adjacent and include large parts of the *nucleus basalis* of Meynert (NBM), which is the main source of cholinergic innervation of the cerebral cortex and the most vulnerable brain region in Alzheimer's disease [331]. Considering the small size of the NBM, one could hypothesize that the decrease in PSR and K_{cplx} in the *globus pallidus* could be due to changes in the NBM rather than in the *globus pallidus;* due to the relative low resolution of PET it is impossible to discriminate between these brain structures. This data are in good agreement with a study from Tours in collaboration with our laboratory (manuscript in

revision in *Theranostics*), where an increase in α7nAChR was found in in the *globus pallidus* of WT rats with age, which did not occur in TG (Figure 71). The increase in α7 nicotinic acetylcholine receptor in various brain regions was also found in human according to the age [332]. The increase in nicotinic receptor in WT rats with age could be a physiological change to compensate aging effect in WT and not occurring in TG rats, leading to an apparent decrease in α7nAChR in late AD, which has been previously reported [333].

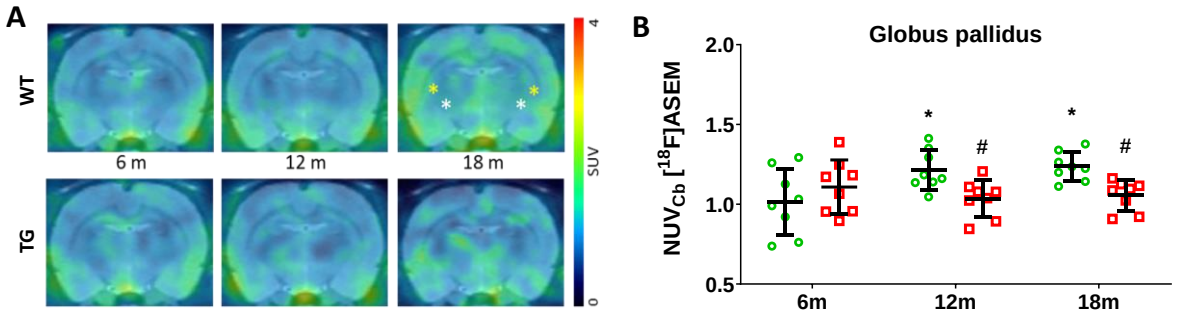

Figure 71: PET images at 6, 12 and 18 months of age of WT and TG rats (sum 49-61 min of [^{18}F]ASEM α7 nicotinic receptor) (A). Yellow stars indicate the striatum and white stars the *glubus pallidus*. (B) Quantification [^{18}F]ASEM uptake in *globus pallidus*. Chaney *et al.* unpublished data.

To summarise, because the PSR values obtained with individual measurements of AIF and unlabelled leucine showed some significant differences at 18 months between genotypes and between age in WT rats, that were lost when using the averaged and scaled population-based input function and averaged values of unlabelled leucine, we can conclude that averaging these input values in the model had likely reduced group differences between age and genotype. We can therefore further surmise that the best approach to measure PSR by using [^{11}C]leucine is via the use of individual IF and plasma values. However, in pre-clinical studies this means using arterial cannulation in each animal for each scan, which is not compatible with longitudinal studies as it is a terminal procedure. Therefore, this also means that cross-sectional studies maybe a preferred method to longitudinal studies in order to better compare the level of measurement accuracy with the statistical gain of repeated measures.

In brain as a whole, the PSR values in human [289] and monkeys [323] are lower (-62% and -44% respectively) than in WT and TG rats. The comparison of PSR with Sprague-Dawley rats also showed a difference when compared to the values obtained in my studies.

Indeed, Sprague-Dawley rats showed higher PSR in all brain regions analysed by Sun *et al.* [326], although this was measured at a much younger age (from 7 days to 60 days post-natal). However, the PSR in Wistar rats used in my study were similar with the Fischer-344 strain (e.g. Wistar hippocampus 5.25±1.67 n.mole/ml/min and averaged WT and TG hippocampus, 4.68 ± 0.47 n.mole/ml/min). The absence of difference in PSR between Wistar and Fischer-344 could be due to the fact that both strain were tested at a young adult age (postnatal days > 60 [334]). Aging indeed is characterised by a cognitive decline and new protein synthesis is known to be indispensable for memory consolidation [335]. Decline and alterations of protein synthesis, degradation, and chaperoning mechanisms are implicated in many disease for which age is a principal risk factor, such as AD [336]. A gradual decline in protein synthesis was shown in Sprague-Dawley rats by Sun *at al.* [326] from 10 days post-natal to 60 days and by Smith *et al.* [337] in older rats from 6 months to 23 months of age. Specifically, in older rats Smith *et al.* [337] showed a statistically significant decrease in PSR mainly in the middle-aged group (15 months of age) when compared to the 6 months and only few brain regions were found with a statistically significant decrease in PSR between young adult (6 months of age) and aged rats (23 months). Although, the low number of brain regions affected by PSR decrease in aged rats could be due to the low number of rats tested at 23 months age (n=3) [337]. These data in Sprague-Dawley differed from my study, in which no differences in PSR were measured between middle age and young aged rats. The discrepancy between Fischer-344 and Sprague-Dawley rats could be due to the different methodology used to study the PSR. Indeed the autoradiography was used in the Sprague-Dawley for PSR analysis and all parameters such as labelled and unlabelled leucine in plasma, metabolites and brain labelled leucine, were measured directly in each experimental animal with the exception of the factor λ which was estimated in separate group of animals [337].

To conclude, I have established in these studies that [^{11}C]leucine can accurately determine PSR in rodent brain and offers significant advantages when compared to other labelled amino acids. Indeed, leucine has a simple metabolic pathway with no multiple radio-metabolites and is exclusively used for protein incorporation, while the recycling of amino acids can be taken into account through the introduction of the factor λ. To have an accurate estimation of PSR, individual blood measurements are however required as averaged- or

population-based values are likely to introduce error or bias likely to cancel differences in PSR between groups.

7.2 [^{18}F]UCB-H

In AD, it is well established that memory impairment are due to neuronal death and synapses loss [233, 338-341] and synaptic loss correlates well with cognitive decline in patients with Mild Cognitive Impairment (MCI) and AD [233, 342-344]. The neuronal circuits that degenerate in AD are also vulnerable in normal aging. Studies have established that during normal aging, there is only a minimal neuronal loss in cortical and hippocampus area and aging in brain is characterised by regressive changes in dendritic arbor, spines, and synapse morphology in specific regions [345-351]. Synapses, and specifically spines, are dynamic structures that can be changed by physiological activity and morphological changes are related to the strength of synapses [352]. Morphological changes do not happen only during development of the brain and learning processes in early life but also happen during the whole life [353]. The dynamic of this structures makes the readout of synapses more complicated, due to the many parameters that need to be considered. A meta-analysis study comparing 22 publications on synapses number and 83 about synaptic marker in AD and healthy controls, in hippocampus, frontal cortex, and in the combined regions of the *cingulate gyrus*, entorhinal cortex, and temporal cortex showed that synapses loss happens in all these brain regions and that the hippocampus is the most affected. Based on the same brain area, 70 publications were reviewed and the analysis of synaptic markers was conducted by categorising the synaptic markers as pre-, post-synaptic and functional (i.e. present at both level). Data showed that pre-synaptic markers are affected more by pathology with the largest loss in hippocampus [354]. Based on this data and on the high dynamicity of dendritic spines, pre-synaptic markers should be preferred to study synapse density.

The synaptic vesicle glycoprotein 2A (SV2A) is a membrane protein expressed ubiquitously in all brain area, essential for synaptic function and modulating the release of neurotransmitters, even if how SV2A modulates the release remains still unclear [355] (see §1.8).

A number of PET tracers have recently been developed and shown to bind the SV2A protein (see §1.11.2). One PET tracer, [^{18}F]UCB-H, has been demonstrated to display

excellent brain penetration (logD values 2.3 [356]) and fast kinetics (reaching peak uptake 5 minutes post-injection [300]) followed by a fast wash-out phase [357]. [^{18}F]UCB-H is a chiral molecule and the (R) enantiomer has a 10-fold higher affinity than the (S) enantiomer [299]. Despite the high affinity for SV2A (pIC50 7.8), [^{18}F]UCB-H also shows a level of binding to the SV2B [357]. Serrano *et al.* showed a significant reduction in [^{18}F]UCB-H (Vt 46.2%) when the SV2A binding was blocked with a selective SV2A compound. No statistically significant inhibition was found when using a SV2C selective ligand. The study with a SV2B compound showed a reduction of Vt (20%) distribution when compared to the scan without pre-treatments. This reduction of [^{18}F]UCB-H Vt values could be due to the fact that the SV2B compound used in this study had an affinity also for SV2A (pIC50=5.6) [357].

Due to the ubiquitous expression of SV2A throughout in brain, this prevents the use of a reference region approach for kinetic analysis, as there is no area of the CNS reasonably devoid of any specific binding for the SV2A. Since blood sampling represents a terminal procedure this prevented us from determining a subject-specific AIF in order to accurately model the PET data obtained from this study. Subsequently, we decided to use blocking scans to obtain values of non-specific binding as a means of analysing this data set. The blocked scans were performed with the injection of an excess of unlabelled UCB-J (1 mg/kg) 10 minutes prior injection of [^{18}F]UCB-H. We chose to use UCB-J because of its slightly higher affinity for SV2A [358].

An estimation of the non-specific binding of [^{18}F]UCB-H was made via the quantification of [^{18}F]UCB-H uptake in blocking scans, assuming a full and specific block to the SV2A. Analysis demonstrated a higher level of non-specific binding in TG rats and an increase in non-specific binding in both genotypes with age (see §4.2, Figure 51). Due to this result, SUV quantification of synaptic density in baseline scans at 7 and 15 months over-estimated the [^{18}F]UCB-H uptake which is therefore not reflecting the specific binding only, hence masking potential differences between age and/or genotype. The non-specific binding did vary significantly between age and genotypes, therefore all blocked scans were not averaged together for the quantification of the PET data. Four groups of blocked scans were therefore determined: WT 7 months, TG 7 months, WT 15 months and TG 15 months. The time-point decided to average the SUV was between 9 and 20 minutes after injection because at this time point the difference between the blocked and non-blocked (baseline)

scans was optimal but also because after 9 minutes the TAC of the blocked scans had reached a plateau. The quantification was done by calculation of Normalised Uptake Value (NUV), coming from the ratio of the SUV of baseline scans and the SUV of blocking scans. In all brain regions analysed a statistically significant decrease in [^{18}F]UCB-H NUV was demonstrated in TG rats at 7 months of age. A reduction of synaptic density was also detected with age but at 15 months the differences between genotypes was not significant (Figure 53). The statistical difference in SV2A between WT and TG at 7 months and the absence of this difference between the two genotypes at the middle age (15 months) could be due e to the fact that the synaptic density seems to be strongly inversely associated with the Aβ deposition during the early stages (stage of Aβ accumulation) when compared to the dementia (Aβ plateau) [359].

As previously discussed, the pre-saturation study showed a significant increase of non-specific binding due to the age in WT rats and even more prominent in TG rats. This data could be explained by the accumulation of lipofuscin in brain with age [360]. The aging brain is more vulnerable to cellular stress and is characterised by dysfunction involving the clearance of damaged molecules and organelles and their substitution. These inefficient mechanisms induce the accumulation of molecules that can interfere with cellular homeostasis. The main molecules that accumulate in aged cells are: protein aggregates, mitochondria with defects and lipofuscin [361]. Cellular stress and alteration of cellular homeostasis has been shown to be important in AD (see §1.5.1) [362]. Therefore, we can hypothesise that the increase of non-specific binding could be due to increased production of lipofuscin and the non-specific (i.e. non-displaceable) binding of the tracer to lipofuscin could be due to the suitability of brain PET tracers that need to be lipophilic to cross passively the BBB and penetrate brain [363]. Another explanation of the increase in non-specific binding in TG rats could be the BBB damage that happens in AD and that occur also in this animal model, as described by Dickie *et al*. in TG rats [364].

[^{11}C]UCB-J and [^{18}F]UCB-H are the main tracers used for SV2A imaging and despite [^{11}C]UCB-J having a higher affinity and selectivity for SV2A than [^{18}F]UCB-H, the short half-life of ^{11}C limits its use in PET centres without access to a cyclotron in a nearby vicinity. SV2A tracers have already been implemented for human studies and in AD, with the aim to investigate the ability of these tracers to detect the neurodegeneration. Regional differences

in volume of distribution (Vt) was shown with white matter being the lowest and increasing from cerebellum, hippocampus, parahippocampal gyrus, parietal cortex, precuneus, frontal regions, amygdala, anterior cingulate cortex, with putamen being the highest [365]. [^{11}C]UCB-J was used in MCI and healthy controls and because the Vt in cerebellum and centrum semiovale were similar and not statistically significant between groups supported the validity in the use of both regions as reference region. The cerebellum was defined as a better region due to the lowest variability of Vt between subjects and the analysis by using cerebellum as a reference region showed a decrease in [^{11}C]UCB-J Vt in all medial temporal regions and neocortical regions and most pronounced in hippocampus and entorhinal cortex [366].These results are in line with data obtained by using [^{18}F]UCB-H in which the image-derived input function and a plasma fraction to scale the IF were used for modelling [301]. [^{18}F]UCB-H uptake was reported to be decreased in cortical area, thalamus and more prominently in hippocampus [301]. The alterations in these regions mirror the finding described in the meta-analysis of AD studies showing that the hippocampus has the strongest synapses degeneration [354]. All these clinical papers and also the meta-analysis studies take into account MCI or AD patients, therefore aged/old subjects and showed a discrepancy if compared to my study in which no statistically relevant decrease in synaptic density were found between WT and TG in aged rats (15 months). This discrepancy between the human studies and mine could be due to the absence of neuronal loss in this AD rat model. Indeed, since the first publication about TgF344-AD rats, mixed results were reported. Choen *et al*. showed a neuronal loss in cortical regions and hippocampus starting from 16 months of age [243]; Leplus *et al*. at 18 months of age in *gyrus dentatus* and cortex [247]; whereas Voorhees *et al.* at 24 months in hippocampus and trending down in cortex regions [245]. No differences in neuronal counting were found between WT and TG at 6, 12 and 18 months by using immunohistochemistry NeuN staining during my Erasmus project in Herve's laboratory even if Voorhees *et al.* noted that NeuN staining could produce false negative due to the phagocytosis of neuronal debris by microglia [245]. In good agreement with my results, a decrease with age of Vt was determined by Bahari *et al*. by using [^{18}F]UCB-H in two young and two old healthy subject [367]. Most of post-mortem studies on early stages of AD are focused on the hippocampus and showed a progressive decline in the number of synapses by using transmission electron microscopy in the outer molecular layer

of the *dentate gyrus* [233] and also detected by immunohistochemistry using synaptophysin antibody [344].

SV2A tracers have also been used in other neurological diseases. Specifically [^{11}C]UCB-J was implemented for the study of schizophrenia in human, and in rats to study the effect of antipsychotic treatments. The study showed a decrease in schizophrenic patients of synaptic density in frontal and anterior cingulate cortices and the study on rats showed the impossibility to detect increase in synapses after induction of antipsychotic drugs for 28 days [368]. All these study confirm the reliability in the use of SV2A as a tracer to measure the synaptic density in neurological disease.

7.3 Behavioural and *ex-vivo* studies

The majority of AD cases are sporadic and the specific causes that lead the development of AD are unknown. Patients with AD show memory deficits, agitation, dysphoria, anxiety, euphoria, apathy, disinhibition, irritability, and aberrant motor behaviour [369]. Different animal models, mice and rats, were developed through the years and expressing different genetic mutations, therefore miming the genetic forms of AD (see §1.9).

The animal model used in this study, the TgF344-AD rat, is an animal model of the familial form of AD (see §1.9.3). This animal model is quite new, indeed the first publication was in 2013 [243] and so far various studies have shown a similar pathological profile of that found in humans [243]. To assess the memory impairment and behavioural changes in this model, different tests were conducted. Specifically, in this study anxiety and stress, the spatial and somatosensory (olfactory) memories were tested. The tests used for the assessment of the spatial memory was the Morris water maze (MWM) and reversal Morris water maze (RMWM), for anxiety and stress was the open field and for olfactory memory two smell tests.

The MWM test is based on the ability of rat to memorise a platform position by using distal clues and in reversal Morris water maze the capacity of the rat to learn a new platform position after a shorter period of training. The spatial memory and the reversal learning were already evaluated in this rat strain in the first study using the Barnes maze [243]. The Barnes maze is based on the ability of the rat to memorise and find an escape after an aversive stimulus (bright light). The alteration of spatial memory was shown to start at 15

months of age and during the reversal phase the impairment started at 15 months and increased further at 24 months in TG rats. In the reversal phase, even at 6 months, TG rats tended towards a statistically significant alteration [243] (Table 7). In another study, using the same model, Voorthees and colleagues (2017) did not find any statistical difference at 15 months of age between WT and TG in the Barnes maze but found that TG rats performed worse than WT at 24 months of age only in the reversal MWM [245] (Table 7); these results were confirmed in a more recent study in which no differences in Barnes maze at 15 months and at 24 months in MWM were evaluated between WT and TG [370]. Another study based on the Barnes maze test showed no statistically significant differences between genotypes in rats aged between 9 and 13 months and only by using specific analysis based on the evaluation of complexity of strategies, the authors could show that TG rats uses weaker search strategies than WT [371]. In young rats however, results are more consistent, and Cohen *et al.* and Pentkowski *et al.* did not find any spatial memory deficit between genotypes with Barnes and MWM respectively [243, 251]. Rorabaugh *et al.* showed a statistically significant spatial memory deficit only during the reversal phase of MWM at 6 months and 16 months of age [250]. No learning and spatial memory impairment in young rats were found in both publication of Voorthees and colleagues [245, 370]. The review of various studies in WT and TG highlights divergent results (Table 7).

The main parameter analysed to determine spatial memory impairment in MWM is the latency, which is defined as the time used by rats to reach the platform and in which a reduction through the days means the acquisition of memory. During the probe test, to determine the acquired memory about the platform position, the time spent in the quadrant where the platform was during the acquisition days is used. Berkowitz *et al.* analysed other, more complex parameters in MWM such as path length, how far the rat swim from the platform and also qualitative swim trajectories analysis, to better examine the rat memory and their behaviours. In this study, they also hypothesised that differences between publications could be due to the use of female and male together [252]. Some publications indeed, describe differences in behaviours in other rodent model of AD due to gender. Berkowitz *et al.* tested rats at three different time-points 4-5, 7-8 and 10-11 months of age, female and male. They showed a spatial navigation impairment starting at 10-11 months of age in TG rats. Indeed, TG rats spent more time to find platform, the distance travel was

longer, they swam in a wider area of the pool instead of the platform region and the path efficiency showed a trend of TG rats to exhibit higher deviation than WT. The qualitative analysis of the rat behaviours was assessed to better understand the type of movements used by rats to reach the platform. The movements were classified in four classes: "target-direct" when the platform was found directly after dropping the rat in the pool, "target-indirect" when the rats spend time around the platform, "spatial-indirect" when rats had movements not directed to the platform but indicative of spatial processing and "non-spatial movements" such as wall hugging, incursion and circle over itself. This analysis showed that TG rats starting from 7-8 months had lower direct movements than WT and at 10-11 months TG rats had also a greater proportion of target-indirect and spatial-indirect trajectories [252].

Table 7: table summarising the behavioural tests used to assess the spatial memory impairment in TgF344-AD. numbers are the rat's age tested. Values in Green means that no statistically significant differences were observed between genotypes, whilst red text means significant differences between WT and TG have been shown.

	Barnes maze (BM)	Reversal phase (BM)	Morris water maze (MWM)	Reversal phase (MWM)
Cohen *et al.* [243]	6-15-24 M	6-15-24 M		
Voorthees *et al.* [245]	5-15 M	15 M	24 M	24 M
Pentkowski *et al.* [251]			4-6 M	
Rorabaugh *et al.* [250]			6-16 M	
Berkowitz *et al.* [252]			4-5;7-8;10-11 M	
Voorthees *et al.* [370]	6-9-12-15 M	6-9-12-15 M	24 M	24 M
Morrone *et al.* [371]	Between 9-13 M	Between 9-13 M		
My PhD			6-12-18 M	6-12-18M

In my PhD study, many parameters were also analysed for the estimation of spatial memory such as duration, the time spent in each quadrant, the time to get closer to the platform, speed, distance travelled and path efficiency during the test. All these parameters were analysed for the MWM and reversal MWM tests, during the acquisition days but also during the probe tests when the platform was removed from the pool. In my study, a statistically significant training effect was found in both genotypes, with a reduction of the

time spent in finding the platform during the acquisition days and a significant age x training effect was also detected in TG rats. In the reversal MWM, both WT and TG rats were not able to acquire a new memory, and there was no statistical effect of age or genotype.
An important parameter measured in my study was the path efficiency, in which a maximum value of 1 indicates a perfect efficiency, i.e. the animal moved in a straight line whereas lower values indicate loss of path efficiency (i.e. longer/indirect path). Because during the MWM rats were able to learn the platform position, we hypothesised to find low values during the first day and a gradual increase due to learning in the following days and also potentially statistically significant differences between age. Path efficiency values in both genotypes and at each age remained low throughout the days, highlighting that both genotypes did not improve their path efficiency to find the platform in both phases of the test (see §5.1, Figure 60). The other parameters: speed, distance and time to getting close to the platform also showed no significant differences between ages or genotypes.

The alteration of spatial memory by using the MWM was well established in another AD rat model, rat Tg6590 (Sprague-Dawley background) [372]. In the MWM, these rats showed spatial learning impairment by 9 months of age characterised by very high difference in latency since the first day of acquisition when compared to WT. This learning deficit in MWM is accompanied with a decrease in swim speed and increase in distance travelled**.** During the probe test a significantly higher preference for the platform quadrants was determined in WT than in Tg6590 [372].

In my study, the reduction in time to reach the platform detected during the acquisition days could be due to a real memorisation or to a coincidence of touching the platform with tail.

A recent study tested the spatial memory impairment in TG rats by using the Y-maze, in which rats are allowed to freely explore the three arms. Over the time, rats should show a tendency to enter a less recently visited arm. By using a video, it was possible to determine the entry in each arm. The number of arm entries and the number of trials were recorded in order to calculate the percentage of alternation. In this recent study, TG rats at 9 months of age showed the same percentage of alteration than WT, highlighting no differences in spatial memory. In the same study the analysis of learning was conducted by using a T-maze. In this

study, the percentage of success TG rats at 10 months of age was shown to be lower than in WT. Therefore, this study highlights the presence of a learning deficit but not a spatial impairment in TG rats [373]. A deficit in learning memory that increased with age was also shown in TG rats by Sarè *et al*. [374], using a reward alternating T-maze. So, to conclude, because no significant differences could be observed between genotypes or age in my MWM study and due to the variable and divergent results obtained in other publications testing spatial memory in this animal model, it is impossible to conclude a real spatial memory impairment in TG vs. WT.

Anxiety was tested in my study by using the Open-field test. To assess the level of anxiety, the time spent in the exploration of a new environment and the time spent close to the wall were examined (see §5.2, Figure 65). These analyses showed that both genotypes, WT and TG, at each age were characterised by high levels of stress, determined by their total inability in performing the test (i.e. very low exploration or time spent moving in the arena and close to the wall). The very low exploration of the centre of arena was found also in another and well characterised animal model for AD, the McGill transgenic rat, in which the absence of differences between WT and TG at 10 months of age was also showed but both genotypes showed however much more movements if compared to my study [375]. The Open-field results found in my project were opposite to that of Cohen *et al.* who showed an hyperactivity in TG rats at 15 months of age, evaluated by studying the beam breaks and rearing activity [243]. Comparing the rearing activity of Fischer-344 strain determined by Choen *et al.* with the McGill strain, Fischer-344 showed however much lower values [376]. In another study, an increase in anxiety behaviours in TG rats compared to WT was demonstrated at 6 months in the elevated plus maze [251] . Conversely to these results, in both studies of Voorthees *et al*., the analysis of locomotor activity showed no significant differences between genotypes and ages (6-9-12-15-24 months of age) [245, 370]. Morrone *et al*. also showed no statistically significant differences between genotypes highlighting that rats spent most of the time in the perimeter of the arena (time spent in the centre ≤ 20%) [371]. A more recent study showed that the absence of differences in activity between age and genotype in male WT and TG was due to an habituation of rats to the environment [374]. All these studies are at least in part in line with my results, in which was highlighted a low exploration time/behaviour, poor performance overall even in WT.

Brain alteration in AD affects regions essential for odour recognition and memory. Deficit in odour detection, recognition and discrimination are present in AD patients and appear before memory impairment, the reduction in detecting a smell (hyposmia) and the complete loss of odour (anosmia) appear also with age [377]. In TgF344-AD rats, a reduction in detecting a smell was found to be lower regardless of age when compared to controls [374]. Different smell tests were performed in my study to determine the olfactory impairment in TG rats (see §3.7.3). At 12 months of age, WT seemed able to memorise the fragrance when tested after a delay of 30 minutes (see §5.3, Figure 66) and lost completely this ability when longer delays were applied. In all smell tests, the time spent smelling was always very low (~20 seconds) over the experimental time. A statistically significant reduction of smelling time was evaluated between WT and TG rats during the first smell presentation and a decrease in smelling time due to the age was found in WT rats only during the first day of test. Trying to better understand the smell ability in WT and TG, the urine test (fox and rabbit) was performed at 12 and 18 months of age. The main goal was to evaluate if rats were able to smell properly odours, as fox urine should induce fear and they should spend very little time sniffing it. The analysis of the urine test showed again very low values in smelling times; opposite to what expected, rats tend to spend more time smelling the predator (fox) urine instead of the non-predator. TG rats showed a statistically significant differences in fox urine smelling time between 12 and 18 months, in which at 18 months rats spent more time smelling fox urine than at 12 months moreover the fox urine smelling time at 18 months of age was statistically higher than smelling rabbit urine (Figure 67).

The reduction of time in smelling the predator urine, due to the fear, was highlighted in a study on Sprague–Dawley rats. In this study, defensive behaviours were observed during the exposition of rats to a predator urine with a reduction of the time spent in the corner with urine predator samples. Longer contact was evaluated with non-predator urine indeed, statistically significant differences were found in smelling time between control and predator's urine but no between control and non-predator urine. However, the smelling time in Sprague–Dawley was ~20 seconds over the experimental time (10 minutes) [378] which is in good agreement with my results.

The inability to characterise the WT and TG behaviourally could be due to the characteristic of the Fischer-344 strain. Anxiety behaviours in rodents are influenced by differences in strains [379]. Differences in locomotor activity evaluated between Wistar (different breeders), Lewis, Brown Norway and Fischer-344 strains, showed that Fischer-344 had the lowest values and Wistar Winkelmann the highest [379]. Also in food deprivation open field, Fischer-344 rats showed lower first feeding than the other strains [379]. In free exploration of a new environment, Fischer-344 showed lower percentage of exploration while the Charles River Wistar and Brown Norway showed the highest. In social interaction, Fischer-344 rats spent less second in interacting with an unfamiliar rat from a different group when compared to the others and the values were statistically significant when compared to the Lewis strain that had the highest values [379]. These data clearly show that Fischer-344 rats are characterised by more anxious behaviours [380]. Despite the fact that the Fischer-344 strain had a more anxious behaviour, learning did not seem to be affected by anxiety. Indeed in the MWM test, the comparison between Wistar and Fischer-344 rats showed no difference in learning [381]. Strain alteration can impact the success of behavioural tests and the Fischer-344 strain showed to develop with age different problems such as ocular and auditory alteration. Indeed, these rats have been shown to be prone to developing ocular changes with spontaneous unilateral degeneration of optic nerve and retina [382] and auditory impairment starting at 12 months of age [383]. Consequently, due to all these strain characteristics, Fischer-344 strain has many limitations for behavioural tests.

This animal model does not seem very suitable for behavioural tests, however alterations in the brain of the TgF344-AD are still similar to patients with AD in term of notably amyloid deposition. In this study, we confirmed the amyloid deposition in cortical and hippocampal regions of TG rats, starting from 6m and progressing to a heavy amyloid deposition at 12m and 18m of age. This observation was in good agreement with the first report of this model [243] and subsequent findings from other laboratories. As described by Cohen *et al.* [243], TG rats also exhibit spontaneous hyperphosphorylated tau accumulation in parallel with an increased neuroinflammation. *Ex-vivo* analysis by immunohistochemistry in this study demonstrated the presence of increased astrogliosis in TG vs. WT. Despite the fact that different markers of protein synthesis (eIF2α, PERK proteins, ATF4, etc.) were found

altered in AD patients or other animal models (see §1.7), I had difficulties in performing an evaluation by immunohistochemistry (IHC) and/or Western Blot (WB) of eIF2α and its phosphorylation at serine 51 (phospho-eIF2α), ATF4 and SV2A in this animal model. The main problem encountered in IHC was the inability to discriminate the real signal to the background, despite different protocols being extensively tested.

For the WB analysis, the main obstacle was to found a specific method to normalise for protein levels. Indeed, an important result found in WB was the difference in the expression of β-Actin at 18 months of age in two brain regions (see §6.2). This protein is widely used as a housekeeping protein and in my study the values of β-Actin were higher in WT than TG. Other housekeeping genes such as Glyceraldehyde-3-phosphate dehydrogenase (GAPDH) or Phosphoglycerate kinase 1 were not possible to be used because their molecular weights were the same of the target proteins of this study. The difference in β-Actin measured at 18 months between WT and TG should be investigated more, because a real difference could lead to a wrong interpretation of data. Further studies with the aims to optimise protocols should be conducted to better compare and validate the data found by PET.

8 Conclusions and future perspectives

The aims of this PhD were to determine *i)* the best approach in the study of protein synthesis in brain in rats and *ii)* if, in this AD model, we could detect a decrease in PSR and synaptic density as early markers of AD pathology *in-vivo* using [^{11}C]leucine and [^{18}]UCB-H PET tracers. Finally, this work also contributes to a better characterisation of this animal model through *in-vivo* imaging, *ex-vivo* measures and behavioural tests and brings the leucine knowledge obtained in my project to a clinical study in AD patients started at the same time of mine.

Data obtained in this study confirmed and validated the use of [^{11}C]leucine as a tracer to measure PSR in rats. Data highlighted that the best approach to estimate PSR was to use individual blood measurements and concentration of unlabelled leucine to establish an IF as the concentrations of amino acids vary between animal species, strains and probably between genotypes. The evaluation of PSR in this AD rat model has only been partially answered and will require further investigation due to some weaknesses such as the unavailability of individual AIF for all animals with [^{11}C]leucine PET.

This study has however cleared many points about the methodology such as the need to of individual blood measurement. Indeed, in my studies I found a genotype differences in PSR at 18 months of age in many brain regions analysed when the individual blood measurements were used but only few rats were tested (WT=4 and TG=5); while by using a population-based IF in the longitudinal study a modest change in PSR was found at 18 months only in *globus pallidus*. The absence of statistically significant PSR differences between genotypes in the other brain regions could come from the use of averaged blood values for unlabelled leucine and IF but also to the methodology used for the measurement of free [^{11}C]leucine in plasma. Indeed the % of free [^{11}C]leucine was calculated by using 70% perchloric acid (PCA) and then the values were converted into 5% PCA, introducing some bias. In the literature, the percentage of PCA used is always low but there is not any studies demonstrating rationally what percentage is best for optimal plasma proteins precipitation; therefore experiments to clarify the differences between the free concentration of [^{11}C]leucine using a range of PCA concentration and its effect on protein precipitation and stability could also be performed. Based on these results, the PSR changes in this AD model and in AD patients still need to be further investigated. In this study, I have also

demonstrated the usefulness of the SV2A PET tracer, [^{18}F]UCB-H, to detect the synaptic loss. The synaptic loss was determined at a young age in TgF344-AD but no at an older age between WT and TG probably due to the absence of neuronal loss in this animal model. An interesting study with [^{18}F]UCB-H could be to scan younger rats to determine at which specific time point synaptic loss starts. *Ex-vivo* and autoradiography study should also be tested to validate the results obtained by PET for both tracers.

Parallel *ex-vivo* analysis highlighted and confirmed the progressive amyloid accumulation and neuroinflammation in the TgF344-AD animals. However, despite the strong correlation between brain changes in TG rats and AD patients, the analysis of behavioural tests did not show any significant alterations between genotype and age in spatial learning evaluated by MWM and RMWM. Importantly, the TG and WT rats both showed high levels of stress evaluated by the absence exploration of new environment in the open field test, confirming results about the anxiety of Fischer-344 strain.

9 References

1. Lau, L.F. and M.A. Brodney, *Therapeutic Approaches for the Treatment of Alzheimer's Disease: An Overview.* Alzheimer's Disease, 2008. **2**: p. 1-24.
2. Tang, Q., P. Song, and L. Xu, *The Government's role in regulating, coordinating, and standardizing the response to Alzheimer's disease: Anticipated international cooperation in the area of intractable and rare diseases.* Intractable Rare Dis Res, 2016. **5**(4): p. 238-243.
3. Allen, S.J., J.J. Watson, and D. Dawbarn, *The neurotrophins and their role in Alzheimer's disease.* Curr Neuropharmacol, 2011. **9**(4): p. 559-73.
4. Glenner, G.G. and C.W. Wong, *Alzheimer's disease: initial report of the purification and characterization of a novel cerebrovascular amyloid protein.* Biochem Biophys Res Commun, 1984. **120**(3): p. 885-90.
5. Grundke-Iqbal, I., et al., *Microtubule-associated protein tau. A component of Alzheimer paired helical filaments.* J Biol Chem, 1986. **261**(13): p. 6084-9.
6. Quon, D., et al., *Formation of beta-amyloid protein deposits in brains of transgenic mice.* Nature, 1991. **352**(6332): p. 239-41.
7. Klunk, W.E., et al., *Imaging brain amyloid in Alzheimer's disease with Pittsburgh Compound-B.* Ann Neurol, 2004. **55**(3): p. 306-19.
8. Van Cauwenberghe, C., C. Van Broeckhoven, and K. Sleegers, *The genetic landscape of Alzheimer disease: clinical implications and perspectives.* Genetics in Medicine, 2016. **18**(5): p. 421-430.
9. Cacace, R., K. Sleegers, and C. Van Broeckhoven, *Molecular genetics of early-onset Alzheimer's disease revisited.* Alzheimers & Dementia, 2016. **12**(6): p. 733-748.
10. Bagyinszky, E., et al., *The genetics of Alzheimer's disease.* Clin Interv Aging, 2014. **9**: p. 535-51.
11. Durmaz, A., et al., *Genetic factors associated with the predisposition to late onset Alzheimer's disease.* Gene, 2019. **707**: p. 212-215.
12. Giri, M., M. Zhang, and Y. Lu, *Genes associated with Alzheimer's disease: an overview and current status.* Clinical Interventions in Aging, 2016. **11**: p. 665-681.
13. Barber, R.C., *The genetics of Alzheimer's disease.* Scientifica (Cairo), 2012. **2012**: p. 246210.
14. Bekris, L.M., et al., *Genetics of Alzheimer disease.* J Geriatr Psychiatry Neurol, 2010. **23**(4): p. 213-27.
15. Kanekiyo, T., H. Xu, and G. Bu, *ApoE and Abeta in Alzheimer's disease: accidental encounters or partners?* Neuron, 2014. **81**(4): p. 740-54.
16. Raulin, A.C., et al., *The Molecular Basis for Apolipoprotein E4 as the Major Risk Factor for Late-Onset Alzheimer's Disease.* J Mol Biol, 2019.
17. Lane-Donovan, C. and J. Herz, *ApoE, ApoE Receptors, and the Synapse in Alzheimer's Disease.* Trends Endocrinol Metab, 2017. **28**(4): p. 273-284.
18. Lane-Donovan, C., G.T. Philips, and J. Herz, *More than cholesterol transporters: lipoprotein receptors in CNS function and neurodegeneration.* Neuron, 2014. **83**(4): p. 771-87.
19. Dong, H.K., et al., *Integrated late onset Alzheimer's disease (LOAD) susceptibility genes: Cholesterol metabolism and trafficking perspectives.* Gene, 2017. **597**: p. 10-16.
20. Liu, C.C., et al., *Apolipoprotein E and Alzheimer disease: risk, mechanisms and therapy.* Nat Rev Neurol, 2013. **9**(2): p. 106-18.
21. Osenkowski, P., et al., *Direct and potent regulation of gamma-secretase by its lipid microenvironment.* J Biol Chem, 2008. **283**(33): p. 22529-40.
22. Ulrich, J.D., et al., *ApoE facilitates the microglial response to amyloid plaque pathology.* J Exp Med, 2018. **215**(4): p. 1047-1058.
23. Joubert, S., et al., *Early-onset and late-onset Alzheimer's disease are associated with distinct patterns of memory impairment.* Cortex, 2016. **74**: p. 217-32.

24. Dickerson, B.C., et al., *Alzheimer's disease: The influence of age on clinical heterogeneity through the human brain connectome.* Alzheimer's & Dementia: Diagnosis, Assessment & Disease Monitoring, 2017. **6**: p. 122-135.
25. Lee, J., K.J. Lee, and H. Kim, *Gender differences in behavioral and psychological symptoms of patients with Alzheimer's disease.* Asian J Psychiatr, 2017. **26**: p. 124-128.
26. Hansson, O., et al., *Association between CSF biomarkers and incipient Alzheimer's disease in patients with mild cognitive impairment: a follow-up study.* Lancet Neurol, 2006. **5**(3): p. 228-34.
27. Shaw, L.M., et al., *Cerebrospinal fluid biomarker signature in Alzheimer's disease neuroimaging initiative subjects.* Ann Neurol, 2009. **65**(4): p. 403-13.
28. Lista, S., et al., *Biomarkers in Sporadic and Familial Alzheimer's Disease.* J Alzheimers Dis, 2015. **47**(2): p. 291-317.
29. Jack, C.R., Jr., et al., *Hypothetical model of dynamic biomarkers of the Alzheimer's pathological cascade.* Lancet Neurol, 2010. **9**(1): p. 119-28.
30. Ricciarelli, R. and E. Fedele, *The Amyloid Cascade Hypothesis in Alzheimer's Disease: It's Time to Change Our Mind.* Curr Neuropharmacol, 2017. **15**(6): p. 926-935.
31. de Paula, V.J.R., et al., *Neurobiological pathways to Alzheimer's disease: Amyloid-beta, TAU protein or both?* Dement Neuropsychol, 2009. **3**(3): p. 188-194.
32. Holmes, C., et al., *Long-term effects of Abeta42 immunisation in Alzheimer's disease: follow-up of a randomised, placebo-controlled phase I trial.* Lancet, 2008. **372**(9634): p. 216-23.
33. Price, J.L., et al., *Neuropathology of nondemented aging: presumptive evidence for preclinical Alzheimer disease.* Neurobiol Aging, 2009. **30**(7): p. 1026-36.
34. Guillozet, A.L., et al., *Neurofibrillary tangles, amyloid, and memory in aging and mild cognitive impairment.* Arch Neurol, 2003. **60**(5): p. 729-36.
35. Herrup, K., *The case for rejecting the amyloid cascade hypothesis.* Nat Neurosci, 2015. **18**(6): p. 794-9.
36. Morris, G.P., I.A. Clark, and B. Vissel, *Inconsistencies and controversies surrounding the amyloid hypothesis of Alzheimer's disease.* Acta Neuropathol Commun, 2014. **2**: p. 135.
37. Mudher, A. and S. Lovestone, *Alzheimer's disease-do tauists and baptists finally shake hands?* Trends Neurosci, 2002. **25**(1): p. 22-6.
38. Braak, H. and E. Braak, *Neuropathological stageing of Alzheimer-related changes.* Acta Neuropathol, 1991. **82**(4): p. 239-59.
39. Kinney, J.W., et al., *Inflammation as a central mechanism in Alzheimer's disease.* Alzheimers Dement (N Y), 2018. **4**: p. 575-590.
40. Breitner, J.C., et al., *Inverse association of anti-inflammatory treatments and Alzheimer's disease: initial results of a co-twin control study.* Neurology, 1994. **44**(2): p. 227-32.
41. Serrano-Pozo, A., et al., *Neuropathological alterations in Alzheimer disease.* Cold Spring Harb Perspect Med, 2011. **1**(1): p. a006189.
42. Atwood, C.S., et al., *Senile plaque composition and posttranslational modification of amyloid-beta peptide and associated proteins.* Peptides, 2002. **23**(7): p. 1343-50.
43. Del Prete, D., et al., *Localization and Processing of the Amyloid-beta Protein Precursor in Mitochondria-Associated Membranes.* J Alzheimers Dis, 2017. **55**(4): p. 1549-1570.
44. Ho, L., K. Fukuchi, and S.G. Younkin, *The alternatively spliced Kunitz protease inhibitor domain alters amyloid beta protein precursor processing and amyloid beta protein production in cultured cells.* J Biol Chem, 1996. **271**(48): p. 30929-34.
45. Sosa, L.J., et al., *The physiological role of the amyloid precursor protein as an adhesion molecule in the developing nervous system.* J Neurochem, 2017. **143**(1): p. 11-29.
46. Haass, C., et al., *Trafficking and proteolytic processing of APP.* Cold Spring Harb Perspect Med, 2012. **2**(5): p. a006270.
47. Zhang, Y.W., et al., *APP processing in Alzheimer's disease.* Mol Brain, 2011. **4**: p. 3.
48. O'Brien, R.J. and P.C. Wong, *Amyloid precursor protein processing and Alzheimer's disease.* Annu Rev Neurosci, 2011. **34**: p. 185-204.

49. Norstrom, E., *Metabolic processing of the amyloid precursor protein -- new pieces of the Alzheimer's puzzle.* Discov Med, 2017. **23**(127): p. 269-276.
50. Bordji, K., et al., *Activation of extrasynaptic, but not synaptic, NMDA receptors modifies amyloid precursor protein expression pattern and increases amyloid-ss production.* J Neurosci, 2010. **30**(47): p. 15927-42.
51. Lesne, S., et al., *NMDA receptor activation inhibits alpha-secretase and promotes neuronal amyloid-beta production.* J Neurosci, 2005. **25**(41): p. 9367-77.
52. Placido, A.I., et al., *The role of endoplasmic reticulum in amyloid precursor protein processing and trafficking: Implications for Alzheimer's disease.* Biochimica Et Biophysica Acta-Molecular Basis of Disease, 2014. **1842**(9): p. 1444-1453.
53. Wilson, C.A., R.W. Doms, and V.M. Lee, *Intracellular APP processing and A beta production in Alzheimer disease.* J Neuropathol Exp Neurol, 1999. **58**(8): p. 787-94.
54. Rajasekhar, K., M. Chakrabarti, and T. Govindaraju, *Function and toxicity of amyloid beta and recent therapeutic interventions targeting amyloid beta in Alzheimer's disease.* Chem Commun (Camb), 2015. **51**(70): p. 13434-50.
55. Roychaudhuri, R., et al., *Amyloid beta-protein assembly and Alzheimer disease.* J Biol Chem, 2009. **284**(8): p. 4749-53.
56. Dinamarca, M.C., J.A. Rios, and N.C. Inestrosa, *Postsynaptic Receptors for Amyloid-beta Oligomers as Mediators of Neuronal Damage in Alzheimer's Disease.* Front Physiol, 2012. **3**: p. 464.
57. Niu, Z., et al., *Interactions between amyloid beta peptide and lipid membranes.* Biochim Biophys Acta Biomembr, 2018.
58. Yu, M.S., et al., *Beta-amyloid peptides induces neuronal apoptosis via a mechanism independent of unfolded protein responses.* Apoptosis, 2006. **11**(5): p. 687-700.
59. Asai, M., et al., *Putative function of ADAM9, ADAM10, and ADAM17 as APP alpha-secretase.* Biochemical and Biophysical Research Communications, 2003. **301**(1): p. 231-235.
60. Lichtenthaler, S.F., *alpha-secretase in Alzheimer's disease: molecular identity, regulation and therapeutic potential.* J Neurochem, 2011. **116**(1): p. 10-21.
61. MacLeod, R., et al., *The role and therapeutic targeting of alpha-, beta- and gamma-secretase in Alzheimer's disease.* Future Sci OA, 2015. **1**(3): p. FSO11.
62. Lammich, S., et al., *Constitutive and regulated alpha-secretase cleavage of Alzheimer's amyloid precursor protein by a disintegrin metalloprotease.* Proc Natl Acad Sci U S A, 1999. **96**(7): p. 3922-7.
63. Skovronsky, D.M., et al., *Protein kinase C-dependent alpha-secretase competes with beta-secretase for cleavage of amyloid-beta precursor protein in the trans-golgi network.* J Biol Chem, 2000. **275**(4): p. 2568-75.
64. Spies, P.E., et al., *Reviewing reasons for the decreased CSF Abeta42 concentration in Alzheimer disease.* Front Biosci (Landmark Ed), 2012. **17**: p. 2024-34.
65. Araki, W., *Post-translational regulation of the beta-secretase BACE1.* Brain Res Bull, 2016. **126**(Pt 2): p. 170-177.
66. Capell, A., et al., *Maturation and pro-peptide cleavage of beta-secretase.* J Biol Chem, 2000. **275**(40): p. 30849-54.
67. Huse, J.T., et al., *Beta-secretase processing in the trans-Golgi network preferentially generates truncated amyloid species that accumulate in Alzheimer's disease brain.* J Biol Chem, 2002. **277**(18): p. 16278-84.
68. Ghosh, A.K. and H.L. Osswald, *BACE1 (beta-secretase) inhibitors for the treatment of Alzheimer's disease.* Chem Soc Rev, 2014. **43**(19): p. 6765-813.
69. Grimm, M.O., et al., *APP Function and Lipids: A Bidirectional Link.* Front Mol Neurosci, 2017. **10**: p. 63.
70. Grimm, M.O., T.L. Rothhaar, and T. Hartmann, *The role of APP proteolytic processing in lipid metabolism.* Exp Brain Res, 2012. **217**(3-4): p. 365-75.

71. Vassar, R., et al., *The beta-secretase enzyme BACE in health and Alzheimer's disease: regulation, cell biology, function, and therapeutic potential.* J Neurosci, 2009. **29**(41): p. 12787-94.
72. Xu, T.H., et al., *Alzheimer's disease-associated mutations increase amyloid precursor protein resistance to gamma-secretase cleavage and the Abeta42/Abeta40 ratio.* Cell Discov, 2016. **2**: p. 16026.
73. Wilkins, H.M. and R.H. Swerdlow, *Amyloid precursor protein processing and bioenergetics.* Brain Res Bull, 2016.
74. Li, Y., et al., *Structural biology of presenilin 1 complexes.* Mol Neurodegener, 2014. **9**: p. 59.
75. Carroll, C.M. and Y.M. Li, *Physiological and pathological roles of the gamma-secretase complex.* Brain Research Bulletin, 2016. **126**: p. 199-206.
76. Avila, J., et al., *Role of tau protein in both physiological and pathological conditions.* Physiological Reviews, 2004. **84**(2): p. 361-384.
77. Lacovich, V., et al., *Tau Isoforms Imbalance Impairs the Axonal Transport of the Amyloid Precursor Protein in Human Neurons.* Journal of Neuroscience, 2017. **37**(1): p. 58-69.
78. Park, S.A., S.I. Ahn, and J.M. Gallo, *Tau mis-splicing in the pathogenesis of neurodegenerative disorders.* BMB Rep, 2016. **49**(8): p. 405-13.
79. Gong, C.X., et al., *Post-translational modifications of tau protein in Alzheimer's disease.* J Neural Transm (Vienna), 2005. **112**(6): p. 813-38.
80. Martin, L., X. Latypova, and F. Terro, *Post-translational modifications of tau protein: implications for Alzheimer's disease.* Neurochem Int, 2011. **58**(4): p. 458-71.
81. Stoothoff, W.H. and G.V. Johnson, *Tau phosphorylation: physiological and pathological consequences.* Biochim Biophys Acta, 2005. **1739**(2-3): p. 280-97.
82. Hooper, C., R. Killick, and S. Lovestone, *The GSK3 hypothesis of Alzheimer's disease.* J Neurochem, 2008. **104**(6): p. 1433-9.
83. Cho, J.H. and G.V. Johnson, *Glycogen synthase kinase 3beta phosphorylates tau at both primed and unprimed sites. Differential impact on microtubule binding.* J Biol Chem, 2003. **278**(1): p. 187-93.
84. Horowitz, P.M., et al., *Early N-terminal changes and caspase-6 cleavage of tau in Alzheimer's disease.* J Neurosci, 2004. **24**(36): p. 7895-902.
85. Goedert, M., D.S. Eisenberg, and R.A. Crowther, *Propagation of Tau Aggregates and Neurodegeneration.* Annu Rev Neurosci, 2017. **40**: p. 189-210.
86. Yan, X., et al., *FRMD4A-cytohesin signaling modulates the cellular release of tau.* J Cell Sci, 2016. **129**(10): p. 2003-15.
87. Perez-Lloret, S. and F.J. Barrantes, *Deficits in cholinergic neurotransmission and their clinical correlates in Parkinson's disease.* NPJ Parkinsons Dis, 2016. **2**: p. 16001.
88. Wenk, G.L., *Neuropathologic changes in Alzheimer's disease.* J Clin Psychiatry, 2003. **64 Suppl 9**: p. 7-10.
89. Schliebs, R. and T. Arendt, *The cholinergic system in aging and neuronal degeneration.* Behav Brain Res, 2011. **221**(2): p. 555-63.
90. Pepeu, G. and M. Grazia Giovannini, *The fate of the brain cholinergic neurons in neurodegenerative diseases.* Brain Res, 2017. **1670**: p. 173-184.
91. Ferreira-Vieira, T.H., et al., *Alzheimer's disease: Targeting the Cholinergic System.* Curr Neuropharmacol, 2016. **14**(1): p. 101-15.
92. Radcliffe, K.A., et al., *Nicotinic modulation of glutamate and GABA synaptic transmission in hippocampal neurons.* Molecular and Functional Diversity of Ion Channels and Receptors, 1999. **868**: p. 591-610.
93. Haam, J. and J.L. Yakel, *Cholinergic modulation of the hippocampal region and memory function.* J Neurochem, 2017. **142 Suppl 2**: p. 111-121.
94. Dineley, K.T., et al., *Beta-amyloid activates the mitogen-activated protein kinase cascade via hippocampal alpha7 nicotinic acetylcholine receptors: In vitro and in vivo mechanisms related to Alzheimer's disease.* J Neurosci, 2001. **21**(12): p. 4125-33.

95. Parri, H.R., C.M. Hernandez, and K.T. Dineley, *Research update: Alpha7 nicotinic acetylcholine receptor mechanisms in Alzheimer's disease.* Biochem Pharmacol, 2011. **82**(8): p. 931-42.
96. Wang, H.Y., et al., *Alpha 7 nicotinic acetylcholine receptors mediate beta-amyloid peptide-induced tau protein phosphorylation.* J Biol Chem, 2003. **278**(34): p. 31547-53.
97. Goold, R.G. and P.R. Gordon-Weeks, *The MAP kinase pathway is upstream of the activation of GSK3beta that enables it to phosphorylate MAP1B and contributes to the stimulation of axon growth.* Mol Cell Neurosci, 2005. **28**(3): p. 524-34.
98. Sabri, O., et al., *Cognitive correlates of alpha4beta2 nicotinic acetylcholine receptors in mild Alzheimer's dementia.* Brain, 2018. **141**(6): p. 1840-1854.
99. Wilcock, G.K., et al., *Alzheimer's disease. Correlation of cortical choline acetyltransferase activity with the severity of dementia and histological abnormalities.* J Neurol Sci, 1982. **57**(2-3): p. 407-17.
100. Gilmor, M.L., et al., *Preservation of nucleus basalis neurons containing choline acetyltransferase and the vesicular acetylcholine transporter in the elderly with mild cognitive impairment and early Alzheimer's disease.* J Comp Neurol, 1999. **411**(4): p. 693-704.
101. Wang, R. and P.H. Reddy, *Role of Glutamate and NMDA Receptors in Alzheimer's Disease.* J Alzheimers Dis, 2017. **57**(4): p. 1041-1048.
102. Spampinato, S.F., et al., *Metabotropic Glutamate Receptors in Glial Cells: A New Potential Target for Neuroprotection?* Front Mol Neurosci, 2018. **11**: p. 414.
103. Ribeiro, F.M., et al., *Metabotropic glutamate receptors and neurodegenerative diseases.* Pharmacol Res, 2017. **115**: p. 179-191.
104. Esposito, Z., et al., *Amyloid beta, glutamate, excitotoxicity in Alzheimer's disease: are we on the right track?* CNS Neurosci Ther, 2013. **19**(8): p. 549-55.
105. Luscher, C. and R.C. Malenka, *NMDA receptor-dependent long-term potentiation and long-term depression (LTP/LTD).* Cold Spring Harb Perspect Biol, 2012. **4**(6).
106. Tu, S., et al., *Oligomeric Abeta-induced synaptic dysfunction in Alzheimer's disease.* Mol Neurodegener, 2014. **9**: p. 48.
107. Guntupalli, S., J. Widagdo, and V. Anggono, *Amyloid-beta-Induced Dysregulation of AMPA Receptor Trafficking.* Neural Plast, 2016. **2016**: p. 3204519.
108. Nelson, C.D., et al., *Phosphorylation of threonine-19 of PSD-95 by GSK-3beta is required for PSD-95 mobilization and long-term depression.* J Neurosci, 2013. **33**(29): p. 12122-35.
109. Schnell, E., et al., *Direct interactions between PSD-95 and stargazin control synaptic AMPA receptor number.* Proc Natl Acad Sci U S A, 2002. **99**(21): p. 13902-7.
110. Nagga, K., N. Bogdanovic, and J. Marcusson, *GABA transporters (GAT-1) in Alzheimer's disease.* Journal of Neural Transmission, 1999. **106**(11-12): p. 1141-1149.
111. Govindpani, K., et al., *Towards a Better Understanding of GABAergic Remodeling in Alzheimer's Disease.* Int J Mol Sci, 2017. **18**(8).
112. Jin, X.T., et al., *Localization and Function of GABA Transporters GAT-1 and GAT-3 in the Basal Ganglia.* Front Syst Neurosci, 2011. **5**: p. 63.
113. Hertz, L. and D.L. Rothman, *Glutamine-Glutamate Cycle Flux Is Similar in Cultured Astrocytes and Brain and Both Glutamate Production and Oxidation Are Mainly Catalyzed by Aspartate Aminotransferase.* Biology (Basel), 2017. **6**(1).
114. Lanctot, K.L., et al., *GABAergic function in Alzheimer's disease: evidence for dysfunction and potential as a therapeutic target for the treatment of behavioural and psychological symptoms of dementia.* Can J Psychiatry, 2004. **49**(7): p. 439-53.
115. Li, Y., et al., *Implications of GABAergic Neurotransmission in Alzheimer's Disease.* Front Aging Neurosci, 2016. **8**: p. 31.
116. Beliveau, V., et al., *A High-Resolution In Vivo Atlas of the Human Brain's Serotonin System.* J Neurosci, 2017. **37**(1): p. 120-128.
117. Rodriguez, J.J., H.N. Noristani, and A. Verkhratsky, *The serotonergic system in ageing and Alzheimer's disease.* Prog Neurobiol, 2012. **99**(1): p. 15-41.

118. Lezoualc'h, F., *5-HT4 receptor and Alzheimer's disease: the amyloid connection.* Exp Neurol, 2007. **205**(2): p. 325-9.
119. Geldenhuys, W.J. and C.J. Van der Schyf, *Role of serotonin in Alzheimer's disease: a new therapeutic target?* CNS Drugs, 2011. **25**(9): p. 765-81.
120. Ramirez, M.J., *5-HT6 receptors and Alzheimer's disease.* Alzheimers Res Ther, 2013. **5**(2): p. 15.
121. Nobili, A., et al., *Dopamine neuronal loss contributes to memory and reward dysfunction in a model of Alzheimer's disease.* Nat Commun, 2017. **8**: p. 14727.
122. Martorana, A. and G. Koch, *"Is dopamine involved in Alzheimer's disease?".* Front Aging Neurosci, 2014. **6**: p. 252.
123. Rasheed, N. and A. Alghasham, *Central dopaminergic system and its implications in stress-mediated neurological disorders and gastric ulcers: short review.* Adv Pharmacol Sci, 2012. **2012**: p. 182671.
124. Rossato, J.I., et al., *Dopamine controls persistence of long-term memory storage.* Science, 2009. **325**(5943): p. 1017-20.
125. Russo, S.J. and E.J. Nestler, *The brain reward circuitry in mood disorders.* Nat Rev Neurosci, 2013. **14**(9): p. 609-25.
126. Storga, D., et al., *Monoaminergic neurotransmitters, their precursors and metabolites in brains of Alzheimer patients.* Neurosci Lett, 1996. **203**(1): p. 29-32.
127. Pan, X., et al., *Dopamine and Dopamine Receptors in Alzheimer's Disease: A Systematic Review and Network Meta-Analysis.* Front Aging Neurosci, 2019. **11**: p. 175.
128. Xu, Y., et al., *Neurotransmitter receptors and cognitive dysfunction in Alzheimer's disease and Parkinson's disease.* Prog Neurobiol, 2012. **97**(1): p. 1-13.
129. Popp, J., et al., *Markers of neuroinflammation associated with Alzheimer's disease pathology in older adults.* Brain Behav Immun, 2017. **62**: p. 203-211.
130. Hane, F.T., B.Y. Lee, and Z. Leonenko, *Recent Progress in Alzheimer's Disease Research, Part 1: Pathology.* J Alzheimers Dis, 2017. **57**(1): p. 1-28.
131. Shi, Y. and D.M. Holtzman, *Interplay between innate immunity and Alzheimer disease: APOE and TREM2 in the spotlight.* Nat Rev Immunol, 2018. **18**(12): p. 759-772.
132. Gehrmann, J., Y. Matsumoto, and G.W. Kreutzberg, *Microglia: intrinsic immuneffector cell of the brain.* Brain Res Brain Res Rev, 1995. **20**(3): p. 269-87.
133. Heneka, M.T., et al., *Neuroinflammation in Alzheimer's disease.* Lancet Neurol, 2015. **14**(4): p. 388-405.
134. Kierdorf, K. and M. Prinz, *Factors regulating microglia activation.* Front Cell Neurosci, 2013. **7**: p. 44.
135. Fiebich, B.L., et al., *Role of Microglia TLRs in Neurodegeneration.* Front Cell Neurosci, 2018. **12**: p. 329.
136. Garcia-Revilla, J., et al., *Reformulating Pro-Oxidant Microglia in Neurodegeneration.* J Clin Med, 2019. **8**(10).
137. Walker, D.G. and L.F. Lue, *Immune phenotypes of microglia in human neurodegenerative disease: challenges to detecting microglial polarization in human brains.* Alzheimers Res Ther, 2015. **7**(1): p. 56.
138. Mantovani, A., et al., *The chemokine system in diverse forms of macrophage activation and polarization.* Trends Immunol, 2004. **25**(12): p. 677-86.
139. Lehrman, E.K., et al., *CD47 Protects Synapses from Excess Microglia-Mediated Pruning during Development.* Neuron, 2018. **100**(1): p. 120-134 e6.
140. Zhou, Y., T.K. Ulland, and M. Colonna, *TREM2-Dependent Effects on Microglia in Alzheimer's Disease.* Front Aging Neurosci, 2018. **10**: p. 202.
141. Ulland, T.K. and M. Colonna, *TREM2 - a key player in microglial biology and Alzheimer disease.* Nat Rev Neurol, 2018. **14**(11): p. 667-675.
142. Gratuze, M., C.E.G. Leyns, and D.M. Holtzman, *New insights into the role of TREM2 in Alzheimer's disease.* Mol Neurodegener, 2018. **13**(1): p. 66.

143. Sarlus, H. and M.T. Heneka, *Microglia in Alzheimer's disease.* J Clin Invest, 2017. **127**(9): p. 3240-3249.
144. Bisht, K., et al., *Dark microglia: A new phenotype predominantly associated with pathological states.* Glia, 2016. **64**(5): p. 826-39.
145. Phillips, E.C., et al., *Astrocytes and neuroinflammation in Alzheimer's disease.* Biochem Soc Trans, 2014. **42**(5): p. 1321-5.
146. Cai, Z., C.Q. Wan, and Z. Liu, *Astrocyte and Alzheimer's disease.* J Neurol, 2017. **264**(10): p. 2068-2074.
147. Fakhoury, M., *Microglia and Astrocytes in Alzheimer's Disease: Implications for Therapy.* Curr Neuropharmacol, 2018. **16**(5): p. 508-518.
148. Kamphuis, W., et al., *Glial fibrillary acidic protein isoform expression in plaque related astrogliosis in Alzheimer's disease.* Neurobiol Aging, 2014. **35**(3): p. 492-510.
149. Liu, C., et al., *Neuroinflammation in Alzheimer's disease: chemokines produced by astrocytes and chemokine receptors.* Int J Clin Exp Pathol, 2014. **7**(12): p. 8342-55.
150. Bagyinszky, E., et al., *Role of inflammatory molecules in the Alzheimer's disease progression and diagnosis.* J Neurol Sci, 2017. **376**: p. 242-254.
151. Zuena, A.R., et al., *Chemokines in Alzheimer's Disease: New Insights Into Prokineticins, Chemokine-Like Proteins.* Front Pharmacol, 2019. **10**: p. 622.
152. Chakraborty, A., et al., *The blood brain barrier in Alzheimer's disease.* Vascul Pharmacol, 2017. **89**: p. 12-18.
153. Obermeier, B., A. Verma, and R.M. Ransohoff, *The blood-brain barrier.* Handb Clin Neurol, 2016. **133**: p. 39-59.
154. Abbott, N.J., L. Ronnback, and E. Hansson, *Astrocyte-endothelial interactions at the blood-brain barrier.* Nat Rev Neurosci, 2006. **7**(1): p. 41-53.
155. Yamazaki, Y. and T. Kanekiyo, *Blood-Brain Barrier Dysfunction and the Pathogenesis of Alzheimer's Disease.* Int J Mol Sci, 2017. **18**(9).
156. Pellerin, L. and P.J. Magistretti, *Sweet sixteen for ANLS.* J Cereb Blood Flow Metab, 2012. **32**(7): p. 1152-66.
157. Pietronigro, E., E. Zenaro, and G. Constantin, *Imaging of Leukocyte Trafficking in Alzheimer's Disease.* Front Immunol, 2016. **7**: p. 33.
158. Simpson, I.A., et al., *Decreased concentrations of GLUT1 and GLUT3 glucose transporters in the brains of patients with Alzheimer's disease.* Ann Neurol, 1994. **35**(5): p. 546-51.
159. Winkler, E.A., et al., *GLUT1 reductions exacerbate Alzheimer's disease vasculo-neuronal dysfunction and degeneration.* Nat Neurosci, 2015. **18**(4): p. 521-530.
160. Shibata, M., et al., *Clearance of Alzheimer's amyloid-ss(1-40) peptide from brain by LDL receptor-related protein-1 at the blood-brain barrier.* J Clin Invest, 2000. **106**(12): p. 1489-99.
161. Deane, R., et al., *A multimodal RAGE-specific inhibitor reduces amyloid beta-mediated brain disorder in a mouse model of Alzheimer disease.* J Clin Invest, 2012. **122**(4): p. 1377-92.
162. Domingues, C., E.S.O.A.B. da Cruz, and A.G. Henriques, *Impact of Cytokines and Chemokines on Alzheimer's Disease Neuropathological Hallmarks.* Curr Alzheimer Res, 2017. **14**(8): p. 870-882.
163. Popescu, B.O., et al., *Blood-brain barrier alterations in ageing and dementia.* J Neurol Sci, 2009. **283**(1-2): p. 99-106.
164. Sengillo, J.D., et al., *Deficiency in mural vascular cells coincides with blood-brain barrier disruption in Alzheimer's disease.* Brain Pathol, 2013. **23**(3): p. 303-10.
165. Uetani, H., et al., *Prevalence and topography of small hypointense foci suggesting microbleeds on 3T susceptibility-weighted imaging in various types of dementia.* AJNR Am J Neuroradiol, 2013. **34**(5): p. 984-9.
166. Kantarci, K., et al., *Focal hemosiderin deposits and beta-amyloid load in the ADNI cohort.* Alzheimers Dement, 2013. **9**(5 Suppl): p. S116-23.
167. Kook, S.Y., et al., *Abeta(1)(-)(4)(2)-RAGE interaction disrupts tight junctions of the blood-brain barrier via Ca(2)(+)-calcineurin signaling.* J Neurosci, 2012. **32**(26): p. 8845-54.

168. Wan, W., et al., *Abeta(1-42) oligomer-induced leakage in an in vitro blood-brain barrier model is associated with up-regulation of RAGE and metalloproteinases, and down-regulation of tight junction scaffold proteins.* J Neurochem, 2015. **134**(2): p. 382-93.
169. Lepelletier, F.X., et al., *Early changes in extracellular matrix in Alzheimer's disease.* Neuropathol Appl Neurobiol, 2017. **43**(2): p. 167-182.
170. Yang, J., et al., *Loss of astrocyte polarization in the tg-ArcSwe mouse model of Alzheimer's disease.* J Alzheimers Dis, 2011. **27**(4): p. 711-22.
171. Izquierdo, I., et al., *Separate mechanisms for short- and long-term memory.* Behavioural Brain Research, 1999. **103**(1): p. 1-11.
172. Kukushkin, N.V. and T.J. Carew, *Memory Takes Time.* Neuron, 2017. **95**(2): p. 259-279.
173. Thompson, R.F. and J.J. Kim, *Memory systems in the brain and localization of a memory.* Proceedings of the National Academy of Sciences of the United States of America, 1996. **93**(24): p. 13438-13444.
174. Amaral, D.G., *Emerging principles of intrinsic hippocampal organization.* Curr Opin Neurobiol, 1993. **3**(2): p. 225-9.
175. Li, Y., Y. Mu, and F.H. Gage, *Development of neural circuits in the adult hippocampus.* Curr Top Dev Biol, 2009. **87**: p. 149-74.
176. Amtul, Z. and R. Atta Ur, *Neural plasticity and memory: molecular mechanism.* Rev Neurosci, 2015. **26**(3): p. 253-68.
177. Zhang, X.M. and J. Zhu, *Kainic Acid-induced neurotoxicity: targeting glial responses and glia-derived cytokines.* Curr Neuropharmacol, 2011. **9**(2): p. 388-98.
178. Hernandez, P.J. and T. Abel, *The role of protein synthesis in memory consolidation: progress amid decades of debate.* Neurobiol Learn Mem, 2008. **89**(3): p. 293-311.
179. Alberini, C.M., *Transcription factors in long-term memory and synaptic plasticity.* Physiol Rev, 2009. **89**(1): p. 121-45.
180. Buffington, S.A., W. Huang, and M. Costa-Mattioli, *Translational control in synaptic plasticity and cognitive dysfunction.* Annu Rev Neurosci, 2014. **37**: p. 17-38.
181. Ohno, M., *Roles of eIF2α kinases in the pathogenesis of Alzheimer's disease.* Front Mol Neurosci, 2014. **7**: p. 22.
182. Jennings, M.D. and G.D. Pavitt, *A new function and complexity for protein translation initiation factor eIF2B.* Cell Cycle, 2014. **13**(17): p. 2660-5.
183. Trinh, M.A. and E. Klann, *Translational control by eIF2alpha kinases in long-lasting synaptic plasticity and long-term memory.* Neurobiol Learn Mem, 2013. **105**: p. 93-9.
184. Chesnokova, E., N. Bal, and P. Kolosov, *Kinases of eIF2a Switch Translation of mRNA Subset during Neuronal Plasticity.* Int J Mol Sci, 2017. **18**(10).
185. Trinh, M.A., et al., *Brain-specific disruption of the eIF2alpha kinase PERK decreases ATF4 expression and impairs behavioral flexibility.* Cell Rep, 2012. **1**(6): p. 676-88.
186. Holcik, M., *Could the eIF2alpha-Independent Translation Be the Achilles Heel of Cancer?* Front Oncol, 2015. **5**: p. 264.
187. Milisav, I., D. Suput, and S. Ribaric, *Unfolded Protein Response and Macroautophagy in Alzheimer's, Parkinson's and Prion Diseases.* Molecules, 2015. **20**(12): p. 22718-56.
188. Imaizumi, K., et al., *The unfolded protein response and Alzheimer's disease.* Biochim Biophys Acta, 2001. **1536**(2-3): p. 85-96.
189. Doyle, K.M., et al., *Unfolded proteins and endoplasmic reticulum stress in neurodegenerative disorders.* Journal of Cellular and Molecular Medicine, 2011. **15**(10): p. 2025-2039.
190. Saito, A. and K. Imaizumi, *The broad spectrum of signaling pathways regulated by unfolded protein response in neuronal homeostasis.* Neurochem Int, 2018. **119**: p. 26-34.
191. Pinto, B.A.S., et al., *Unfolded Protein Response: Cause or Consequence of Lipid and Lipoprotein Metabolism Disturbances?* Adv Exp Med Biol, 2019. **1127**: p. 67-82.
192. Roussel, B.D., et al., *Endoplasmic reticulum dysfunction in neurological disease.* Lancet Neurol, 2013. **12**(1): p. 105-18.

193. Printsev, I., D. Curiel, and K.L. Carraway, 3rd, *Membrane Protein Quantity Control at the Endoplasmic Reticulum.* J Membr Biol, 2016.
194. Hetz, C., *The unfolded protein response: controlling cell fate decisions under ER stress and beyond.* Nat Rev Mol Cell Biol, 2012. **13**(2): p. 89-102.
195. Wei, N., L.Q. Zhu, and D. Liu, *ATF4: a Novel Potential Therapeutic Target for Alzheimer's Disease.* Molecular Neurobiology, 2015. **52**(3): p. 1765-1770.
196. Ameri, K. and A.L. Harris, *Activating transcription factor 4.* Int J Biochem Cell Biol, 2008. **40**(1): p. 14-21.
197. Rozpedek, W., et al., *The Role of the PERK/eIF2alpha/ATF4/CHOP Signaling Pathway in Tumor Progression During Endoplasmic Reticulum Stress.* Curr Mol Med, 2016. **16**(6): p. 533-44.
198. Cheng, J., et al., *The emerging roles of protein homeostasis-governing pathways in Alzheimer's disease.* Aging Cell, 2018. **17**(5): p. e12801.
199. Perluigi, M., F. Di Domenico, and D.A. Butterfield, *mTOR signaling in aging and neurodegeneration: At the crossroad between metabolism dysfunction and impairment of autophagy.* Neurobiol Dis, 2015. **84**: p. 39-49.
200. Talboom, J.S., R. Velazquez, and S. Oddo, *The mammalian target of rapamycin at the crossroad between cognitive aging and Alzheimer's disease.* NPJ Aging Mech Dis, 2015. **1**: p. 15008.
201. Morita, M., et al., *mTOR coordinates protein synthesis, mitochondrial activity and proliferation.* Cell Cycle, 2015. **14**(4): p. 473-80.
202. Saxton, R.A. and D.M. Sabatini, *mTOR Signaling in Growth, Metabolism, and Disease.* Cell, 2017. **169**(2): p. 361-371.
203. Wang, X., et al., *Regulation of elongation factor 2 kinase by p90(RSK1) and p70 S6 kinase.* EMBO J, 2001. **20**(16): p. 4370-9.
204. Dunlop, E.A. and A.R. Tee, *mTOR and autophagy: a dynamic relationship governed by nutrients and energy.* Semin Cell Dev Biol, 2014. **36**: p. 121-9.
205. Morita, M., et al., *mTOR Controls Mitochondrial Dynamics and Cell Survival via MTFP1.* Mol Cell, 2017. **67**(6): p. 922-935 e5.
206. Youle, R.J. and A.M. van der Bliek, *Mitochondrial fission, fusion, and stress.* Science, 2012. **337**(6098): p. 1062-5.
207. Ryskalin, L., et al., *mTOR-Dependent Cell Proliferation in the Brain.* Biomed Res Int, 2017. **2017**: p. 7082696.
208. Elmore, S., *Apoptosis: a review of programmed cell death.* Toxicol Pathol, 2007. **35**(4): p. 495-516.
209. Obulesu, M. and M.J. Lakshmi, *Apoptosis in Alzheimer's disease: an understanding of the physiology, pathology and therapeutic avenues.* Neurochem Res, 2014. **39**(12): p. 2301-12.
210. Sovolyova, N., et al., *Stressed to death - mechanisms of ER stress-induced cell death.* Biol Chem, 2014. **395**(1): p. 1-13.
211. Galehdar, Z., et al., *Neuronal apoptosis induced by endoplasmic reticulum stress is regulated by ATF4-CHOP-mediated induction of the Bcl-2 homology 3-only member PUMA.* J Neurosci, 2010. **30**(50): p. 16938-48.
212. Fribley, A., K. Zhang, and R.J. Kaufman, *Regulation of apoptosis by the unfolded protein response.* Methods Mol Biol, 2009. **559**: p. 191-204.
213. Faitova, J., et al., *Endoplasmic reticulum stress and apoptosis.* Cell Mol Biol Lett, 2006. **11**(4): p. 488-505.
214. Lee, S. and K.T. Min, *The Interface Between ER and Mitochondria: Molecular Compositions and Functions.* Mol Cells, 2018. **41**(12): p. 1000-1007.
215. Schon, E.A. and E. Area-Gomez, *Mitochondria-associated ER membranes in Alzheimer disease.* Molecular and Cellular Neuroscience, 2013. **55**: p. 26-36.
216. Cenini, G. and W. Voos, *Mitochondria as Potential Targets in Alzheimer Disease Therapy: An Update.* Front Pharmacol, 2019. **10**: p. 902.

217. Valko, M., et al., *Free radicals and antioxidants in normal physiological functions and human disease.* Int J Biochem Cell Biol, 2007. **39**(1): p. 44-84.
218. Guo, T., W. Noble, and D.P. Hanger, *Roles of tau protein in health and disease.* Acta Neuropathol, 2017. **133**(5): p. 665-704.
219. Casas, C., *GRP78 at the Centre of the Stage in Cancer and Neuroprotection.* Front Neurosci, 2017. **11**: p. 177.
220. Hoozemans, J.J., et al., *The unfolded protein response is activated in Alzheimer's disease.* Acta Neuropathol, 2005. **110**(2): p. 165-72.
221. Soejima, N., et al., *Intracellular accumulation of toxic turn amyloid-beta is associated with endoplasmic reticulum stress in Alzheimer's disease.* Curr Alzheimer Res, 2013. **10**(1): p. 11-20.
222. Ma, T., et al., *Suppression of eIF2alpha kinases alleviates Alzheimer's disease-related plasticity and memory deficits.* Nat Neurosci, 2013. **16**(9): p. 1299-305.
223. Devi, L. and M. Ohno, *PERK mediates eIF2alpha phosphorylation responsible for BACE1 elevation, CREB dysfunction and neurodegeneration in a mouse model of Alzheimer's disease.* Neurobiol Aging, 2014. **35**(10): p. 2272-81.
224. Spilman, P., et al., *Inhibition of mTOR by rapamycin abolishes cognitive deficits and reduces amyloid-beta levels in a mouse model of Alzheimer's disease.* PLoS One, 2010. **5**(4): p. e9979.
225. Caccamo, A., et al., *Molecular interplay between mammalian target of rapamycin (mTOR), amyloid-beta, and Tau: effects on cognitive impairments.* J Biol Chem, 2010. **285**(17): p. 13107-20.
226. Jiang, T., et al., *Temsirolimus promotes autophagic clearance of amyloid-beta and provides protective effects in cellular and animal models of Alzheimer's disease.* Pharmacol Res, 2014. **81**: p. 54-63.
227. Lovinger, D.M., *Communication networks in the brain: neurons, receptors, neurotransmitters, and alcohol.* Alcohol Res Health, 2008. **31**(3): p. 196-214.
228. Janz, R., et al., *SV2A and SV2B function as redundant Ca2+ regulators in neurotransmitter release.* Neuron, 1999. **24**(4): p. 1003-16.
229. Stout, K.A., et al., *The Synaptic Vesicle Glycoprotein 2: Structure, Function, and Disease Relevance.* ACS Chem Neurosci, 2019. **10**(9): p. 3927-3938.
230. Tokudome, K., et al., *Synaptic vesicle glycoprotein 2A (SV2A) regulates kindling epileptogenesis via GABAergic neurotransmission.* Sci Rep, 2016. **6**: p. 27420.
231. Robinson, J.L., et al., *Perforant path synaptic loss correlates with cognitive impairment and Alzheimer's disease in the oldest-old.* Brain, 2014. **137**(Pt 9): p. 2578-87.
232. Sanchez, P.E., et al., *Levetiracetam suppresses neuronal network dysfunction and reverses synaptic and cognitive deficits in an Alzheimer's disease model.* Proc Natl Acad Sci U S A, 2012. **109**(42): p. E2895-903.
233. Scheff, S.W., et al., *Hippocampal synaptic loss in early Alzheimer's disease and mild cognitive impairment.* Neurobiol Aging, 2006. **27**(10): p. 1372-84.
234. Hamos, J.E., L.J. DeGennaro, and D.A. Drachman, *Synaptic loss in Alzheimer's disease and other dementias.* Neurology, 1989. **39**(3): p. 355-61.
235. Sze, C.I., et al., *Loss of the presynaptic vesicle protein synaptophysin in hippocampus correlates with cognitive decline in Alzheimer disease.* J Neuropathol Exp Neurol, 1997. **56**(8): p. 933-44.
236. Mufson, E.J., et al., *Hippocampal plasticity during the progression of Alzheimer's disease.* Neuroscience, 2015. **309**: p. 51-67.
237. Broadhouse, K.M., et al., *Hippocampal plasticity underpins long-term cognitive gains from resistance exercise in MCI.* Neuroimage Clin, 2020. **25**: p. 102182.
238. Drummond, E. and T. Wisniewski, *Alzheimer's disease: experimental models and reality.* Acta Neuropathol, 2017. **133**(2): p. 155-175.
239. Sasaguri, H., et al., *APP mouse models for Alzheimer's disease preclinical studies.* EMBO J, 2017. **36**(17): p. 2473-2487.

240. Jankowsky, J.L. and H. Zheng, *Practical considerations for choosing a mouse model of Alzheimer's disease.* Mol Neurodegener, 2017. **12**(1): p. 89.
241. Do Carmo, S. and A.C. Cuello, *Modeling Alzheimer's disease in transgenic rats.* Mol Neurodegener, 2013. **8**: p. 37.
242. Benedikz, E., E. Kloskowska, and B. Winblad, *The rat as an animal model of Alzheimer's disease.* J Cell Mol Med, 2009. **13**(6): p. 1034-42.
243. Cohen, R.M., et al., *A transgenic Alzheimer rat with plaques, tau pathology, behavioral impairment, oligomeric aβ, and frank neuronal loss.* J Neurosci, 2013. **33**(15): p. 6245-56.
244. Joo, I.L., et al., *Early neurovascular dysfunction in a transgenic rat model of Alzheimer's disease.* Sci Rep, 2017. **7**: p. 46427.
245. Voorhees, J.R., et al., *(-)-P7C3-S243 Protects a Rat Model of Alzheimer's Disease From Neuropsychiatric Deficits and Neurodegeneration Without Altering Amyloid Deposition or Reactive Glia.* Biol Psychiatry, 2018. **84**(7): p. 488-498.
246. Anckaerts, C., et al., *Early functional connectivity deficits and progressive microstructural alterations in the TgF344-AD rat model of Alzheimer's Disease: A longitudinal MRI study.* Neurobiol Dis, 2019. **124**: p. 93-107.
247. Leplus, A., et al., *Chronic fornix deep brain stimulation in a transgenic Alzheimer's rat model reduces amyloid burden, inflammation, and neuronal loss.* Brain Struct Funct, 2019. **224**(1): p. 363-372.
248. Smith, L.A. and L.L. McMahon, *Deficits in synaptic function occur at medial perforant path-dentate granule cell synapses prior to Schaffer collateral-CA1 pyramidal cell synapses in the novel TgF344-Alzheimer's Disease Rat Model.* Neurobiol Dis, 2018. **110**: p. 166-179.
249. Munoz-Moreno, E., et al., *Brain connectivity during Alzheimer's disease progression and its cognitive impact in a transgenic rat model.* Netw Neurosci, 2020. **4**(2): p. 397-415.
250. Rorabaugh, J.M., et al., *Chemogenetic locus coeruleus activation restores reversal learning in a rat model of Alzheimer's disease.* Brain, 2017. **140**(11): p. 3023-3038.
251. Pentkowski, N.S., et al., *Anxiety-like behavior as an early endophenotype in the TgF344-AD rat model of Alzheimer's disease.* Neurobiol Aging, 2018. **61**: p. 169-176.
252. Berkowitz, L.E., et al., *Progressive impairment of directional and spatially precise trajectories by TgF344-Alzheimer's disease rats in the Morris Water Task.* Sci Rep, 2018. **8**(1): p. 16153.
253. Mosconi, L., et al., *Pre-clinical detection of Alzheimer's disease using FDG-PET, with or without amyloid imaging.* J Alzheimers Dis, 2010. **20**(3): p. 843-54.
254. Saha, G.B., *Basics of PET imaging physics, chemistry, and regulations.* 2005.
255. Melcher, C.L., *Scintillation crystals for PET.* J Nucl Med, 2000. **41**(6): p. 1051-5.
256. Shukla, A.K. and U. Kumar, *Positron emission tomography: An overview.* J Med Phys, 2006. **31**(1): p. 13-21.
257. Anizan, N., et al., *dAcquisition setting optimization and quantitative imaging for 124I studies with the Inveon microPET-CT system.* EJNMMI Res, 2012. **2**: p. 7.
258. Bolus, N.E., et al., *PET/MRI: the blended-modality choice of the future?* J Nucl Med Technol, 2009. **37**(2): p. 63-71; quiz 72-3.
259. Dahlbom, S.R.C.a.M., *PET: Physics, Instrumentation, and Scanners.* 2006.
260. Kinahan, P.E., B.H. Hasegawa, and T. Beyer, *X-ray-based attenuation correction for positron emission tomography/computed tomography scanners.* Semin Nucl Med, 2003. **33**(3): p. 166-79.
261. Maroy, R., et al., *Segmentation of rodent whole-body dynamic PET images: an unsupervised method based on voxel dynamics.* IEEE Trans Med Imaging, 2008. **27**(3): p. 342-54.
262. Maroy, R., et al., *Quantitative organ time activity curve extraction from rodent PET images without anatomical prior.* Med Phys, 2010. **37**(4): p. 1507-17.
263. Thal, D.R., et al., *[(18)F]flutemetamol amyloid positron emission tomography in preclinical and symptomatic Alzheimer's disease: specific detection of advanced phases of amyloid-beta pathology.* Alzheimers Dement, 2015. **11**(8): p. 975-85.

264. Martinez, G., et al., *18F PET with florbetapir for the early diagnosis of Alzheimer's disease dementia and other dementias in people with mild cognitive impairment (MCI).* Cochrane Database Syst Rev, 2017. **11**: p. CD012216.
265. Sabri, O., et al., *Beta-amyloid imaging with florbetaben.* Clin Transl Imaging, 2015. **3**(1): p. 13-26.
266. Nordberg, A., et al., *The use of PET in Alzheimer disease.* Nat Rev Neurol, 2010. **6**(2): p. 78-87.
267. Lowe, V.J., et al., *Comparison of 18F-FDG and PiB PET in cognitive impairment.* J Nucl Med, 2009. **50**(6): p. 878-86.
268. Wang, Y.T. and P. Edison, *Tau Imaging in Neurodegenerative Diseases Using Positron Emission Tomography.* Curr Neurol Neurosci Rep, 2019. **19**(7): p. 45.
269. Shah, M. and A.M. Catafau, *Molecular Imaging Insights into Neurodegeneration: Focus on Tau PET Radiotracers.* J Nucl Med, 2014. **55**(6): p. 871-4.
270. Okamura, N., et al., *The development and validation of tau PET tracers: current status and future directions.* Clin Transl Imaging, 2018. **6**(4): p. 305-316.
271. Rinne, J.O., et al., *Brain acetylcholinesterase activity in mild cognitive impairment and early Alzheimer's disease.* J Neurol Neurosurg Psychiatry, 2003. **74**(1): p. 113-5.
272. Xu, J., et al., *Translocator protein in late stage Alzheimer's disease and Dementia with Lewy bodies brains.* Ann Clin Transl Neurol, 2019. **6**(8): p. 1423-1434.
273. Lavisse, S., et al., *Reactive astrocytes overexpress TSPO and are detected by TSPO positron emission tomography imaging.* J Neurosci, 2012. **32**(32): p. 10809-18.
274. Pannell, M., et al., *Imaging of translocator protein upregulation is selective for pro-inflammatory polarized astrocytes and microglia.* Glia, 2020. **68**(2): p. 280-297.
275. Shah, F., et al., *Synthesis of the enantiomers of [N-methyl-11C]PK 11195 and comparison of their behaviours as radioligands for PK binding sites in rats.* Nucl Med Biol, 1994. **21**(4): p. 573-81.
276. Lockhart, A., et al., *The peripheral benzodiazepine receptor ligand PK11195 binds with high affinity to the acute phase reactant alpha1-acid glycoprotein: implications for the use of the ligand as a CNS inflammatory marker.* Nucl Med Biol, 2003. **30**(2): p. 199-206.
277. Groom, G.N., et al., *PET of peripheral benzodiazepine binding sites in the microgliosis of Alzheimer's disease.* J Nucl Med, 1995. **36**(12): p. 2207-10.
278. Cagnin, A., et al., *In-vivo measurement of activated microglia in dementia.* Lancet, 2001. **358**(9280): p. 461-7.
279. Hamelin, L., et al., *Early and protective microglial activation in Alzheimer's disease: a prospective study using 18F-DPA-714 PET imaging.* Brain, 2016. **139**(Pt 4): p. 1252-64.
280. Schilling, L.P., et al., *Imaging Alzheimer's disease pathophysiology with PET.* Dement Neuropsychol, 2016. **10**(2): p. 79-90.
281. Berroteran-Infante, N., et al., *Binding Affinity of Some Endogenous and Synthetic TSPO Ligands Regarding the rs6971 Polymorphism.* Int J Mol Sci, 2019. **20**(3).
282. Owen, D.R., et al., *An 18-kDa translocator protein (TSPO) polymorphism explains differences in binding affinity of the PET radioligand PBR28.* J Cereb Blood Flow Metab, 2012. **32**(1): p. 1-5.
283. Lagarde, J., M. Sarazin, and M. Bottlaender, *In vivo PET imaging of neuroinflammation in Alzheimer's disease.* J Neural Transm (Vienna), 2018. **125**(5): p. 847-867.
284. Hamelin, L., et al., *Early and protective microglial activation in Alzheimer's disease: a prospective study using 18F-DPA-714 PET imaging.* Brain, 2016. **139**(Pt 4): p. 1252-64.
285. Vaalburg, W., et al., *Amino acids for the measurement of protein synthesis in vivo by PET.* Int J Rad Appl Instrum B, 1992. **19**(2): p. 227-37.
286. Phelps, M.E., et al., *Criteria for the Tracer Kinetic Measurement of Cerebral Protein-Synthesis in Humans with Positron Emission Tomography.* Annals of Neurology, 1984. **15**: p. S192-S202.
287. Oldendorf, W.H., *Brain uptake of radiolabeled amino acids, amines, and hexoses after arterial injection.* Am J Physiol, 1971. **221**(6): p. 1629-39.

288. Sun, A., X. Liu, and G. Tang, *Carbon-11 and Fluorine-18 Labeled Amino Acid Tracers for Positron Emission Tomography Imaging of Tumors.* Front Chem, 2017. **5**: p. 124.
289. Bishu, S., et al., *Regional rates of cerebral protein synthesis measured with L-[1-11C]leucine and PET in conscious, young adult men: normal values, variability, and reproducibility.* J Cereb Blood Flow Metab, 2008. **28**(8): p. 1502-13.
290. Kido, Y., et al., *Molecular and functional identification of large neutral amino acid transporters LAT1 and LAT2 and their pharmacological relevance at the blood-brain barrier.* J Pharm Pharmacol, 2001. **53**(4): p. 497-503.
291. Smith, Q.R., *Transport of glutamate and other amino acids at the blood-brain barrier.* J Nutr, 2000. **130**(4S Suppl): p. 1016S-22S.
292. Pardridge, W.M., *Blood-brain barrier carrier-mediated transport and brain metabolism of amino acids.* Neurochemical Research, 1998. **23**(5): p. 635-644.
293. Schmidt, K.C., et al., *Measurement of regional rates of cerebral protein synthesis with L-[1-11C]leucine and PET with correction for recycling of tissue amino acids: I. Kinetic modeling approach.* J Cereb Blood Flow Metab, 2005. **25**(5): p. 617-28.
294. Keen, R.E., et al., *In vivo cerebral protein synthesis rates with leucyl-transfer RNA used as a precursor pool: determination of biochemical parameters to structure tracer kinetic models for positron emission tomography.* J Cereb Blood Flow Metab, 1989. **9**(4): p. 429-45.
295. Watabe, H., et al., *PET kinetic analysis - compartmental model.* Annals of Nuclear Medicine, 2006. **20**(9): p. 583-588.
296. Smith, C.B., et al., *Measurement of local cerebral protein synthesis in vivo: influence of recycling of amino acids derived from protein degradation.* Proc Natl Acad Sci U S A, 1988. **85**(23): p. 9341-5.
297. Sundaram, S.K., et al., *Quantification of protein synthesis in the human brain using L-[1-11C]-leucine PET: incorporation of factors for large neutral amino acids in plasma and for amino acids recycled from tissue.* J Nucl Med, 2006. **47**(11): p. 1787-95.
298. Cai, Z., et al., *PET imaging of synaptic density: A new tool for investigation of neuropsychiatric diseases.* Neurosci Lett, 2019. **691**: p. 44-50.
299. Heurling, K., et al., *Synaptic vesicle protein 2A as a potential biomarker in synaptopathies.* Mol Cell Neurosci, 2019. **97**: p. 34-42.
300. Becker, G., et al., *Pharmacokinetic Characterization of [(18)F]UCB-H PET Radiopharmaceutical in the Rat Brain.* Mol Pharm, 2017. **14**(8): p. 2719-2725.
301. Bastin, C., et al., *In vivo imaging of synaptic loss in Alzheimer's disease with [18F]UCB-H positron emission tomography.* Eur J Nucl Med Mol Imaging, 2020. **47**(2): p. 390-402.
302. Chen, M.K., et al., *Assessing Synaptic Density in Alzheimer Disease With Synaptic Vesicle Glycoprotein 2A Positron Emission Tomographic Imaging.* JAMA Neurol, 2018. **75**(10): p. 1215-1224.
303. Boutin, H., et al., *18F-GE-180: a novel TSPO radiotracer compared to 11C-R-PK11195 in a preclinical model of stroke.* Eur J Nucl Med Mol Imaging, 2015. **42**(3): p. 503-11.
304. Visser, E.P., et al., *Spatial resolution and sensitivity of the Inveon small-animal PET scanner.* J Nucl Med, 2009. **50**(1): p. 139-47.
305. Bolcaen, J., et al., *Kinetic Modeling and Graphical Analysis of 18F-Fluoromethylcholine (FCho), 18F-Fluoroethyltyrosine (FET) and 18F-Fluorodeoxyglucose (FDG) PET for the Fiscrimination between High-Grade Glioma and Radiation Necrosis in Rats.* PLoS One, 2016. **11**(8): p. e0161845.
306. Lee, H.B. and M.D. Blaufox, *Blood volume in the rat.* J Nucl Med, 1985. **26**(1): p. 72-6.
307. Mercier, J., L. Provins, and A. Valade, *Discovery and development of SV2A PET tracers: Potential for imaging synaptic density and clinical applications.* Drug Discov Today Technol, 2017. **25**: p. 45-52.
308. Maroy, R., et al., *Local Means Analysis: an unsupervised method for the segmentation of rodent whole-body dynamic PET images.* 2007 4th Ieee International Symposium on Biomedical Imaging : Macro to Nano, Vols 1-3, 2007: p. 324-327.

309. Schwarz, A.J., et al., *A stereotaxic MRI template set for the rat brain with tissue class distribution maps and co-registered anatomical atlas: application to pharmacological MRI.* Neuroimage, 2006. **32**(2): p. 538-50.
310. Zanotti-Fregonara, P., et al., *Image-derived input function for brain PET studies: many challenges and few opportunities.* J Cereb Blood Flow Metab, 2011. **31**(10): p. 1986-98.
311. Veronese, M., et al., *Spectral Analysis of Dynamic PET Studies: A Review of 20 Years of Method Developments and Applications.* Comput Math Methods Med, 2016. **2016**: p. 7187541.
312. Schweikhard, E.S. and C.M. Ziegler, *Amino acid secondary transporters: toward a common transport mechanism.* Curr Top Membr, 2012. **70**: p. 1-28.
313. Klann, E., et al., *Synaptic plasticity and translation initiation.* Learn Mem, 2004. **11**(4): p. 365-72.
314. Nader, K., G.E. Schafe, and J.E. Le Doux, *Fear memories require protein synthesis in the amygdala for reconsolidation after retrieval.* Nature, 2000. **406**(6797): p. 722-6.
315. Park, H. and B.K. Kaang, *Balanced actions of protein synthesis and degradation in memory formation.* Learn Mem, 2019. **26**(9): p. 299-306.
316. Sen, N., *ER Stress, CREB, and Memory: A Tangled Emerging Link in Disease.* Neuroscientist, 2019. **25**(5): p. 420-433.
317. Hetz, C., J.M. Axten, and J.B. Patterson, *Publisher Correction: Pharmacological targeting of the unfolded protein response for disease intervention.* Nat Chem Biol, 2019. **15**(11): p. 1129.
318. Axten, J.M., et al., *Discovery of GSK2656157: An Optimized PERK Inhibitor Selected for Preclinical Development.* ACS Med Chem Lett, 2013. **4**(10): p. 964-8.
319. Radford, H., et al., *PERK inhibition prevents tau-mediated neurodegeneration in a mouse model of frontotemporal dementia.* Acta Neuropathol, 2015. **130**(5): p. 633-42.
320. Ishiwata, K., et al., *Metabolic studies with L-[1-14C]tyrosine for the investigation of a kinetic model to measure protein synthesis rates with PET.* J Nucl Med, 1988. **29**(4): p. 524-9.
321. Ishiwata, K., et al., *Comparison of L-[1-11C]methionine and L-methyl-[11C]methionine for measuring in vivo protein synthesis rates with PET.* J Nucl Med, 1988. **29**(8): p. 1419-27.
322. Jonec, V. and C.G. Walsterlain, *Effect of inhibitors of protein synthesis on the development of kindled seizures in rats.* Exp Neurol, 1979. **66**(3): p. 524-32.
323. Smith, C.B., et al., *Measurement of regional rates of cerebral protein synthesis with L-[1-11C]leucine and PET with correction for recycling of tissue amino acids: II. Validation in rhesus monkeys.* J Cereb Blood Flow Metab, 2005. **25**(5): p. 629-40.
324. Tomasi, G., et al., *Substitution of venous for arterial blood sampling in the determination of regional rates of cerebral protein synthesis with L-[1-(11)C]leucine PET: A validation study.* J Cereb Blood Flow Metab, 2018: p. 271678X18771242.
325. Lasnon, C., et al., *Quantifying and correcting for tail vein extravasation in small animal PET scans in cancer research: is there an impact on therapy assessment?* EJNMMI Res, 2015. **5**(1): p. 61.
326. Sun, Y., et al., *Rates of local cerebral protein synthesis in the rat during normal postnatal development.* Am J Physiol, 1995. **268**(2 Pt 2): p. R549-61.
327. Hawkins, R.A., et al., *Estimation of local cerebral protein synthesis rates with L-[1-11C]leucine and PET: methods, model, and results in animals and humans.* J Cereb Blood Flow Metab, 1989. **9**(4): p. 446-60.
328. Bishu, S., et al., *Propofol anesthesia does not alter regional rates of cerebral protein synthesis measured with L-[1-(11)C]leucine and PET in healthy male subjects.* J Cereb Blood Flow Metab, 2009. **29**(5): p. 1035-47.
329. De Montis, M.G., et al., *Increase in large neutral amino acid transport into brain by insulin.* J Neurochem, 1978. **30**(1): p. 121-4.
330. Rajalingam, D., et al., *Trichloroacetic acid-induced protein precipitation involves the reversible association of a stable partially structured intermediate.* Protein Sci, 2009. **18**(5): p. 980-93.

331. Liu, A.K., et al., *Nucleus basalis of Meynert revisited: anatomy, history and differential involvement in Alzheimer's and Parkinson's disease.* Acta Neuropathol, 2015. **129**(4): p. 527-40.
332. Coughlin, J.M., et al., *The distribution of the alpha7 nicotinic acetylcholine receptor in healthy aging: An in vivo positron emission tomography study with [(18)F]ASEM.* Neuroimage, 2018. **165**: p. 118-124.
333. Court, J., et al., *Nicotinic receptor abnormalities in Alzheimer's disease.* Biol Psychiatry, 2001. **49**(3): p. 175-84.
334. Sengupta, P., *The Laboratory Rat: Relating Its Age With Human's.* Int J Prev Med, 2013. **4**(6): p. 624-30.
335. Schimanski, L.A. and C.A. Barnes, *Neural Protein Synthesis during Aging: Effects on Plasticity and Memory.* Front Aging Neurosci, 2010. **2**.
336. Santra, M., K.A. Dill, and A.M.R. de Graff, *Proteostasis collapse is a driver of cell aging and death.* Proc Natl Acad Sci U S A, 2019. **116**(44): p. 22173-22178.
337. Smith, C.B., Y. Sun, and L. Sokoloff, *Effects of aging on regional rates of cerebral protein synthesis in the Sprague-Dawley rat: examination of the influence of recycling of amino acids derived from protein degradation into the precursor pool.* Neurochem Int, 1995. **27**(4-5): p. 407-16.
338. Hof, P.R. and J.H. Morrison, *The aging brain: morphomolecular senescence of cortical circuits.* Trends Neurosci, 2004. **27**(10): p. 607-13.
339. Niikura, T., H. Tajima, and Y. Kita, *Neuronal cell death in Alzheimer's disease and a neuroprotective factor, humanin.* Curr Neuropharmacol, 2006. **4**(2): p. 139-47.
340. Donev, R., et al., *Neuronal death in Alzheimer's disease and therapeutic opportunities.* J Cell Mol Med, 2009. **13**(11-12): p. 4329-48.
341. DeKosky, S.T. and S.W. Scheff, *Synapse loss in frontal cortex biopsies in Alzheimer's disease: correlation with cognitive severity.* Ann Neurol, 1990. **27**(5): p. 457-64.
342. Terry, R.D., et al., *Physical basis of cognitive alterations in Alzheimer's disease: synapse loss is the major correlate of cognitive impairment.* Ann Neurol, 1991. **30**(4): p. 572-80.
343. Scheff, S.W., et al., *Synaptic loss in the inferior temporal gyrus in mild cognitive impairment and Alzheimer's disease.* J Alzheimers Dis, 2011. **24**(3): p. 547-57.
344. Masliah, E., et al., *Synaptic and neuritic alterations during the progression of Alzheimer's disease.* Neurosci Lett, 1994. **174**(1): p. 67-72.
345. West, M.J., et al., *Differences in the pattern of hippocampal neuronal loss in normal ageing and Alzheimer's disease.* Lancet, 1994. **344**(8925): p. 769-72.
346. West, M.J., et al., *Hippocampal neurons in pre-clinical Alzheimer's disease.* Neurobiol Aging, 2004. **25**(9): p. 1205-12.
347. Morrison, J.H. and P.R. Hof, *Life and death of neurons in the aging brain.* Science, 1997. **278**(5337): p. 412-9.
348. Anderson, B. and V. Rutledge, *Age and hemisphere effects on dendritic structure.* Brain, 1996. **119 (Pt 6)**: p. 1983-90.
349. Jacobs, B., L. Driscoll, and M. Schall, *Life-span dendritic and spine changes in areas 10 and 18 of human cortex: a quantitative Golgi study.* J Comp Neurol, 1997. **386**(4): p. 661-80.
350. Dickstein, D.L., et al., *Dendritic spine changes associated with normal aging.* Neuroscience, 2013. **251**: p. 21-32.
351. Dickstein, D.L., et al., *Changes in the structural complexity of the aged brain.* Aging Cell, 2007. **6**(3): p. 275-84.
352. Bhatt, D.H., S. Zhang, and W.B. Gan, *Dendritic spine dynamics.* Annu Rev Physiol, 2009. **71**: p. 261-82.
353. van der Zee, E.A., *Synapses, spines and kinases in mammalian learning and memory, and the impact of aging.* Neurosci Biobehav Rev, 2015. **50**: p. 77-85.

354. de Wilde, M.C., et al., *Meta-analysis of synaptic pathology in Alzheimer's disease reveals selective molecular vesicular machinery vulnerability.* Alzheimers Dement, 2016. **12**(6): p. 633-44.
355. Mendoza-Torreblanca, J.G., et al., *Synaptic vesicle protein 2A: basic facts and role in synaptic function.* Eur J Neurosci, 2013. **38**(11): p. 3529-39.
356. Becker, G., et al., *The Rise of Synaptic Density PET Imaging.* Molecules, 2020. **25**(10).
357. Serrano, M.E., et al., *Evaluating the In Vivo Specificity of [(18)F]UCB-H for the SV2A Protein, Compared with SV2B and SV2C in Rats Using microPET.* Molecules, 2019. **24**(9).
358. Mercier, J., et al., *Discovery of heterocyclic nonacetamide synaptic vesicle protein 2A (SV2A) ligands with single-digit nanomolar potency: opening avenues towards the first SV2A positron emission tomography (PET) ligands.* ChemMedChem, 2014. **9**(4): p. 693-8.
359. O'Dell, R.S., et al., *Association of Abeta deposition and regional synaptic density in early Alzheimer's disease: a PET imaging study with [(11)C]UCB-J.* Alzheimers Res Ther, 2021. **13**(1): p. 11.
360. Goyal, V.K., *Lipofuscin pigment accumulation in human brain during aging.* Exp Gerontol, 1982. **17**(6): p. 481-7.
361. Moreno-Garcia, A., et al., *An Overview of the Role of Lipofuscin in Age-Related Neurodegeneration.* Front Neurosci, 2018. **12**: p. 464.
362. Sun, A., M. Liu, and G. Bing, *Improving the specificity of immunological detection in aged human brain tissue samples.* Int J Physiol Pathophysiol Pharmacol, 2009. **2**(1): p. 29-35.
363. Pike, V.W., *PET radiotracers: crossing the blood-brain barrier and surviving metabolism.* Trends Pharmacol Sci, 2009. **30**(8): p. 431-40.
364. Dickie, B.R., et al., *Water-exchange MRI detects subtle blood-brain barrier breakdown in Alzheimer's disease rats.* Neuroimage, 2019. **184**: p. 349-358.
365. Finnema, S.J., et al., *Imaging synaptic density in the living human brain.* Sci Transl Med, 2016. **8**(348): p. 348ra96.
366. Mecca, A.P., et al., *In vivo measurement of widespread synaptic loss in Alzheimer's disease with SV2A PET.* Alzheimers Dement, 2020. **16**(7): p. 974-982.
367. Bahri, M.A., et al., *Measuring brain synaptic vesicle protein 2A with positron emission tomography and [(18)F]UCB-H.* Alzheimers Dement (N Y), 2017. **3**(4): p. 481-486.
368. Onwordi, E.C., et al., *Synaptic density marker SV2A is reduced in schizophrenia patients and unaffected by antipsychotics in rats.* Nat Commun, 2020. **11**(1): p. 246.
369. Mega, M.S., et al., *The spectrum of behavioral changes in Alzheimer's disease.* Neurology, 1996. **46**(1): p. 130-5.
370. Voorhees, J.R., et al., *Occupational-like organophosphate exposure disrupts microglia and accelerates deficits in a rat model of Alzheimer's disease.* NPJ Aging Mech Dis, 2019. **5**: p. 3.
371. Morrone, C.D., et al., *Regional differences in Alzheimer's disease pathology confound behavioural rescue after amyloid-beta attenuation.* Brain, 2020. **143**(1): p. 359-373.
372. Kloskowska, E., et al., *Cognitive impairment in the Tg6590 transgenic rat model of Alzheimer's disease.* J Cell Mol Med, 2010. **14**(6B): p. 1816-23.
373. Tournier, B.B., et al., *Spatial reference learning deficits in absence of dysfunctional working memory in the TgF344-AD rat model of Alzheimer's disease.* Genes Brain Behav, 2020: p. e12712.
374. Sare, R.M., et al., *Behavioral Phenotype in the TgF344-AD Rat Model of Alzheimer's Disease.* Front Neurosci, 2020. **14**: p. 601.
375. Petrasek, T., et al., *The McGill Transgenic Rat Model of Alzheimer's Disease Displays Cognitive and Motor Impairments, Changes in Anxiety and Social Behavior, and Altered Circadian Activity.* Front Aging Neurosci, 2018. **10**: p. 250.
376. Galeano, P., et al., *Longitudinal analysis of the behavioral phenotype in a novel transgenic rat model of early stages of Alzheimer's disease.* Front Behav Neurosci, 2014. **8**: p. 321.
377. Kotecha, A.M., et al., *Olfactory Dysfunction as a Global Biomarker for Sniffing out Alzheimer's Disease: A Meta-Analysis.* Biosensors (Basel), 2018. **8**(2).

378. Fendt, M., *Exposure to urine of canids and felids, but not of herbivores, induces defensive behavior in laboratory rats.* J Chem Ecol, 2006. **32**(12): p. 2617-27.
379. Rex, A., et al., *Strain differences in fear-motivated behavior of rats.* Pharmacol Biochem Behav, 1996. **54**(1): p. 107-11.
380. Rex, A., J.P. Voigt, and H. Fink, *Behavioral and neurochemical differences between Fischer 344 and Harlan-Wistar rats raised identically.* Behav Genet, 1999. **29**(3): p. 187-92.
381. Bert, B., et al., *Fischer 344 and wistar rats differ in anxiety and habituation but not in water maze performance.* Neurobiol Learn Mem, 2002. **78**(1): p. 11-22.
382. Lee, E.W., et al., *Unilateral degeneration of retina and optic nerve in Fischer-344 rats.* Vet Pathol, 1990. **27**(6): p. 439-44.
383. Bielefeld, E.C., et al., *Age-related hearing loss in the Fischer 344/NHsd rat substrain.* Hear Res, 2008. **241**(1-2): p. 26-33.

10 Appendix

10.1 Appendix: future publications planned

1. Methodology to measure protein synthesis rate (PSR) *in-vivo* by using [^{11}C]leucine PET imaging
2. Synaptic density decrease evaluated by using [^{18}F]UCB-H in young TgF344-AD rats

10.2 Appendix: previous published work

1. Longitudinal investigation of neuroinflammation and metabolite profiles in the APPswe×PS1Δe9 transgenic mouse model of Alzheimer's disease.
2. Prodromal neuroinflammatory, cholinergic and metabolite dysfunction detected by PET and MRS in the TgF344-AD transgenic rat model of AD - a multi-modal and multi-centre study

10.3 Appendix: poster and oral presentation

• European Association of Nuclear Medicine (EANM) (Düsseldorf, October 2018): Development of [^{11}C]leucine PET as a tool to measure brain protein synthesis in rats

• Preclinical Nuclear Imaging symposium (London, November 2018): Development of [^{11}C]leucine PET as a tool to measure brain protein synthesis in rats.

• European Molecular Imaging Meeting (Glasgow, March 2019): [^{11}C]leucine PET imaging to measure cerebral protein synthesis rate in rats.

• PET is Wonderful Annual Meeting (Edinburgh, October 2019): Measurement of protein synthesis rates by [^{11}C]leucine PET imaging in a model of Alzheimer's disease

• PhD conference at the University of Manchester (Manchester, April 2019): [^{11}C]leucine PET imaging to measure cerebral protein synthesis rate in rats

• FENS Forum of Neuroscience (on-line, July 2020): Alteration in SV2A density in transgenic rat model of AD TgF344-AD and with age measurement by [^{18}F]UCB-H *in-vivo* PET imaging

• European Molecular Imaging Meeting (EMIM) (on-line, August 2020): Alteration in SV2A density in transgenic rat model of AD TgF344-AD and with age measurement by [^{18}F]UCB-H *in-vivo* PET imaging

• European Molecular Imaging Meeting (EMIM) (on-line, August 2020): Longitudinal measure of protein synthesis rate in the transgenic rat model of Alzheimer's disease TgF344-AD by [^{11}C]leucine PET imaging

Oral presentation:

Division of Informatics, Imaging and Data Sciences Postgraduate Student Showcase (January 2018-2019-2020): Measurement of protein synthesis rates by [^{11}C]leucine PET imaging in a model of Alzheimer's disease.

10.4 Ex-vivo protocols

10.4.1 Immunohistochemistry (IHC)/Immunofluorescence

Immunofluorescence was done on WT and TG rats at different ages by using the antibodies 6E10 (Aβ marker) and GFAP (astrocyte marker) to test the presence of amyloid deposition and the increase of neuroinflammation. Brains were collected and put quickly in isopentane for few minutes and then stored at -80°. Brains were sectioned at 20µm using a cryostat (Leica CM3050s, Leica Biosystems Nussloch GmbH, Germany).

Reagents for IHC:

- in phosphate buffered saline (PBS) 1X
- Triton X-100 (to be diluted @ 0.1% in PBS 1X)
- Citrate buffer: 1,92g citric acid in 1 L H_2O + 0.05% tween. Adjust the PH with NaOH (pH=6)
- Sodium Borohydride: 1 mg/mL solution of sodium borohydride in a physiological buffer such as PBS.
- Serum: 2% normal donkey serum + 0.1% Triton X-100 in PBS
- Primary antibodies:
    - 6E10 BioLegend (803001), 1:1000
    - GFAP Dako (Z0334), 1:1000
- Alexa Fluor 488nm Donkey anti rabbit IgG 1:500 for GFAP
- Alexa Fluor 594nm Donkey anti-mouse IgG 1:500 for 6E10

Standard protocol used for 6E10 and GFAP:

- Fixation in 4% paraformaldehyde for 10 minutes at room temperature
- 6 washes in for 5 minutes in PBS

- 30 minutes incubation in 2% normal donkey serum and 0.1% Triton X-100 in PBS to permeabilize and block non-specific binding.
- Primary antibody (6E10 BioLegend (803001), 1.1000 and GFAP Dako (Z0334), 1:1000) incubation overnight at 4°C with serum
- 3 washes for 10 minutes in PBS
- Secondary antibody incubation for 2 hours at room temperature in serum
- 3 washes in PBS for 10 minutes
- Few drops of Prolong anti-fade kit (Molecular Probes, Invitrogen) with DAPI

Other factors involved in the attenuation of protein synthesis and in memory consolidation have been evaluate by using the antibodies: eIF2α (Santa Cruz, 133132), phospho-eIF2α (abcam, 32157) and ATF4 (Proteintech, 10835-1-AP). Standard protocol, antigen retrieval, sodium borohydride and DAB (3,3'-Diaminobenzidine) staining have been tested. The antigen retrieval and the sodium borohydride have few more steps compared to the standard protocol. In antigen retrieval the citrate buffer at the PH=6 is used for 20 minutes at 95˚C before the blocking step; and 3 washes per 10 minutes in sodium borohydride are present in the third protocol. The secondary antibodies used are: Alexa Fluor 594nm Donkey anti-mouse IgG 1:500 for eIF2α and Alexa Fluor 488nm Donkey anti-rabbit IgG 1:500 for phospho-eIF2α and ATF4.

10.4.2 DAB staining protocol

3,3'-Diaminobenzidine (DAB) is a derivate of benzene s an organic compound that is used in the staining of nucleic acids and proteins, most commonly for immunohistochemical procedures. When oxidised it forms water insoluble brown precipitates.

Reagents for DAB staining:

- Xylene
- Ethanol 100%
- Citrate Buffer 100mM PH=6
- Deionized dH_2O
- Peroxide 30%
- Methanol
- DAB (tablets from Sigma) 1 tablet in 5ml of deionized dH_2O

- ABC Vector Laboratories kit
- Phosphate buffered saline (PBS 1X)
- Haematoxylin
- DPX Mountant for histology

Protocol:

- Xylenefor 5 minutes
- Xylene for 5 minutes
- Ethanol 100% for 5 minutes
- Ethanol 100% for 5 minutes
- Ethanol 90% for 5 minutes
- Ethanol 70% for 5 minutes
- 3 washes in dH_2O over 5 minutes
- Citrate Buffer, PH 6 10mM, incubation for 25 minutes in pre-heated in steamer
- Wash slides in dH2O, 3 changes over 5 minutes
- Incubate slides in 0.3% Peroxide in Methanol at room temp for 30 minutes
- Wash slides in dH2O, 3 changes over 5 minutes
- Apply hydrophobic barrier around section with wax pen
- Wash slides in PBS for 5 minutes
- Block overnight in Blocking Buffer at 4˚C (from Vector Laboratories kit)
- Add primary antibody for 1 hour at room temp
- Wash slides in PBS, 3 changes over 5 minutes
- Make up biotinylated secondary antibody (from Vector kit), incubate for 30 minutes at RT. Also make ABC reagent at this time
- Wash slides in PBS, 3 changes over 5 minutes
- Incubate with ABC reagent for 30 minutes at RT
- Wash slides in PBS, 3 changes over 5 minutes
- Add DAB solution for 5 minutes
- Wash in tap water
- Counter-stain with haematoxylin for a few seconds
- Wash in tap water then dH2O
- Ethanol 70% for 5 minutes

- Ethanol 90% for5 minutes
- Ethanol 100% for 5 minutes
- Ethanol 100% for 5 minutes
- Xylenefor 5 minutes
- Xylene for 5 minutes
- Mount in DPX

10.4.3 Homogenisation samples

Half brains have also been dissected in different brain regions: hippocampus, cortex, cerebellum, striatum and rest (in which there were all the other brain parts). Dissected regions have been stored in -80˚C and used then for Western Blot (WB) analysis. The same antibodies used for IHC have been tested for WB: eIF2α (Santa Cruz, 133132), phospho-eIF2α (abcam, 32157) and ATF4 (Proteintech, 10835-1-AP).

Homogenisation reagents:

- Absolute Ethanol
- Ethanol 70%
- PBS 1X
- Homogenisation buffer:
    - Trizma® base 242.28mg
    - Sucrose 21.9mg
    - EDTA 148.9mg
- PMSF 0.1 M: 87.10mg of PMSF in 5ml of ethanol absolute
- Sodium orthovanadate 0.1M: 91.96mg of sodium orthovanadate in 5ml of distilled H_2O
- Homogenisation solution
    - PMSF 100µL
    - Sodium orthovanadate 100µL
    - Protease inhibitor cocktail complete® 1/5 tablet

Homogenisation Protocol:

- Add the homogenisation solution (10 time the sample volume).
- Gently homogenise using the pestle until a cloudy solution with no visible pieces of tissue is left.

- Centrifuge samples for 15 minutes at 3,200rpm at +4°C
- Discard the pellet (P1)
- Centrifuge supernatant for 20 min at 12,200rpm at +4°C
- Freeze supernatant at -20˚C (used)
- Suspend pellet with PBS and freeze at -20˚C

10.4.4 Bradford protein assay

The Bradford protein assay is a procedure used to determine the protein concentration in a solution. It is based on the absorbance shift of the dye reagent. Hydrophobic and ionic interactions stabilize the anionic form of the dye, causing a visible colour change.

Reagents and instruments:

- Bovine Serum Albumins (BSA) 2 mg/ml (Sigma-Aldrich)
- Protein assay dye reagent (Bio-Rad Protein Assay Dye Reagent Concentrate) dilution 1:5
- 10X Samples Buffer (Protein simple) concentration 0.1X in deionized water or the same buffer that will be used for Western Blot
- 96-well plate
- Plate reader (BioTek µQuant microplate spectrophotometer)

Procedure:

Prepare 200 µl of 2X BSA then standards:

Table 8: Preparation of standard BSA

standard	Concentration BSA [mg/ml]	Volume BSA	Volume Buffer [µl]	Final volume [µl]
F	1	150µl of **2X**	150	300
E	0.75	75µl of F	25	100
D	0.5	50µl of F	50	100
C	0.2	20µl of F	80	100
B	0.1	10µl of F	90	100
A	0	0	100	100

- Pipette 10µl of each of the BSA standards (A-F) in triplicate, putting 10µL into three wells for each standard
- In the remaining wells, pipette 10µL of your diluted samples. Once again doing each sample in triplicate
- Add 200µL of dye reagent to each well
- Leave the plate at room temperature while gently mixing on a rocker/shaker
- Red the plate at 595nM by using the spectrophotometer

10.4.5 Western Blot

To perform the Western Blot (WB) it has been used an automated Western (Protein Simple) mainly characterised by the absence of gels, transfer devices, film, etc. The advances in using the automated Wes is the possibility to process in 1 plate 25 samples and different antibodies can be used at the same time. Quantitative data are available after few hours. the immunoassay happens in a capillary in which samples are separated by size. The immobilized proteins are detected by a primary antibody, an HRP-conjugated secondary antibody and chemiluminescent substrate will be than used to generate a chemiluminescent signal that is detected and quantitated.

Reagents:

- Standard pack reagents (Wes kit):
    - DTT + 40µl deionized water
    - Fluorescent 5X master mix +20µl DTT+ 20µl 10X sample Buffer
    - Biotinylated ladder +20µl deionized water
- 10X Sample Buffer diluted with distilled or ultra-pure water to 1X
- 12-230 KDa Wes plates
- Capillary cartridge
- Deionized water
- Wes kit:
    - Luminol (200µl)
    - Peroxide (200µl)
    - Antibody diluent (min 260µl)
    - Secondary antibodies: anti-mouse, anti –rabbit
    - Streptavidin-HRP

- Primary antibodies: eIF2α, phospho-eIF2α, ATF4, GAPDH, β-actin (Aldrich A5441), PSD95 (abcam 2723), SNAP25 (abcam 5666)

Procedure:

After defining the samples concentration 1 part of 5X fluorescent master mix is combined with 4 part of lysate. Samples are then denaturation by using heat and after vortex they will be loaded on the plate.